

STATUS OF THESIS

Title of thesis

FISCHER-TROPSCH SYNTHESIS OVER MWCNT
AND SBA-15 BASED COBALT CATALYSTS
PROMOTED WITH RUTHENIUM

I ADKHAM YAKUBOV
(CAPITAL LETTERS)

hereby allow my thesis to be placed at the Information Resource Center (IRC) of
Universiti Teknologi PETRONAS (UTP) with the following conditions:

1. The thesis becomes the property of UTP
2. The IRC of UTP may make copies of the thesis for academic purposes only.
3. This thesis is classified as

Confidential

Non-confidential

If this thesis is confidential, please state the reason:

The contents of the thesis will remain confidential for _____ years.

Remarks on disclosure:

Endorsed by

Signature of Author

Signature of Supervisor

Permanent address: Uchtepa District,
Nashriyot st. 79. Tashkent, Uzbekistan

Dr. Maizatul Shima Shaharun

Date: _____

Date: _____

FISCHER-TROPSCH SYNTHESIS OVER MWCNT
AND SBA-15 BASED COBALT CATALYSTS
PROMOTED WITH RUTHENIUM

By

ADKHAM YAKUBOV

The undersigned certify that they have read, and recommend to the Postgraduate Studies Programme for acceptance this thesis for the fulfillment of the requirements for the degree stated.

Signature: _____

Main Supervisor: Dr. Maizatul Shima Shaharun

Signature: _____

Co-Supervisor: Dr. Suriati Sufian

Signature: _____

Head of Department: Assos. Prof. Dr. Mohd Azmi B Bustam

Date: _____

FISCHER-TROPSCH SYNTHESIS OVER MWCNT
AND SBA-15 BASED COBALT CATALYSTS
PROMOTED WITH RUTHENIUM

by

ADKHAM YAKUBOV

A Thesis

Submitted to the Postgraduate Studies Program

as a Requirement for the Degree of

MASTERS OF SCIENCE

CHEMICAL ENGINEERING

UNIVERSITI TEKNOLOGI PETRONAS

BANDAR SERI ISKANDAR,

PERAK

JUNE 2013

DECLARATION OF THESIS

Title of thesis

FISCHER-TROPSCH SYNTHESIS OVER MWCNT
AND SBA-15 BASED COBALT CATALYSTS
PROMOTED WITH RUTHENIUM

I _____ ADKHAM YAKUBOV
(CAPITAL LETTERS)

hereby declare that the thesis is based on my original work except for quotations and citations which have been duly acknowledged. I also declare that it has not been previously or concurrently submitted for any other degree at UTP or other institutions.

Witnessed by

Signature of Author

Signature of Supervisor

Permanent address: Uchtepa district,
Nashriyot st. 79. Tashkent, Uzbekistan

Dr. Maizatul Shima Shaharun

Date: _____

Date: _____

DEDICATION

This thesis is especially dedicated to my beloved family. I am eternally grateful for their sincere support over the course of my studies and their unconditional endless love. May Allah bless them always.

ACKNOWLEDGEMENTS

I am heartily thankful to my dear supervisors Dr Maizatul Shima Shaharun and Dr Suriati Sufian for their encouragement, guidance and support which enabled me to develop, understand and complete this exciting project.

Also I would like to express my sincere appreciation to Professor Sharifa Bee Abd Hamid and all members of COMBICAT for aiding me with sample characterizations as well as technical support, besides creating a motivated and enjoyable working environment.

My great appreciation also goes to Dr. Muralithran Kutty who really helped and supported me with valuable ideas and thoughts over the course of my experimental period.

I am sincerely thankful also to my research mate Siew Pei Lee and Jasvinder Singh Gill for supporting me in any respect during the completion of the project. Not forgotten, gratitude also goes to my dear friend Davron Yusupov for his kind assistance.

I am also grateful to Mr. Idrus Mr Anuar and Mr. Hisbullah for providing the assistance with necessary analytical equipment, and to all technicians from Chemical Engineering Department.

Last but not least, I am thankful to my family and friends for their continuous encouragement and help.

ABSTRACT

Gas-to-Liquid (GTL), in particular Fisher-Tropsch synthesis (FTS) is a process of converting coal, natural gas and biomass derived synthesis gas into transportable liquid fuels. A series of ruthenium promoted Co catalyst supported on multiwall carbon nanotube (MWCNT) and Santa Barbara amorphous (SBA-15) were prepared by incipient wetness impregnation method. In addition 10Co/MWCNT and 10Co/SBA-15 were prepared as the reference catalysts to study the effect of ruthenium promoter. The catalysts and support materials were characterized by field emission scanning electron microscope (FESEM) equipped with energy dispersive X-ray spectroscopy (EDX), surface area analyzer, X-ray diffractometer (XRD), transmission electron microscope (TEM) and temperature-programmed reduction (TPR). Characterization results showed that cobalt particles were formed in the range of 3.4 to 8.3 nm. The pore size of MWCNT and SBA-15 after cobalt/ruthenium impregnation was between 6.4 to 8.8 nm. FTS was carried out under reaction temperature of 493 K, total gas pressure of 2 MPa and 1 g of catalyst, using semi-batch three phase stirred reactor where the catalyst was suspended in *n*-hexadecane. The best performance was observed in 10Co/SBA-15 (S2) based catalyst showing 98.6 % of CO conversion and better yield of liquid hydrocarbon (HC) which is 17,765 ppm. The lowest CO conversion (92%) is observed using unpromoted 10Co/MWCNT (M2) catalyst. However, the selectivity to C₈₊ hydrocarbons was very low, around 3% in both, unpromoted and promoted MWCNT and SBA-15 based catalysts. Low selectivity of catalysts can be attributed to small cobalt particle size (3.4-8.3 nm) and narrow pore size (6.4-8.8 nm) of the catalysts. In such characteristics tendency of CH₄ and gaseous products formation is high.

Addition of ruthenium oxide did not make significant contribution to product yield, but positively affected the catalyst reduction temperature and metal particle size dispersion on MWCNT.

ABSTRAK

Gas-ke-cecair (GTL), khususnya Sintesis Fisher-Tropsch (FTS) merupakan satu proses penukaran arang batu, gas asli dan sintesis gas berasaskan biomas kepada bahan bakar cecair boleh angkut. Satu siri pemangkin Co yang dianjurkan oleh ruthenium dan disokong atas karbon nanotub berbilang-dinding (MWCNT) dan gumpalan SBA-15 telah disediakan melalui kaedah penyerapan. 10Co/MWCNT dan 10Co/SBA-15 telah disediakan sebagai pemangkin rujukan untuk mengkaji kesan penganjuran ruthenium. Pencirian pemangkin dan bahan sokongan telah dicirikan dengan menggunakan mikroskop imbasan elektron medan pencahayaan (FESEM) yang dilengkapi dengan spektroskopi serakan tenaga sinar-X (EDX), penganalisa luas permukaan, kaedah pembelauan sinar-X (XRD), mikroskop pancaran elektron (TEM) dan proses penurunan suhu berprogram (TPR). Keputusan pencirian menunjukkan saiz partikel Co adalah dalam lingkungan 3.4-3.8nm. Manakala, saiz liang bagi MWCNT dan SBA-15 selepas penyerapan cobalt/ruthenium adalah antara 6.4-8.8 nm. Sintesis FT telah dijalankan pada suhu tindakbalas 493 K, manakala jumlah tekanan gas pada 2 MPa dan 1 g pemangkin dengan menggunakan reaktor boleh-aduk di mana pemangkin bertebaran dalam pelarut n-hexane. Perlaksanaan yang terbaik telah dikaji dalam pemangkin berdasarkan 10Co/SBA-15 (S2) yang menunjukkan perubahan CO sebanyak 98.6% dan hasil cecair hidrokarbon yang lebih baik iaitu 17,765 ppm. Perubahan CO yang paling rendah iaitu 92% didapati dengan menggunakan pemangkin 10Co/MWCNT (M2). Walaubagaimanapun, penghasilan hidrokarbon (HC) C₈₊ adalah sangat rendah iaitu 3% dalam kedua-dua pemangkin MWCNT juga SBA-15 yang dianjurkan dan tidak dianjurkan. Pemangkin yang mempunyai kebolehpilihan yang rendah boleh dikaitkan dengan pemangkin yang mempunyai saiz partikel kobalt yang kecil (3.4-8.3 nm) dan saiz liang yang sempit (6.4-8.8 nm). Dalam kecenderungan pencirian, CH₄ dan penghasilan formasi gas adalah tinggi.

Penambahan ruthenium oksida tidak menyumbangkan hasil produk tetapi memberi kesan positif kepada penurunan suhu pemangkin dan penyebaran partikel logam di atas MWCNT.

In compliance with the terms of the Copyright Act 1987 and the IP Policy of the university, the copyright of this thesis has been reassigned by the author to the legal entity of the university,

Institute of Technology PETRONAS Sdn Bhd.

Due acknowledgement shall always be made of the use of any material contained in, or derived from, this thesis.

© Adkham Yakubov, 2012

Institute of Technology PETRONAS Sdn Bhd

All rights reserved.

2.2.1	Catalyst preparation methods.....	12
2.2.2	Incipient wetness impregnation method	13
2.3	Fischer-Tropsch synthesis process	14
2.3.1	Overall background of Fischer-Tropsch synthesis (FTS).....	14
2.3.2	Chemistry and mechanism of Fischer-Tropsch synthesis.....	16
2.3.3	Synthesis gas as a raw material for FT process	18
2.3.4	Fisher-Tropsch synthesis products.....	19
2.3.5	Fischer-Tropsch synthesis catalysts	23
2.3.6	FT reactors	28
2.4	Characterization of catalyst support and catalyst precursors	34
2.4.1	BET surface area measurements	34
2.4.2	Thermogravimetric Analysis - Mass Spectroscopy (TGA-MS)	34
2.4.3	Field Emission Scanning Electron Microscope/Energy Dispersive X-Ray (FESEM/EDX).....	36
2.4.4	X-Ray Diffraction (XRD)	38
2.4.5	Temperature Programmed Reduction (TPR)	40
2.4.6	Transmission Electron Microscopy (TEM).....	41
2.5	Multiwall Carbon Nanotubes (MWCNT) and Multiwall carbon Nanofibers (MWCNF) as a catalyst support	42
2.6	Santa Barbara amorphous - 15 (SBA-15) as a catalyst support	42
2.7	CNT and CNF based Co/Ru catalysts for FTS and CO hydrogenation	43
2.8	SBA-15 based Cobalt and Ruthenium catalysts for FTS	51
2.9	Pore size effect on FTS	54
2.10	Particle size effects on FTS	55
2.11	Fischer-Tropsch synthesis in slurry environment	57
CHAPTER 3.....		60
MATERIAL AND EXPERIMENTAL METHOD		60
3.1	Materials.....	60
3.2	Preparation of catalyst support.....	61
3.2.1	Multi Wall Carbon Nanotube (MWCNT).....	61
3.2.2	Santa Barbara Amorphous -15 (SBA-15)	63

3.3	Preparation of catalyst.....	64
3.3.1	10Co/1Ru/MWCNT and SBA-15 supported catalyst.....	65
3.3.2	Nomenclature of prepared catalysts.....	65
3.4	Reactor system	66
3.4.1	Catalyst reduction	66
3.4.2	Glove box for transferring reduced catalyst from fixed bed reduction system to autoclave vessel	69
3.4.3	Reactor system (Description of 200mL Autoclave Batch reactor)71	
3.5	Fischer-Tropsch synthesis.....	73
3.5.1	Pressure test	75
3.5.2	Catalyst activity studies	77
3.6	Characterization of catalyst support and catalyst precursors	80
3.6.1	BET surface area measurements.....	80
3.6.2	Thermogravimetric Analysis - Mass Spectroscopy (TGA-MS)...	80
3.6.3	Field Emission Scanning Electron Microscope/Energy Dispersive X-Ray (FESEM/EDX)	81
3.6.4	X-Ray Diffraction (XRD).....	81
3.6.5	Temperature Programmed Reduction (TPR).....	82
3.6.6	Transmission Electron Microscopy (TEM)	82
3.7	Product characterization.....	82
3.7.1	Gas Chromatography	82
3.7.2	Product analysis by Gas chromatography.....	83
3.7.3	GC/MS and oven conditions.....	85
CHAPTER 4		86
RESULTS AND DISCUSSION		86
4.1	Support material characterization	86
4.1.1	Characterization of MWCNT	86
4.1.2	Characterization of pure SBA-15	92
4.2	Characterization of MWCNT and SBA-15 supported cobalt catalysts 96	
4.2.1	Determination of calcination temperature.....	96

4.2.2	Morphology and particle size distribution in Co/Ru/MWCNT catalysts	102
4.2.3	Morphology and particle size distribution in Co/Ru/SBA-15 catalysts	106
4.2.4	Elemental composition analysis of MWCNT and SBA-15 based catalysts	111
4.2.5	Surface area, pore volume and porosity of MWCNT and SBA-15 based Co/Ru catalysts.....	115
4.2.6	Cobalt crystallite size and its chemical form in MWCNT and SBA-15 based Co/Ru catalysts	118
4.2.7	Catalyst reducibility	120
4.2.8	Particle size and distribution of metal oxides	127
4.3	The Fischer-Tropsch activity of the catalysts	134
4.3.1	CH yield, and its relation to particle size and pore size.....	137
4.3.2	Analysis of CO conversion and Selectivity	140
CHAPTER 5.....		146
CONCLUSION AND RECOMMENDATIONS.....		146
5.1	Conclusion.....	146
5.2	Recommendations	148
REFERENCES.....		151
APPENDIX A		167
APPENDIX B		168
APPENDIX C		172
APPENDIX D		187

LIST OF TABLES

Table 1.1: Operation parameters, typical dimensions and selectivity data of three reactor types (Fe catalyst) [13].....	5
Table 2.1: Summary of major findings	59
Table 3.1: List of chemicals and gas used in the experiments	61
Table 3.2: Specifications of unpurified MWCNT.....	62
Table 3.3: Codes of prepared catalysts	66
Table 3.4: Constituents of reduction system	67
Table 3.5: Specifications of 200 mL autoclave hastelloy reactor	71
Table 3.6: Reduction parameters of MWCNT and SBA-15 supported cobalt catalysts	74
Table 3.7: Fischer-Tropsch reaction parameters of MWCNT and SBA-15 supported cobalt catalysts	74
Table 3.8: Consumption of feed gas and calculated moles of CO using Ideal Gas Equation	79
Table 3.9: Details of the “BPX5” GC column produced by SGE Analytical Science	84
Table 4.1: BET measurements of unpurified/purified MWCNT and Pure SBA-15..	89
Table 4.2: Elemental composition of MWCNT and SBA-15 based catalysts	114
Table 4.3: Results of BET measurements of MWCNT and SBA-15 supported catalysts	117
Table 4.4: Cobalt crystallite sizes of MWCNT and SBA-15 based catalysts	120
Table 4.5: Particle size details of cobalt oxide deposited on MWCNT and SBA-15 catalysts	128
Table 4.6: Overall concentrations and concentrations of certain products (in ppm)	135
Table 4.7: Relation of product yield to cobalt particle size and pore size of the support.....	140

LIST OF FIGURES

Figure 2.1: Generic potential energy diagram showing the effect of a catalyst[23] ..	11
Figure 2.2: The main mechanism of FT reaction [1].	16
Figure 2.3: Current (2004) High Temperature Fischer-Tropsch refinery used at Secunda [1].....	21
Figure 2.4 a and b : (a) (LEFT) The Multiubular Fixed Bed Reactor and (b) (RIGHT) Slurry Phase Bubbling Bed Reactors [1].....	29
Figure 2.5: (a) (LEFT) Circulating fluidized bed reactor CFB; (b) (right) fixed fluidized bed reactors FFB [1]	31
Figure 2.6: A schematic of a thermo analysis setup.....	35
Figure 2.7: TGA spectrum of multiple process types. (a) Thermal decomposition with the formation of volatile compounds. (b) Metal oxidation. (c) Combustion when gas switches from N ₂ to O ₂ . (d) Multi step decomposition. (e) Explosive decomposition with recoil effect	36
Figure 2.8: Functional parts of a Scanning Electron Microscope	37
Figure 2.9: X-ray reflection on two atomic planes of a crystalline solid	39
Figure 2.10: FTS rate, %CO conversion, WGS rate and product selectivity of the A ₁ and C ₁ catalysts (T=220 °C, P=1 bar and H ₂ /CO=2) [88].....	44
Figure 2.11: TEM image showing cobalt particles with high dispersion for the acid treated loaded catalyst and showing the open caps of the CNTs: (A) Outside, (B) Inside. [90]	45
Figure 3.1: Reflux system	63
Figure 3.2: Catalyst preparation diagram.....	64
Figure 3.3: Catalyst reduction system	68
Figure 3.4: Image of self-designed glove box.....	69
Figure 3.5: Autoclave reactor which is located in COMBICAT University Malaya (A - general view)	72
Figure 3.6: Autoclave reactor which is located in COMBICAT University Malaya (B - detailed view).....	73
Figure 3.7: Schematic diagram of the experimental set-up.....	73

Figure 3.8: Data of feed gas consumption identified by reactor	78
Figure 3.9: The GC 7890A” and Mass Spectroscopy with the series of “5975” produced by Agilent Technologies	84
Figure 3.10: Oven conditions	85
Figure 4.1: The HRTEM of MWCNT (A) Pristine and (B) purified.....	87
Figure 4.2: Chemical composition of MWCNT before and after purification	88
Figure 4.3: N ₂ sorption isotherm of (A) unpurified, (B) purified MWCNT and (C) pure SBA-15	90
Figure 4.4: XRD results for unpurified and purified MWCNT	92
Figure 4.5: HRTEM of pure SBA-15 S1 (A) – front view, S1 (B) – side view.....	93
Figure 4.6: FESEM images of pure SBA-15 in different magnifications (A) 50K, (B) 5K, (C) 10K.....	94
Figure 4.7: EDX results of Pure SBA-15.....	95
Figure 4.8: XRD results of pure SBA-15.....	95
Figure 4.9: Thermal decomposition of 10Co/MWCNT and 10Co/SBA-15	96
Figure 4.10: Thermal decomposition of 10Co/1Ru/MWCNT.....	97
Figure 4.11: Mass Spectroscopy results using 10Co/1Ru/MWCNT	98
Figure 4.12: The result of blank MWCNT towards weight loss.....	99
Figure 4.13: Thermal decomposition of 10Co/1Ru/SBA-15	100
Figure 4.14: Mass Spectroscopy results using 10Co/1Ru/SBA-15	101
Figure 4.15: TEM images of 10Co/1Ru/MWCNT (M3) in different dimensions: A) 10 nm, B) 20 nm, C) 50 nm	103
Figure 4.16: TEM images of 30Co/1Ru/MWCNT (M4) in different dimensions: A) 20 nm, B) 50 nm, C) 100 nm	103
Figure 4.17: TEM images of 10Co/MWCNT (M2) in different dimensions: A) 10 nm, B) 20 nm, C) 100 nm	105
Figure 4.18: FESEM images of 10Co/1Ru/MWCNT (M3) and 30Co/1Ru/MWCNT (M4) catalysts at different magnifications: M3 :- A) 50K, B) 100K, C) 100K, and M4 :-A) 20K, B) 100K, C) 100K.....	106
Figure 4.19: The HRTEM images of 10Co/SBA-15 (S2), 10Co/1Ru/SBA-15 (S3) and 30Co/1Ru/SBA-15 (S4) in different dimensions: S2 – A) 100 nm, B) 100 nm, S3 – A) 10 nm, B) 50 nm, C) 100 nm, S4 – A) 10 nm, B) 20 nm, C) 100 nm.	107

Figure 4.20: FESEM images of Pure SBA-15 (S1), 10Co/1Ru/SBA-15 (S3) and 30Co/1Ru/SBA-15 (S4) catalysts in different magnifications: S1: – A) 10K, B) 10K, C) 50K; S3: –A) 10K, B) 50K, C) 50K; S4: – A) 10K, B) 50K, C) 50K.....	110
Figure 4.21: EDX of 10Co/MWCNT (M2)	112
Figure 4.22: EDX of 10Co/1Ru/MWCNT (M3).....	112
Figure 4.23: EDX of 30Co/1Ru/MWCNT (M4).....	113
Figure 4.24: EDX of 10Co/1Ru/SBA-15 (S3)	114
Figure 4.25: EDX of 30Co/1Ru/SBA-15 (S4)	114
Figure 4.26: Nitrogen sorption isotherms of M2 (A) and M4 (B) catalysts.....	115
Figure 4.27: Nitrogen sorption isotherm of S3 (A) and S4 (B) catalysts.....	116
Figure 4.28: XRD patterns of MWCNT and SBA-15 based Co/Ru catalysts	119
Figure 4.29: TPR results of 10Co/MWCNT (M2), 10Co/1Ru/MWCNT (M3), 30Co/1Ru/MWCNT catalysts	122
Figure 4.30: TPR results of 10Co/SBA-15 (S2), 10Co/1Ru/SBA-15 (S3) and 30Co/1Ru/SBA-15 (S4) catalysts.....	125
Figure 4.31: Cobalt particle size distribution in MWCNT and SBA-15 based catalysts	130
Figure 4.32: Concentration of light fuel fractions and wax	137
Figure 4.33: Percentage of CO conversion and C ₈₊ selectivity.....	141

LIST OF SYMBOLS

γ -alumina	-	Gamma type Alumina
Co	-	Cobalt atom
Ru	-	Ruthenium Atom
Al	-	Alumina Atom
Å	-	Angstrom unit (10 ⁻¹⁰ m)
θ	-	Reflection/diffraction angle, ° Theta
λ	-	Wavelength radiation (nm)
Nm	-	nanometer
keV	-	Kilo electroVolt
R	-	Ideal gas constant,
T	-	Temperature, °C
P	-	Pressure, bar
RPM	-	Rotation per minute
Mol	-	moles
Wt%	-	Weight percentage
MW	-	Molecular weight.
ρ	-	Density, cm ³ /g
CO conv.	-	Conversion of CO, %
gcat	-	Catalyst mass, g
S	-	Selectivity of product %

LIST OF ABBREVIATIONS

Syngas	-	Synthesis gas (CO+H ₂)
Ar	-	Argon
He	-	Helium
CO	-	Carbon monoxide
CO ₂	-	Carbon dioxide
H ₂	-	Hydrogen
CH ₄	-	Methane
C ₅₊	-	Carbon ₅₊
N ₂	-	Nitrogen
NO	-	Nitrogen monoxide
NO ₂	-	Nitrogen dioxide
HNO ₃	-	Nitric acid
HCl	-	Hydrochloric acid
TEOS	-	Tetraethyl orthosilicate
C ₂ H ₅ OH	-	Ethyl alcohol
Co(NO ₃) ₂ ·6H ₂ O	-	Cobalt (II) nitrate hexahydrate
(C ₅ H ₇ O ₂) ₃ Ru	-	Ruthenium (III) acetylacetonate for synthesis
MWCNT	-	Multi Wall Carbon Nanotubes
CNF	-	Carbon Nanofibers
SBA-15	-	Santa Barbara Amorphous -15
Ppm	-	Part per million
TEM	-	Transmission electron microscopy

CHAPTER 1

INTRODUCTION

This chapter deals with general overview of Fischer-Tropsch synthesis (FTS) and specifically includes its very brief history of development, chemistry of FTS and its commercial implementation. Technology has been matured over the course of eighty years which allows production of synthetic oil products, high quality waxes and ultraclean motor fuels. Since FT technology occurs in the catalytic environment, types of utilized catalysts with its catalyst supports and reaction parameters are included. Problem statement enlightens current challenges in the field of FT technology. Research activities, such as, catalyst preparation, its physical and chemical comparison, their characterizations are briefly included. Materials of this chapter can be considered as a brief review for the following chapters.

1.1 Fischer-Tropsch Technology

The Fischer-Tropsch (FT) process obtained its name from inventors Franz Fischer and Hans Tropsch, the German coal researchers who discovered in 1923 synthesis of valuable hydrocarbons and motor fuels through catalytic process. Fischer-Tropsch Synthesis (FTS) is the heart of Gas to Liquid (GTL) technologies. Almost exclusively the FTS process is carried out in the presence of heterogeneous cobalt or iron catalysts. The advantages of the Co catalysts are the milder reaction conditions and higher activity when the feedstock is natural gas [1], [2]. The catalysts consist of metal promoted cobalt and iron supported on high-surface-area binders or supports such as silica, alumina, or zeolites. Commonly the FTS reactions are carried out in multi-tubular fixed bed, fluidized bed and slurry reactors operated at about 20-30 bars and 200-350°C [3], [4]. Depending on process conditions and the type of the

catalyst, the high quality fuels and valuable chemicals are produced in FTS process [5].

Generally there are two operation modes in Fischer-Tropsch synthesis which are “High temperature Fischer-Tropsch” (HTFT) and “Low Temperature Fischer-Tropsch” (LTFT). Temperature in HTFT varies in the range of 300 to 350°C while operation of LTFT occurs in 200 to 260°C. Choice of reactor and catalyst in it, strongly depend on the desired product. The key distinguishing attribute between HTFT and LTFT reactors is that process in high temperature Fischer-Tropsch includes “two phase” which is solid and gas. Catalyst is not surrounded by liquid phase (solvent of product). Formation of liquid phase is unacceptable in HTFT which will lead to serious problems such as catalyst agglomeration and loss of fluidization [1], [6]. LTFT takes place in “three phase” which means catalyst is surrounded by liquid phase. HTFT with iron based catalysts is applied for the production of gasoline and low molecular mass olefins, while LTFT with either iron or cobalt catalysts is used for the production of high molecular mass linear waxes and further ultra clean diesel fuel.

As mentioned above, cobalt catalysts are preferred choice for FTS when the source is natural gas derived synthesis gas. The water-gas shift activity of cobalt-based catalysts is low and water is the main oxygen containing by-product of the reaction. Also cobalt-based catalysts are very suitable for wax formation in slurry bubble columns and can operate at high per pass conversion.

Preparation of cobalt supported catalysts involves several important steps: choice of appropriate catalyst support, choice of active metal deposition method, catalyst promotion, oxidative and reductive treatments and so on. The goal of active metal deposition is to spread cobalt onto porous supports. In industrial scale silica, titania or alumina are used widely as a catalyst carriers [7]. Except conventional catalyst supports, new materials such as multiwall carbon nanotubes (MWCNT) and mesoporous silica materials that is, Santa-Barbara-Amorphous-15 (SBA-15) have been proposed as a new type of catalyst supports for heterogeneous catalysts [8][9] [10]. Studies comparing the catalytic activity of metal catalysts supported on various

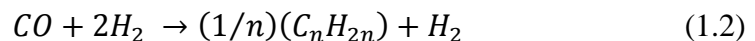
oxides, amorphous carbon and CNTs showed that catalytic performance was generally excellent on CNTs. Serp. *et al.*[11]in their research described mechanical and thermal properties of CNTs that they are very flexible and can be bent several times at 900°C without undergoing structural changes. The use of SBA-15 as a support for preparing Co-based catalysts has been recently explored [10]. SBA-15 possesses a high surface area (600-1000 m²/g) and is formed by a hexagonal array of uniform tubular channels with pore diameters ranging from 5 to 30 nm. Also SBA-15 possesses thicker pore walls. In their work D. Zhao *et al.* [12] identified that thicker walls lead to the greater hydrothermal stability.

Resources such as natural gas, coal and biomass can be efficiently converted to valuable synthetic hydrocarbons via Fischer Tropsch synthesis. Unlike LNG production, FTS involves chemical process for converting those resources into liquid hydrocarbons. There are 3 general steps in FTS which are:

- Synthesis gas generation.
- Synthesis gas conversion to liquid hydrocarbons.
- Upgrading of initial hydrocarbon wax into valuable fuel and chemical feedstocks.

In FT synthesis, gas generation is considered the most costly part of the whole process. Almost 50% of the total capital is spent for generation of synthesis gas.

The chemistry of Fischer-Tropsch synthesis process can be described by the following set of reactions:



Reaction (1.1) is the formation of methane, reaction (1.2) is the synthesis of hydrocarbons heavier than methane, reaction (1.3) is the water gas shift reaction and reaction (1.4) is the Boudouard reaction resulting in deposition of carbon. Generally, nickel catalysts are very active for reaction (1.3) relative to reaction (1.4) and hence

most selective for methane compared to Co, Fe and Ru catalysts; under typical synthesis conditions (e.g. 180 - 250°C, H₂ : CO = 2) the latter three catalyst types promote reaction (1.4). Relative to reaction 1.3 and hence are more selective for C₂₊ hydrocarbons. However, the selectivity for C₂₊ hydrocarbons is strongly influenced by reaction conditions and catalyst composition. For example, C₂₊ hydrocarbon makes decreases while methane makes increases with increasing H₂:CO ratio, increasing reaction temperature and decreasing pressure [7].

In Fischer-Tropsch synthesis hydrocarbon product selectivities are determined by the ability of a catalyst to catalyze chain propagation versus chain termination steps. The distribution of hydrocarbon products in FTS is generally described by a chain polymerization kinetics model involving the stepwise addition of one carbon atom to the growing chain. This model is ascribed to Anderson, Schulz and Flory henceforth referred to as the Anderson-Schulz-Flory (ASF) model. The ASF product distribution is mathematically represented by the equation:

$$W_n/n = (1 - \alpha)^2 \alpha^{n-1} \quad (1.5)$$

where n is the number of carbon atoms in the product, W_n is a weight fraction of product containing n carbon atoms, α is the chain growth propagation probability [7]. Generally the value of α is obtained by a least squares linear regression of the logarithmic form of equation 1.5, the slope and intercept yielding α:

$$\ln(W_n/n) = 2 \ln(1 - \alpha) + (n - 1) \ln \alpha \quad (1.6)$$

Values of α are influenced in the same way as C₂₊ hydrocarbon selectivity by reaction conditions and catalyst composition [3], [7]. For example, values of α increase with decreasing H₂:CO ratio, decreasing reaction temperature and increasing pressure. Operation parameters and typical dimensions of commercial reactors are provided in Table 1.1.

Table 1.1: Operation parameters, typical dimensions and selectivity data of three reactor types (Fe catalyst) [13]

	Multi-tubular fixed bed reactor	Riser reactor	Slurry reactor
<i>Dimensions</i>			
Reactor length (m)	12	46	22
Reactor Ø (m)	-	2.3	5
Tube Ø (m)	0.05	-	-
Number of tubes	>2000	-	-
Catalyst	Extrudates (1-3mm)	40-150µm	~50µm
<i>Conditions</i>			
Inlet T (°C)	223	320	260
Outlet T (°C)	236	325	265
Pressure (bar)	25	23	15
H ₂ /CO feed ratio	1.7	2.54	0.68 ^a
Conversion (%)	60-66	85	87
<i>Products (wt. %)</i>			
CH ₄	2.0	10.0	6.8
C ₂ H ₄	0.1	4.0	1.6
C ₂ H ₆	1.8	4.0	2.8
C ₃ H ₆	2.7	12.0	7.5
C ₃ H ₈	1.7	2.0	1.8
C ₄ H ₈	2.8	9.0	6.2
C ₄ H ₁₀	1.7	2.0	1.8
C ₅ H ₁₁ (gasoline)	18.0	40.0	18.6
C ₁₂ H ₁₈ (diesel)	14.0	7.0	14.3
C ₁₉₊ (waxes)	52.0	4.0	37.1
Oxygenates	3.2	6.0	1.0

Note:^a - High ratio is also possible

1.2 Problem Statement

Due to the high cost of cobalt catalyst, it is required to minimize the quantity of cobalt metal up to an optimum amount, and at the same time to have a high cobalt metal surface area, high catalyst activity and stability. This is usually achieved by supporting cobalt on different supports such as silica, titania or alumina. These catalyst supports are high surface area metal oxides. Nevertheless, the drawback of using these supports is their reactivity towards Co metal which could lead to formation of mixed oxides (aluminate or silicate) [2]. The formation of Co support compounds is irreversible, and it is difficult to be reduced even at temperature of 700°C [14]. Insufficient reduction of Co species on the support surface causes the number of active sites to decrease and therefore degrades the catalytic properties of the catalyst [15]. Strengthening of catalyst quality by MWCNT and SBA-15 supports has been attracting the attention of researchers.

Since FT synthesis is highly exothermic [16], it is important to efficiently remove the heat of reaction from the catalyst particles in order to avoid overheating of the catalyst which would otherwise result in an increased rate of deactivation due to sintering and fouling and also in the undesirable high production of methane.

1.3. Research Hypothesis

To address the above problems in FT process, the research work is based on the following hypothesis:

- I. Carbon materials have inert surface and possibility to form cobalt aluminates and silicates are very low. Carbon material is considered as possible new supports for FT reactions due to the unique properties such as uniform pore size distribution, meso and macro pore structure, inert surface properties, and resistance to acid and base environment [88, 105].
- II. SBA-15 has recently been synthesized and was found to possess a high surface area (600–1000 m² g⁻¹) and hexagonal array of uniform tubular

channel with pore diameters ranging from 5 to 30 nm. These characteristics make it suitable for use as support for FT synthesis [10].

- III. The use of catalyst promoter as ruthenium will improve CO conversion, volumetric productivity, C₅₊ selectivity and catalyst reducibility due to its synergetic effect with cobalt.
- IV. The reaction will be more favorable when it is carried out in slurry phase/medium comparing to fixed bed system, as liquid medium efficiently removes heat of reaction comparing to gas phase.

1.4. Objective of Study

- I. To synthesize Co and Co-Ru catalyst supported on MWCNT and SBA-15 using wet impregnation method.
- II. To study physicochemical properties of the catalysts.
- III. To investigate the performance of the catalysts using semi – batch slurry reactor.
- IV. To characterize produced FT wax in terms of product distribution.

1.5. Scope of Study

Catalysts consist of support and active metals. MWCNT was commercially obtained and purified. Before and after purification of MWCNT, it was characterized by N₂-adsorption, FESEM/EDX, XRD and TEM. Mesoporous silica SBA-15 was synthesized and characterized by aforementioned techniques. Loading of 10, 30 wt% Cobalt and 1wt% ruthenium precursors will be deposited on SBA-15 and MWCNT supports via incipient wetness impregnation method. MWCNT and SBA-15 based catalysts with 10wt% cobalt and was prepared as a reference catalyst in order to evaluate the effects of ruthenium as a promoter. Based on the active metals' feature, choice of solvent, either distilled water or alcohol (ethanol) for incipient wetness

impregnation was chosen. Further catalysts were characterized by using N₂-adsorption, TG-MS, XRD, FESEM & EDX, TPR and TEM.

Evaluation of ruthenium promoted cobalt catalysts will be carried out in a batch stirred reactor. Parameters of the reaction are chosen based on the reaction parameters of the commercialized FTS process which are T = 220°C, P = 20 bar and feed gas ratio (H₂/CO) = 2 to 1. In needed basis, reactor will be modified to continuous flow system from batch system. Produced FT wax is expected to be characterized in terms of product distribution.

CHAPTER 2

LITERATURE REVIEW

2.1 Gas To Liquid (GTL) technology

2.1.1 GTL technology as a process for conversion of gas phase to liquid

GTL is the process of converting natural gas, coal or biomass into a longer chain transportable hydrocarbons[19]. Even though production of Liquefied Natural Gas (LNG) looks like one of the forms of GTL technology, it is excluded from this group. Unlike LNG process, GTL technology involves and represents chemical process which is generation of synthesis gas (mixture of CO and H₂) and its conversion to liquid hydrocarbons. Ammonia synthesis, Methanol synthesis and Fischer-Tropsch synthesis are noticeable representatives of this technology. The key factors that drive growth in the GTL industry are:[5], [20].

- The necessity to monetize the considerable existing stranded natural gas reserves
- The market and legislative demand for cleaner fuels and new cheaper chemical feedstock
- Technological advancement which is leading to cost effectiveness of FTS technology from development of more active catalysts and improved reactor systems
- Increased interest from gas-rich host countries
- The need to diversify economies and to create new employment opportunities

The GTL process can be divided into three steps; syngas generation, syngas conversion and hydro processing [21]. Syngas generation typically accounts for more than 50% of the capital expenditure in the process [22]. Syngas can be generated from steam reforming, partial oxidation, autothermal reforming or combined two step reforming of methane [21]. Syngas conversion is the core of the process and the aim here is to produce paraffinic wax using low temperature FTS, preferably on cobalt catalysts. Last step is hydroprocessing where wax is hydroisomerized /hydrocracked to produce diesel (C₁₁-C₁₈) and naphtha (C₅-C₁₀) [7], [1].

2.2 Catalytic process and catalysts

Catalysis is a process which accelerates the rate of the reaction due to the participation of the substance called “catalyst”. The origin of word “catalysis” comes from Greek Katalysis “dissolution”, from Katalyein “to dissolve”. There are presently four basic variables available to control chemical reactions. They are: Temperature, Pressure, Concentration, and Contact time. Application of the phenomena called “catalysis” to the chemical process contributes to the lowering the expenditure of the aforementioned reaction parameters which will eventually effect to the cost of the product production.

Nowadays our modern life is almost unimaginable without catalytic processes. Economy in the global scale is fully based on catalytic production of chemicals and fuels – over USD 10 trillion per year [7]. Much of foods we consume and clothes we use are preprocessed catalytically. Fuels our vehicles burn every day produced through catalytic process. And generally nearly all chemicals, fuels, polymers drugs and fibers are manufactured which we use in our daily life today go through certain catalytic process.

A catalyst is a substance that changes the speed of a chemical reaction without undergoing a permanent chemical change itself in the process. Overall scheme of catalytic process is shown in Figure 2.1.

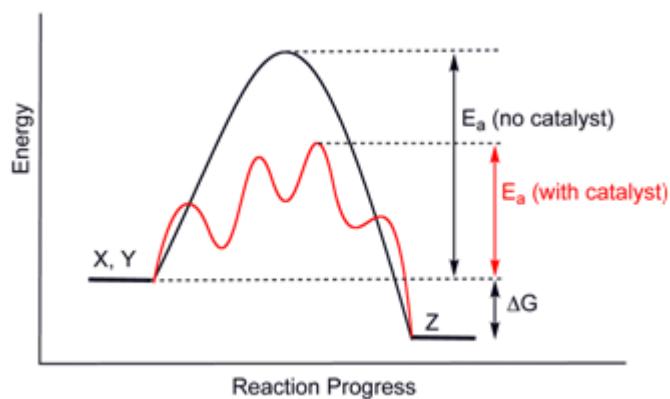


Figure 2.1: Generic potential energy diagram showing the effect of a catalyst [23]

Generic potential energy diagram showing the effect of a catalyst in a hypothetical exothermic chemical reaction $X + Y$ to give Z . The presence of the catalyst opens a different reaction pathway with lower activation energy. The final result and the overall thermodynamics are the same [23]. Catalysts are very common. Most reactions in our body, the atmosphere, and the oceans or in chemical industry occur with the help of catalysts. There are generally two types of catalysts which are homogeneous and heterogeneous catalysts. The catalyst that is present in the same phase as the reacting molecules is called a homogeneous catalyst. Typically homogeneous catalyst is dissolved with substrates. One example of homogeneous catalysis involves the influence of H^+ on the esterification of esters, e.g. methyl acetate from acetic acid and methanol [24]. For inorganic chemists, homogeneous catalysis is often synonymous with organometallic catalysts [25]. A heterogeneous catalyst exists in a different phase from the reactant molecules usually as a solid in contact either with gaseous reactants or with reactants in a liquid solution. Many industrially important reactions are catalyzed by the surfaces of solids. For example, hydrocarbon molecules are rearranged to form gasoline with “cracking” catalysts. Heterogeneous catalysts are often composed of metals or metal oxides. Because the catalyzed reaction occurs on the surface special methods are often used to prepare catalysts so that they have very large surface areas. The initial step in heterogeneous catalysis is usually adsorption of reactants. Adsorption occurs because the atoms or ions at the surface of a solid are extremely reactive. Unlike their counterparts in the interior of the substance, they have unfulfilled valence requirements [26]. The

unused bonding capability of surface atoms or ions may be used to bond the molecules from the gas or solution phase to the surface of the solid [26]. In practice not all the atoms or ions of the surface are reactive; various impurities may be adsorbed at the surface, and this may occupy many potential reaction sites and block further reaction. The places where reacting molecules may become adsorbed are called active sites. The number of active sites per unit amount of catalyst depends on the nature of the catalyst on its method of preparation and on its treatment before use.

2.2.1 Catalyst preparation methods

Generally heterogeneous catalyst consists of 3 major components [7], they are:

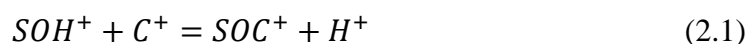
- I. An active catalytic phase (usually salts of transition metals as a metal precursors)
- II. High surface area carriers/supports which serve to facilitate the dispersion and stability of active catalytic phases.
- III. A promoter which increases activity and/or stability of main active metal.

Making of the finished catalyst generally involves one of three general approaches:

- I. Deposition of the active component onto a carrier by impregnation, adsorption, ion exchange or precipitation followed by washing, drying, calcination, and activation.
- II. Precipitation of a complex high surface area oxide or carbonate containing the active component followed by drying, calcination and activation.
- III. Preparation of a dense, nonporous compound or alloy containing the active component followed by extraction of inactive material leaving a porous high surface area active phase.

Impregnation method involves three steps: (1) contacting the support with the impregnating solution for a certain period of time, (2) drying the support to remove

the imbibed liquid and (3) activating the catalyst by calcination, reduction, or other appropriate treatment. Two methods such as “excess of solution” and “incipient wetness impregnation” of contacting may be distinguished, depending on the total amount of solution. Adsorption / Ion exchange support surfaces in contact with metal salt solutions adsorb equilibrium amounts of either cations or anions (or sometimes both) on active sites containing either protons or hydroxyl groups according to the following reactions:



The objective of precipitation method is to precipitate the catalyst precursor in the form of a hydroxide or carbonate in the pores and on the surface of the carrier by adjusting the pH of the metal salt solution support slurry through addition of a base such as NaOH, NH₄OH or Na₂CO₃. Alternatively, support and catalyst precursor are co precipitated together, such as the co precipitation of Ni hydroxide on silica by pouring together aqueous solutions of sodium silicate and nickel nitrate.

2.2.2 Incipient wetness impregnation method

Incipient wetness impregnation method is the simplest and probably the most common procedure for dispersing a catalytic species on a carrier by impregnating the predried support to incipient wetness with in aqueous or non-aqueous solution containing a salt (precursor) of the catalytic element or elements. The precursor salt is dissolved in a volume of solvent equal to the catalyst pore volume, and this solution is added slowly (sometimes dropwise) to the support in which capillary forces of up to several hundred atmospheres draw the liquid in to the pores. Addition of solution continues until the pores of the support are saturated as evident by the beading of the excess solvent. In this manner the precise amount of catalytic species is assured to be present in the carrier.

2.3 Fischer-Tropsch synthesis process

2.3.1 Overall background of Fischer-Tropsch synthesis (FTS)

Fischer-Tropsch Synthesis (FTS) is the heart of Gas to Liquid (GTL) technologies. Almost exclusively the FTS process is carried out in the presence of heterogeneous cobalt or iron catalysts. The advantages of the Co catalysts are the milder reaction conditions and higher activity when the feedstock is natural gas [1], [2]. The catalysts consist of metal promoted cobalt and iron supported on high-surface-area binders or supports such as silica, alumina, or zeolites. Commonly the FTS reactions are carried out in multi-tubular fixed bed and fluidized bed reactors operated at about 30 bars and 200-350°C [3],[4]. Depending on process conditions and the type of the catalyst, the high quality fuels and valuable chemicals are produced in FTS process [5].

Professor Franz Fischer and Doctor Hans Tropsch proposed the Synthol process which gave, under high pressure (>100 bar), a mixture of aliphatic oxygenated compounds via reaction of carbon monoxide with hydrogen over alkalized iron chips at 673 K [27]. This product was transformed after heating under pressure into “Synthine”, a mixture of hydrocarbons. Important progress in the development of Fischer-Tropsch synthesis was made in 1923. It was found that more and more heavy hydrocarbons could be produced when the Synthol process was conducted at lower pressure (7 bar) [26]. Heavy hydrocarbons were the main products of carbon monoxide hydrogenation on Fe/ZnO and Co/Cr₂O₃ contacts. In 1926, Hans Fischer and Franz Tropsch published their first reports about hydrocarbon synthesis [29].

After 1927 under the supervision of Roelen, the problems of chemical engineering had been tackled. A series of fixed bed and circulating bed reactors was developed. These reactors had already a presentiment of the later industrial processes. In 1934, the FT process was licensed by Ruhrchemie and reached industrial maturity in 2 years. In April 1936, the first large-scale FT plant operated in Braunkohle-Benzin. In 1938, Germany had a capacity of 660 000 tons of primary products per year. After World War II, ARGE (Arbeitsgemeinschaft Ruhrchemie und Lurgi) developed a large-scale process with a fixed bed FT reactor. At the same

period, Kellogg proposed a technology based on circulating catalyst bed. Both the ARGE and Kellogg processes were realized by Sasol in South Africa. The Sasol One plant was built in Sasolburg in 1955. In 1969, the Natref crude oil refinery was commissioned. In 1980 and 1982, Sasol Two and Sasol Three, respectively, began production in Secunda[30]. Major accomplishments of Sasol in the design of catalysts, reactors, and processes for FT synthesis have been summarized in a recently published monograph [1]. In the 1980s, expensive investments in the FT research and development programs picked up again in major petroleum companies. The global resurgence of interest in FT synthesis has been primarily driven by the problems of utilization of stranded gas, diversification of sources of fossil fuels, and environmental concerns. Synthetic liquid fuels generally have a very low content of sulfur and aromatic compounds compared to gasoline or diesel from crude oil. FT synthesis has been considered as a part of gas to liquids (GTL) technology, which converts natural and associated gases to more valuable middle distillates and lubricants.

The abundant reserves of natural gas in many parts of the world have made it attractive to commission new plants based on FT technology. In 1993, the Shell Bintulu 12 500 barrels per day (bpd) plant came into operation. In June 2006, the Sasol Oryx 34 000 bpd plant was inaugurated. SasolChevron is currently building its Escarvos GTL plant in Nigeria. Shell and Exxon signed the agreement on building 140 000 and 150 000 bpd GTL-FT plants in Qatar. Thus, after several decades of research and development, FT technology has finally come to the stage of full-scale industry and worldwide commercialization. The history of catalyst design for FT synthesis has been recently reviewed by Bartholomew [31]. Today, more than seventy years, after discovery of Franz Fischer and Hans Tropsch, there is a deep interest in the process. Various factors and demands contribute for this, such as rising price of crude oil that makes the production of synthetic fuels from alternative sources attractive. Both GTL and Coal to Liquid (CTL) fuels are cleaner than those, derived from crude oil. For example, the quality of GTL diesel is significantly higher than the quality of diesel which obtained by conventional way. GTL diesel differs from diesel derived from crude oil with its high cetane number (at least 70 compared

with a 45 to 55 rating of most diesels) low sulfur(less than 5 ppm), low aromatics (less than 1 %) and good cold flow characteristics, which can be optimized to suit specific applications. GTL diesel is postulated as a clean premium product or as a blend stock to enhance the quality of conventional diesels [5].

2.3.2 Chemistry and mechanism of Fischer-Tropsch synthesis

In Fischer-Tropsch like in other catalytic reactions the understanding of processes occurring on the surface of the catalysts is very vital. This will lead to improved catalytic and reactor design for the FT process. Accordingly, reaction parameters can then be selected to optimize product formation. Knowing the possible surface species on the catalyst surface and their reactivity enables the formulation of reaction pathways. A large number of surface species may exist on the catalyst surface at steady-state in the Fischer-Tropsch synthesis. The most common experimentally observed surface species which appear on the surface of metal catalyst are summarized in Figure 2.2.

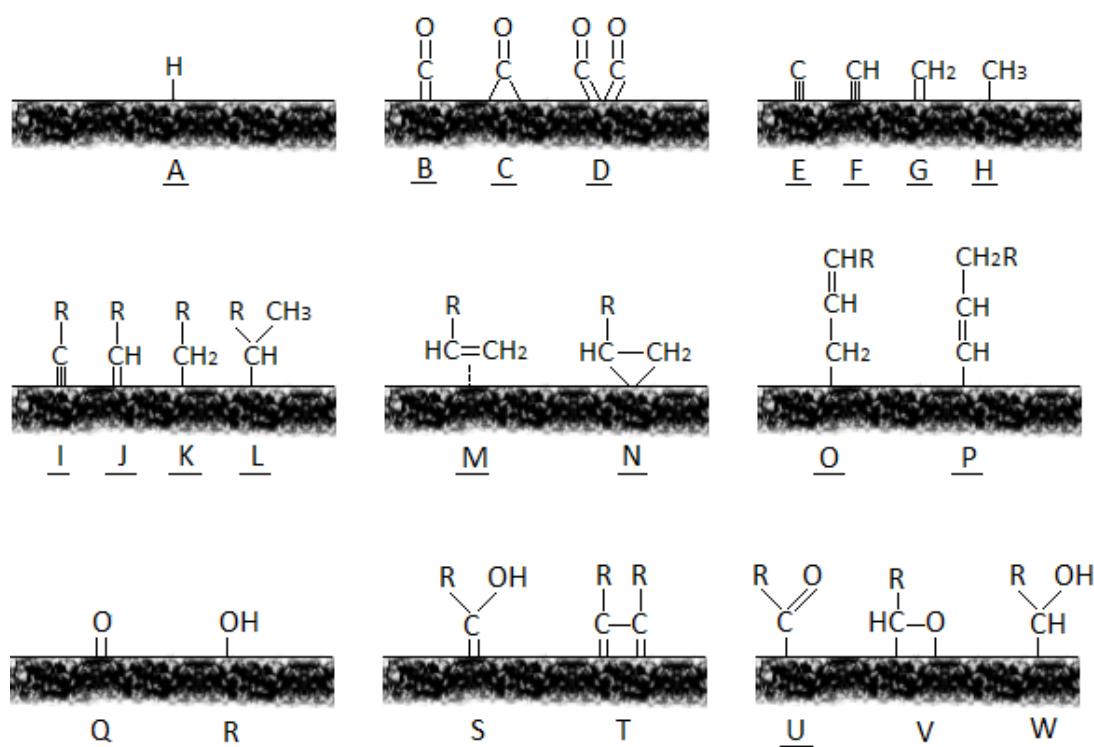


Figure 2.2: The main mechanism of FT reaction [1].

All these surface species can be generated from the reactants hydrogen and carbon monoxide on metal surfaces, which are catalytically active in the FT synthesis. The beginning process of chain growth starts from activation and yielding of monatomic hydrogen indicated with letter (A) [20 [32]. This hydrogen further chemisorbed preferentially on three fold hollow sites on all metal surfaces active in FT synthesis that is Ru (001)[33], Fe (110) [34], Co (0001) and Ni (111) [35]. Subsurface hydrogen has been postulated as a possible source of hydrogen in the FT synthesis [36], but is slightly less stable than hydrogen adsorbed at the surface [35]. Hence subsurface hydrogen is not likely to play an important role in the FT synthesis. Because of chemisorbed monatomic hydrogen has high surface mobility, it is assumed that hydrogen reacts with other surface species during the FT synthesis [37], [38]. The high mobility of hydrogen means that adsorption of hydrogen and its consumption for the formation of organic surface species does not necessarily take place at the same site and may even spillover to another metal crystallite [39].

The chemisorption of carbon monoxide on metal surface has been well studied by several researchers in the past. The adsorption of carbon monoxide on metal surfaces is mainly due to the interaction of the filled 5σ and the double generated $2\pi^*$ orbital of CO and the center of the metal d-band. [40]-[43]. There are three different modes of chemisorbed CO, which are “at the top” (B), “bridged” (C), and “vicinal” (D). “Atop” and “bridged” mode CO has been shown by using IR-measurements [44]. These modes of adsorption have also been confirmed using low energy electron diffraction (LEED) and photon electron spectroscopy (PES). The preferential adsorption site for CO on metal surfaces capable of catalyzing the FT synthesis is the on-top site (Co(0001), [45], (Ru(0001) [46]), except on Ni(111) where the bridge site seems to be preferred [47]. Chemisorbed CO can dissociate yielding surface carbon (E) and surface oxygen (Q). The dissociative adsorption of CO seems to be suppressed going from left to right and from 3d to 5d in the periodic table of transitional metal atoms [47]-[49]. Surface carbon which is preferentially located in hollow sites may diffuse into the bulk of the metal yielding carbidic carbon or agglomerate yielding graphitic carbon [48]. Sequential hydrogenation of surface carbon (E) produces surface methylidyne, (F), further surface methylene (G) and

surface methyl (H) species. The existence of HC_x – species ($x=1-3$) on a nickel surface after CO hydrogenation was demonstrated using secondary ion mass spectroscopy (SIMS) [50] and on Ruthenium based catalysts using IR studies [51]. Surface species (I) and (K) can be generated from reaction between surface species (E), (F) or (G) with a surface alkyl group species, that is: (H) or (K). The alkylidyne species (I) has been identified as a species present on the metal surface during olefin, especially ethene hydrogenation [52]. The surface alkyl species (K) has been observed under Fischer-Tropsch conditions [53]. The surface alkyl species (L) might be a precursor for the formation of branched products in the FT synthesis. It might be generated by the reaction of a surface alkylidyne species (J) with a surface methyl species or by a re-adsorption of a primarily formed α -olefin. Surface species (M) and (N) represent π -coordinated adsorbed olefin and the di- σ -coordinated olefin complex. Analogues of this type of bonding are well known in coordination chemistry [54]. These surface species might be important in the re-adsorption of reactive olefins under Fischer-Tropsch conditions. The surface allyl species (O) and vinyl species (P) are key intermediates in the alkenyl mechanism [55]. Surface oxygen (Q) is generated by the unassisted dissociation of chemisorbed CO. Surface oxygen can react with adsorbed hydrogen yielding a surface hydroxyl group (R), react with adsorbed CO yielding CO_2 , diffuse in to the bulk of the metal causing the generation of the oxide phase, e.g., with Fe based catalysts the formation of magnetite under Fischer-Tropsch conditions from α -Fe is well documented [56]. The surface species (S) and (T) are key intermediates in the enol-mechanism [57]. The oxygen containing surface species (U) to (W) have been proposed as intermediates in the CO-insertion mechanism [58].

2.3.3 Synthesis gas as a raw material for FT process

Syngas (from synthetic gas or synthesis gas) is the name given to a gas mixture that contains varying amounts of carbon monoxide and hydrogen. Examples of production methods include steam reforming of natural gas or liquid hydrocarbons to produce hydrogen or the gasification of coal [59]. Syngas consists primarily of hydrogen, carbon monoxide, and very often some carbon dioxide.

The technology used to prepare synthesis gas used for Fischer-Tropsch synthesis can be separated into two main categories, gasification and reforming. Gasification is used to describe process for conversion of solid or heavy liquid feedstock to synthesis gas while reforming is used for conversion of gaseous or light liquid feedstock to synthesis gas. The most common feeds used to prepare synthesis gas for FT synthesis are coal which is rich in carbon, and natural gas which is rich in methane. The term “carbonaceous” feed is commonly used and this implies any carbon containing feed material. Other feedstock examples are coal bed methane, heavy oils, bitumen, and petroleum coke (petcoke). In general the feed become more desirable as the hydrogen content increases.

The synthesis gas preparation section is an important part of the entire GTL complex. It is the most expensive of the three process sections which are synthesis gas preparation, FT synthesis, and product work-up. Also it is responsible for the largest energy conversion in the plant. The design of the synthesis gas preparation unit is therefore critical for the economics of a GTL project.

2.3.4 Fisher-Tropsch synthesis products

The refining of FT products is very different from crude oil refining, in terms of feed composition, refining focus, and heat management [60]. Despite these differences the refining of FT products is not widespread enough to have attracted FT specific refining technologies. The same basic technologies and commercial catalysts which are used in crude oil refining [61] have been applied for use in FT primary product refining. The refinery configuration and choice of refining technologies depend largely on the split between chemicals and fuel production. Valuable products like linear alpha-olefins can be extracted from the FT product. A huge variety of products of different chain length and different functionality is formed in Fischer-Tropsch synthesis. The actual composition distribution of Fischer-Tropsch process on many reaction variables such as reaction conditions (temperature and partial pressures of the reactions and product water), the reactor system used, as well as the catalyst

formulation and physical properties of the catalyst. The general main products of Fischer-Tropsch are:

- n-Olefins (mainly α -olefins, also olefins with internal double bond)
- n-Paraffins

Typical side products are:

- Oxygenates (1-alcohols, aldehydes, ketones, carboxylic acids)
- Branched compounds (mainly mono-methyl branched)

The original Sasol 1 production facility in Sasolburg had both ARGE Low Temperature Fischer-Tropsch (LTFT) and Synthol High Temperature Fischer Tropsch (HTFT) synthesis technology operating parallel. The Synthol refinery produced mainly petrol (also termed gasoline or mogas, in other words spark ignition engine fuel) while the ARGE product refinery produced mainly heavier products i.e. diesel (compression ignition engine fuel) and wax [62], [63], [64]. The HTFT plant in Brownsville, Texas (Hydrocol process) [65],[66] that processed the Sasolburg facility also targeted petrol as the main fuel product. Fuel specifications in the 1950's were not very demanding and product upgrading was mainly by distillation, hydrogenation, clay treatment, (to decrease the oxygenates and increase the aromatic contents) and oligomerization of light olefins. Lead containing additives were used to increase octane as was common practice in oil refineries at that time. The refinery designs not only reflected the prevailing fuel specifications but also the fact that the HTFT were seen as mainly fuels producers. The potential to extract chemicals was noted [67] but not incorporated in the design. The first change in this perspective started in the 1960's with the announcement that ethylene from FT synthesis and nitrogen from the air separation plant would be recovered for the production of plastic and ammonia at the Sasol 1 facility [68]. The separation of ethylene and propylene was incorporated in the later Secunda designs. This was taken a step further in the 1990's with the recovery and purification of linear alpha olefins as co-monomers for the polymer industry. Similarly, heavier alpha-olefins are now recovered and purified for detergent alcohol production via hydroformylation. HTFT product refining is shown in Figure 2.3.

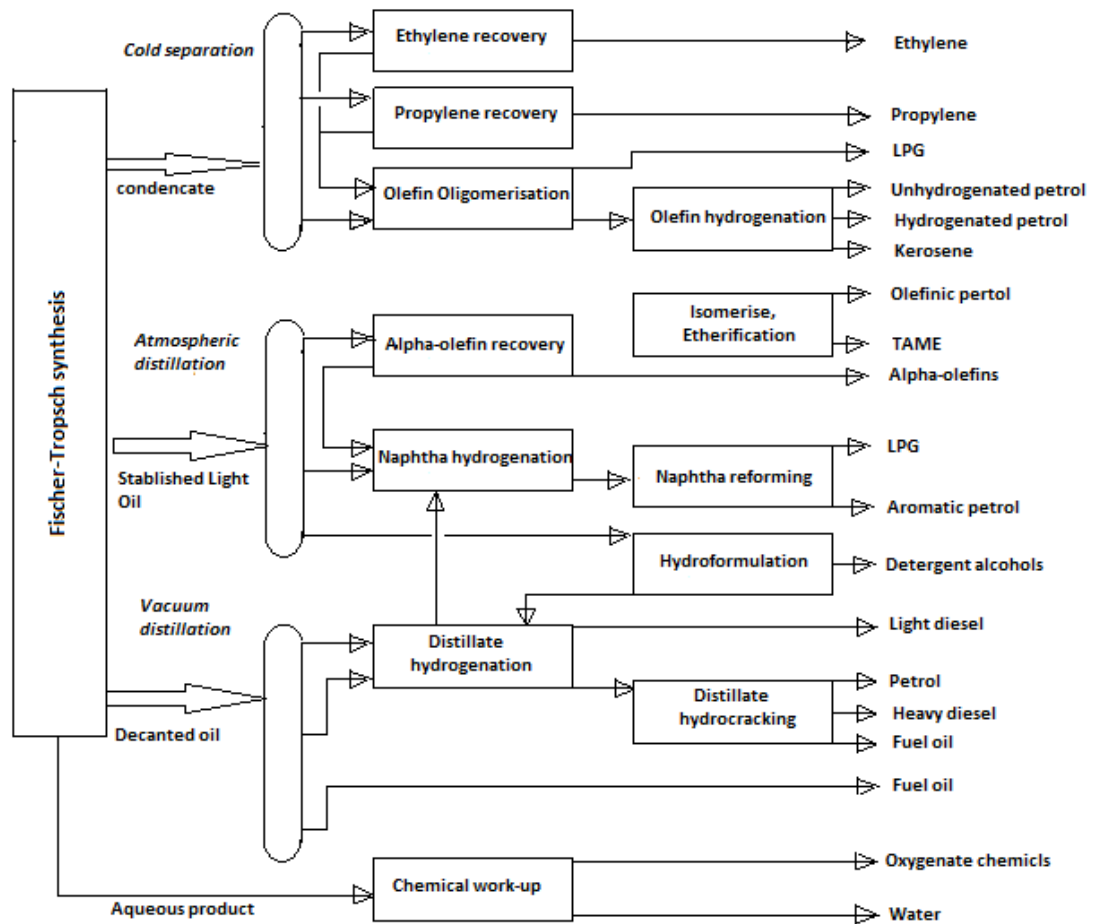


Figure 2.3: Current (2004) High Temperature Fischer-Tropsch refinery used at Secunda [1].

The most obvious advantage of FT products is its very low sulfur content. There is no need to worry about deep hydrodesulphurization or other sulfur reduction technologies to meet fuel sulfur specifications. There is also no need to worry about sulfur sensitivity of catalysts and high activity unsulfured catalysts can in principle be used for hydrotreating. It can be said that, what is bad for octane is generally good for cetane, so the low aromatics content and low degree of branching are very beneficial for the cetane number. Conversely the low degree of branching results in poor cold properties and the low aromatic content in a low density. However hydrotreated, slightly hydroisomerized FT products in general make a good diesel and an excellent blending component to enhance the properties of crude oil derived diesel blending material. The primary product from HTFT processes is more branched and more olefinic than the LTFT material; moreover the HTFT product

contains some aromatics while aromatics are almost totally absent from the LTFT material. As mentioned above, some aromatic content is desirable to increase the diesel density.

The typical LTFT plant would produce two primary products a light fraction which is usually liquid at room temperature and a heavy fraction usually solid at the same conditions. The former is often named hydrocarbon condensate or simply condensate and includes hydrocarbon species with a final boiling point around 370°C [7]. The latter also known as wax, includes the heavy paraffin. There are two other product streams: (i) light hydrocarbons gases, mostly generated during the FT synthesis, and (ii) reaction water which include some dissolved oxygenates. Like alcohols and organic acids. The gas stream can have many applications as a fuel gas. The reaction water need to be further processed and at some locations might even become a valuable product. In contrast with petroleum hydrocracking feedstocks, the LTFT wax is predominantly paraffinic, sulfur free and practically aromatics free. These characteristics are ideal for hydrocracking, and as a consequence LTFT feeds can be processed under much milder conditions than typical crude oil derived feeds, e.g. vacuum gas oils. In the hydrocracking of crude oil derived feeds pressures of typically as high as 150 bar are required to prevent cooking of the catalyst by the aromatic compounds. This is not necessary with paraffinic feeds and pressures between 3 to 70 bars are used to hydrocrack LTFT products using commercial hydrocracking catalysts [1].

Twenty percent of the FT product is propene and butene. These can be oligomerized to gasoline and because the oligomers are highly branched has a high octane value. The straight run gasoline, however, has a low octane value because of its high linearity and low aromatic content. The C₅/C₆ cut needs to be hydrogenated and isomerised and the C₇–C₁₀ cut needs severe platinum reforming to increase the octane value of these two cuts. Di-isopropyl ether can be produced from propene and water and this will further boost the octane number of the gasoline pool. The overall complexity of gasoline production, however, makes it less attractive than the diesel fuel option.

The high-temperature fluidized bed FT reactors with iron catalyst are ideal for the production of large amounts of linear α -olefins. As petrochemicals they are sold at much higher prices than fuels. The olefin content of the C₃, C₅–C₁₂, and C₁₃–C₁₈ cuts are typically 85, 70 and 60%, respectively. Ethylene goes to the production of polyethylene, polyvinylchloride, etc. and propylene to polypropylene, acrylonitrile, etc. The extracted and purified C₅–C₈ linear olefins are used as co-monomers in polyethylene production. The longer chain olefins can be converted to linear alcohols by hydroformylation. The only required purification of the narrow feed cuts is the removal of the acids. The hydroformylation was investigated at the Sasol R&D laboratories in the early 1990's. The alcohols are used in the production of biodegradable detergents. Their selling prices are about six times higher than that of fuel. The LTFT processes produce predominantly longer chain linear paraffins. After mild hydrotreatment conversion of olefins and oxygenates to paraffins the linear oils and various grades of linear waxes are sold at high prices [3].

2.3.5 Fischer-Tropsch synthesis catalysts

FTS catalysts mainly consist of two major groups:

- Fused iron catalysts and precipitated iron catalysts
- Supported cobalt catalysts

Only the metals Fe, Ni, Co and Ru have the required FT activity for commercial application. Among them Ruthenium is the best metal, working at the lowest reaction temperature, but very high price of Ruthenium makes it insufficient for large scale application. At elevated pressure nickel tends to form nickel carbonyl. With increasing reaction temperature the selectivity changes to mainly methane with nickel. So far commercially desirable catalysts are cobalt and iron.

2.3.5.1 Iron based catalysts for FTS

For the fused iron catalysts alkali promotion is used to enhance catalyst activity and selectivity. In addition structural promoters may be used to enhance the surface area of the final catalyst. These promoters are added into a molten bath of magnetite. The magnetite is then cooled to form a solid that is converted into a fine powder for use in fluidized bed reactors. The magnetite powder is first reduced with H_2 to form the metallic catalyst before being loaded into the synthesis reactor. High alkali levels are desirable to decrease CH_4 selectivity. The liquid products produced by fused iron catalysts are highly olefinic. This makes fused iron the most desirable catalyst for the production of olefins for use in the petrochemical industry. Secondary reactions occur in which the light olefins, particularly ethylene, are hydrogenated and also converted to higher hydrocarbons. Promotion interventions may be desired to enhance the light olefin content inhibiting these secondary reactions. Other promoter interventions may be aimed at decreasing the rate of carbon formation and/or organic acid formation. Precipitated iron based catalysts used for wax production (LTFT process) are currently prepared by precipitation techniques, promoted with Cu and K_2O and bound with SiO_2 . The iron content is high: typically the composition is 5g K_2O , 5g Cu and 25g SiO_2 per 100g Fe [69]. Prior to FT application the catalysts are usually partially pre-reduced with either H_2 or mixtures of H_2 and CO. With iron catalysts two directions of selectivity have been pursued. One direction has aimed at a low molecular weight olefinic hydrocarbon mixture to be produced in an entrained phase or fluid bed process (Sasol Synthol process). Due to the relatively high reaction temperature ($\approx 340^\circ C$), the average molecular weight of the product is so low that no liquid product phase occurs under reaction conditions. The second direction of iron catalyst development has aimed at highest catalyst activity to be used at low reaction temperature where most of the hydrocarbon product is in the liquid phase under reaction conditions. Typically, such catalysts are obtained through precipitation from nitrate solutions. A high content of a carrier provides mechanical strength and wide pores for easy mass transfer of the reactants in the liquid product filling the pores. The main product fraction then is a paraffin wax, which is refined to

marketable wax materials at Sasol [70], however, also can be very selectively hydrocracked to a high quality diesel fuel.

2.3.5.2 Cobalt based catalysts for FTS

The first cobalt catalyst used at Mülheim was a 100 Co/18 ThO₂/100 Kieselguhr catalyst [71], [6]. Otto Roelen a PhD student of F. Fischer, played an important role in the preparation of the technologically relevant catalysts [72]. It was reported that the preparation of cobalt catalysts by co-precipitating the nitrates of cobalt and thorium (or zirconium or magnesium) with a basic solution in the presence of kieselguhr to obtain a mixture of the oxides supported on the kieselguhr [4]. This catalyst can be considered as the predecessor of modern cobalt catalysts. Cobalt catalysts, developed by Fischer, Meyer and Koch have been applied in the first FT plant of Ruhrchemie in 1935 [73], [74]. Cobalt based catalysts are only used in Low Temperature Fischer-Tropsch (LTFT) process, since in high temperature the yield of CH₄ is increased, which is unwanted commercially. Because of the high price of Co, it is desirable to minimize the amount used but to maximize the available surface area of the metal. To achieve this, different carriers (supports) such as silica, titania or alumina are used [75]. They are porous, high surface area metal oxides. Nevertheless, a drawback for these supports is their reactivity towards Co metal which could lead to formation of mixed oxides (aluminate or silicate) [12]. The formation of Co support compounds is irreversible, and it is difficult to be reduced even at more than 700°C [14]. Insufficient reduction of Co species on the support surface causes the decreasing the number of active sites, and accordingly degrades the catalytic properties of the catalyst [15]. Modern cobalt catalysts are prepared by depositing the cobalt on a pre-shaped refractory oxide support. The support would typically be prepared using a spray dryer to provide a desired particle sizes for use in a slurry phase reactor. This might be followed by a classification step to refine the size distribution. Extrusion techniques will typically be used to shape the support for fixed bed applications. The shaped support is heat treated to improve the mechanical strength. The control of the pore size in the support is important factor in determining the amount of cobalt that can be placed on the support and the subsequent catalyst

performance. Cobalt is then impregnated onto the support together with promoter metals such as lanthanum, platinum, palladium, rhenium and ruthenium. These metals are known to enhance subsequent reduction step that provides cobalt metal on the catalyst surface. Metals such as lanthanum, ruthenium, and rhenium have been reported to be effective to facilitate catalyst re-reduction. The impregnated support is dried and then reduced using hydrogen at high temperatures.

The hydrocarbon products from supported cobalt catalysts comprise predominantly paraffins in contrast with the iron catalysts that usually produce olefins as the predominant product. With small catalyst particle sizes and CO rich synthesis gas the olefin content in the product from supported cobalt catalysts in slurry phase reactors may be high enough to justify the use of the olefins for chemical applications. The primary hydrocarbon products are also highly linear. Compared to the LTFT precipitated iron catalyst the methane selectivity is high and the selectivity to oxygenated hydrocarbons in the aqueous phase is lower. The best cobalt catalysts have carbon selectivity to methane of about 5%. An important characteristic for the best cobalt catalysts for natural gas applications is the absence of water-gas-shift activity so that significant amounts of carbon dioxide are not produced in the FT reactor. This advantage is only applicable to a comparison with the LTFT precipitated iron catalysts. Cobalt catalysts are not suitable for coal applications due to the risk of catalyst poisoning from various impurities that are usually present on coal. These impurities are difficult to remove to the required low levels. The syngas compositions obtained from coal gasification are in any case generally considered to be better suited for processing by iron catalysts.

2.3.5.3 *Deactivation of FT catalysts*

One of the greatest challenges in the design and operation of a large-scale catalytic process is the prevention of catalyst deactivation. There are so many ways in which catalyst may decay. It may be poisoned for example by any of a dozen contaminants present in the feed gas, or in water or steam used to pretreat the feed stream and/or in a diluent which is combined with the feed. At the same time surface, pores and voids

may be fouled by carbon or coke produced by cracking and/or condensation reactions of hydrocarbon reactants, intermediates, and/or products. In the treatment of a power plant flue gas, the catalyst could be dusted or eroded by and/or plugged with fly ash. If the catalytic reaction is conducted at high temperatures or involves a high exothermic reaction in a large scale fixed bed, thermal degradation may occur in the form of sintering of the active phases, collapse of the carrier (support) and/or solid state reactions of the active phase with the carrier or promoters. In addition the presence of oxygen or chloride in the feed gas should lead to formation of volatile oxides or chlorides of the active phase followed by gas phase transfer from the reactor [7]. Similarly changes in the oxidation state of the active catalytic phase could be induced by the presence of reactive gases in the feed. Catalyst deactivation problems are hardly limited to large reactors.

There are many ways in which catalyst deactivate, nevertheless these can be grouped basically into 5 intrinsic mechanisms of catalyst decay: Poisoning, Fouling, thermal degradation, loss of catalytic phases by vapor compound formation accompanied by transport and attrition. Poisoning and loss of catalytic phases by vapor compound formation are basically chemical in nature, whereas fouling and attrition are mechanical. Accordingly the causes of deactivation are basically three kinds: chemical, mechanical and thermal. Poisoning is a strong chemisorption of the reactants, products, or impurities on sites, otherwise available for catalysts. Thus, poisoning has an operational meaning that is whether a species act as a poison depends upon its adsorption strength relative to the other species competing for the catalytic sites. For example oxygen can be a reactant in partial oxidation of methane to methanol and a poison in ammonia synthesis. Fouling is the physical (mechanical) deposition of species from the fluid phase onto the catalyst surface, which results in activity loss due to blockage of sites and/or pores. In its advanced stages it may result in disintegration of catalyst particles and the plugging of the reactor voids. Important examples include mechanical deposits of carbon and coke, in porous catalysts. Although carbon- and coke-forming processes also involve chemisorption of condensed hydrocarbons which may act as catalyst poisons. Nevertheless, because of their large mechanical effects, carbon and coke deposition processes are typically

discussed in connection with fouling. Thermal degradation and sintering results from (1) loss of catalytic surface area due to crystallite growth in the catalytic phase, (2) loss of support area due to support collapse and of catalytic surface area due to pore collapse of metal crystallites, and/or (3) transformations of catalytic phases to non-catalytic phases. The first two processes are typically referred to as sintering. Sintering process generally takes place at high reaction temperatures (above 500°C) and are generally accelerated by a presence of water vapor. Loss of catalytic material due to attrition in moving or fluidized beds is a serious source of deactivation since the catalyst is continuously being abraded away. The demand for attrition resistant catalysts for fluid bed catalytic cracking is extremely important, since the process operates with regeneration and catalyst recycle. Similarly, for powdered catalysts used in slurry phase processes, it is common to filter and reuse the catalyst repeatedly, but the fines do not settle well and can pug the filters. They also contaminate and/or discolor product. Attrition is evident by a reduction in the particle size or a rounding or smoothing of the catalyst particle, easily observed under an optical or electron microscope.

2.3.6 FT reactors

There are four types of Fischer-Tropsch reactors in commercial use at present. They are:

- Tubular fixed bed reactor (LTFT)
- Slurry phase reactor (LTFT)
- Circulating fluidized bed reactor (HTFT)
- Fluidized bed reactor (HTFT)

2.3.6.1 Reactors for Low Temperature Fischer-Tropsch (LTFT)

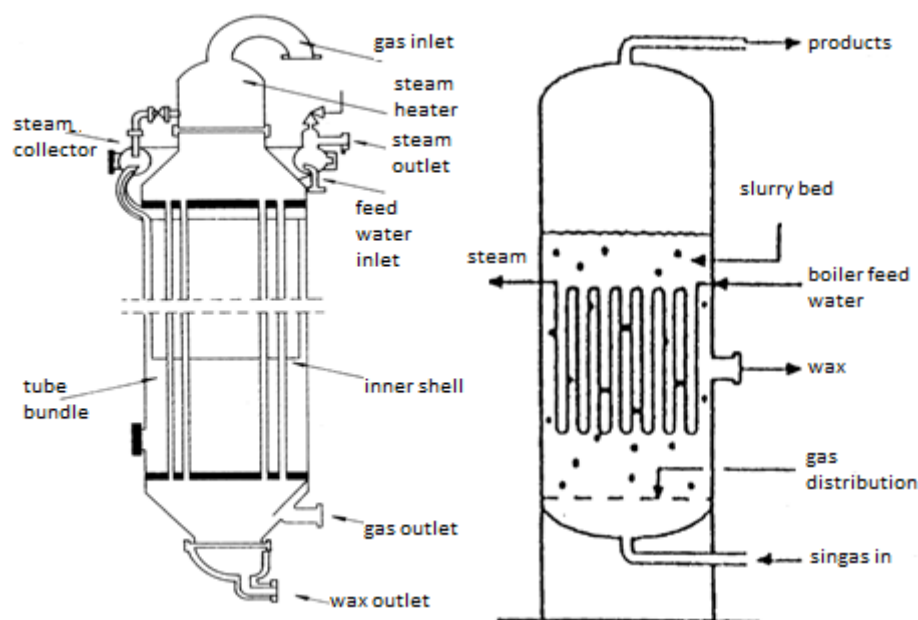


Figure 2.4 a and b: (a) (LEFT) The Multiubular Fixed Bed Reactor and (b) (RIGHT) Slurry Phase Bubbling Bed Reactors [1].

As mentioned above, low temperature operation is suitable for the production of high quality long chain paraffins. These types of FT reactors (Figure 2.4 a, b) operate in “three phase” which are liquid, solid (catalyst) and gas. In multitubular fixed bed reactors (Figure 2.4 a) the produced wax trickles down and out of the catalyst bed. One of the advantages of this reactor is its simplicity in operation. There is no any special equipment required to separate the heavy wax products. Once wax trickles down the bed, they are collected in a downstream knock-out pot. Next advantage of fixed bed system over any fluidized bed system is that should any catalyst poison such as H_2S enter the reactor, all of the catalyst is deactivated, whereas in a fixed bed reactor all the H_2S is absorbed by the top layers of the catalyst, leaving the balance of the bed essentially unscathed. Finally the most important for the fixed bed multitubular reactor, is that the performance of the large scale commercial reactor can be predicted with relative certainty based on the performance of a pilot unit consisting of single reactor tube. Unlike multitubular fixed bed reactors, produced wax in slurry phase reactors accumulates inside the reactor, so the net wax produced needs to be continuously removed from the reactor. Further additional equipment is

required to achieve the complete separation of the finely divided catalyst from the liquid wax. For the Sasolburg FT plant which came on stream in 1955 five multitubular ARGE (Arbeitsgemeinschaft – promptly abbreviated to ARGE at SASOL) reactors designed by Lurgi and Ruhrchemie were installed for wax productions [69]. These reactors are currently still in use. Each reactor contained 2050 tubes, 5cm i.d. and 12m long. They operate at 2.7 MPa and 230°C. Production capacity of each is about 21×10^3 t per year. Based on SASOL R&D pilot plant studies an additional high capacity reactor operating at 4.5 MPa was installed in 1987 [77]. Currently there are four large multitubular reactors are functioning in Shell Bintulu plant (Malaysia) which came on stream in 1993. They operate with cobalt-based catalysts. Each reactor contains about 10,000 tubes and the capacity of each is 125×10^3 t per year. As cobalt-based catalysts are used which are much more reactive than the iron-based catalysts used in Sasolburg reactors, the tube diameters of the Shell reactors are narrower in order to cope with high rate of the reaction heat released [3].

The use of slurry bed reactors for FT synthesis was studied by several investigators in the 1950s, e.g. Kölbel developed and operated a 1.5m i.d. unit [78]. In the late 1970s Sasol R&D compared the performance of fixed and slurry bed systems in their 5 cm i.d. pilot plants and found the conversions and selectivities to be similar [24]]. Further development was delayed because a reliable system was required to separate the net liquid wax produced from the fine friable precipitated iron-based catalyst used. In 1990 an efficient filtration device was tested in a 1m i.d. demonstration slurry bed reactor. In 1993 a 5m i.d. commercial unit was commissioned and has been in operation ever since [79]. Its capacity is about 100×10^3 t per year which equals that of the combined production of the original five ARGE reactors. Note again that only about 40 years after Kölbel's pioneering work did the first commercial slurry reactor come on-line. Using a cobalt-based catalyst Exxon successfully operated a 1.2m i.d. slurry bed reactor for wax production [80]. The unit's capacity was 8.5×10^3 t per year. The advantages of slurry over multitubular reactors are as follows:

- The cost of a reactor train is only 25% of that of a multitubular system.
- The differential pressure over the reactor is about four times lower which results in lower gas compression costs.
- The lower catalyst loading translates to four-fold lower catalyst consumption per tonne of product.
- The slurry bed is more isothermal and so can operate at a higher average temperature resulting in higher conversions.
- On-line removal/addition of catalyst allows longer reactor runs.

For the slurry test at 324°C the wax inside the reactor was continuously being hydrocracked and so make-up wax was added daily. Such high temperature slurry phase operation is therefore not practical or viable. Slurry bed reactors with a capacity of at least 20,000 barrel/day (850×10³ t per year) are feasible [79] and in fact Sasol reactors with a capacity of 17,000 barrel/day are currently in use in Qatar.

2.3.6.2 Reactors for High Temperature Fischer-Tropsch (HTFT)

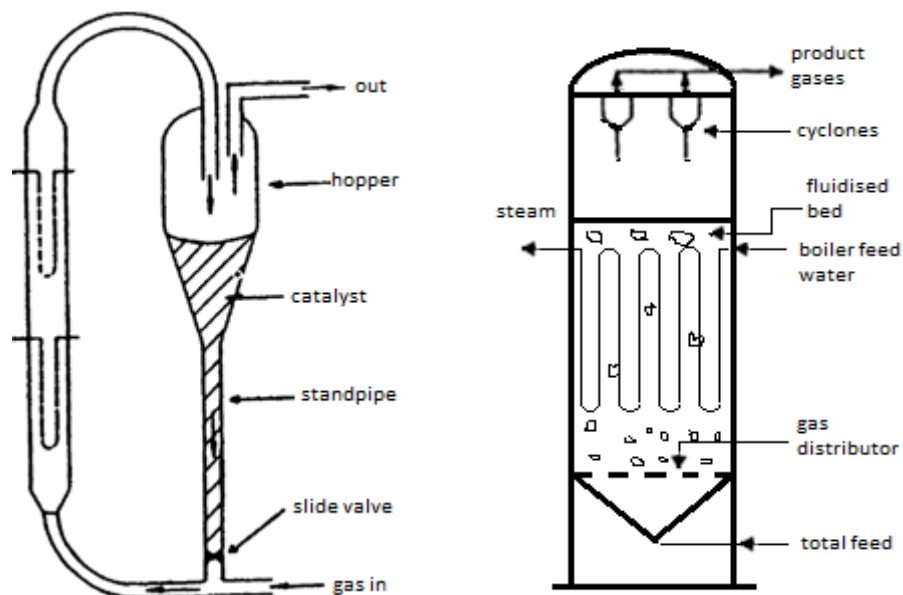


Figure 2.5: (a) (LEFT) Circulating fluidized bed reactor CFB; (b) (right) fixed fluidized bed reactors FFB [1]

As mentioned above, neither fixed bed nor slurry bed reactors can be utilized in high temperature FT process for the production of light alkenes and/or gasoline. For the production of these hydrocarbons two-phase fluidized bed reactors are the unit of choice. There are two types of fluidized bed reactors currently in commercial use which are the circulating fluidized bed (CFB) and the turbulent or fixed fluidized bed reactors. (Figure 2.5 a and b). Later fixed fluidized bed FFB reactors have been named Sasol Advanced Synthol (SAS) reactors by the developers of this advanced technology. There is high degree of turbulence in fluidized bed reactors, hence these reactors exhibit very high rates of heat exchange. This means they can cope with the large amounts of reaction heat released at high conversions with high feed gas throughputs that can be achieved at high operating temperatures. Despite this the beds are efficiently isothermal which means temperature differences between the bottom and top of the reactor being only a few degrees. It is important however that process conditions must be such that the selectivity of a long chain hydrocarbons is limited to ensure that excessive condensation of liquid hydrocarbons in the pores of catalyst does not occur. The consequence of liquid phase formation in the outer surface of the particles will lead to the agglomeration of the finely divided particles, eventually it will negatively affect in the fluidization of the catalyst and the unit would then cease to function. In 1950's Sasol operated circulating fluidized bed reactors CFB's (Figure 2.5a) in its original plant at Sasolburg. The gas linear velocities in CFB reactors are three to four times higher than in the FFB's (Figure 2.5 b). The size of reactors in Sasolburg plant was 2.3m ID and 46m high. After many teething troubles several design as well as catalyst formulation changes were made and these resulted in satisfactory performances of the units. These reactors were also renamed Synthol reactors and were operated successfully for many years. For the two new Sasol plants constructed about 25 years later at Secunda the same type of reactors were installed but with improved heat exchangers and the capacity per reactor was increased three-fold (wider diameter and higher operating pressure). The same larger type of CFB reactors, with further improved heat exchangers were installed in the Mossgas FT complex. It should be noted that in CFB reactors, there are two phases of fluidized catalyst. Catalyst moves down the standpipe in dense phase while it is transported up the "reaction" zone (Figure 2.5 a) in lean phase. To

avoid the feed-gas going up the standpipe the differential pressure over the standpipe must always exceed that over the reaction zone. At the high operating temperature carbon is deposited on the iron-based catalysts and this lowers the bulk density of the catalyst and thus the differential pressure over the standpipe. It is therefore not possible to raise the catalyst loading in the reaction section in order to compensate for the normal decline of catalyst activity with time-on-stream. In 1984 a 1m ID FFB demonstration reactor, designed by Badger, was brought on-line at the Sasolburg plant. In 1989 a 5m i.d., 22m high commercial unit came on stream and it met all expectations [81]. From 1995 to 1999 the 16 second generation CFB reactors at Secunda were replaced by eight FFB reactors, four of 8m i.d. with capacities of 470×10^3 t per year each and four of 10.7m i.d. each with a capacity of 850×10^3 t per year.

The main advantages of FFB over CFB reactors are as follows:

- The construction cost is 40% lower. For the same capacity the FFB reactor is much smaller overall.
- Because of the wider reaction section more cooling coils can be installed increasing its capacity. (More fresh gas can be fed by either increasing the volumetric flow or by increasing operating pressure. Pressures up to 4MPa are feasible)
- At any moment all of the catalyst charge participates in the reaction, whereas in the CFB only a portion of it does.
- The lowering of the bulk density by carbon deposition is of less significance in the FFB and thus a lower rate of on-line catalyst removal and replacement with fresh catalyst is required to maintain high conversions. This lowers the overall catalyst consumption.
- Because the iron carbide catalyst is very abrasive and the gas/catalyst linear velocities in the narrower sections of the CFB reactors is very high these sections are ceramic lined and regular maintenance is essential. This problem is absent in the lower linear velocities FFB reactors and this allows longer on-stream times between maintenance inspections.

2.4 Characterization of catalyst support and catalyst precursors

The unpurified/purified MWCNT and SBA-15 in its pure form, including all catalyst precursors were characterized using surface measurement techniques and high resolution microscopes. BET was used to identify surface area and pore volume of the materials. Detection of ion decomposition was carried out by thermogravimetric analysis equipped with mass spectroscopy (TGA-MS). Type and size of crystallites after impregnation of active metal to catalyst support were measured using X-ray diffraction (XRD). Surface species and composition of both, catalysts and supports were investigated via two types of high resolution microscopes such as field emission scanning electron microscopy equipped with energy dispersive X-ray (FESEM/EDX) and high resolution transmission electron microscopy (HRTEM). Reduction temperature of the catalysts was identified by temperature programmed reduction (TPR).

2.4.1 BET surface area measurements

The surface area and porosity of MWCNTs and SBA-15 before and after impregnation of active metals were measured using Quantachrome Autosorb Automated Gas Sorption System. 0.02 g of sample was weighed and characterized in each case. Prior to measurement, samples were degassed in a vacuum in 120°C for 5 hours in order to remove possible moistures from pores of samples. After degassing procedure liquid nitrogen was introduced to the system and sample was kept in nitrogen environment 11 hours.

2.4.2 Thermogravimetric Analysis - Mass Spectroscopy (TGA-MS)

Thermogravimetry analysis (TGA) is a quantitative technique used to measure the change in weight of a sample as a function of temperature (dynamically) or time (isothermally) under a controlled atmosphere. The thermogravimetric curve obtained gives information on the sample composition, its thermal stability and the thermal composition at different temperature during measurement. The common way of

expressing the data is by plotting the percentage of weight changes against the temperature or time.

The gas supply to the sample during the heating would have to be suitable to the desired analysis whether oxidizing, reducing or inert. A choice of reactant gas to observe thermal degradation during reaction is also possible.

Mass change or differential can be plotted against time or temperature to analyze mass change at every given temperature or moment in time. This method is known as the differential thermogravimetric or DTG analysis. A schematic of a thermo analysis setup is shown in Figure 2.6.

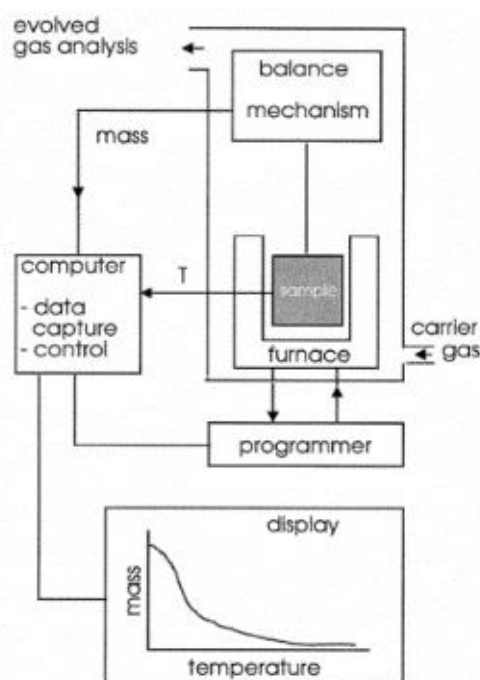


Figure 2.6: A schematic of a thermo analysis setup

Mass of the sample changes in many ways as it interacts with its surrounding gas at a given Temperature. The sample mass can increase or decrease depending on the type of interaction it has with its surrounding gas or the effect of variable temperature on it. Oxidation of metals is an example of sample mass increasing whereas oxide reduction and thermal decomposition is an instance of sample mass decreasing over time. The decomposition process often occurs in several steps as shown in Figure 2.7.

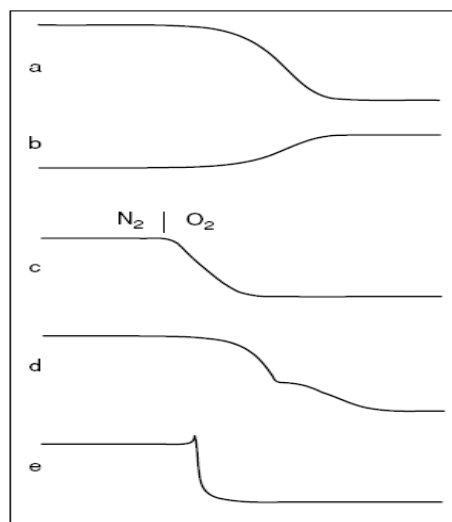


Figure 2.7: TGA spectrum of multiple process types. (a) Thermal decomposition with the formation of volatile compounds. (b) Metal oxidation. (c) Combustion when gas switches from N_2 to O_2 . (d) Multi step decomposition. (e) Explosive decomposition with recoil effect

2.4.3 Field Emission Scanning Electron Microscope/Energy Dispersive X-Ray (FESEM/EDX)

Electron Microscopy is a powerful tool that allows us to observe the chemical structure, morphology, surface texture and crystalline size of catalysts from resolution in the range of micro to nanometers. In brief it allows not only aerial image of the surface that is invisible to the naked eye but also the angular topology which enables to visualize the catalyst in a 3 dimensional space.

The diagram in Figure 2.8 shows the major components of a conventional SEM. These components are part of seven primary operational systems: vacuum, beam generation, beam manipulation, beam interaction, detection, signal processing, and display and record. These systems function together to determine the results and qualities of a micrograph such as magnification, resolution, depth of field, contrast, and brightness.

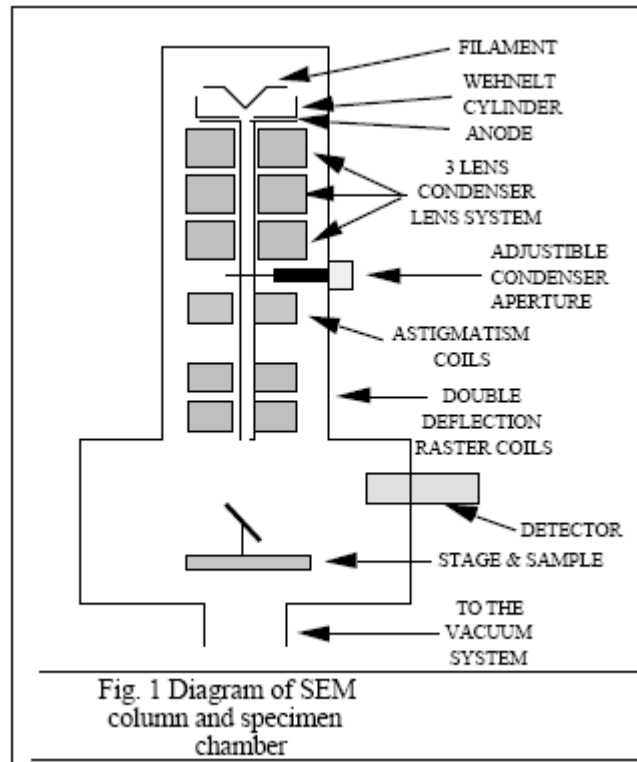


Figure 2.8: Functional parts of a Scanning Electron Microscope

Electrons in a SEM are ejected by a thermostat after it is heated and these electrons are focused into a fine beam by a magnetic lens. Field Emission Scanning Electron Microscope (FESEM) is a special kind of electron microscope whose electrons are ejected after a strong electric field is applied to the source causing the electrons to gain sufficient energy to overcome its atomic forces to the atoms. The ejected electron field of an FESEM is also focused not by a magnetic but an electrostatic lens. FESEM also gives much higher resolution than the conventional SEM as well as better imaging of trenches and deep holes.

The ejected beam from the electron gun is bombarded to the surface of the sample that needs to be investigated. The backscattered and/or secondary electrons from the surface at particular energies could determine the composite material that makes the surface. Backscattered or reflected source electrons are detected by the BSE detector while the secondary electrons ejected from the sample are detected by the SE detector. The SE detector is placed at an angle above horizontal so as to enable topographical information to be analyzed.

Another detector, the in lens detector is placed vertically and inside the electron acceleration column to detect high energy secondary electrons which provides extremely high resolution of the sample surface.

Quantitative compositional analysis of materials that make up the catalyst on the surface assuming homogeneity can be determined by the Energy Dispersive Spectrometer (EDS) which detects X-rays released by the surface after electron bombardment and the X-rays are characteristic of an element. Also, Wavelength Dispersive Analysis (WDS) allow elemental mapping on the sample surface by introducing false colors for each element.

2.4.4 X-Ray Diffraction (XRD)

X-Ray diffraction is often cited as the fundamental tool in the study of solid states. Solid can be divided in two main categories, crystalline and amorphous solids. In crystalline solids, atoms are arranged in a regular pattern, and there is as smallest volume element that by repetition in three dimensions describes the crystal. This smallest volume element is known as a unit cell. The dimensions of the unit cell are described by three axes, a, b, c and the angles between them alpha, beta, and gamma. On the contrary, in amorphous solids, the atoms are arranged in a random way similar to the disorder we find in a liquid. Glasses for instance are amorphous materials.

About 95% of all solid materials can be described as crystalline [117]. When X-rays interact with a crystalline substance (Phase), one gets a diffraction pattern. The X-Ray diffraction of a pure substance is thus more generally described as its fingerprint. The powder diffraction method is therefore an ideal tool to characterize and identify polycrystalline phases.

Today about 50,000 inorganic and 25,000 organic single components, crystalline phases, and diffraction patterns have been collected and stored on magnetic or optical media as standards [117]. The main use of powder diffraction is to identify

components in a sample by a search/match procedure. Furthermore, the areas under the peak are related to the amount of each phase present in the sample.

Once the material has been identified, x-ray crystallography may be used to determine its structure (how the atoms pack together in the crystalline state and what the interatomic distance and angle are). Figure 2.9 shows the reflection of x-rays from two planes of atoms in a solid. During diffraction, x-rays impinge on the crystal and are coherently scattered. The scattered radiation can be well observed only in directions in which the beams reflected from the crystal plane under each other are amplified by interference.

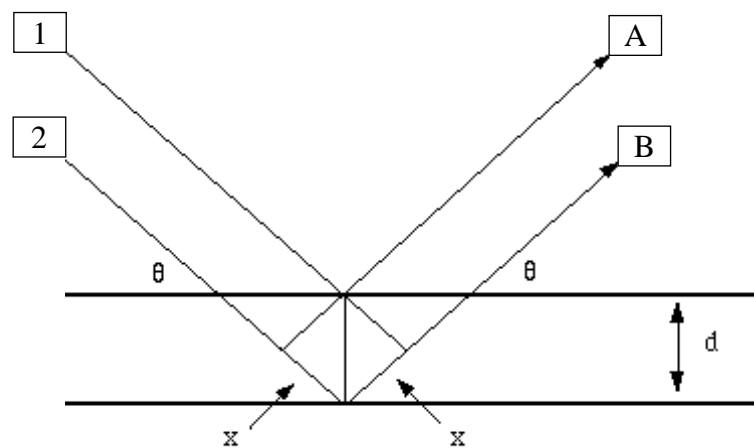


Figure 2.9: X-ray reflection on two atomic planes of a crystalline solid

The two parallel incident rays 1 and 2 make an angle Θ with these planes. A reflected beam of maximum intensity will result if the waves represented by the x-ray termed 1 and 2 are in phase. The difference in path length between 1 to A and 2 to B or simply labeled as d must then be an integral number of wavelengths, λ . This relationship is described mathematically by Bragg's law as:

$$n\lambda = 2d_{hkl} \sin\theta \quad (2.3)$$

Where n is an integer, hkl is the Miller indices of the plane. This equation is a general simplification of a now more elaborate field of X-ray crystallography.

2.4.5 Temperature Programmed Reduction (TPR)

Temperature-programmed reduction (TPR) is a widely used tool for the characterization of metal oxides, mixed metal oxides, and metal oxides dispersed on a support. The TPR method yields quantitative information of the reducibility of the oxide's surface, as well as the heterogeneity of the reducible surface. TPR is a method in which a reducing gas mixture (typically 3% to 17% hydrogen diluted in argon or nitrogen) flows over the sample. A thermal conductivity detector (TCD) is used to measure changes in the thermal conductivity of the gas stream. The TCD signal is then converted to concentration of active gas using a level calibration. A TPR study unit can more generally be classified as a miniature reactor together with a furnace for sample heating as well as a Thermal Conductivity Detector (TCD).

The reaction of the reducible materials with H_2 is a surface chemical reaction. This allows an access to a great deal of information on the material under investigation [89]. Consequently, it is widely employed for the verification of the nature of species in calcined catalysts.

Common information which can be obtained from the TPR study is:

- Optimum Reduction Temperatures
- Amount of active sites present
- Dispersion of Active metals on catalyst surface.
- Active metal particle size in catalyst (nm)

The reactions are usually carried out to match its industrial or lab reactor experiment as much as possible. Usually the sample is previously oxidized or pretreated to eliminate possible contaminants and completely oxidize the metal portion of the catalyst. Also, the sample is submitted to a linear increase of temperature and to a constant flow of the gas mixture. The reaction generally starts at room temperature, but at an extremely low speed, therefore negligible. At a certain temperature, the reaction speed becomes considerable and the hydrogen consumption can be monitored through the TCD detector. A thermal conductivity detector measures the H_2 concentration in the effluent gas with respect to the initial percentage, monitors the reaction progress. The signal integration allows us to

calculate the quantity of hydrogen consumed and therefore the number of reacting sites. A quadrupole mass spectrometer can also be used as a detector. Due to the large difference in thermal conductivities between hydrogen and nitrogen, it was possible to detect hydrogen consumption as low as 1 μmol . This ensured high detection sensitivity and consequently, a low detection limit for the TPR technique. The TPR analysis also enlightens the presence of different states of oxidation of the contained metals.

2.4.6 Transmission Electron Microscopy (TEM)

In TEM, a thin specimen is irradiated with a parallel electron beam and magnified images of the sample are formed by combining the transmitted electrons by means of an electromagnetic objective lens. The lens produce a 2D diffraction pattern of the sample in its focal plane and these diffracted beams recombine to form the image. A magnified image or the diffraction pattern on a detection device (CCD camera or photographic film) is observed by varying the excitation of a series of projection lenses. The most commonly used TEM instruments operate in the 100-400 kV range; the higher the energy, the better the resolution. TEM offers two operating modes: conventional TEM (CTEM) and high resolution TEM (HRTEM). In CTEM, two imaging modes are possible: bright field and dark field. In bright field imaging, all diffracted electrons are excluded by the aperture in forming the image. In order to detect the presence of metallic particles, this image mode is preferred. If the image is formed from diffracted electrons alone and the central beam is excluded by the objective aperture, a dark field image is obtained. Two beam imaging refers to the condition where the crystal is oriented to yield transmitted and diffracted beams of equal intensity. The bright field, dark field, and two beam imaging modes are broadly applied in studying defects and morphology of thin crystals. Meanwhile, HRTEM technique is performed using an objective aperture which allows diffracted beams to interfere with the axial transmitted beam to form the image. Phase contrast imaging is the preferred imaging mode for resolving the atomic lattice of the specimen.

2.5 Multiwall Carbon Nanotubes (MWCNT) and Multiwall carbon Nanofibers (MWCNF) as a catalyst support

Use of carbon nanotubes and nanofibers as a support material for heterogeneous catalysis has been explored by a number of researchers [8], [9]. Studies comparing the catalytic activity of metal catalysts supported on various oxides, amorphous carbon and CNTs showed that catalytic performance was generally the best on CNTs. Serp *et al.* in their research [11] describe mechanical and thermal properties of CNTs that they are very flexible and can be bent several times at 90° without undergoing structural changes. The structure is not easily changed with the effects of pressure and it has been demonstrated [82] that CNT are only undergoing permanent structural changing at very high pressures (over 1.5 GPa) and that below the value the deformations are totally elastic. On research done by J. Garcia *et al* [83] multi-wall CNT (MWCNT) – supported platinum catalyst showed superior activity in catalytic wet air oxidation of nitrogen containing compounds. Platinum catalyst supported with CNT did so in the oxidation of environmentally harmful organic compounds to CO₂ [84].

Carbon nanofibers (CNFs) have recently been proposed for cobalt catalysts [85] ,[11] by several research groups. The CNFs have several interesting properties such as chemical inertness, high purity, high surface area, high mechanical strength, high thermal stability, and tunable bulk density [86]. Also it was established that carbon nanofibers interweave during growth, resulting in the formation of mechanically strong tangled agglomerates. The agglomerates facilitate an open pore volume a pore size distribution a predominant mesoporous structure, high filterability and high mechanical strength, thus rendering carbon nanofibers suitable as a support in the field of heterogeneous catalysis.

2.6 Santa Barbara amorphous - 15 (SBA-15) as a catalyst support

The use of mesoporous silica such as SBA-15 as support for preparing Co-based catalysts has been recently explored [10]. SBA-15 possesses a high surface area (600-1000 m²/g) and is formed by a hexagonal array of uniform tubular channels

with pore diameters ranging from 5 to 30 nm. Also SBA-15 possesses thicker pore walls. In their work Zhao *et al.* [12] identified that thicker walls lead to the greater hydrothermal stability. In analysis conducted on SBA-15 which is calcined in 500°C, the same number of peaks before and after calcination was observed in XRD, confirming that hexagonal SBA-15 is thermally stable. At the same time high surface area gives high metal dispersions at high cobalt loadings which were observed by the group of researchers headed by Wang [87]. In their work they found that hexagonal mesoscopic organization of the SBA-15 with pore diameter 5.5 nm is almost retained even after edition of 20 mass% Co

2.7 CNT and CNF based Co/Ru catalysts for FTS and CO hydrogenation

As mentioned in Chapter 1, new carbon based materials are drawing more attention of scientists in different areas of science including surface chemistry and catalysis. Carbon nanotubes (CNT) and nanofibers (CNF) are very promising due to their superior properties that outperform conventional supports.

Tavasoli *et al.* investigated carbon nanotubes as a support for Fisher-Tropsch Cobalt catalyst [88]. They prepared 2 types of cobalt catalyst supported with conventional γ -alumina (A₁-A₄) and carbon nanotubes (C₁-C₄) via sequential impregnation method with cobalt loading in both catalysts of 15, 25, 35 and 40 wt.%. Catalysts were evaluated in tubular fixed-bed micro-reactor. The results of this research work are shown briefly in Figure 2.10.

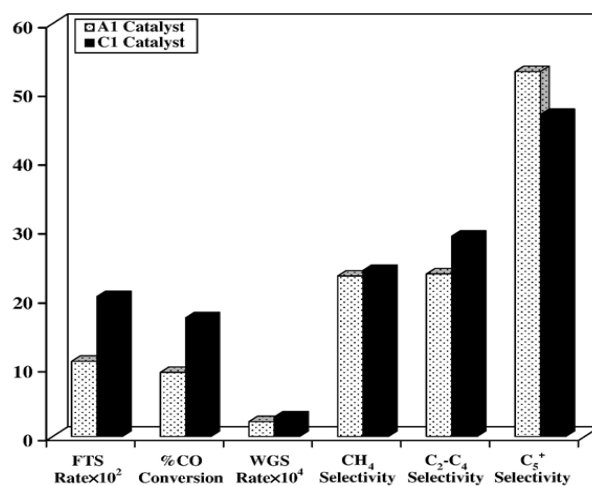


Figure 2.10: FTS rate, %CO conversion, WGS rate and product selectivity of the A₁ and C₁ catalysts (T=220 °C, P=1 bar and H₂/CO=2) [88]

In another work done by A. Tavasoli *et al.* [89] performance of CNT supported Co catalysts was studied in slurry phase reactor. According to the results, application of carbon nanotubes as cobalt catalyst support caused considerable positive changes in various parameters, such as an interaction between cobalt surface species decreased greatly. The reduction temperature of cobalt oxide species shifted to lower temperatures and the reducibility of the catalyst improved significantly. CNT aided in dispersion of metal clusters and average cobalt clusters size decreased. From a catalytic activity point of view, the FTS rate and percentage CO conversion obtained by carbon nanotubes as cobalt catalysts were much larger (80–90%) than that obtained from cobalt on alumina supports. The only setback in using CNT is a slight decrease in the FTS product distribution to lower molecular weight hydrocarbons.

Influence of acid treatment to CNTs was observed by Tripanier *et al.* [90]. In their work purified MWCNT was applied as a support material for the preparation of cobalt FTS catalysts. Figure 2.11 shows the TEM of cobalt loaded catalysts. It demonstrates the encapsulated cobalt particles on a selected tube with higher resolution.

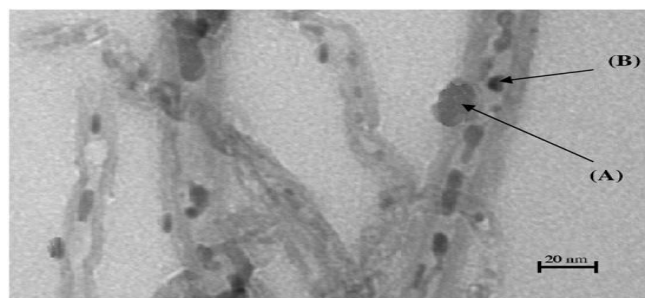


Figure 2.11: TEM image showing cobalt particles with high dispersion for the acid treated loaded catalyst and showing the open caps of the CNTs: (A) Outside, (B) Inside. [90]

According to the results of this research, acid treatment of carbon nanotubes at 25 and 100 °C opened the caps, broke carbon nanotubes and introduced a large number of defects and acidic functional groups on the nanotubes. Treatment of cobalt FTS catalyst support with 30% HNO₃ at 25 and 100 °C, increased the BET surface area by 18 and 25%, decreased the cobalt particle size and increased the cobalt dispersion.

Trepanier *et al.* [91] studied the effects of Co, Ru and K loadings to the selectivity and activity of cobalt based catalyst supported on carbon nanotubes for FT synthesis. In their work they prepared series of Co/CNT catalysts with different loadings of cobalt (15-30 wt.%). The effect of the Co loading on the physico-chemical properties of the catalysts was investigated. The catalysts were evaluated in terms of their FTS activity (g HC produced /g cat./h) and selectivity (the % of the converted CO that appears as HC products) in fixed bed micro reactor.

Also according to the results, increase in Co loading from 15 to 30 wt % increased the CO conversion from 48 to 86% and the C₅₊ selectivity from 70 to 77%. Ruthenium promoter enhanced the reducibility, increased the dispersion and decreased the average cobalt cluster sizes.

Zaman *et al.* [14] studied the behavior of cobalt catalysts supported on CNT with alumina and magnesium oxide under various FT conditions. Amount of Co loading was 15 wt% in all catalysts. In terms of CO conversion and selectivity performance

of Co/MWCNT towards CO conversion was better (18.8 %), while C₅₊ selectivity was greater in cobalt catalysts supported in MWCNT with MgO (49.9 %).

Tavasoli *et al.* [92] investigated bimetallic Co and Fe catalysts supported on CNTs for Fischer-Tropsch synthesis. The objective was to study and determine the best ratio of Fe to Co to maximize the benefits of the performance of Co/Fe catalysts. Four types of bimetallic Co-Fe catalysts were prepared with fixed amount of Co (10 wt%) and different amount of Fe (0.5, 1, 2 and 4 wt%). Reference catalysts which contain only 10Co/CNT and 10Fe/CNT for comparison were also prepared. Most of the metal particles were homogeneously distributed inside the tubes, and the rest on the outer surface of the CNTs. When 0.5 wt% iron was added to Co catalyst (10Co0.5Fe/CNT), it caused FTS reaction rate and CO conversion to increase dramatically. At the same time, the addition of iron to cobalt catalyst increased the WGS reaction rate too. The monometallic cobalt catalyst exhibited fairly high selectivity (85.1%) toward C₅₊ liquid hydrocarbons, while addition of small amounts of iron did not change the product selectivity significantly. The bimetallic Co-Fe/CNT catalysts proved to be much more attractive in terms of alcohol formation. The introduction of 4 wt% of iron to the cobalt catalyst increased the alcohol selectivity from 2.3 to 26.3%. The Co-Fe alloys appear to be responsible for the rather high selectivity toward alcohol formation.

Synthesis of CNT supported cobalt nanoparticle catalysts using a microemulsion technique for Fischer-Tropsch synthesis was studied by M. Trepanier *et al.* [93]. In their work researchers compared microemulsion technique for catalyst preparation with the conventional incipient wetness impregnation method for the control of cobalt metal particle size using CNTs as a catalyst carrier. Two types of CNT catalysts were prepared by two different methods. According to the results, cobalt nanoparticles produced at relatively high loadings of 10 wt% by using the microemulsion technique revealed a narrow particle size distribution. In terms of activity and selectivity for FTS, catalysts with Co particle size of 3-5 nm have high selectivity towards CH₄, and relatively low selectivity C₅₊ hydrocarbons. Carbon nanotubes as a catalyst carrier-support with Co nanoparticles retained high

reducibility of Co. The proposed microemulsion technique also increased the CO conversion by 15% compared to those prepared by incipient wetness impregnation.

Zhang *et al.* [94] studied the nature of cobalt species in carbon nanotubes and their catalytic performance in Fischer-Tropsch reaction. The objective of their work was to clarify the effects of the acid treatment and carbon nanotube diameter on the structure of supported cobalt species, interaction between active metal and CNTs and their performance in FT synthesis. According to the results the effects due to MWCNTs treatment with nitric acid was summarized as follows: (1) MWCNTs surface impurities was removed; (2) functional groups such as hydroxyls or carboxyls were introduced. The catalytic tests at 20 bar showed that acid pretreatment resulted in a 25% increase in FT catalytic activity. No significant influence of nanotube diameter on FT catalytic performance was detected. Oxidation of carbon nanotube surface with nitric acid or use of carbon nanotubes with different outer diameters did not affect cobalt dispersion. They concluded that the variation of nanotube diameter did not have any significant influence on FT catalytic performance.

Another group of researchers that is M. Rengel *et al.* [95] investigated the characterization of cobalt nanoparticles on MWCNT and Al₂O₃ supports for FT synthesis. According to the results of their work the images obtained from HRTEM showed a high amount of cobalt clusters on alumina, with an irregular distribution as a result of different stages of aggregation. In the case of carbon nanotube supported catalyst, cobalt particles with poorly-defined shapes, like layers of plates with around 10nm and 1nm width were found. The difficulty to obtain diffraction images for a large amount of cobalt aggregates confirms their nanometer-order thickness.

Zhang *et al.* studied the effects of MWCNTs as a promoter for synthesis of high alcohols from syngas [97] in continuous flow reactor-GC combination system. In their work they reported the development of CNT promoted Co-Cu catalyst which was highly active for higher alcohol synthesis. Results showed that CO conversion observed on the Co₃Cu₁₋₁₁% CNT catalyst reached 38.0% which was 1.50 times that of the CNT-free counterpart. Moreover appropriate incorporation of CNT into

Co_3Cu_1 not only increased the catalyst activity for CO conversion significantly, but also alcohol formation was improved dramatically. The CNT-promoted Co_3Cu_1 catalyst achieved highly selective formation of BuOH and DME from syngas, comparing with the results of CNT free Co_3Cu_1 catalyst.

Effect of MWCNTs as a promoter in Co-Mo-K sulfide-based catalyst for higher alcohol synthesis from synthesis gas was investigated by Xiaoming *et al.* [97]. Catalysts were prepared by co-precipitation and impregnation methods. A fixed-bed continuous flow reactor and gas chromatograph (GC) combination system were used in order to evaluate the performance of the catalysts. As a result of their work, catalyst with addition of 10 wt% CNT showed the best catalytic performance. The yield of $\text{C}_1\text{-C}_4$ alcohols reached 11.0 % over this catalyst while the yield of $\text{C}_1\text{-C}_4$ alcohols over other catalysts was lower respectively. Over the CNT-promoted catalyst, CO conversion reached 21.6% with the selectivity for total alcohols and C_{2+} alcohols higher than that over the CNT free counterparts. Also, the selectivity for total alcohols and C_{2-4} alcohols reached 61.5% and 41.3% respectively which were higher than those over $\text{Co}_1\text{Mo}_1\text{K}_{0.3}$.

Another group of researchers Wu *et al.* [98] investigated the role of Co-decorated carbon nanotubes as a promoter for synthesis of higher alcohols from synthesis gas. A series of X% Co/MWCNT promoted Co-Mo-K oxide based catalysts was prepared by the combined co-precipitation and impregnation method. According to results of experiments, Co-decorated MWCNTs performed well in terms of selectivity towards the formation of C_{2+} alcohols from syngas. Incorporation of a proper amount of the Co-decorated MWCNTs into the Co-Mo-K catalyst caused little change in E_a for HAS reaction, but led to an increase of surface concentration of the two kinds of catalytically active species ($\text{CoO}(\text{OH})/\text{Co}_3\text{O}_4$) and Mo^{4+} , both closely associated with the alcohol generation.

Next research work performed by Dong *et al.* [99], described the preparation and characterization of CNT promoted Co-Cu catalyst for higher alcohol synthesis from synthesis gas. Two types of CNTs which are “herringbone type” (symbolized as CNT h-type) and “parallel type” (symbolized as CNT p-type) was used as a promoter

for Co-Cu catalysts. CNTs were twice treated with boiling concentrated nitric acid for 4h, followed by rinsing with de-ionized water, and then drying at 473 K under dried nitrogen. It caused to obtain open-end CNTs with hydrophilic surface. Results of experiments showed that the catalyst with 11% of CNT-content is the optimum amount for the highest catalytic activity. Co/Cu 3:1 molar ratio was also most favorable concentration for achieving the highest catalytic activity.

Carbon nanotube supported Mo catalyst promoted with Co metal for synthesis of high alcohols from syngas was studied by Surisetty *et al.* [100]. In this work a series of Co (3, 4.5, and 6 wt %) promoted alkali modified molybdenum based catalysts (9 wt% K and 15 wt% Mo) supported on MWCNTs were prepared by sequential pore volume impregnation. Also MWCNT supported catalyst with 15 wt% Mo and 9 wt% K (Mo-K/MWCNT) were prepared as a reference catalyst to distinguish the effects of Co promoter. CNT was chosen because of its unique properties such as, appropriate pore size distribution, favoring maximum metallic dispersion, highly graphitized tube walls, and nano-sized channels [97], [101]. In this work much attention was paid to the effect of Co to Mo catalyst as a promoter. Influence of CNT is not described broadly.

Bezemer *et al.* [102] investigated the effect of manganese as a promoter in nanofiber supported cobalt catalyst for Fischer-Tropsch synthesis. Catalysts with Co/Mn molar ratios varying from 11 to 431 were prepared. CNF of the fishbone type were purified by refluxing in 1 M KOH, and adsorption sites were created by using concentrated HNO₃. In this work, the effect of MnO as a promoter was described largely. Using CNF as a support material was desirable, as MnO did not interact with the inert graphite surface (e.g., Mn carbides were not observed in XPS) [20]. It made CNF suitable material for studying the manganese promotion effect in Co based FT catalysts.

Bezemer and co-workers studied the properties of Fischer-Tropsch cobalt catalyst supported on carbon nanofibers and silica prepared by homogeneous deposition-precipitation method [103]. In this research, catalysts by deposition-precipitation method from low pH and from high pH were prepared and denoted as

L-CNF and L-SiO₂ (where “L” is low pH), H-CNF and H-SiO₂ (where “H” is high pH). Catalytic tests showed that the catalysts prepared from high pH outperformed the catalysts prepared from low pH. Depending on the support material the activity increased by a factor of between 2 to 4. Remarkably high and stable C₅₊ selectivity of around 53 wt% was found for H-CNF catalyst.

Carbon nanofiber supported cobalt catalyst for FTS with high activity and selectivity were prepared and characterized by Yu *et al.* [167]. Two types of carbon nanofibers were tested as a support material, such as platelet and fishbone types. In their work they found that cobalt supported on carbon nanofibers with platelet structure can easily achieve high dispersion probably because of a high number of edge sites and thus also oxygen groups. According to results the platelet CNFs combined two attractive features of the alumina supports such as high activity of γ -Al₂O₃ and the high C₅₊ selectivity of α -Al₂O₃.

Yu *et al.* [104] investigated the role of surface oxygen towards deactivation, preparation and activity of CNF supported cobalt catalysts for FTS. According to results, they have found that the treated CNFs with surface carboxyl groups are important for highly dispersed cobalt particles and the stabilization of cobalt particles against sintering. Re-reduction with hydrogen can restore most of the initial activities of catalysts. Spent catalysts were characterized by TEM, and concluded that the catalysts are deactivated most likely by oxidation of the cobalt particles which is further ascribed to the surface oxygen groups of CNFs.

Effect of particle size on carbon nanofiber supported cobalt catalysts for Fischer-Tropsch reaction has been studied by Bezemer *et al.* [105]. In their work they concluded that catalysts with sizes smaller than 5nm have progressive high methane selectivity. For catalysts with high methane selectivities also lower chain growth probabilities were found, resulting in an even lower selectivity to heavy weight hydrocarbons. High selectivity to methane indicates a lower abundance of sites active for chain growth, resulting in more carbon species at the surface that become fully hydrogenated to methane. The catalytic performance in Fischer-Tropsch

reaction was independent of cobalt particle size for catalysts with size larger than 6-8 nm.

Johan *et al.* [106] studied the CNF supported cobalt catalyst with maximum activity for FT synthesis. According to the analysis, an optimum cobalt particle size of 4.7 ± 0.2 nm and a concurrent maximum activity $(4.5 \pm 0.2) \times 10^{-5}$ mol Cog Co⁻¹ s⁻¹ was calculated for Co/CNF catalysts in the FT reaction (1 bar and 220°C).

In recent research, done by Tavasoli and co-workers [107], researchers studied the effect of confinement in carbon nanotubes on the activity, selectivity and lifetime of FT Co/CNT catalysts. Also the deactivation properties of CNT-supported cobalt catalysts during continuous FT synthesis were investigated.

2.8 SBA-15 based Cobalt and Ruthenium catalysts for FTS

The use of mesoporous silica as a support for preparing Co-based catalysts has been recently explored by Yin *et al.* [10]. In their work they used hexagonal mesoporous silica (HMS) as a support for cobalt based Fischer-Tropsch catalysts. Different catalysts were prepared by pore volume impregnation. FT reaction was conducted in continuous flow fixed bed stainless steel reactor. According to the results in terms of FT activity, the long chain HCs (wax) was the main product for mesoporous molecular sieves supported Co catalysts. HMS mesoporous sieves which possesses shorter channel, smaller domain size, and larger textural mesoporosity than MCM-41, showed better activity and C₅₊ selectivity. All species incorporated in HMS which caused its pore size to decrease of activity and FT selectivity.

The group of researchers lead by Wang [87] studied the SBA-15 mesoporous silica as a support for high loading of cobalt FT catalysts. Catalyst performance was carried out in stainless steel high pressure system under 532 K, and 2.0MPa having 2:1 ratio of H₂/CO fed gas. Results showed that CO conversion over 20mass% Co/SBA-15 increased with increasing time on stream up to roughly 1 hour and appeared to be steady after 2 hours. The catalyst with larger pore diameter and larger size of Co particles showed the slightly high conversion at 523 K. It can be expressed

that the reducibility, in other words, the catalytic activity is improved by adding a small amount of a noble metal such as Ru [108].

Khodakov *et al.* [109] investigated pore size effects of mesoporous silicas over Fischer-Tropsch Co catalysts. 5wt % cobalt was loaded on supports via incipient wetness impregnation using solutions of cobalt nitrate. Catalytic and characterization results showed strong impact of support porosity on the structure, reducibility, and FT catalytic behavior of cobalt species. Characterization techniques uncovered that both, the size of supported Co_3O_4 crystallites and their reducibility strongly depend on the pore diameter of mesoporous silicas. Small pores present in MCM-41 materials lead to a smaller size of the supported Co clusters and to their lower reducibility in hydrogen. According to catalytic experiments towards FT synthesis, Co species which located in the narrow pore silicas were less active and produced methane with selectivities high than larger cobalt particles in the wide pore supports. Lower FT activities and higher methane selectivities observed on the narrow pore cobalt catalysts were principally attributed to the lower reducibility of small cobalt particles.

The influence of metal loading, cobalt precursor and promoters (Re and Mn) on Co/SBA-15 catalyst for Fischer-Tropsch synthesis was investigated by Martinez *et al.* [110]. Co/SBA-15 catalysts with different Co loading (10-40 wt%) were prepared via impregnation method using ethanol as a solvent. The FTS reaction was conducted in fixed bed stainless steel reactor with 1g catalyst. After reduction procedure, ($\text{CO}/\text{H}_2=2$) gas was introduced to catalyst bed and reaction was conducted under 20 bar and 493 K. Maximum CO conversion (43%) and C_{5+} selectivity was obtained for catalyst 20Co/1Re/SBA-15.

Cai *et al.* [111] studied catalytic properties of the ruthenium promoted Co/SBA-15 catalysts for FTS researchers prepared catalysts with 5% Co loading on each. Ru in the amount of 0.05, 0.1 and 0.5wt % was loaded by using $\text{Ru}(\text{NO})(\text{NO}_3)$. FT synthesis test were conducted in fixed bed reactor (ID=2cm). Based on the results obtained from experiment, researchers concluded that Ru performed remarkable promoting effect in terms of catalytic activity of a Co/SBA-15 catalyst. With increase

of Ru loading, the activity of a Co catalyst for FTS increased due to increased reducibility of the catalyst and the synergetic effect of Ru and Co. Meanwhile the higher C₅₊ hydrocarbon selectivity and the lower methane selectivity was obtained with higher Ru loading which is also attributable to the higher catalyst reducibility.

Next team of researchers leaded by Xiong [112] investigated the role of pore size in Co/SBA-15 catalysts. According to obtained data, wide pore size catalysts exhibited much more CO adsorption sites both linear and bridge type at room temperature unlike small pore size catalyst. The wider pore size catalysts lead to the formation of larger cobalt cluster size, lower dispersion and higher reducibility. The larger cobalt cluster size gave rise to the enhancement of bridge-type CO during FTS. CO conversion is found to increase and then decrease with increasing pore size studied. The results also showed that the cobalt particle size should be of primary importance for the C₅₊ selectivity.

In their very next work Xiong *et al.* investigated the effect of ruthenium promotion on high loaded Co/SBA-15 catalysts for FTS [113]. In this study two types of catalysts, one with Ru (0.05 and 0.5wt %) and second without Ru were investigated. It was concluded by researchers that the addition of a small amount of Ru promoter to 30 wt% Co/SBA-15 shifted the reduction temperature of both steps (Co₃O₄→CoO and CoO→Co⁰) to lower temperatures and decreased the amounts of Co²⁺ species. After reduction, ruthenium atoms were partially encapsulated within cobalt clusters, in direct contact with cobalt atoms. A part of Ru atoms took part in hydrogen spillover from Ru to cobalt oxide clusters and strong electronic interaction between metal cobalt and ruthenium has not been observed. With increasing ruthenium content, catalyst reducibility increased and cobalt atom became enriched at the surface of support. Moreover, the peak intensities of both the linear and bridge types CO adsorption increased with the increase of ruthenium content, leading to the increased activity. The decreased CH₄ selectivity was due to the decrease of Co²⁺ and Co³⁺ species at the catalyst surface with the addition of ruthenium.

Prieto *et al.* [114] investigated the impact of pore length on metal dispersion, and catalytic activity of Co/SBA-15 catalysts in the FTS. Researchers used a wide-pore

(11 nm) SBA-15 mesostructures displaying markedly different morphologies and pore lengths (0.3–5.7 μm) as support for catalysts. Also catalyst supported on conventional narrow (7 nm)-pore SBA-15 displaying high pore length (6.9 μm) has also been synthesized as a reference. After catalyst preparation all catalysts were characterized and evaluated for the FTS under conditions $T = 493 \text{ K}$, $P = 2.0 \text{ MPa}$ in a down-flow fixed-bed stainless steel reactor with 1.0 g catalyst. Based on the results researchers concluded that the use of novel short-pore SBA-15 mesostructures for preparing 1 wt% Ru–20 wt% Co catalysts lead to higher metal dispersions as compared to samples supported on conventional SBA-15 which displayed long and highly curved pores. High pore lengths lead to higher pore-residence time for the endo-generated gases during the thermal decomposition of the Co nitrate precursor which have a detrimental effect on metal dispersion, promoting the formation of large rod-like Co_3O_4 particles. The higher metal dispersion attained for short-pore RuCo/SBA-15 catalysts translates into a higher Co-time-yield (CTY) under realistic FT conditions. Additionally, at 55% CO conversion levels, the selectivity toward the desired C_{5+} fraction progressively increases when the pore length of the supporting SBA-15 mesostructured silica is gradually shortened, reflecting a facilitated diffusional access of CO to the active sites through the wax-filled regular mesopores.

2.9 Pore size effect on FTS

Song *et al.* [168] investigated the effect of catalyst pore size using commercial silica with different pore sizes. The results showed that the support porosity in the range of 6-10 nm displayed high CO conversion (>65%) and high C_{5+} selectivity (>85%).

The effect of catalyst pore size was investigated by Witoon *et al.* [169] where they found that the CO_2 selectivity was very high with the catalysts of small pore diameters which are in the range of 2 to 9 nm. They attributed this phenomenon to the irreducibility of the cobalt species existed in the small pores. At the same time methane selectivity was also higher in the small pores comparing to wide pore catalysts.

Jung, *et al.* [170] studied the effect of pore and particle size of different mesoporous silica supported catalysts on FT synthesis using cobalt as an active metal. Results revealed that the higher CO conversion (75.5%), C₅₊ selectivity (70.4%) and lower CH₄ selectivity (19.84%) were observed in the catalysts with pore size of <10 nm and cobalt particle size of < 10 nm.

Effect of ruthenium as a promoter to FT activity of Co/SBA-15 catalysts was studied by Rodrigues *et al.* [171]. According to the results, the addition of ruthenium caused the improvement in cobalt reducibility and FT activity of Co/SBA-15 catalysts. They phenomenon attributed this to the synergetic effect between Co and Ru. In terms of FT activity Ru/Co/SBA-15 catalysts showed moderate conversion (40%) and high selectivity towards the production of C₅₊ (80 wt%).

The influence of the effect of average pore diameter of silica support on the physical and chemical properties of supported cobalt catalysts and their performance in the FT synthesis was investigated by Saib *et al.* [173]. The researchers tested silicas with different pore diameters in the range of 2 to 15 nm, impregnating them with 20 wt% cobalt. The crystallite size and the degree of reduction were found to increase with increasing pore diameter of the support. With increasing average pore diameter, size of the cobalt clusters also increased. In the FT synthesis, catalysts with 10 nm pore diameter performed well with maximum CO conversion of 60%, while support with 2 nm showed 16% CO conversion. Accordingly C₅₊ selectivity of the catalyst with 10 nm pore size was the highest with 74%.

2.10 Particle size effects on FTS

The influence of cobalt particle size to FT synthesis in terms of C₅₊ selectivity was investigated by Borg *et al.* [174]. The experiment was conducted in the range of 3 to 18 nm cobalt particle size and maximum selectivity was observed in cobalt particle size with 7-8 nm.

The effect of cobalt metal particle size was extensively investigated by Khodakov [157]. He stated that cobalt particles in activated catalysts should not be

smaller than optimum size of 6 – 8 nm. Small cobalt particles in the range of 4 – 6 nm do not normally exhibit acceptable catalytic performance.

Prieto *et al.* [175] studied the effect of cobalt particle size in FTS using Co/ITQ-2 and Co/SiO₂ catalysts. Formation of barely reducible surface and bulk and cobalt silicate species was observed for Co₃O₄ ≤ 5.9 nm. Under realistic FT conditions (220°C, 2.0 MPa) the TOF increased from 1.2 × 10⁻³ to 8.6 × 10⁻³ s⁻¹ when d (Co⁰) increased from 5.6 to 10.4 nm.

The influence of pore diameter on turnover frequency was studied by Ghampson *et al.* [176] using Co/SiO₂ catalysts. The studies were carried on in a series of mesoporous silica supported cobalt catalysts with pore diameters from 3 to 22 nm. It was found that there is a linear relationship between TOF and pore diameter up to 13 nm. At pore diameters larger than 13 nm the TOF was insensitive to pore diameter.

Another group of researchers Wang *et al.* [177] investigated intrinsic particle size effects of cobalt metal to Fisher-Tropsch synthesis using Co/SiO₂ catalysts and batch reactor. Co/SiO₂ was prepared with cobalt particle size 1.4 - 10.5 nm which was measured from TEM images. XPS spectra showed that small cobalt particles in the size 1.4- 2.5 nm were readily oxidized by water vapor, while in the relatively larger particles (3.5-10.5 nm) such oxidation was not evident. In terms of FT activity, oxidation of small particles led to lower TOF and higher methane selectivity comparing to relatively larger particles.

Relation between hydrocarbon selectivity and cobalt particle size was studied by Rane *et al.* [178] using Co/Al₂O₃ FT catalysts. Relation between methane olefin and C₅₊ selectivities were studied for 2-14 nm cobalt particles. Researchers found the increase in C₅₊ selectivity with increasing Co particle size for particles less than 8-9 nm, where selectivity was in maximum level. Accordingly the lowest CH₄ selectivity and the highest olefin to paraffin ratio were obtained with Co particle size of 8-9 nm.

Fu *et al.* [179] investigated effect of multiwall carbon nanotube support to FT activity and product distribution by making comparison between CNT, ordered mesoporous carbon and activated carbon. Among all catalysts better CO conversion

(64%), lowest methane selectivity (10.6%) and higher C₅₊ selectivity (87.3%) was observed in Co/CNT catalyst.

Effect of cobalt crystallite size to Fischer-Tropsch activity was studied by Fischer *et al.* [180] using Al₂O₃ as a support. Researchers found that 4.7 nm sized freshly reduced cobalt crystallites displayed better conditions for CO hydrogenation. Methane selectivity increased with decreasing crystallite size in parallel with a decrease of C₅₊ selectivity.

Liu *et al.* [181] studied the effect of pore size and application of laboratory scale (0.5 L) and pilot (12.5 L) continuous slurry phase reactors in FTS using Co/SiO₂ catalysts. Results revealed that Co supported on SiO₂ with an average pore size of 10 nm showed high catalytic performance of the FT synthesis due to the suitable cobalt particle size in the catalyst. N-hexadecane was suitable for laboratory scale reactor, while diesel was suitable for 12.5 L FT plant reactor (in order to reduce the cost). They also found that stirring was very important for both reactors in order to increase CO conversion where they found 700 rpm was optimum for both reactors. In 700 rpm CO conversion in 0.5 L reactor reached to 40%, while in 12.5 L reactor it was 72%.

2.11 Fischer-Tropsch synthesis in slurry environment

Optimum condition of FT synthesis was investigated by Woo *et al.* [182] using continuous flow slurry bubble column reactor. Research was carried out in varying conditions of temperature (210-250°C), pressure (1.0-3.0 MPa), GHSV (1000-6000 L/kg/h), superficial gas velocity ($U_G = 1.7-13.6$ cm/s) and slurry concentration ($C_S = 9.09-26.67$ wt%). Studies showed that the overall CO conversion increased with increasing reaction temperature, system pressure and catalyst concentration. They concluded that the optimum operating conditions based on the yield of hydrocarbons and wax products were; superficial gas velocity $U_G = 6.8-10$ cm/s, $C_S = 15$ wt%, $T = 220-230$ °C and $P = 2.0$ MPa.

Chambrey *et al.* [183] compared FT synthesis performance in single channel milli-fixed bed reactor, conventional centimetric fixed bed and slurry stirred tank reactor using platinum promoted alumina supported cobalt catalyst. Among three reactors, the single channel milli-fixed bed reactor displayed higher initial FT rate, which was assigned to a better temperature control and less significant catalyst deactivation during startup period. The slurry stirred tank reactor showed much lower hydrocarbon productivity than the milli- and centimetric fixed bed reactors, and it was referred to difficulties in obtaining highly reduced cobalt catalysts.

Optimum parameters in slurry bubble column for FT synthesis were investigated by Kwack *et al.* [184]. Based on simulation and experimental findings they found that by increasing of reaction temperature from 210 to 240°C conversion of CO increased from 30 to almost 90%. CO conversion also increased when the hydrogen to carbon monoxide ratio increased from 1 to 2.5 mol. Increase in pressure from 10 to 25 bar also positively affected in CO conversion.

Liu *et al.* [185] investigated the effect of water in FTS by adding it prior to reaction to batch slurry reactor in molar ratio of $H_2O/CO = 12$. The addition of water vapor exhibited a marked effect on the product selectivity, which contradicts to classical ASF concept. Addition of water vapor played the role of a promoter and resulted in remarkable increase of heavy products' up to 87.3% against 32% in unpromoted FT process with water.

Fischer-Tropsch synthesis was carried out by Chen *et al.* [186] in testing eggshell-type Co/SiO_2 using continuous flow slurry batch reactor. Results revealed that eggshell type Co/SiO_2 catalyst showed better results in generating long chain HCs and relatively low methane formation comparing to conventional impregnated catalyst under $P=1.0$ MPa, $T= 503K$ $W/F=5.0g$ -cat h/mol and $CO/H_2 =2$. The use of MWCNT, SBA-15, the effect of pore size and particle size is summarized in Table 2.1 below.

Table 2.1: Summary of major findings

Material/ Phenomena	Ref#	Author& reference	Results/effects
MWCNT	[88]	Tavasoli, et al., Fuel Proc. Tech, 89, pp. 491-498, (2008)	Interaction with Co decreased, reduction t° decreased, well dispersion of Co clusters, CO conv. 80-90%, C ₅₊ increase 70-77%, slight decrease to lower MW CHs, By treating with HNO ₃ - caps opened surface area increased, reducibility increased
	[90]	Trepanier et al. Fuel Proc Tech, 90, pp 367-374, 2009)	
	[172]	J. Lü, et al., J. N.Gas Chem, 21, pp. 37-42, (2012)	
	[179]	Fu, et al, Fuel Proc Tech 2013	
SBA-15	[87]	Wang <i>et al</i> , Catalysis Today , 68, pp 3-9, (2001)	Co located on SBA-15 pores active for FT, Co loading on SBA-15 showed better activity and C ₅₊ selectivity comparing to MCM-41 due to shorter channel, smaller domain size, larger textural mesoporosity
	[109]	Khodakov <i>et al</i> , J. Catalysis, 206, pp 230-241 (2002),	
	[110]	Martinez <i>et al</i> , J. Catalysis 220, pp 486-499 (2003)	
	[171]	Rodrigues <i>et al</i> , J.N. Gas Chem 21, pp 722-728 (2012).	
Ruthenium	[91]	Trépanier <i>et al</i> , Appl. Cat. A: General, 353, 193-202, (2009)	Increase of CO conversion, increase of selectivity, enhancement in Co reducibility, increase in Co dispersion decrease in average Co cluster size, synergetic effect of Ru and Co
	[111]	Cai <i>et al</i> , Cat. Communications 9, 2003-2006, (2008)	
	[113]	Xiong <i>et al</i> , Fuel processing technology 90 237-246,(2009)	
	[171]	Rodrigues <i>et al</i> , J.N. Gas Chem 21, pp 722-728 (2012).	
Particle size	[105]	Bezemer <i>et al</i> . J. Am. Ch. Soc, 128, pp. 3956-3964, (2006)	FT results are independent from Co particle size for catalysts with sizes larger than 6 nm 8 nm, TOF decrease, selectivity decrease were observed with decreasing of particle size from 16 to 2.6 nm. Optimum size should not be smaller than 6 – 8 nm.
	[157]	Khodakov <i>et al</i> , Catalysis Today, 144, 251–257 (2009)	
	[177]	Wang <i>et al.</i> , Catalysis Today, 181, pp. 75-81, (2012).	
	[178]	Rane, <i>et al</i> , Applied Catalysis A: General, 437–438, 10-17, (2012)	
Pore size	[112]	Xiong et al. Jour. Mol. Catal A: Chemical 295 68-76,(2008)	The support porosity higher than 10 nm displayed high CO conversion high C ₅₊ selectivity. CH ₄ and CO ₂ selectivity was higher in the pores smaller than 10 nm.
	[169]	Witton, <i>et al</i> , Fuel Proc Tech, 92, pp. 1498-1505 (2011)	
	[170]	Jung, <i>et al</i> , Catalysis Today, 185, 168-174, (2012).	

CHAPTER 3

MATERIAL AND EXPERIMENTAL METHOD

In this chapter methods to purify MWCNT along with SBA-15 synthesis are described and steps of cobalt catalyst preparation are included. Further catalyst reduction system together with application of autoclave reactor briefly highlighted. Since catalyst characterization techniques are essential in catalyst research, their general functions are also specified. Finally essential constituents of product (produces FT wax) characterization is highlighted in brief. Preparation, characterization and activity test of the catalysts were conducted in combinatorial catalysis laboratory COMBICAT in University Malaya under Professor Dr Sharifah Bee Abd Hamid's supervision. Catalyst characterization techniques such as N₂-adsorption measurements, TGA-MS, XRD, SEM and TPR were provided by COMBICAT. The 200 ml autoclave reactor was also provided by COMBICAT and was applied in order to test catalyst FT activity.

3.1 Materials

In present work, Cobalt (II) nitrate hexahydrate and ruthenium (III) acetylacetonate were the key reactants used in preparation of MWCNT and SBA-15 based Fischer-Tropsch catalysts. The mixture of CO and H₂ in the ratio of 1:2 was applied as a synthesis gas in order to evaluate the activity of the catalysts. The chemicals and gases used for FT catalyst preparation and reaction are listed in Table 3.1.

Table 3.1: List of chemicals and gas used in the experiments

#	Chemical/Gas	Supplier	Molecular formula
1	Unpurified multiwall carbon nanotubes (MWCNT)	Bayer, Baytubes C 150 P	C
2	Pluronic® P-123	Sigma Aldrich	(C ₃ H ₆ O·C ₂ H ₄ O) _x
3	Hydrochloric acid fuming 37% GR for analysis ACS	Merck	HCl
4	Tetraethyl orthosilicate (TEOS)	Merck	SiC ₈ H ₂₀ O ₄
5	Cobalt (II) nitrate hexahydrate for analysis emsure®	Merck	Co(NO ₃) ₂ ·6H ₂ O
6	Ruthenium (III) acetylacetonate for synthesis	Merck	(C ₅ H ₇ O ₂) ₃ Ru
7	Nitric acid 65% for analysis ensure® ISO	Merck	HNO ₃
8	N-hexadecane for synthesis	Merck	C ₁₆ H ₃₄
9	Synthesis gas (33% CO in H ₂)	Su Jin Enterprise	CO+2H ₂
10	Mixed gas (5% H ₂ in Ar)	MOX	5%H ₂ +95%Ar

3.2 Preparation of catalyst support

3.2.1 Multi Wall Carbon Nanotube (MWCNT)

Multiwall Carbon Nanotubes were obtained commercially from “Bayer, Baytubes C 150 P” and purified. Major specification of MWCNT from supplier is given in Table 3.2 [115]:

Table 3.2: Specifications of unpurified MWCNT

Properties	Value
C-purity (wt %)	≥ 95
Free amorphous carbon (wt %)	No detectable
Outer mean diameter (nm)	± 13
Inner mean diameter (nm)	± 4
Length (μm)	>1
Bulk density (kg/cm^3)	130-150

Before applying MWCNT as a support, it was purified in 65 wt% concentrated HNO_3 (Merck) with 14.65 molarity, by using reflux system shown in Figure 3.1. In the first step, oil bath was heated up to 100°C . The MWCNT in the amount of 10 g and 1000 mL of nitric acid was transferred into 1000 mL round bottom flask. The round bottom flask was set up to reflux system with oil bath and the mixture was kept at 100°C for two hours with stirring. In the second step, the mixture was cooled down to room temperature and diluted with 1500 mL of distilled water. The MWCNT was separated via filtering using Buchner funnel. In the next step, purified MWCNT was rinsed with 1000 mL of distilled water and redispersed again with 500 mL of distilled water and left for stirring overnight. In the last step, stirred MWCNT was separated again, by using Buchner funnel and washed with distilled water until the pH reached 5-7. The pH of the filtrate was measured using pH meter. Finally purified MWCNT was transferred into a beaker and dried overnight at 110°C in an oven.

Reflux system consists of a heater, oil bath, thermometer, round bottom flask, cooling zone, and base container. When temperature is increased up to 100°C , nitric acid starts to boil, since its boiling point is 83°C . Evaporated nitric acid goes through the cooling system and condenses back. Non condensed acid flowed into the receiver containing sodium hydroxide which acts as a neutralizer.

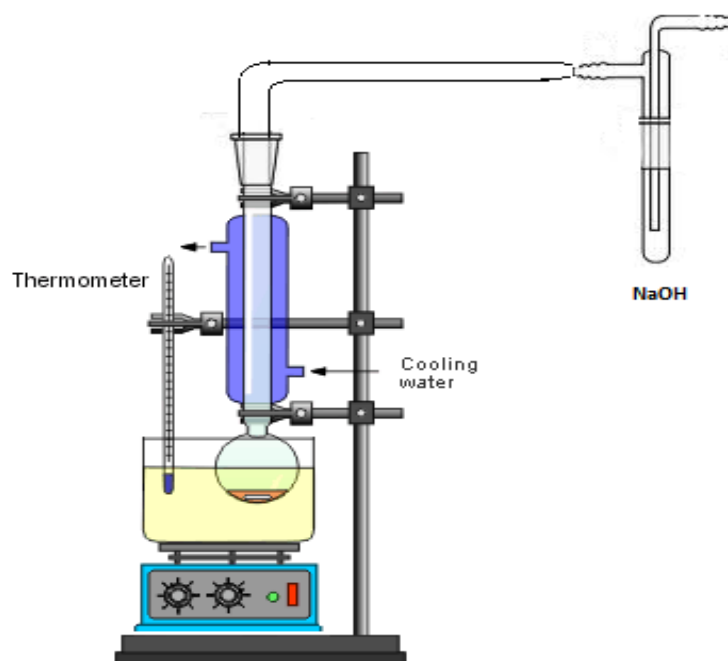


Figure 3.1: Reflux system

3.2.2 Santa Barbara Amorphous -15 (SBA-15)

SBA-15 was synthesized using pluronic® P-123, hydrochloric acid fuming 37% and Tetraethyl orthosilicate (TEOS) [12]. 8g of pluronic® P123 was placed in a 500 mL beaker, together with 240 mL of hydrochloric acid and stirred in room temperature by using magnetic stirrer until P123 was dissolved completely in the concentrated HCl. Once pluronic® P123 was dissolved completely, 18.2 mL of tetraethyl orthosilicate (TEOS) was added and the solution was transferred to 500 mL round bottom flask. The round bottom flask with solution was connected to reflux system and heated with oil bath until temperature reached 35-38°C and left for 24 hours. The temperature was increased up to 80°C and the solution was further stirred at this temperature for 48 hours. In the following step, the solution was cooled down to room temperature and the SBA-15 formed was separated with filter paper using Buchner funnel. Finally, obtained SBA-15 was dried overnight at 100°C and calcined in 550°C for 4 hours. The same instruments and setup which is shown in Figure 3.1 was used to synthesize SBA-15.

3.3 Preparation of catalyst

Preparation of MWCNT and SBA-15 based cobalt catalyst with ruthenium promoter was carried out using incipient wetness impregnation method. This method is simple and the most common procedure for dispersing a catalytic species on a carrier by impregnating the predried support to incipient wetness with an aqueous or non-aqueous solution containing a salt (precursor) of the catalytic element or elements. The precursor salt is dissolved in a volume of solvent equal to the catalyst pore volume, and this solution is added slowly (sometimes dropwise) to the support in which capillary forces draw the liquid into the pores. Addition of solution continues until the pores of the support are saturated as evident by the beading of the excess solvent. In this manner the precise amount of catalytic species is assured to be present in the carrier [116]. Steps of catalyst preparation are shown in Figure 3.2. Experimental procedure of 10Co1Ru/MWCNT is given below as an example, which is applied for remaining catalysts as well.

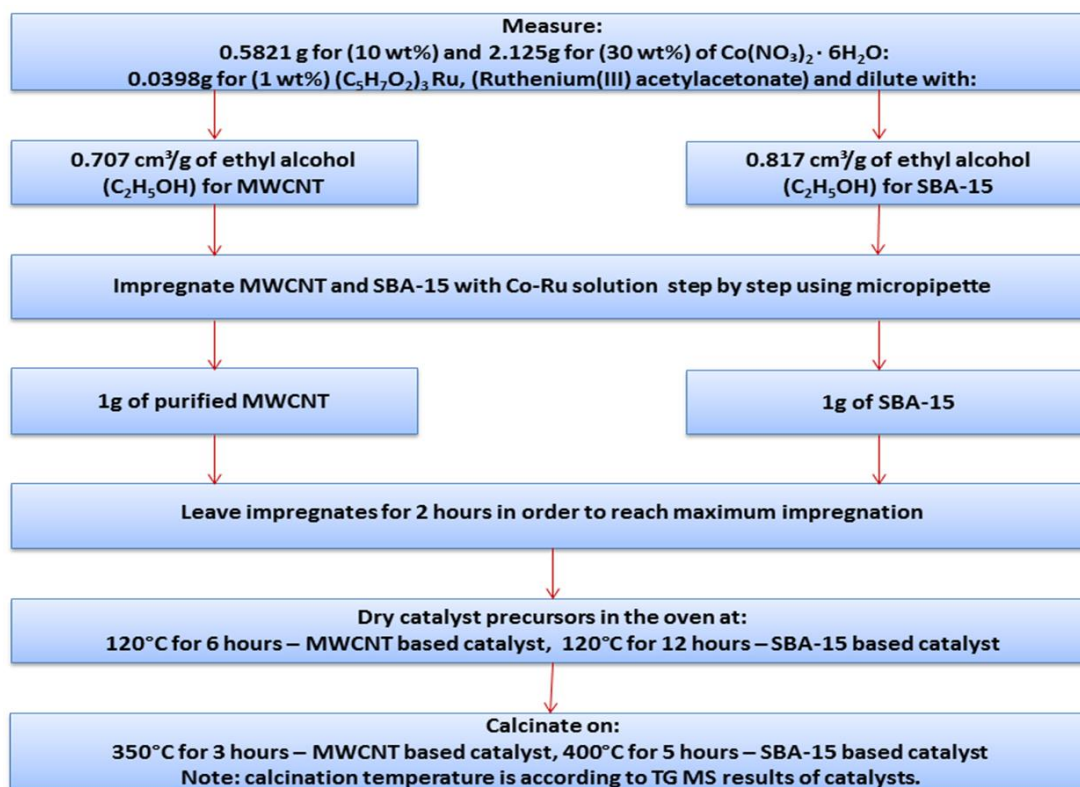


Figure 3.2: Catalyst preparation diagram

3.3.1 10Co/1Ru/MWCNT and SBA-15 supported catalyst

1 g of support (MWCNT or SBA-15), 0.5821 g of cobalt nitrate hexahydrate ($\text{Co}(\text{NO}_3)_2 \cdot 6\text{H}_2\text{O}$), 0.0398 g of ruthenium (III) acetylacetonate (calculation of weight percent from metal precursors is provided in APPENDIX A, Table A-1) were dissolved in ethanol ($\text{C}_2\text{H}_5\text{OH}$). The volume of ethanol used for each catalyst support was determined from the BET analysis (Table 4.1). The MWCNT and SBA-15's pore volume is 0.707 mL/g and 0.817 mL/g, respectively. Therefore the volume of ethanol used to synthesize MWCNT and SBA-15 was 0.707 mL and 0.817 mL, respectively. The metal salt solution was impregnated to support material dropwise. After impregnation, catalyst precursors were stirred manually with spatula in order to distribute metal solution along the support and left for two hours in order to achieve maximum impregnation. Subsequently, SBA-15 and MWCNT based catalysts were dried in the oven at 120°C for 6 hours and 12 hours respectively. Then the SBA-15 based catalysts was calcined at 400°C for 5 hours, and MWCNT based catalysts at 350°C for 3 hours, based on the results of TGA (Figure 4.10 and 4.13).

3.3.2 Nomenclature of prepared catalysts.

Based on aforementioned method, six catalysts with 10 and 30wt% Cobalt and 1wt% Ruthenium were prepared. Ruthenium was used as a promoter to the cobalt which are labeled as M3 and M4, S3 and S4. Also 10 wt% cobalt/MWCNT and 10 wt% cobalt/SBA-15 based catalysts without ruthenium (M2 and S2) were prepared in order to study the effects of ruthenium in the catalysts. Besides the catalysts, pure SBA-15 and pure MWCNT (M1 and M2) were used as a blank material. The catalyst nomenclature is presented in Table 3.3.

Table 3.3: Codes of prepared catalysts

#	Catalyst name	Composition of catalysts		Catalyst label
		Co (wt %)	Ru (wt %)	
1	Pure MWCNT	-	-	M1
2	10Co/MWCNT	10	-	M2
3	10Co/1Ru/MWCNT	10	1	M3
4	30Co/1Ru/MWCNT	30	1	M4
5	Pure SBA-15	-	-	S1
6	10Co/SBA-15	10	-	S2
7	10Co/1Ru/SBA-15	10	1	S3
8	30Co/1Ru/SBA-15	30	1	S4

3.4 Reactor system

The description of catalyst reduction system, 200 mL autoclave reactor and glove box for transferring the reduced catalyst is reported below. Before the exploitation of catalyst reduction system and 200 mL autoclave reactor, the pressure test and leak check test was conducted.

3.4.1 Catalyst reduction

General setup for this system was assembled using tubular furnace, stainless still tubes with ID 0.175 mm and ID 8.5 mm, high pressure regulator and 50 ml burette. 0.175 mm stainless still tubes were used as an inlet and outlet lines of the system and 8.5 mm stainless still tube was used as a fixed bed catalyst container (reactor) for reducing catalysts. Tubular furnace was used in order to provide necessary temperature for reduction of the catalyst. The high presser regulator (<25 bar) was applied as a back pressure regulator in order to maintain required pressure in the system. The burette was used as a bubble meter in order to control the flow rate of the gas in the system. Inlet line was connected to a regulator which was installed to

gas containing cylinder. Fixed bed tube was located inside the furnace. Back pressure regulator and bubble meter were connected in outlet line of the system. The spare parts of the system are depicted in Table 3.4.

Table 3.4: Constituents of reduction system

Spare parts	Function	Parameters
Stainless steel tube	Reactor (fixed bed catalyst container)	450 mm length, 8.5 mm ID
High pressure regulator for flammable gases.	Back pressure regulator	<25 bar
Burette	Bubble-meter	50 mL.
Rotary kiln furnace	Tubular Furnace	< 600 °C
Stainless steel tubing	Inlet and Outlet lines	0.175 mm

Before testing the catalyst performance for Fisher-Tropsch synthesis in an autoclave reactor, the catalysts were reduced at 400°C for 10 hours in a self-designed fixed bed reduction system which is shown in Figure 3.3. All catalysts, which contain active metal, were reduced in this system. Reduction temperature was identified using TPR define surface analysis technique. 5 % hydrogen in argon was used as a reactive gas. Pressure of the system was kept at 2.5 bars. Flow rate of reactive gas was 80-85 mL/min, which was controlled by back pressure regulator and monitored by bubble meter using snoop water. One gram of calcined catalyst was measured and placed in fixed bed catalyst container. Ends of the tube were blocked with quartz wool in order to keep the catalyst particles from blowing during introduction of hydrogen containing gas.

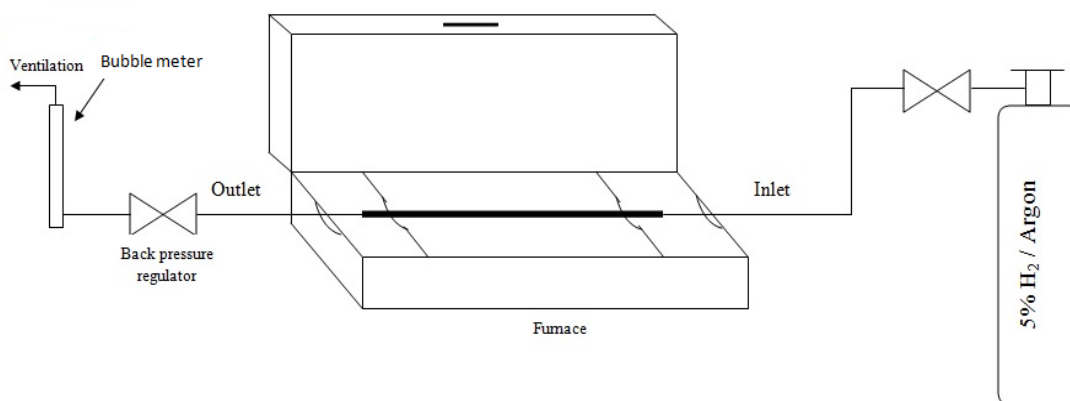


Figure 3.3: Catalyst reduction system

Once catalyst was loaded on reduction system, the back pressure regulator was tightened. The hydrogen gas slowly introduced to the system by opening the regulator which is installed in cylinder gas. Pressure increased up to 2.5 bars step by step. When pressure in the system reached 2.5 bars, back pressure regulator was loosened slightly in order to adjust and maintain the desired pressure in the system. At the same time bubble meter was loaded with a few drops snoop water and the flow rate of the hydrogen gas was adjusted and maintained in 80-85 ml/min. Once pressure and flow rate of the system was maintained, the furnace was switched on and the temperature started to rise up to 400°C by ramping of 10°C/min. After reaching of temperature to 400°C, reduction system was left for 10 hours. During 10 hours, the gas flow rate and pressure was monitored periodically in order to assure that the parameters are maintained in proper order. After 10 hours of the reaction period temperature of the furnace was reduced to 25°C, pressure was reduced to 0.5 bar and flow rate slowed down to 20ml/min. After few hours of cooling period, the supply of the hydrogen gas from cylinder was stopped and fixed bed catalyst container was disconnected from the system carefully. The ends of the fixed bed tube were sealed immediately with parafilm in order to avoid possible contact of air with reduced catalyst inside the tube. Catalyst container was brought to self-fabricated glove box (Figure 3.4) in order to transfer reduced catalyst to 200 ml autoclave vessel.

3.4.2 Glove box for transferring reduced catalyst from fixed bed reduction system to autoclave vessel



Figure 3.4: Image of self-designed glove box

The image of glove box is given in Figure 3.4. The glove box was self-fabricated using 0.15 m³ of plastic box, rubber gloves, and transparent plastic material as a cap for glove box and aluminum foils for connecting rubber gloves with plastic box. Box has inlet and outlet lines assembled with valves for connecting inert gas line. The center of the original cap was cut and removed in order to stick a transparent plastic material on it. The material was tightened with wire from different places and connections were filled with silica grease in order to prevent the leakage during usage. The edges of the cap from inside was assembled with special rubber line with the purpose to seal the cap properly when it is closed. Two holes were cut at the side of the plastic box and special elastic tubes wrapped with aluminum foil fastened to holes in order to connect the rubber gloves.

Box was used to transfer reduced catalyst from reduction tube to 200 mL autoclave vessel. After catalyst was reduced in reduction system, the reduction tube was transferred into a box together with 200 mL autoclave vessel and adjustable spanner and spatula. Nitrogen was introduced for 30 min. Before putting 200 mL autoclave vessel into a glove box it was filled with 50 mL of n-hexadecane (n-C₁₆H₃₄). The purpose of filling of 200 mL autoclave vessel with 50 mL of hexadecane before putting catalyst into it, is to protect the reduced catalyst exposing to the air, even though catalyst was located within the box and the box was continuously being flushed with nitrogen gas. The purpose of spatula was to transfer all reduced catalyst particles from tube to the vessel, while the function of adjustable spanner is to loosen the bolts from both sides of reduction tube (Fixed bed). After putting of the fixed bed tube and 200 ml vessel filled with necessary amount of solvent to glove box, it was closed and sealed properly. The nitrogen gas was introduced to glove box and vessel together with fixed bed tube was kept in nitrogen environment for 15 minutes. After 15 minutes fixed bed tube was opened and reduced catalyst was transferred into the vessel using rubber gloves. After transferring reduced catalyst to the vessel, the nitrogen gas flow was stopped and cap of the glove box opened. The vessel containing reduced catalyst and solvent was taken carefully from glove box and installed in the reactor.

3.4.3 Reactor system (Description of 200mL Autoclave Batch reactor)

200 mL autoclave 1458 1000 type hastelloy reactor, designed by “Top Industries S.A” was used to test the catalysts for Fischer-Tropsch process. The reactor includes pneumatic valves which work in 5 atm. The pressure in the reactor system is controlled by using these valves. The reactor specifications are given in Table 3.5.

Table 3.5: Specifications of 200 mL autoclave hastelloy reactor

Dimensions	105 mm Ø, 158 mm height
Volume	0.196 liter
Operating pressure	1 to 300 bar
Operating temperature	15 to 250°C
Stirring speed	0 to 1500 rpm

Once catalyst is transferred into a 200 mL vessel, it is sealed tightly. The images of the reactor are shown in Figures 3.5 (general view) and 3.6 (autoclave view) respectively. Process parameters are controlled by the software which allows choice of which parameter to increase first, in terms of pressure to temperature or vice versa. Reactor system has two inlet lines, one for the reactive gas which is “Line A” and the second line is for inert gas which is “Line B”. Feed line of autoclave is brought until the bottom of the vessel. Outlet line is not immersed in the liquid. Main constitutes of reactor is depicted in Figure 3.7.

The synthesis gas is injected from the “Line A” and passes through the pneumatic valves VP11 and VP12. Pressure in the system is built by these two valves. There is a “Capacity tank” between them which is calibrated with a known volume by the manufacturer. In each time when pressure drops in the system, VP12 is opened and the known volume of stored synthesis gas in the capacity tank is introduced to the reactor. Accordingly VP11 is opened and fills the capacity tank with a feed gas, once capacity tank is empty. The software “Top view” calculates the number of opening and closing of these two pneumatic valves. By this way, the volume of the consumed gas is calculated. The reactor itself is not calibrated for a

certain type of gas. The volume of any gas which is injected to the system can be identified by this way. In case of pressure exceed above allowed norm, which is set and controlled by the software, safety valve CP10 will work and release the pressure.

Reactor can be exploited in two modes, that is, automatic mode and manual mode which is controlled by software ‘Top view’ during automatic mode. The software only supports batch type, since the reactor is designed to run in batch system. In case of continuous reaction, reaction parameters are monitored by the software, but reactor is controlled manually. Main parts of the reactor are 200 mL Hastelloy vessel, stirrer, pneumatic valves and needle valves, which makes usage of the unit quite simple. Pneumatic valves are controlled via compressed air which provides pressure of about 5 bars.



Figure 3.5: Autoclave reactor which is located in COMBICAT University Malaya
(A - general view)

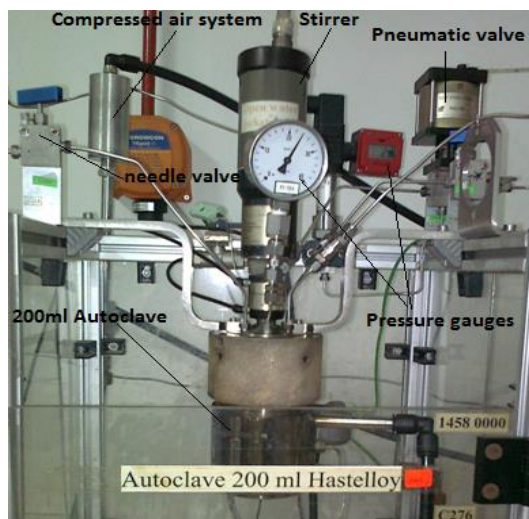


Figure 3.6: Autoclave reactor which is located in COMBICAT University Malaya (B - detailed view)

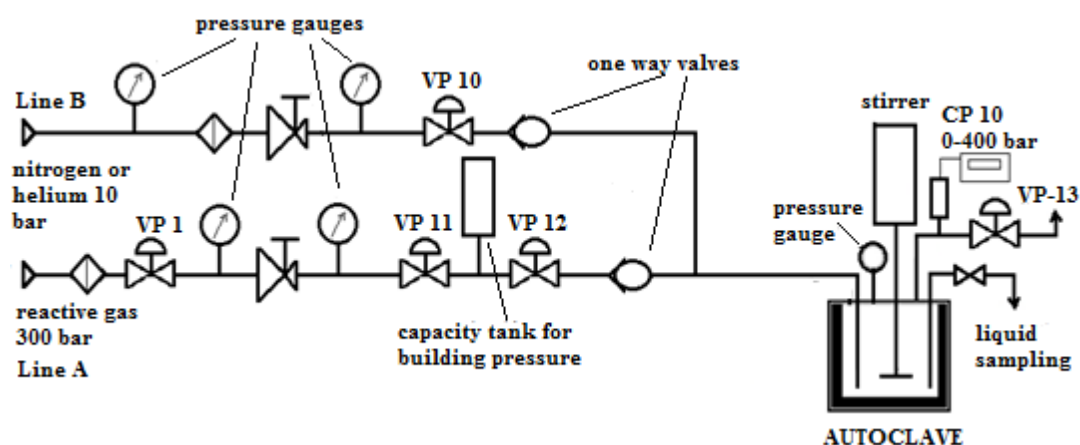


Figure 3.7: Schematic diagram of the experimental set-up

3.5 Fischer-Tropsch synthesis

Fischer-Tropsch synthesis was carried out in 200 mL autoclave reactor which is shown above. Process parameters of the reaction were chosen based on industrial parameters of low temperature Fischer-Tropsch synthesis process. Quite a big number of existing literature use similar parameters in testing MWCNT based catalysts for Fischer-Tropsch synthesis. Reduction temperature of catalyst precursors was chosen based on data obtained from TPR as mentioned earlier. Hence catalyst

reduction and Fischer-Tropsch reaction parameters are summarized in Tables 3.6 and 3.7 respectively.

Table 3.6: Reduction parameters of MWCNT and SBA-15 supported cobalt catalysts

Parameters	
Pressure	2.5 bar
Temperature	400 °C
Duration	10 hour
Gas	5 % H ₂ in Argon
Flow rate	80-85 mL/min

Table 3.7: Fischer-Tropsch reaction parameters of MWCNT and SBA-15 supported cobalt catalysts

Parameters	
Pressure	20 bar
Temperature	220 °C
Duration	17 hours
Synthesis gas CO+H ₂	1:2 mole
Catalyst/solvent ratio	1.0/50 g/mL
Stirrer	300 rotation per minute (RPM)
Solvent	n-hexadecane (C ₁₆ H ₃₄)

3.5.1 Pressure test

Before using the reduction system and the autoclave reactor, pressure tests were conducted in order to identify gas leakage by using snoop (Swagelok). Reduction unit was tested under the pressure of 3.5 bars, while autoclave reactor was tested under 25 bar using nitrogen.

3.5.1.1 Reduction system

During pressure test, main leakage of gas was identified in the connections and joints of fixed bed reactor (stainless steel tube) both, in the inlet and outlet. The snoop water was used to detect the leakage in the joints. When leakage was detected, the pressure inside the system was released and joints were loosened. Silicon grease was used in order to eliminate the leakage. The treads of joints were coated with high vacuum silicone grease in order to eliminate the leakage and to make the proper sealing. After using the silicone grease, the pressure was increased up to 3.5 bars and held for 10 minutes.

3.5.1.2 Autoclave reactor

Autoclave reactor was tested under 25 bars in order to identify gas leakage by using nitrogen and snoop water. The pressure increased gradually starting from 2 bars up to 25 bars. The pressure increase was 2 bars in each time and held for 5 min. Meanwhile each connections and joints of the reactor were checked by using snoop water. The reactor was pressurized by opening VP1 and closing VP10 and VP13 (Figure 3.6 and 3.7). Once bubbles were visible, the pressure was released by opening VP13 in order to tighten the lose joints. After tightening the joints, pressure was built up again, and tightened joints were checked once again for the leakage. The process was repeated until no more leaks were detected. When no more leakage were detected, the reactor was pressurized up to 25 bar and held for 10 min. Pressure gauge at the autoclave and pressure recorder by the software was not changed during

this period, indicating that there was no leakage and the reactor system was tightened/sealed properly.

As shown in Figure 3.7, reactor system has a separate “Line B” for nitrogen or helium. The “Line B” allows purging the reactor system with inert gas, by controlling the pneumatic valve VP1 and VP10 manually, through the software. The system also can be purged with the reactant gas before starting the main reaction, by using “Line A” which is controlled by the software. In the beginning of the reaction process, software “Top view” opens VP1, VP11 and 12 and closes VP13. The system is flushed with reactant gas for 10 seconds under 10 bars and pressure in the system is released by opening the VP13 and closing VP1.

The feed mixture with the catalyst (1 g/50 mL) was introduced to reactor. Before starting the run, the reactor was purged and syngas successfully and then adjusted to the temperature. It was then pressurized with the mixture of CO and H₂ to a desired total pressure gradually in avoiding the feed mixture from spilling out from the liner. The reaction parameters were controlled by the software “Top View”. After 17 hours of the reaction period the process was stopped by cooling down the 200 mL autoclave vessel to room temperature. Meanwhile, the pressure was realized gradually, while temperature went down. By that time, after 17 hours software stopped measurements of the RPM, pressure, consumption of the feed gas and the temperature. The analysis of liquid products were carried out by the gas chromatographic method using GC/MS, series of “GC 7890A”, and mass spectroscopy with the series of “5975” produced by “Agilent Technologies”. Each type of experiment was more than 2 times to check for reproducibility. Unfortunately, due to unavailability of the gas chromatograph (GC), it was not possible to quantify the composition of the gaseous product in the reactor during the reaction period. Fischer-Tropsch activity of the cobalt catalysts in terms of CO conversion and selectivity was measured using equations 3.1 and 3.5.

3.5.2 Catalyst activity studies

3.5.2.1 Analysis of CO conversion

In the Fischer-Tropsch synthesis, CO conversion is a primary indicator of catalyst activity as CO is the limiting reactant. The amount of H₂ in synthesis gas mixture is excess in industrial settings. Since reactor was not connected to online GC (the lack of the equipment), the percentage of CO conversion into desired products was defined by the following equations and steps:

$$CO_{conversion} \% = \frac{\Sigma \text{ moles of CO consumed}}{\Sigma \text{ moles of CO (initial+consumed)}} \times 100\% \quad (3.1)$$

The number of total moles of CO_(in) was identified by Ideal Gas Equation. (3.2).

$$\frac{PV}{RT} = znRT \quad (3.2)$$

Where:
$$n = \frac{PV}{zRT} \quad (3.3)$$

Compressibility factor “z” was calculated using generalized compressibility chart. Compressibility is required because of the 20 bars of pressure in the system.

Critical values (c) of T and P: $T_c = -140.3^\circ\text{C} + 273 = 133 \text{ K}$

$$P_c = 34.987 \text{ bar} \approx 34.529 \text{ atm}$$

Reduced values (r) of T and P: $T_r = \frac{T}{T_c} = \frac{493\text{k}}{133\text{k}} = 3.71$

$$P_r = \frac{P}{P_c} = \frac{20}{34.529} = 0.58$$

Based on the generalized compressibility chart, Z value was identified, which is **0.9996**.

Generally volume of the autoclave vessel is 200 mL. 50 mL of the volume is filled with n- hexadecane where 1 g of catalyst is suspended. Remaining 150 mL of the volume is occupied with feed gas. The mole ratio of the feed gas is H₂/ CO is 2. Accordingly, the volume ratio will be 1/3 for CO gas.

During 17 hours of reaction period, different volume of synthesis gas was utilized by different catalysts, which was identified by reactor software “Top View” and displayed in the graph in the form of “mL/h” Figure 3.8.

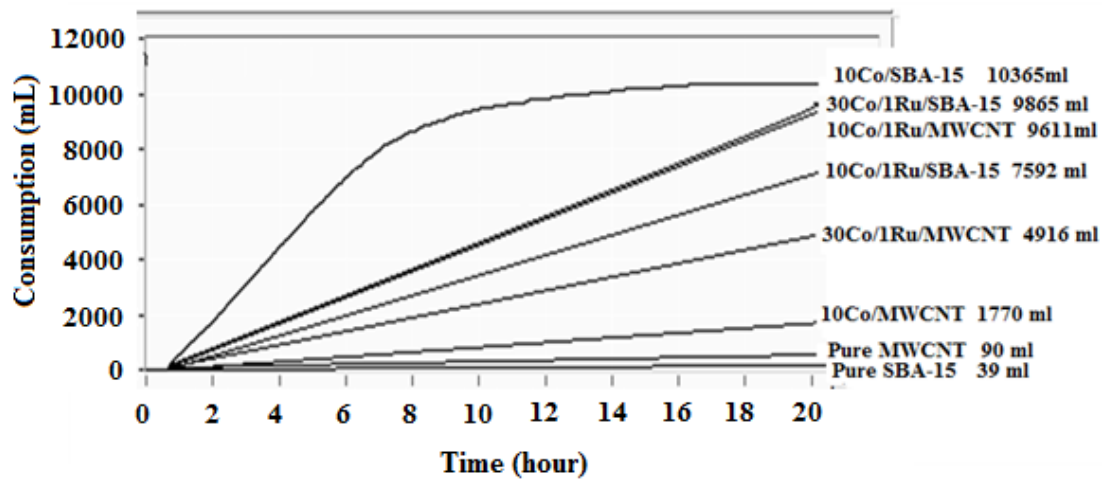


Figure 3.8: Data of feed gas consumption identified by reactor

The details of feed gas consumed and total moles of CO (in) are given in Table 3.8. Based on the feed gas consumption, the volume of spent CO for different catalysts was identified by the following equation:

$$V = \frac{1}{3} \times \left(x \frac{ml}{h} \right) \quad (3.4)$$

Where x is a spent volume of the feed gas for each catalyst.

Table 3.8: Consumption of feed gas and calculated moles of CO using Ideal Gas Equation

#	Catalysts	Overall volume of feed gas consumed (mL/17h)	Volume of CO consumed in liters (V=1/3*X)	Total moles of CO (in)
1	(M3)	9,611	3.204	1.585
2	(M4)	4,916	1.639	0.811
3	(M2)	1,770	0.59	0.292
4	(M1)	90	0.03	0.015
5	(S3)	7,592	2.531	1.252
6	(S4)	9,865	3.288	1.626
7	(S2)	10,365	3.455	1.709
8	(S1)	39	0.013	0.006

Using an equation 3.3 number of moles of each catalyst was calculated (APPENDIX B)

Before starting the reaction, reactor was heated to the operating temperature. It means that before reaction starts, reactor will already have a certain amounts of moles inside the vessel under 20 bars, 220°C, and 50 mL of volume (equation 3.4). This amount of CO is initial, which will be included to the calculation of CO conversion of each catalyst.

$$n(\text{initial}) = \frac{19.738 \text{ atm} * 0.05 \text{ L}}{0.9996 * 0.08206 \left(\frac{\text{atm L}}{\text{K}} \text{ mol} \right) * 493 \text{ K}} = 0.025 \text{ mol}$$

Accordingly CO conversion for each catalyst was calculated using equation 3.1 which is given in APPENDIX B.

3.5.2.2 *Selectivity*

The concentration of HCs is given in ppm. In order to identify the selectivity of each catalyst, the concentrations of HCs were converted into moles using the steps described in APPENDIX B.

The selectivity of the catalysts towards C₈-C₄₀ was calculated using the following formula:

$$\text{Selectivity (C}_{8+}\text{)} = \frac{\text{Moles of liquid C}_{8+}}{\text{Moles of CO consumed}} \times 100\% \quad (3.5)$$

The selectivity of each catalyst towards liquid HC was calculated using equation 3.5. Calculation of selectivity for each catalyst is provided in APPENDIX B.

3.6 **Characterization of catalyst support and catalyst precursors**

3.6.1 **BET surface area measurements**

The surface area and porosity of MWCNTs and SBA-15 before and after impregnation of active metals were measured using Quantachrome Autosorb Automated Gas Sorption System. 0.02 g of sample was weighed and characterized in each case. Prior to measurement, samples were degassed in a vacuum in 120°C for 5 hours in order to remove possible moistures from pores of samples. After degassing procedure liquid nitrogen was introduced to the system and sample was kept in nitrogen environment 11 hours.

3.6.2 **Thermogravimetric Analysis - Mass Spectroscopy (TGA-MS)**

The TGA analysis was carried out using METTLER TOLEDO TGA/SDTA 851e equipped with a cooling system. The instrumentation involved a microbalance and a furnace that are capable to heat up the sample while measuring the weight. This instrument allows the horizontal flow of gases that minimizes chimney effect and

provides more stable weight signal. Samples of 8 to 13 mg were placed in alumina crucible and weighed. The experiment was performed using nitrogen gas as a blanket to avoid harmful gases from flowing back towards the microbalance. The results obtained were evaluated with V 7.01 STAR^e software package.

3.6.3 Field Emission Scanning Electron Microscope/Energy Dispersive X-Ray (FESEM/EDX)

Field Emission Scanning Electron Microscope (FESEM) was used to analyze the surfaces of both supports and prepared catalysts. Field emission scanning electron microscopes, (FESEM, Zeiss Gemini) delivers ultra-high resolutions down to 1 nm for the most demanding electron microscope applications. The small amount of sample was adhered to the aluminum stub using carbon conductive tape. The stub was mounted on the stub holder and loaded into the chamber. Vacuum pump was used to create the vacuum inside the analysis chamber. The test is then initiated using the software provided by the manufacturer. Once the surface image is obtained, Electron Dispersive X-ray (EDX) is used to analyze and calculate the elemental composition on the surface.

3.6.4 X-Ray Diffraction (XRD)

XRD measurements of MWCNT, SBA-15 and calcined catalysts were conducted with a Philips PW1840 X-ray diffractometer with monochromatized Cu/K α radiation using EVA software system. The average particle size of the metal crystallites in the calcined catalysts was estimated by Scherrer equation using FWHM (Full-Width, (at) Half-Maximum (height)) data which was generated by software EVA. Before XRD measurements, 2 mg of sample was grained to make the powder finer and placed to plastic sample holder. XRD measurement conducted between 10 to 80 θ theta with the step size 0.02°/sec for 80min.

3.6.5 Temperature Programmed Reduction (TPR)

TPR of catalysts was conducted by TPDRO 110 “Thermo” in the presence of 5% hydrogen in nitrogen. 0.03 g of sample was placed inside the bulb and analyzed within 480 min in the range of 40 to 600°C, while having temperature ramping of 40°C/min.

3.6.6 Transmission Electron Microscopy (TEM)

The morphology of MWCNT, SBA-15, cobalt catalysts supported on MWCNT, and cobalt catalysts supported on SBA-15 were investigated by high resolution Transmission Electron Microscopy (HRTEM) by using “Zeiss 4BRA 200FE” at accelerating voltage of 200 kv. Before characterization samples were suspended in isopropyl alcohol and sonicated for one hour in order to separate the finest particles of each sample. After sonication finest particles of samples were collected from on top of the isopropyl alcohol by using disposable pipette and were transferred to carbon enhanced copper grids and dried in air.

3.7 Product characterization

The Fischer-Tropsch products were characterized by using Gas-Chromatography assembled with Mass Spectroscopy (GC-MS) produced by an “Agilent Technologies. 0.2 µL of product produced by each catalyst was transferred to GC vial and injected automatically by using auto sampler. The analysis period was 70 min. After completion of quality characterization, the quantity of synthesized individual hydrocarbon was calculated automatically by GC.

3.7.1 Gas Chromatography

Chromatography is one of the most versatile separation techniques in the modern day chemical analysis. In addition to its versatility, speed and applicability are also

promising advantages of chromatography. Chromatography can be defined as the separation of a mixture into various fractions through distribution between two phases, one phase being stationary and remaining phase being mobile. The underlining principle of chromatography is that different substances have different partition coefficients between the stationary and mobile phases. A compound that interacts weakly with the stationary phase will spend most of its time in the mobile phase and move rapidly through the chromatographic system. Compounds that interact strongly with a stationary phase will move very slowly. In the ideal case, each component of a mixture will have different partition coefficient between the mobile and the stationary phases, and consequently each will move through the system at a different rate resulting in complete separation. Employing a gas as the mobile phase is termed gas chromatography or vapor chromatography. Liquid chromatography (LC) refers to any chromatography process that employs a mobile liquid phase.

In gas chromatography, the stationary phase is a liquid and the moving phase is a gas (the carrier gas). It is powerful technique for the separation of volatile mixtures, the components of which may differ in boiling points, by only a few tenths of a degree. The main process of separation occurs inside the micro tubes which are called GC “columns”.

3.7.2 Product analysis by Gas chromatography

The gas chromatograph and mass spectroscopy (GC-MS) was employed for the identification and quantification of the liquid FT products. The gas chromatographer with the series of “GC 7890A”, and mass spectroscopy with the series of “5975” produced by “Agilent Technologies” are depicted in the Figure 3.9. The GC was equipped with a capillary column “BPX5”, produced by “SGE Analytical Science”. The details of the GC columns are shown in Table 3.9.

Table 3.9: Details of the “BPX5” GC column produced by SGE Analytical Science

Type	Material	Column Details			Max Temp. (°C)	Gas Flow (ml/min)
		Length (m)	Film thickness (micron)	I.D. (mm)		
Bonded phase	Fused Silica (non-polar)	30	0.25	0.25	370	0.88



Figure 3.9: The GC 7890A” and Mass Spectroscopy with the series of “5975” produced by Agilent Technologies

The identification of quality and quantity of liquid HCs produced during the FT reaction was conducted based on the standard hydrocarbon mixture DRH-0085-R2 Hydrocarbon Window Defining Standard produced by “Accul Standard” with known amount of desired product. The range of the standard was between C₈ and C₄₀. Therefore produced liquid product was characterized in the range of C₈-C₄₀. The standard HC mixture was injected into the GC/MS to identify hydrocarbons by its retention time as well its concentration in ppm. The calibration of GC/MS by the

standard mixture and raw chromatograms of standard mixture together with samples are given in APPENDIX C. Concentration of each fraction (C₈-C₄₀) was determined comparing the response factor of standard with response factor of each fraction using the equation 3.6:

$$\text{Concentration } (C_n) = \text{Response factor}_{(fr)} \times \frac{\text{Concentration}_{(st)}}{\text{Response factor}_{(st)}} \quad (3.6)$$

Where: fr – fraction, st – standard

Response factors of standard, samples and the calculation of quantity of all fractions using response factors are given in APPENDIX C.

3.7.3 GC/MS and oven conditions

The method was named “hydrocarbon” and run under following conditions: temperature increase of the oven started from 40°C and continued until 260°C. Separation of the hydrocarbons occurred in the range of 40-260°C. Oven equilibrium time was 3 min. The scheme of the oven conditions is depicted in **Figure 3.10** below.

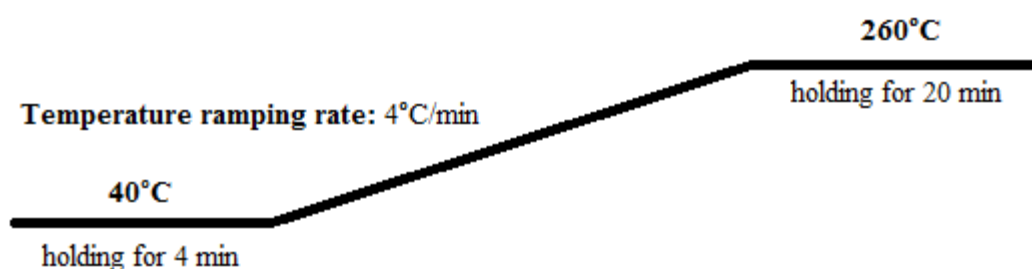


Figure 3.10: Oven conditions

When temperature reached 40°C it held for 4 min and started to increase in the temperature ramping rate of 4°C/min. After reaching 260°C, it held for 20 minutes. The samples were injected by auto injection system which is installed in GC/MS. The injection volume of the samples was 1 µL. The samples were injected from SS inlet under 7.0699 psi, in temperature of 340°C. The samples were carried through column by helium and the flow of column was 1.1685 ml/min. The temperature of MS was 230°C with energy of 70 eV.

CHAPTER 4

RESULTS AND DISCUSSION

This chapter summarizes the data and results of experimental work, conducted during the research period. Subchapter 4.1 deals with catalyst support materials which are Multiwall Carbon Nanotubes (MWCNT) and Santa-Barbara-Amorphous (SBA-15), its preparation and characterization. In subchapter 4.2 characterization results of prepared catalysts in different techniques are described. Subchapter 4.3 portrays Fischer-Tropsch reaction results which were conducted in 200 mL autoclave reactor. Also product characterization in Gas Chromatography-Mass Spectroscopy (GC/MS) in terms of quality and quantity are described. Finally the selectivity of catalysts towards light fuels and CO conversion studies are discussed.

4.1 Support material characterization

4.1.1 Characterization of MWCNT

4.1.1.1 Morphology and physical properties of MWCNT

The morphology and physical properties of MWCNT were studied by HRTEM. The images of pristine and purified MWCNT are given in Figure 4.1 (A - pristine, B - purified). From these images can be seen that the structure of CNT represents multiwall morphology [118]. The walls are parallel to the main axis of the tubes. The pristine MWCNT has an amorphous carbon around the tubes (Figure 4.1(A)). Also the HRTEM image shows the thickness of the walls which is 5.9 nm and inner diameter is 3.3 nm. In addition, the inner and outer diameters of MWCNT provided

From the supplier are ± 4 nm and 20nm, respectively the images of pristine MWCNT also show that the ends of MWCNT are closed. It is known that acid oxidation leads to remarkable structural changes by opening ends and creating defects on MWCNT walls [119], [120]. These defects are crucial for the anchoring active metals.

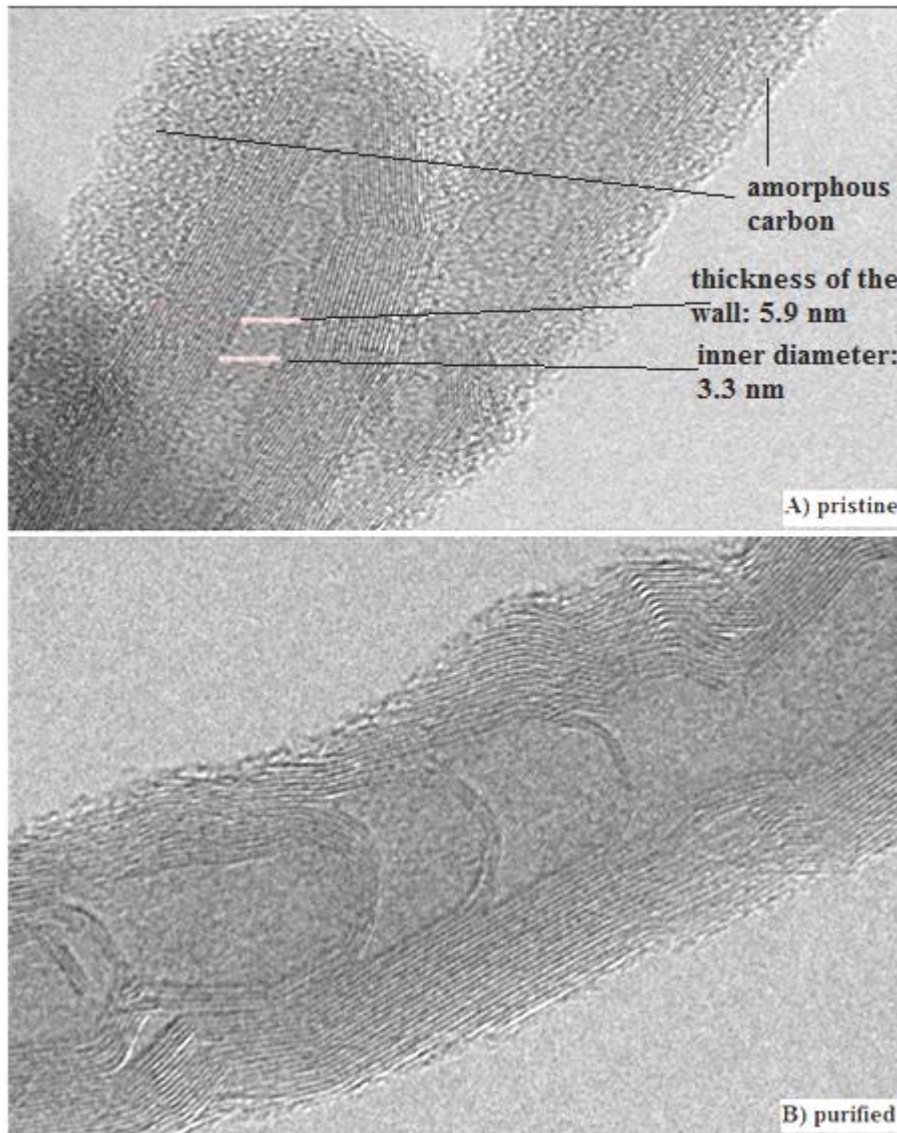


Figure 4.1: The HRTEM of MWCNT (A) Pristine and (B) purified

After purification with nitric acid most of the amorphous carbon was removed. At the same time acid treatment created some defects on the walls of MWCNT and partially opened the ends.

4.1.1.2 Chemical composition of MWCNT

Figure 4.2 represents the EDX results of pristine and purified MWCNT and includes spectrum, peaks of detected elements and the table of the detected elements before and after purification with their weight percent and atomic weight. The pristine MWCNT contains a certain amounts of Co, Mn, Al, Mg, and O. The percentage of carbon atom is high which is 96.16 wt%. Co, Mn, Al, Mg elements are used during MWCNT production which should be removed by washing with strong acids.

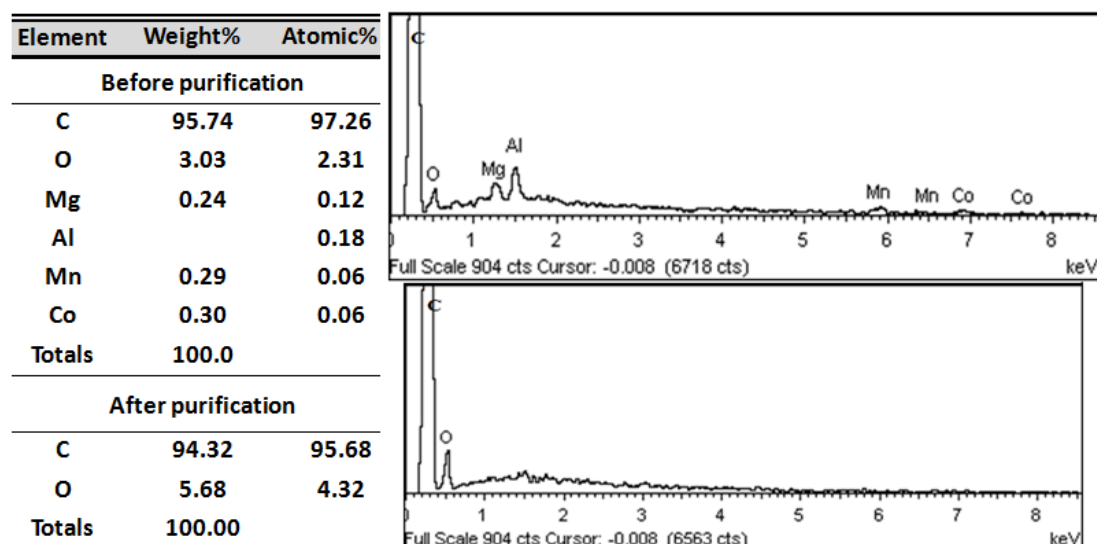


Figure 4.2: Chemical composition of MWCNT before and after purification

After purification step the peaks appeared for pristine MWCNT has disappeared except for carbon and oxygen. In Addition the percentage of oxygen increased from 2 wt% to 5.86 wt%. The increase in the amount of oxygen is due to oxidation by nitric acid which was used during purification process. Wu *et al.* [98] suggested that the surface oxygen can be originated from the pre-oxidation /carboxylation treatment of the MWCNT by concentrated nitric acid. Oxidation of carbon nano fibers by nitric acid or other oxidants has been reported to be a highly effective way to introduce active surface defects and/or hydrophloric surface functional groups [121]. Z. Yu *et al.* [104] reported that introduction of surface carboxyl groups after treatment with concentrated nitric acid plays important role, as they contribute for the dispersion of cobalt particles and stabilization of cobalt particles against sintering.

4.1.1.3 Surface area and porosity of MWCNT and SBA-15

Both supports, unpurified/purified MWCNT and SBA-15 were investigated by Brunnauer-Emmet-Teller (BET) measurement to identify porosity and specific surface area of the materials. General report of pristine/purified MWCNT and SBA-15 in terms of BET surface area and porosity is given in Table 4.1. The surface area of unpurified MWCNT is higher, than that of purified MWCNT which is 357.4 m²/g and 255.3 m²/g respectively. Accordingly the total pore volume of unpurified MWCNT is higher that is 0.956 cm³/g, comparing to purified MWCNT which is 0.7075 cm³/g. Based on the HRTEM results of these materials (Figure 4.1 (A)) can be seen that pristine MWCNT contains some amounts of amorphous carbon which is located all around MWCNT. Amorphous carbon creates additional surface area. Accordingly N₂ consumption is higher in pristine MWCNT which results in higher surface area. On the other hand, Zhang *et al.* [94] observed slide improvement of purified MWCNT's surface area from 143.17 to 163.37 m²/g. Solhy *et al.* reported that total surface are of carbon materials such as MWCNT and CNFs could increase after undergoing acidic environment (oxidation treatment) because of the removal of impurities on the MWCNT's surface and formation of some functional groups such as COOH or COH [122].

Table 4.1: BET measurements of unpurified/purified MWCNT and Pure SBA-15

Support material	Surface area (m²/g)	Total pore Volume (cm³/g)	Average pore size Ø (nm)
Unpurified MWCNT	357.4	0.956	10.7
Purified MWCNT (M1)	255.3	0.7075	11.09
Pure SBA-15 (S1)	660	0.817	4.95

The BET surface area, total pore volume, and average pore size of calcined SBA-15 (660 m²/g, 0.817 cm³/g, and 49.5 nm) are shown in Table 4.1. The parameters of calcined SBA-15 are significantly higher than that of MWCNT. Different BET surface area results in the range of 520 to 817 m²/g were obtained by a number of researchers [123], [125].

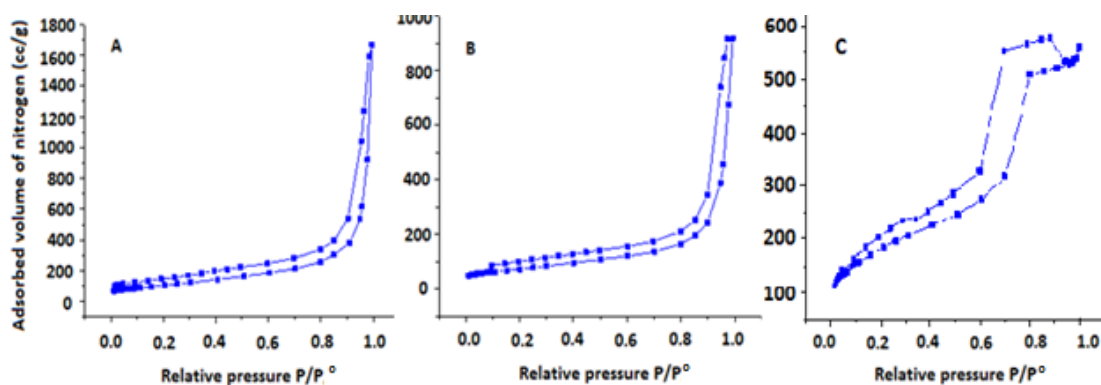


Figure 4.3: N₂ sorption isotherm of (A) unpurified, (B) purified MWCNT and (C) pure SBA-15

Figure 4.3 represents nitrogen adsorption/desorption isotherms of (A) unpurified and (B) purified MWCNT and (C) pure SBA 15. The curvatures A and B are convex to P/P° axis and represent reversible type III. The reversible type III isotherm is convex to the P/P° axis over its entire range and therefore does not exhibit a point “B” [126]. At the same time hysteresis loops of these isotherms are significant. This makes possible to relate this isotherm to type V [126]. The Type V isotherm is highly uncommon and it is related to the Type III isotherm in that the adsorbent-adsorbate interaction is weak, but is obtained with certain porous adsorbents [126], [127]. From hysteresis point of view, curvatures fall to type “A” hysteresis. One of the functions of hysteresis are, they indicate the presence of mesopores and provide information regarding pore sizes [127]. According to type “A” hysteresis, MWCNT consist of cylindrical pore shapes.

The curvature C represents the nitrogen adsorption isotherm of pure SBA-15. Shape of isotherm is convex to P/P° axis, but according to Lowell *et al.* [127] this isotherm is related to type IV. The initial part of the Type IV isotherm follows the same path as type II, and it is attributed to monolayer-multilayer adsorption. The type IV isotherms exhibit mesoporous solids. At the same time, isotherm is followed by very obvious desorption hysteresis loop. Produced hysteresis loop is related to type “H1” [126] of type “A” [127]. Based on these loops it can be speculated that SBA-15 material belongs to porous adsorbents e.g. inorganic oxide gels and porous glasses, which tend to give Type “H1” loops [126] or type “A” loops [127]. From pore shape

point of view, adsorption-desorption process which is related to type “A”/type “H1” occurs in approximately uniform spheres in fairly regular array, and hence to have narrow distributions of pore size. Similar feature of N₂ physisorption occurred in research done by Kruk *et al.* [125] where they observed hysteresis loops with sharp adsorption and desorption branches, similar to current research work. The sharpness of the adsorption branches indicated narrow mesoporous size distribution. This type of materials usually possesses “cylindrical” pores. Song *et al.* [128] suggested that the changes in the molar ratio of TEOS may lead to distortion of the isotherm.

4.1.1.4 Chemical phase composition of MWCNT before and after purification

Profile of XRD is shown in Figure 4.4. The spectrum for purified and unpurified MWCNTs from XRD is depicted in APPENDIX D. The sharp peak at 2 theta of 26° correspond to (002) plane of graphite [129] and other smaller picks at 2 theta of 43° and 78° are fingerprints of graphite of different plane structure, based on the XRD library. The intensity of diffraction peak at (002) in acid treated MWCNTs increased as compared to the unpurified MWCNT which are 145 (a.u) and 120 (a.u) respectively. It may happen due to the removal of amorphous carbon on top of the surface of MWCNT which might have a partial interruption of the contact of X-rays with crystal carbon phase. In their work Buang *et al.* [130] offered that increase of the intensity is due to the loose of the carbon nanotubes floss after the acid treatment and form more ordered CNTs floss in the acid functionalized MWCNTs. Tessonnier *et al.* [118] investigated the same type of commercial carbon nanotubes which is “Baytubes” [115]. XRD patterns for unpurified and purified MWCNT obtained by present research work match with their XRD results. The unpurified MWCNT contains metals such as Mg, Al, Mn, and Co, which were detected by EDX. But there are no other peaks in XRD data representing the presence of aforementioned metals or some other impurities. This may be due to the very small percentage of metals on MWCNT, which are: 0.39 wt% 0.74 wt% Co, 0.48 wt% and 0.22 wt% for Mn, Co, Al and Mg, respectively. However, according to Tessonnier [118] characterization of carbon nanotubes by XRD is not straightforward. Their sizes, their strong curvature which may induce strain can lead to peak shifts, peak broadening and even

suppression of some reflections. In MWCNT characterization by XRD, the patterns of graphite will be used to interpret the diffraction peaks.

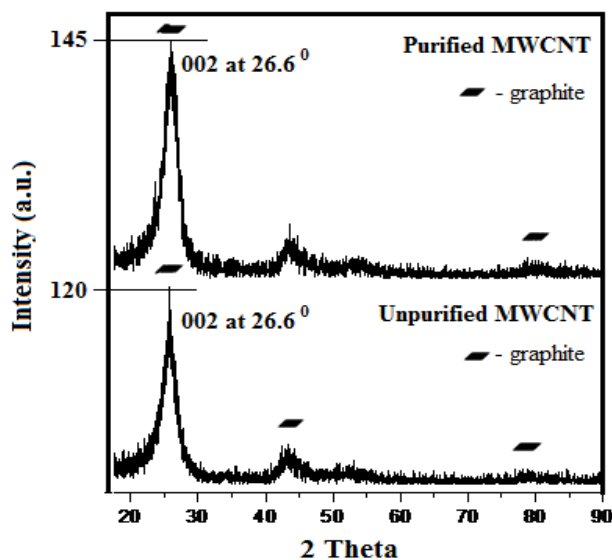


Figure 4.4: XRD results for unpurified and purified MWCNT

4.1.2 Characterization of pure SBA-15

4.1.2.1 Morphology and physical properties of pure SBA-15

The morphology of pure SBA-15 was studied by HRTEM. Before observing the sample under HRTEM, it was suspended in isopropanol and ultra-sonicated for one hour in order to separate the finest particles of the sample. After ultra-sonication the SBA-15 was transferred to copper grid using disposable micropipette. Figure 4.5 (S1 (A)) shows the morphology of SBA-15 which clearly represents hexagonal pore arrangement. Although these images are performed in 2D, it can be speculated that (S1(A)) represents front view of the material, and S1 (B) represents side view of the material. Figure 4.5 (S1(B)) shows that, the structure of SBA-15 from side view represents micro channels/pores with uniform diameter of 5-6 nm between each other. There are considered as pores of SBA-15. The thickness of the walls is 2-3 nm, and the average diameter of the hexagonal shapes (S1 (A)) has dimensions

around 2 to 3 nm each. In their studies Chareonpanich *et al.* [131] observed the same morphology of mesoporous silica SBA-15. Also F.Azimov *et al.* [132] observed close dimensions of SBA-15 from their work.

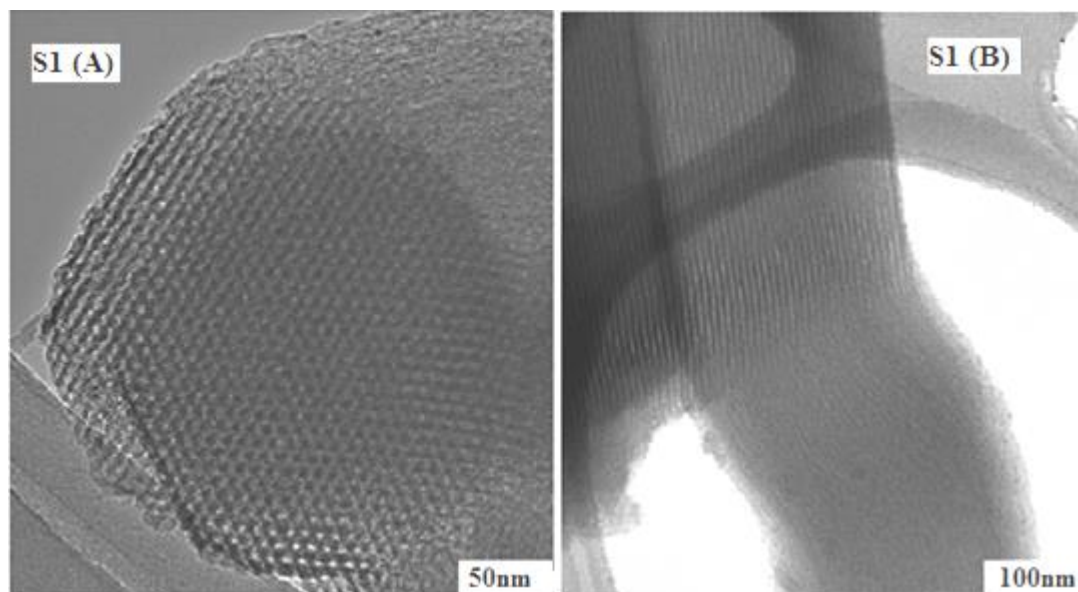


Figure 4.5: HRTEM of pure SBA-15 S1 (A) – front view, S1 (B) – side view

4.1.2.2 Morphology and elemental composition of pure SBA-15

The morphology of pure SBA-15 was also studied by FESEM, and elemental composition of SBA-15 was studied by EDX. The FESEM images of pure SBA-15 are depicted in Figure 4.6 where SBA-15 is coded as **S1** and shown in 3 different magnifications which are 5, 10 and 50K. The morphology of SBA-15 was studied by FESEM represents a “necklace” structure [12]. Similar results were reported by Prieto *et al.* [114] and the morphology was called “rope-like” structure. Based on SEM images [114] the particles showed curved aspect at medium resolution and frequently appeared as organized in plait-like assemblies. The image S1 (A) represents the form of the particle as a hexagonal shape, which is shown by TEM as well. The average outer diameter of the particles is 505 nm, while the length of the particle is 1.2 μm . The S1 (A) image showed that the ends of the hexagonal particles are open, unlike MWCNTs. This feature of SBA-15 allows more active metals to

adsorb on the surface. The morphology and dimensions of SBA-15 strongly depend on the synthesis procedure. Jo *et al.* [133] applied different methods of SBA-15 synthesis. In one of the methods the mixture of chemicals (SiO_2 , Na_2O and H_2O) was added by controlling the dropwise addition over the course of longer time and left to the stirring. In another way he added the tetraethyl orthosilicate once into the solution and then left to the stirring. The second method of preparation is almost similar to the method used in this research work. Accordingly results are the same with that of C. Jo applied. In studies done by Zhao *et al.* [12], SBA-15 was observed under SEM before and after calcination in 500°C . In both cases SEM showed the same structure which can be attributed to thermal stability of mesoporous silica SBA-15.

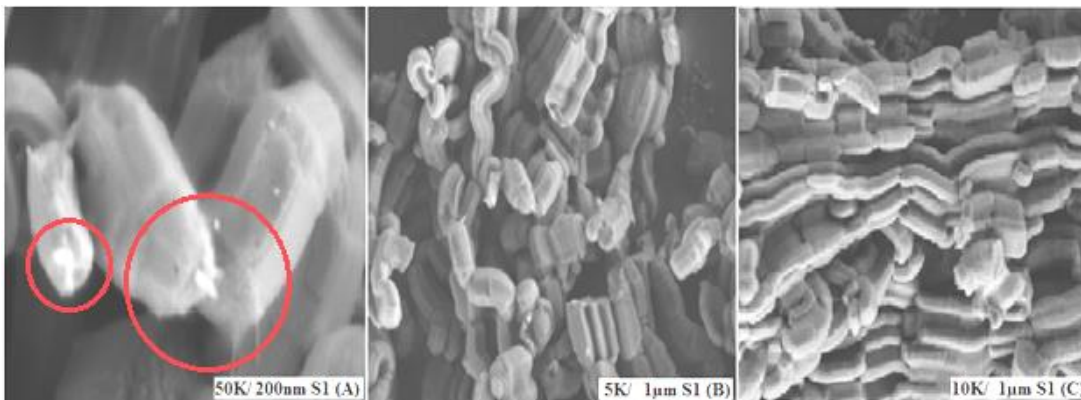


Figure 4.6: FESEM images of pure SBA-15 in different magnifications (A) 50K, (B) 5K, (C) 10K

The EDX results of Pure SBA-15 are summarized in Figure 4.7. Elemental composition of the sample at its surface is obtained by X-Ray Energy Dispersive analysis. X-rays are released by the sample surface after electron bombardment and each element releases x-rays of a particular energy (keV). The EDX was conducted on an image of width $6\mu\text{m}$. Based on the results, the content of Si is 14.58 and O is 55.42 wt%. At the same time the content of C is 30 wt% in the chosen spot. Wu *et al.* [134] suggested that the signals of carbon may come from supporting membranes under the specimen..

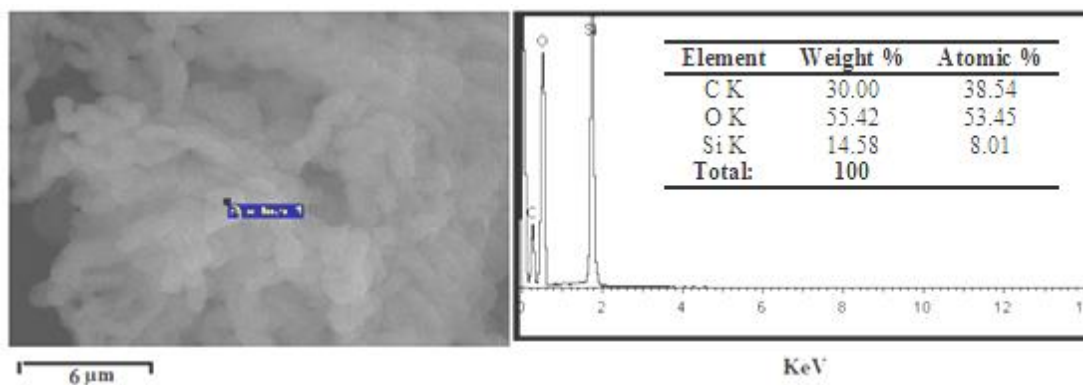


Figure 4.7: EDX results of Pure SBA-15

4.1.2.3 Chemical phase composition of pure SBA-15

Figure 4.8 shows XRD high angle region results of pure SBA-15. The measurement was conducted between 2° to 80° with the step size 0.02°/sec for 80 min. The broad peak at 2 theta of 23° corresponds to silica fingerprints based on the XRD library which is amorphous silica [135], [136]. XRD Spectrum of Pure SBA-15 (S1) is shown in APPENDIX D.

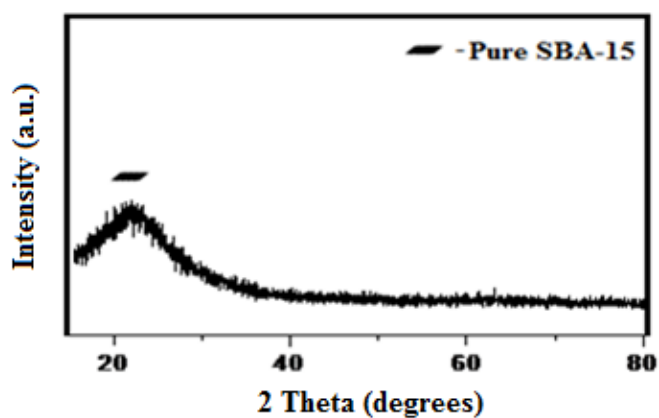


Figure 4.8: XRD results of pure SBA-15

4.2 Characterization of MWCNT and SBA-15 supported cobalt catalysts

4.2.1 Determination of calcination temperature

Figure 4.9 shows the results of thermal gravimetric analysis of 10Co/MWCNT and 10Co/SBA-15 catalysts. TGA analysis was performed in temperature range between 30-600°C at a heating rate of 5°C/min in the flow of pure nitrogen. Figure 4.9 depicts the graph of catalyst weight loss versus temperature. In dried 10Co/MWCNT catalyst thermal decomposition of nitrates of cobalt precursor into metal oxide occurred at temperature below 350°C. Weight loss in 10Co/SBA-15 catalyst occurred in the range of 50 to 400°C. In both catalysts rapid weight loss occurred in the range of 50 to 200°C, which covers the boiling point temperature range of cobalt nitrate hexahydrate which is 100-105°C.

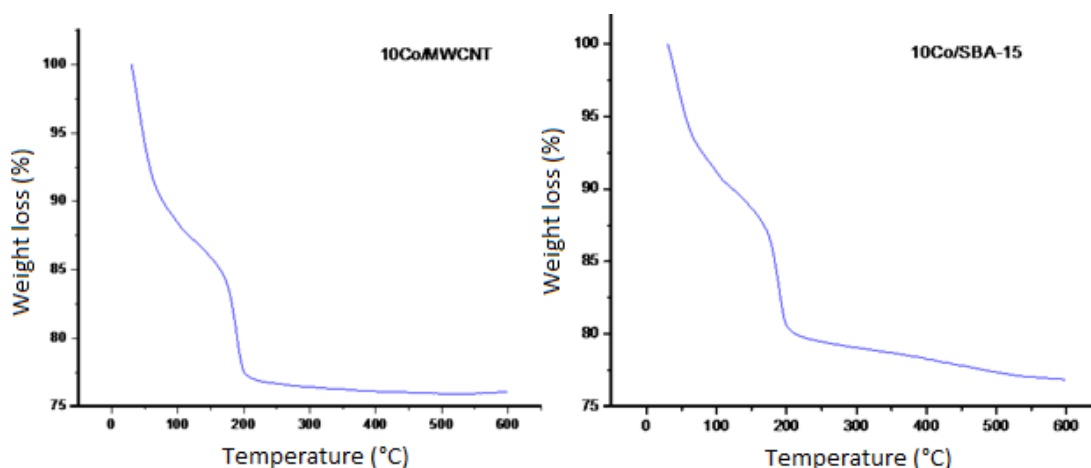


Figure 4.9: Thermal decomposition of 10Co/MWCNT and 10Co/SBA-15

The characterization of 10Co/1Ru/MWCNT can be viewed in Figures 4.10 and 4.11, where Figure 4.11 represents mass spectrometry (MS) results of this catalyst. The TGMS analysis was conducted at the same conditions with 10Co/MWCNT and 10Co/SBA-15 based catalyst, where temperature range is 30 to 600°C with 5°C ramping in the flow of pure nitrogen. The first decomposition occurred in the range of 30 to 126°C which is 2% of total weight loss. This weight loss was followed by rapid decomposition which happened in the range of 126 to

265°C which is equal to 10%. This weight loss occurred in the range of 30 to 265°C can be attributed to water moisture. Next 11% of weight loss occurred in the range of 265 to 598°C. According to results of the mass spectroscopy, the nitrate ions (A30) were detected in the temperature range of 120 to 350°C which can be seen from Figure 4.11. Also in this range CO₂ ions (A44) were decomposed, which was detected by MS. The sharp peak was detected by MS in the region of 400 to 550°C. Also as can be seen from TGA graph, sudden, 9% weight loss occurred in the range of 400 to 600°C. In both graphs, in TGA an MS, this weight loss continues even after 600°C. This active decomposition may be attributed to carbon which is coming from MWCNT. It means that increasing of the temperature from 350°C may lead to loss of catalyst support (MWCNT).

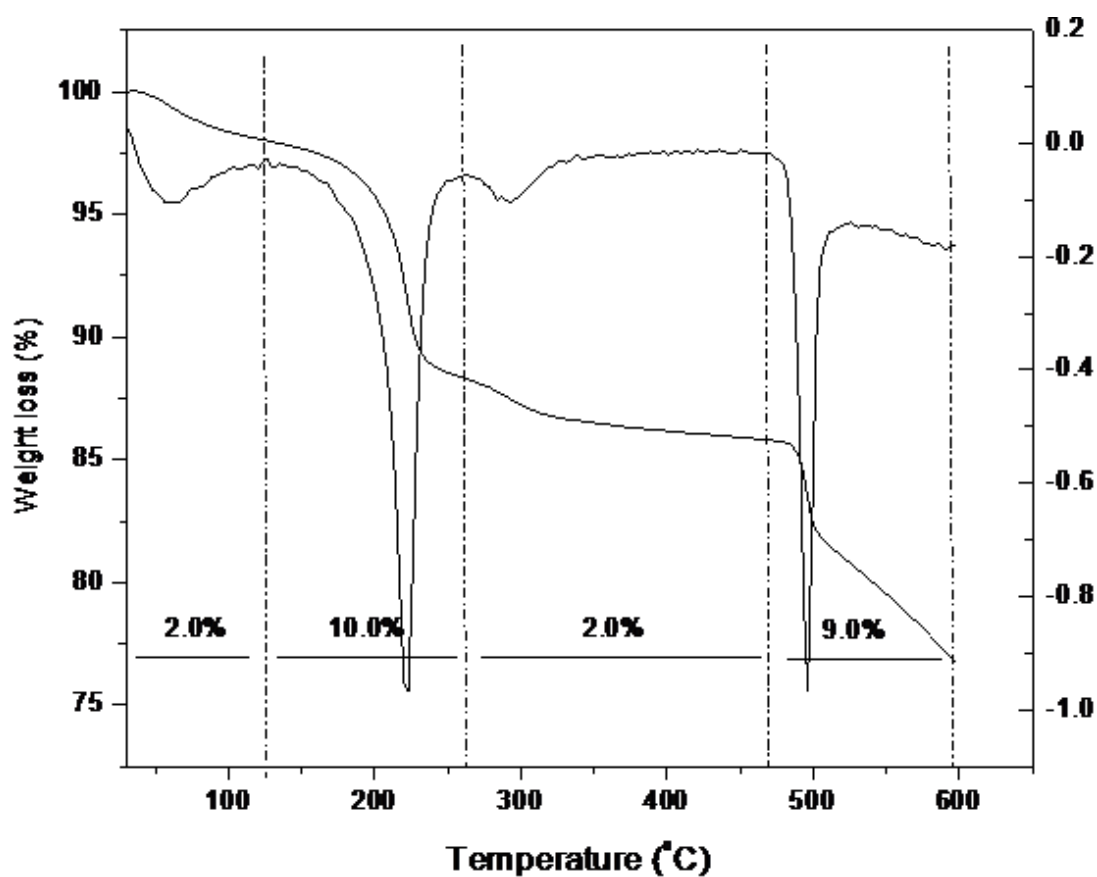


Figure 4.10: Thermal decomposition of 10Co/1Ru/MWCNT

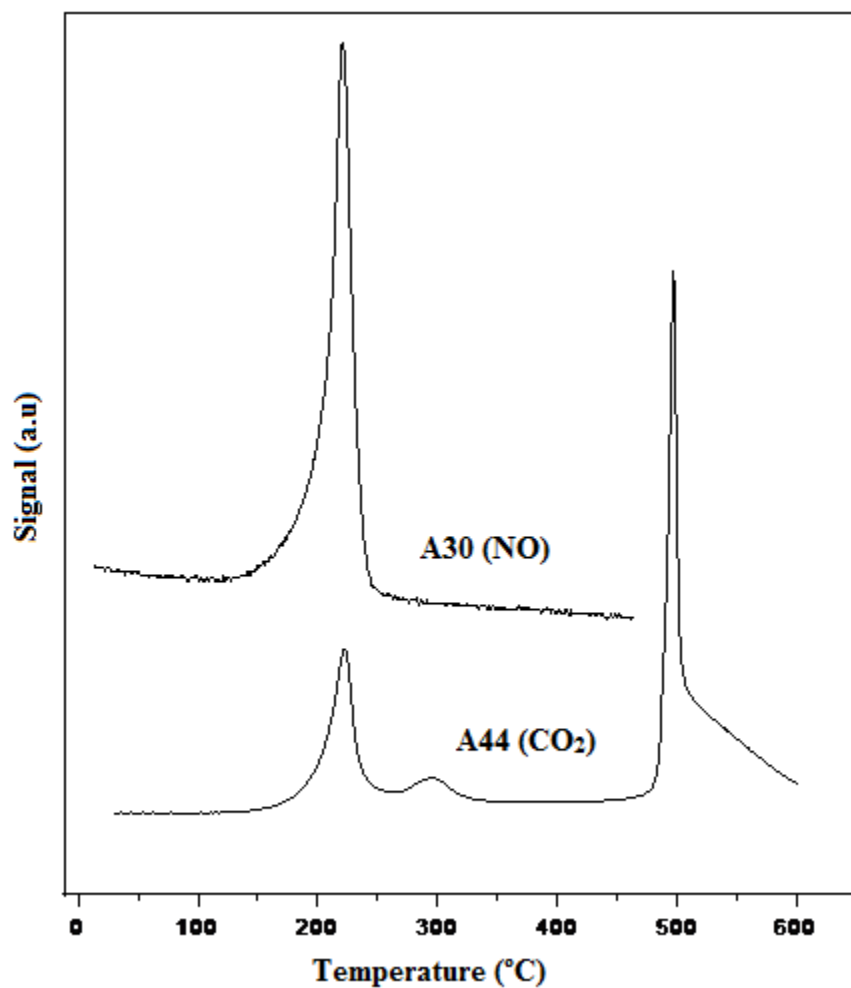


Figure 4.11: Mass Spectroscopy results using 10Co/1Ru/MWCNT

In order to check the stability of MWCNT to high temperature, blank MWCNT was investigated separately by calcining it in different temperatures in the furnace. The data was replotted in the graph “temperature versus percentage weight loss”. The result of blank MWCNT towards weight loss is depicted in Figure 4.12.

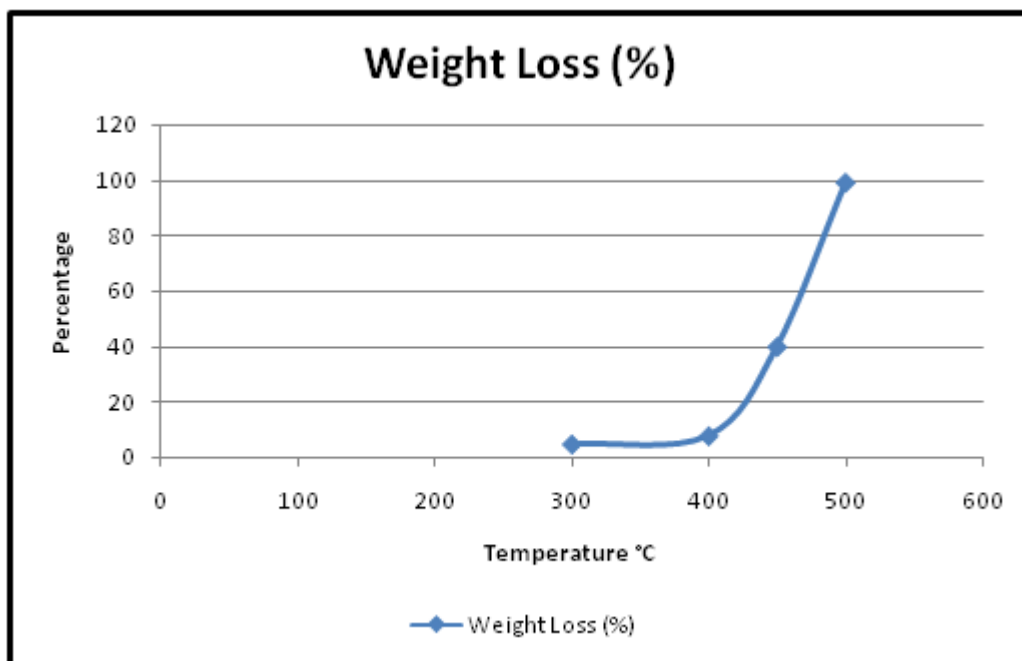


Figure 4.12: The result of blank MWCNT towards weight loss

The graph shows that MWCNT was stable in 300°C. Once temperature increased up to 350°C, MWCNT started decompose and 8.5% of weight loss observed. In temperature 450°C 40% of weight was lost. MWCNT decomposed completely when temperature reached up to 500°C.

Since decomposition of NO and CO₂ ions occurred in the temperature range of 120 to 350°C, calcination temperature of MWCNT based catalysts was chosen as 350°C.

Figures 4.13 and 4.14 depict TGA-MS results of 10Co/1Ru/SBA-15 catalysts. The TGMS analysis was conducted at the same conditions with 10Co/MWCNT and 10Co/SBA-15 based catalyst, where temperature range is 30 to 600°C with 5°C ramping in the flow of pure nitrogen. Figure 4.13 shows that decomposition of ions from dried 10Co/1Ru/SBA-15 catalyst occurred in 3 stages. First decomposition started between 30 to 140°C which is 6% of total weight loss. Further, rapid weight loss was observed between 140 to 269°C which was counted as a 10% of total weight loss. In the range of 269 to 598°C 2% of decomposition occurred. It can be

speculated that in the range of 30 to 269°C mostly moistures of water decomposed, as it was observed in 10Co/1Ru/MWCNT catalyst.

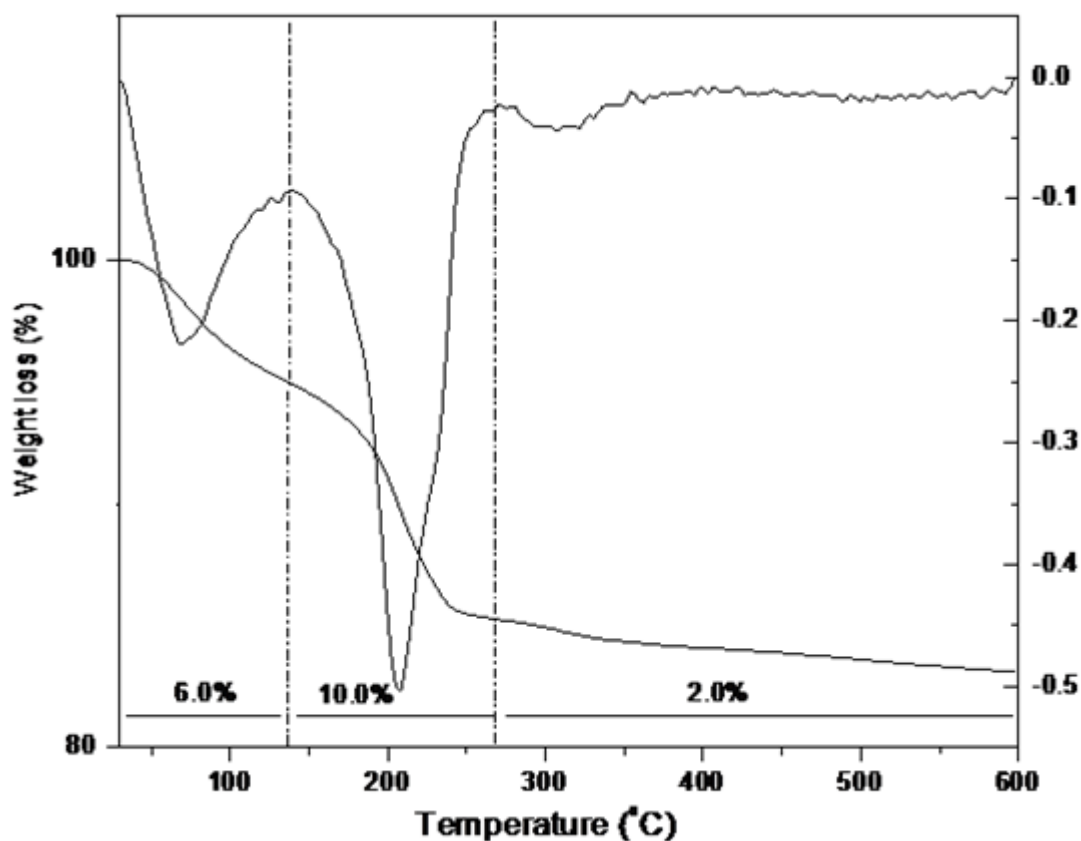


Figure 4.13: Thermal decomposition of 10Co/1Ru/SBA-15

According to the mass spectroscopy results of 10Co/1Ru/SBA-15 catalyst (Figure 4.14), the nitrate ions decomposed in the range of 150 to 350°C which is labeled as B30. In the range of 110 to 400°C the CO₂ ions released which is labeled as B44. Based on the data provided by TGA-MS, the calcination temperature of MWCNT and SBA-15 based catalysts were chosen as 350 and 400°C respectively. During calcination process cobalt nitrate phase was converted to cobalt oxide (Co₃O₄) [137] which were confirmed by XRD results (Figure 4.28).

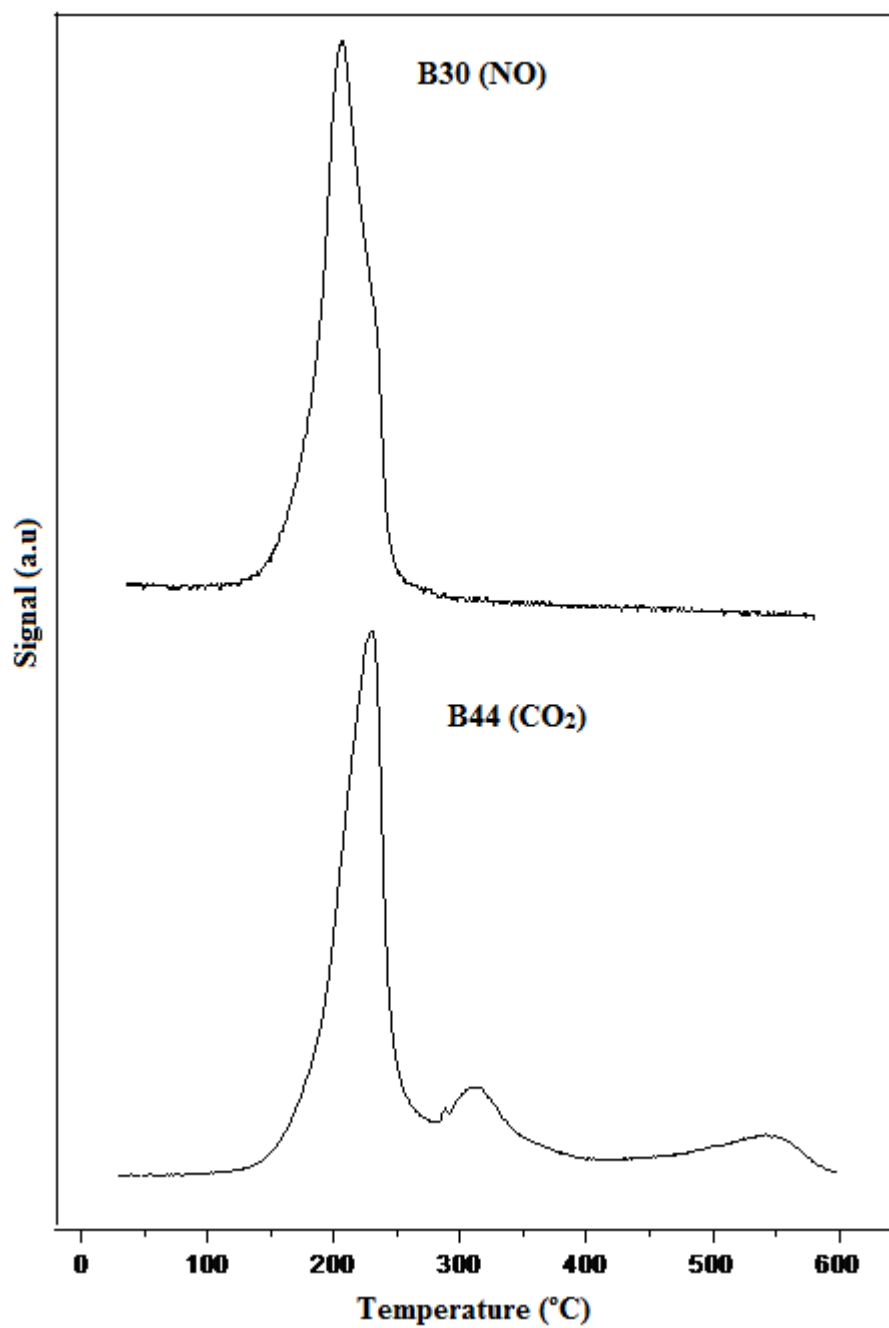


Figure 4.14: Mass Spectroscopy results using 10Co/1Ru/SBA-15

4.2.2 Morphology and particle size distribution in Co/Ru/MWCNT catalysts

The morphology of the catalyst and distribution of cobalt particles were investigated by HRTEM. The image of 10Co/1Ru/MWCNT based catalysts after loading of cobalt and ruthenium is depicted in Figure 4.15 in 3 dimensions: A) 10 nm, B) 20 nm and C) 50 nm. The particles are indicated with white color circles. In those images, the cobalt particles are located inside and outside the tubes. Figure 4.15 (A, B) clearly shows that particles were attached to the MWCNT's walls, on the defects which were formed during the treatment of the MWCNT with nitric acid. The particles inside the tubes are spread uniformly with the average size of 3-7 nm, whereas, the particles attached on the external wall have a size of 5 to 10 nm. Since the inner diameter of MWCNTs is approximately 3-4 nm particles with diameter size larger than 4 nm were attached on the external wall. Moreover MWCNT channels have restricted the growth of particles inside the tubes [89]. It is known that exterior surfaces of MWCNTs are electron rich, but interior walls are electron deficient [11]. This phenomenon will influence metal oxide particles in contact with either surface. Theoretical studies on non-catalytic gas phase reaction have prefigured that restriction of the particles within the narrow channels could increase the density of the reactants and accordingly create locally high pressure which will be favorable to synthesis gas conversion into hydrocarbons in the present case [89]. The broader view of 10Co/1Ru/MWCNT is presented in Figure 4.9 (C) with 50 nm scale bar. The image clearly shows particles inside the MWCNTs which ranged between 3 to 7 nm. Nevertheless the major amount of cobalt particles is located outside having the particle size of approximately 15 to 30 nm. The cobalt oxide agglomeration inside the MWCNT channels is not observed in terms of strong interaction of cobalt metal with inner surface of the tubes. However cobalt particles which are attached to exterior surface of the MWCNT formed an agglomeration. Agglomeration of cobalt metal is not favorable, that it causes lowering of metal active sites under FT conditions and negatively affects CO conversion to a desired product [107].

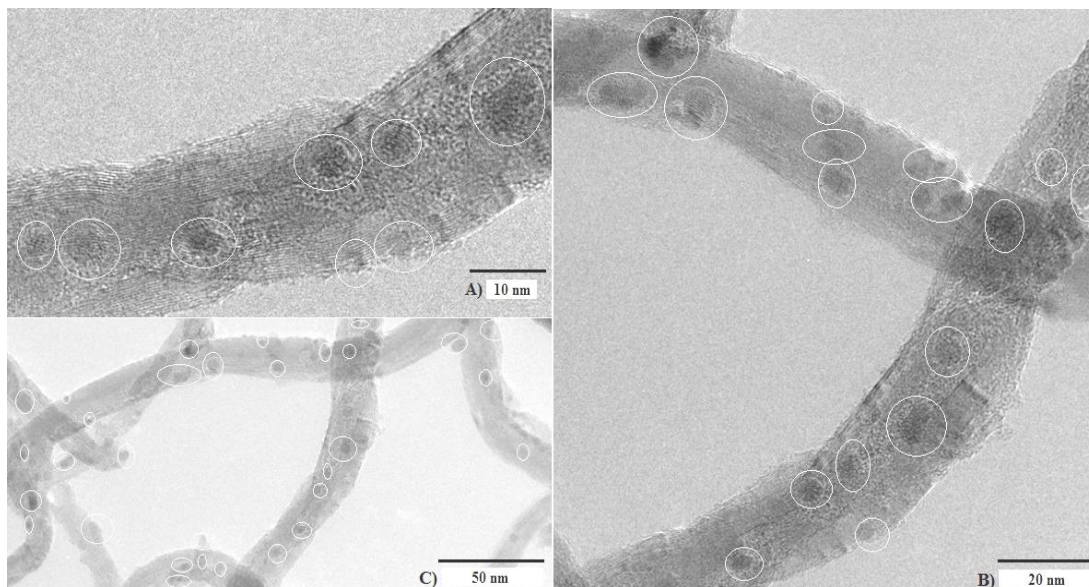


Figure 4.15: TEM images of 10Co/1Ru/MWCNT (M3) in different dimensions:
A) 10 nm, B) 20 nm, C) 50 nm

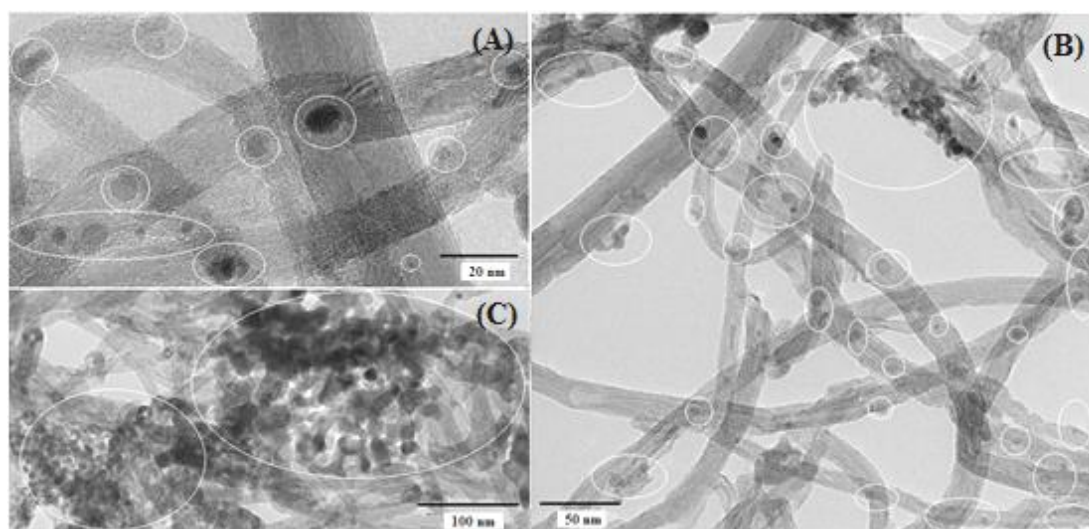


Figure 4.16: TEM images of 30Co/1Ru/MWCNT (M4) in different dimensions:
A) 20 nm, B) 50 nm, C) 100 nm

Figure 4.16 represents TEM images of 30Co/1Ru/MWCNT in 3 dimensions: A) 20 nm, B) 50 nm and C) 100 nm. The images show that cobalt particles were located inside the tubes. Particles inside the channels mostly have the size of 3-7 nm, while

the particles anchored to outer walls reached between 15-30 nm. The metal-oxide nanoparticles attached to the outer walls of the MWCNTs were larger than the ones encapsulated inside the CNTs due to restricted growth of the nanoparticles by the inner diameter of the CNTs. It can be seen in Figure 4.16 (B, C) that the most of the cobalt particles were located on top of the channels forming agglomerations of cobalt oxide. This may indicate a rapid growth of cobalt precipitate, growing disconnected from MWCNT. Bezemer *et al.* [103] suggested that it might be a reason of lack of insufficient nucleation sites in support material, where growth process occurs. Since the images are in two dimensional space, it may be not accurate to say that the particles are located inside the tubes. Instead, they might be attached to external walls of CNTs which are facing towards TEM camera.

The HRTEM images of 10Co/MWCNT are shown in Figure 4.17 in 3 different dimensions: A) 10 nm, B) 20 nm and C) 100 nm. Most of the MWCNT caps are found to be open in these images, resulting from the acid treatment prior to impregnation. The size of unpromoted cobalt particles ranged around ± 5 nm, both, in inner and outer walls of MWCNT. The TEM also revealed that the cobalt particles are not well dispersed inside and outside of MWCNT's walls, as comparing to metal dispersion on 1 wt% ruthenium promoted 10 and 30 wt % cobalt catalysts. The metal particle dispersion on ruthenium promoted catalysts is more frequent comparing to unpromoted catalysts. The main reason for this phenomenon can be an interaction of ruthenium metal with cobalt, which contributed in better dispersion of cobalt particles inside and outside of MWCNT walls. Hosseini [137] observed that the addition of Ru improved the dispersion of cobalt throughout the support. Also effect of ruthenium over cobalt catalysts found to be positive in terms of average cobalt clusters' decrease and their dispersion on the support surface [91]. Kogelbauer *et al.* [15] studied the effect of ruthenium by H₂ chemisorption and stated that the amount of metal atoms exposed on the surface increased by a factor of 3 upon ruthenium promotion.

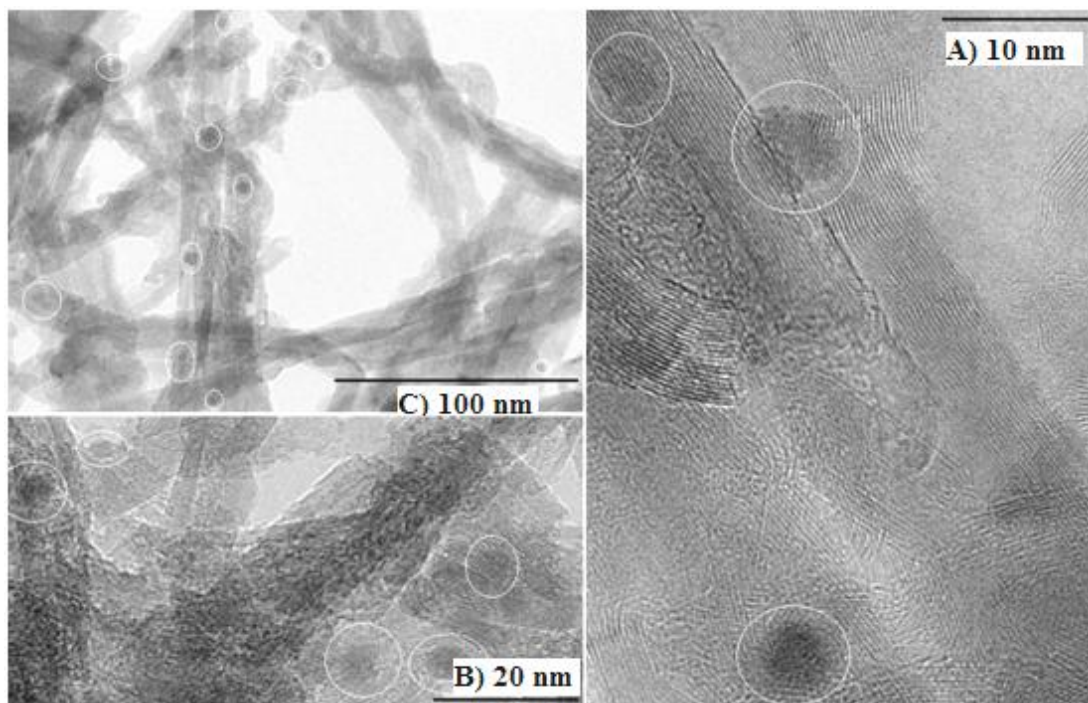


Figure 4.17: TEM images of 10Co/MWCNT (M2) in different dimensions:
 A) 10 nm, B) 20 nm, C) 100 nm

In addition cobalt particle size distribution was studied by FESEM. Figure 4.18 shows FESEM images of 10Co/1Ru/MWCNT (M3) and 30Co/1Ru/MWCNT (M4) catalysts at different magnifications, which are **M3**:– A) 50K, B) 100K, C) 100K, and **M4**:–A) 20K, B) 100K, C) 100K respectively. From M3 (C) it can be viewed that some agglomeration occurred on the outer surface of 10Co/1Ru/MWCNT, that cobalt clusters are located in the distance between 15 to 30 nm from each other. It is quite difficult to observe inner surface of MWCNT, but still images under FESEM consistent and support images of the catalysts from HRTEM. There is significant difference between 10Co/1Ru/MWCNT and 30Co/1Ru/MWCNT which can be seen by comparing M3 (A, B, C) and M4 (A, B, C) images. Image of M4 (A) showed that high loading of cobalt caused the agglomeration of cobalt species by forming clusters. Similar image was observed by TEM which is shown in Figure 4.16. Agglomeration of cobalt species is not desirable in FT process due to the reasons such as high cost of cobalt, decreasing of cobalt metal dispersion, surface area and decreasing of cobalt active sites [1].

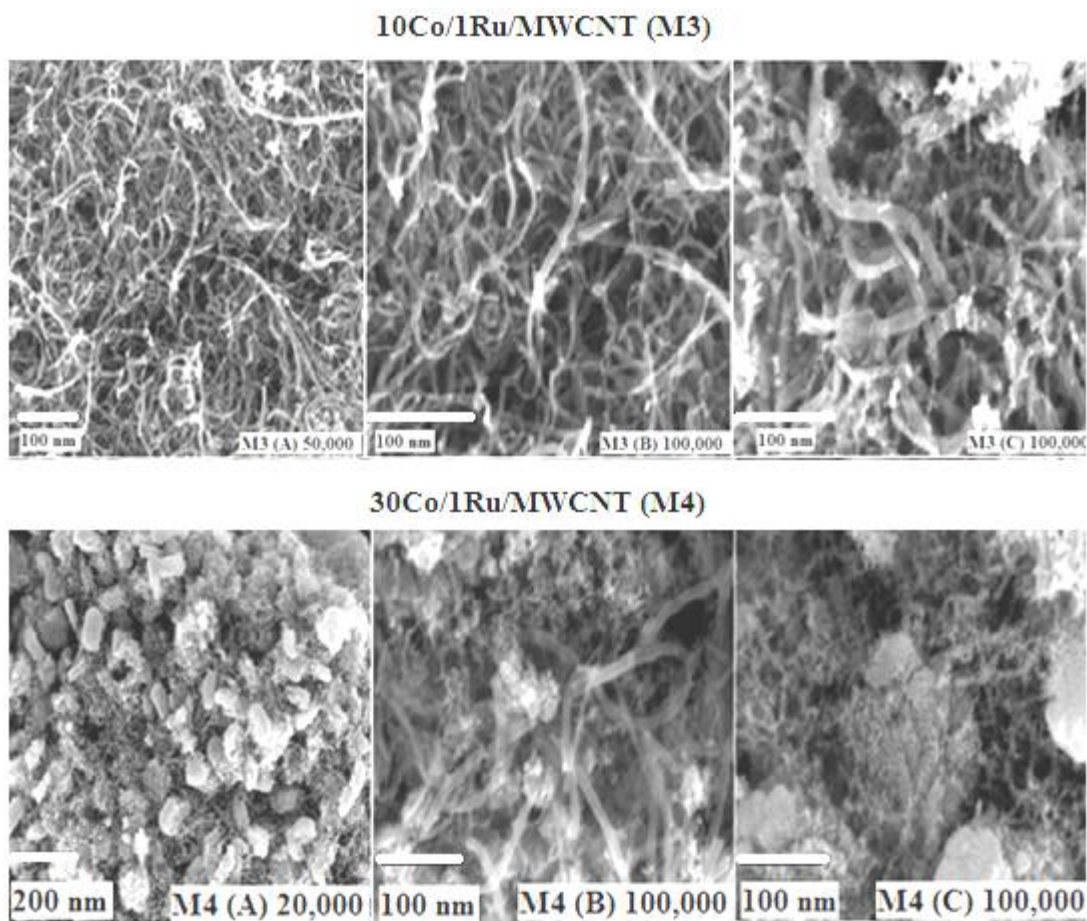


Figure 4.18: FESEM images of 10Co/1Ru/MWCNT (M3) and 30Co/1Ru/MWCNT (M4) catalysts at different magnifications: **M3**:– A) 50K, B) 100K, C) 100K, and **M4**:–A) 20K, B) 100K, C) 100K

4.2.3 Morphology and particle size distribution in Co/Ru/SBA-15 catalysts

High resolution TEM images of 10Co/SBA-15 (S2), 10Co/1Ru/SBA-15 (S3) and 30Co/1Ru/SBA-15 (S4) are depicted in Figure 4.19 in different dimensions: **S2** – A) 100 nm, B) 100 nm, **S3** – A) 10 nm, B) 50 nm, C) 100 nm, **S4** – A) 10 nm, B) 20 nm, C) 100 nm. As shown in Figure 4.19 (S2 (A) and (B)) metal aggregates are found inside and outside of ordered mesopores. These large aggregates consist of group of Co_3O_4 nanocrystals hosted in individual mesopores [114]. Unlike MWCNT supports it is difficult to measure cobalt particle size.

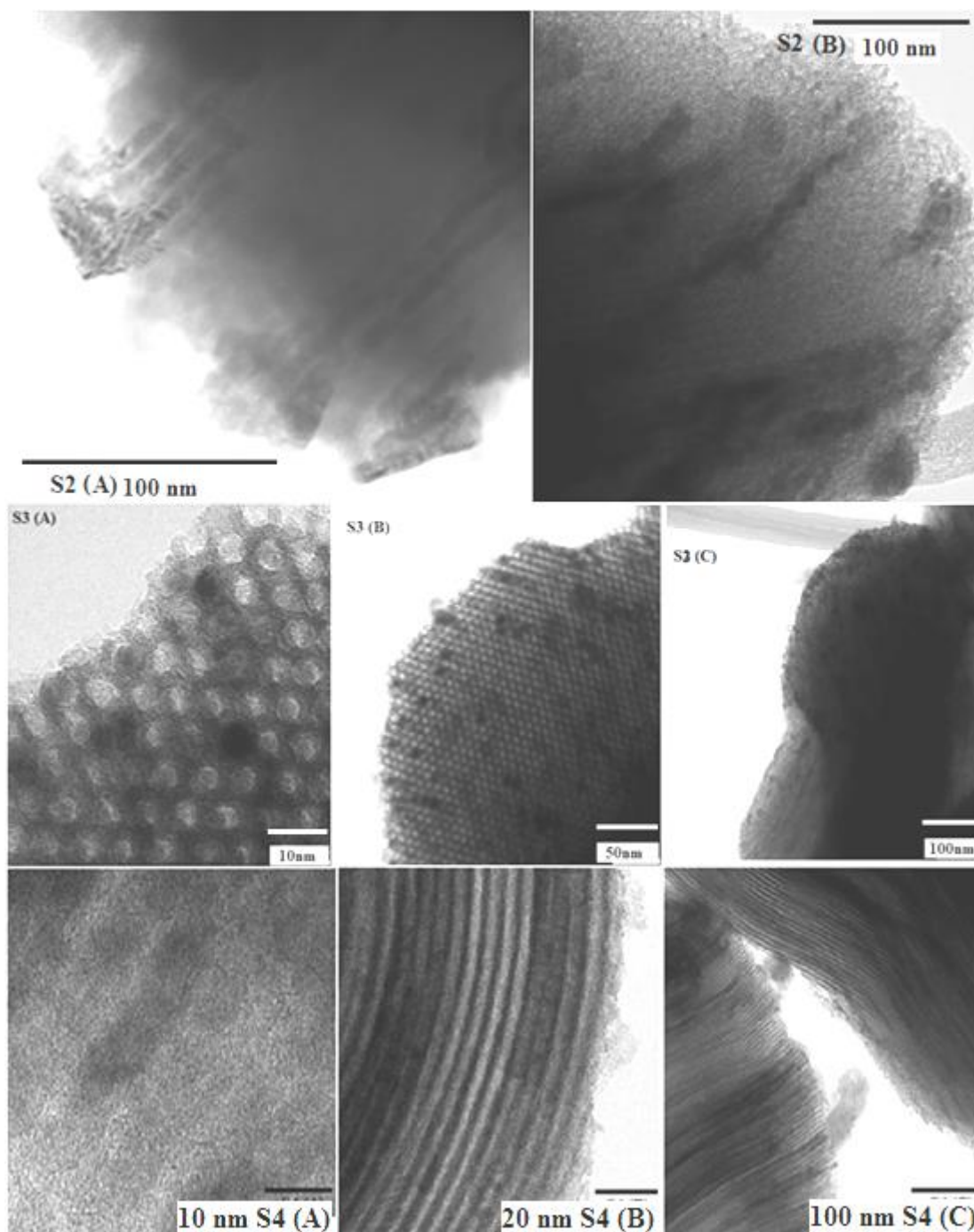


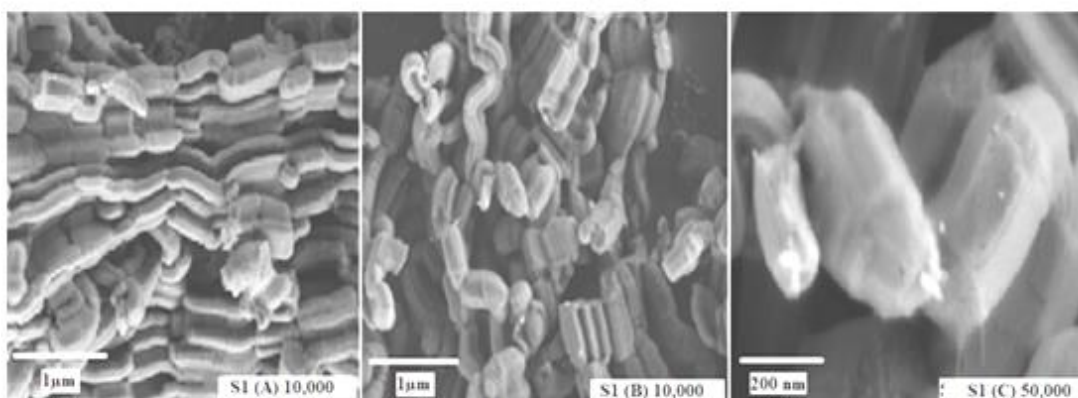
Figure 4.19: The HRTEM images of 10Co/SBA-15 (**S2**), 10Co/1Ru/SBA-15 (**S3**) and 30Co/1Ru/SBA-15 (**S4**) in different dimensions: **S2** – A) 100 nm, B) 100 nm, **S3**– A) 10 nm, B) 50 nm, C) 100 nm, **S4** – A) 10 nm, B) 20 nm, C) 100 nm.

Images of 10Co/1Ru/SBA-15 (S3 A, B and C) showed that metal particles were distributed uniformly on the surface. S3 (A) and (B) also show that the cobalt metal particles, located in interior surface of SBA-15. The size of the particles attached to the interior surface ranged between 5-10 nm, while the range of size of particle attached to outer layer was higher, which was 15-30 nm. Image S3 (C) showed that the cobalt particles spread uniformly on the outer layer of SBA-15. Images of 30Co/1Ru/SBA-15 are shown in Figure 4.19 (S4) (A, B and C) as well. Unlike 10Co/1Ru/SBA-15 (S3 (A) and (B)), 30Co/1Ru/SBA-15 (S4) (A, B, C) show that in high cobalt loading of cobalt caused the particles' agglomeration on the outer surface of the support forming some clusters (S4 (C) 100 nm). For such high cobalt loading, cobalt exists as clusters and some clusters may be agglomerated to form islands consisting of small particles [112]. According to Storsater *et al.* [138] it is impossible to determine the cobalt particle size from the TEM because of the lack of contrast between metal and support.

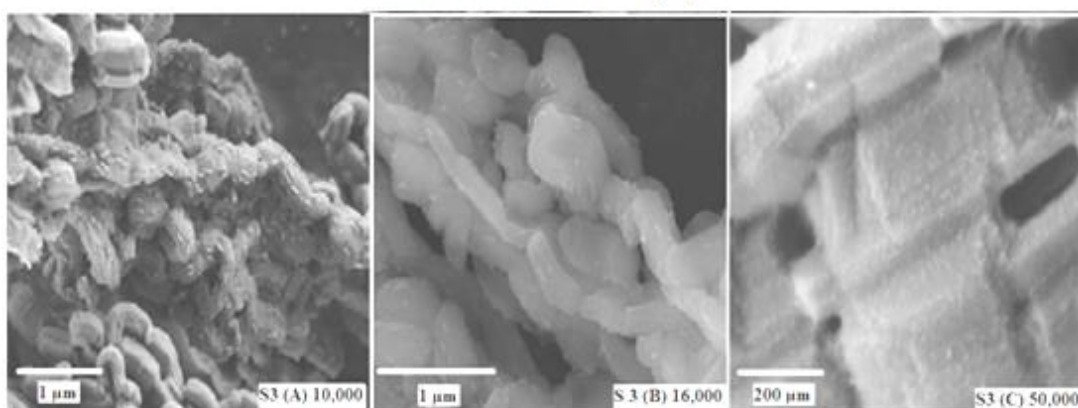
The SBA-15 based Co/Ru catalysts were further scanned using FESEM in different magnifications in the range of 10 to 50K. The images of pure SBA-15 (S1), 10Co/1Ru/SBA-15 (S3) and 30Co/1Ru/SBA-15 (S4) are depicted in Figure 4.20. Pure SBA-15 (S1) was included for making a comparison between pure and metal loaded SBA-15. The pure SBA-15 images reveal that the morphology of SBA-15 consists of aggregated necklace-like structure. The images of 10Co/1Ru/SBA-15 are shown in Figure 4.20, S3 (A, B and C) where the difference after adding of 10 wt% cobalt and 1 wt % ruthenium can be seen clearly. Cobalt clusters were distributed along the SBA-15's surface quite uniformly. Image S3 (A) showed that the cobalt formed clusters with size of 0.1 μm , but uniformly distributed along the SBA-15 outer surface. There is no significant image from FESEM which may show presence of active metals inside the channels of SBA-15, but it can be supported by HRTEM images of 10Co/1Ru/SBA-15 (Figure 4.19 S3 (A, B and C)) which clearly shows that the cobalt species are located inside the channels. Also S3 (C) in high magnification (50K) shows matters/dots on top of the SBA-15's domain, which may be an evidence for cobalt's uniform distribution on the outer layer.

There is significant difference between 10Co/1Ru/SBA-15 and 30Co/1Ru/SBA-15, which can be studied by comparing S3 and S4 views of Figure 4.20. In case of high cobalt loading, metal was also distributed along the surface of SBA-15 domains. The forms of agglomeration cannot be directly seen from S4 (A, B and C) images, but can be assumed that loading of 30 wt % of cobalt caused a formation of cobalt clusters which are spread along the surface. The images S4 (A, B, C) of Figure 4.20 can be supported by Figure 4.19 (S4 (A, B and C)) from TEM as well. The major difference between 10Co/1Ru/SBA-15 and 30Co/1Ru/SBA-15 can be noticed by making comparison of S3 (C) and S4 (B, C) images. The S4 (C) reveals that the cobalt species are spread along the surface. Also S4 (C) shows “cross- section” view of SBA-15 domain which is indicated in red circle. From that spot can be assumed that cobalt metal has spread into a bulk. Spreading of active metal into the inner channels can be favorable in FT synthesis. Location of active sites inside the channels can create local pressure which may contribute for a better CO conversion [89].

Pure SBA-15 (S1)



10Co/1Ru/SBA-15 (S3)



30Co/1Ru/SBA-15 (S4)

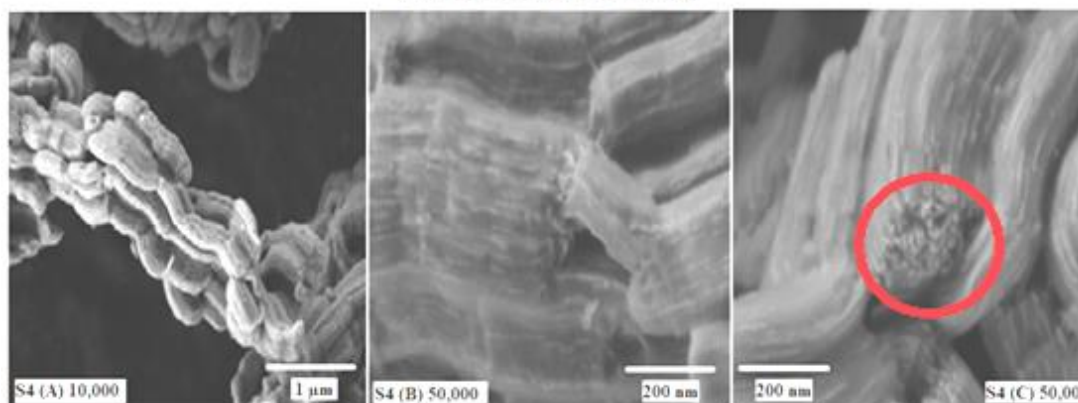


Figure 4.20: FESEM images of Pure SBA-15 (S1), 10Co/1Ru/SBA-15 (S3) and 30Co/1Ru/SBA-15 (S4) catalysts in different magnifications: **S1**:– A) 10K, B) 10K, C) 50K; **S3**:–A) 10K, B) 50K, C) 50K; **S4**:– A) 10K, B) 50K, C) 50K.

4.2.4 Elemental composition analysis of MWCNT and SBA-15 based catalysts

Elemental composition of MWCNT and SBA-15 based catalysts were studied using in energy dispersive x-ray analysis (EDX). The results of 10Co/MWCNT (M2), 10Co/1Ru/MWCNT (M3) and 30Co/1Ru/MWCNT (M4) catalysts presented in Figures 4.21, 4.22 and 4.23 respectively, while Figures 4.18 and 4.19 represent EDX results of 10Co/1Ru/SBA-15 (S3) and 30Co/1Ru/SBA-15 (S4) catalysts, respectively. The ratio of elements of MWCNT and SBA-15 based catalysts were presented in Table 4.2. The results of spectrum of all catalysts showed that cobalt particles are present in 0.775, 6.9 and 7.7 keV [98] which can be seen from Figures 4.17 to 4.21. The EDX also detected a certain amounts of oxygen. The source of oxygen was from ethanol (solvent), cobalt and ruthenium precursors. All elements were detected in K edge level except ruthenium. Because of the very low amount of ruthenium, its signal was obtained from L edge by EDX in the spectrum of 2.5 and 3.2 keV.

4.2.4.1 MWCNT based catalysts

The EDX analysis for 10Co/MWCNT catalyst were done by choosing a certain spots which are shown in Figure 4.21 while the EDX were done for 10 and 30Co/1Ru/MWCNTs by choosing a broader areas which can be viewed in Figures 4.22 and 4.23. Amount of carbon is different in MWCNT based catalysts which is 21 wt% in 10Co/MWCNT, 67.64 wt% in 10Co/1Ru/MWCNT and 33.11 wt% in 30Co/1Ru/MWCNT, respectively. Also weight percentage of cobalt metal is different in these catalysts which are: 42 wt% in 10Co/MWCNT, 12 wt% in 10Co/1Ru/MWCNT and 33 wt% in 30Co/1Ru/MWCNT. In 10Co/MWCNT catalysts the main reason for such carbon/cobalt ratio (21/42) can be related to a chosen spots which might contain mostly cobalt metal compared to carbon. The scanned area for 10Co/MWCNT is 10 μm . The same assumption can be done towards other MWCNT based catalysts. The carbon/cobalt ratio of 10Co/1Ru/MWCNT is 67/13 weight percent. Two scanned areas were chosen for this catalyst each with 50 μm and 9 μm . These areas are much broader than

10Co/MWCNT's area (10 μm). It can be speculated that, in general, chosen areas contain less cobalt. Outer surface of MWCNT is not covered by cobalt species which can be supported by TEM and FESEM images (Figures 4.15 and 4.18, respectively). The ratio of carbon/cobalt in 30Co/1Ru/MWCNT is 33/34 weight percent. Two scanned areas were chosen with areas 10 μm and 30 μm for EDX analysis. Both, TEM and FESEM images (Figures 4.16 and 4.18, respectively) of 30Co/1Ru/MWCNT show that cobalt clusters were formed on outer layer of MWCNT and the surface was coated with cobalt species. Because of the coating, detection of carbon was less while detection of cobalt was higher.

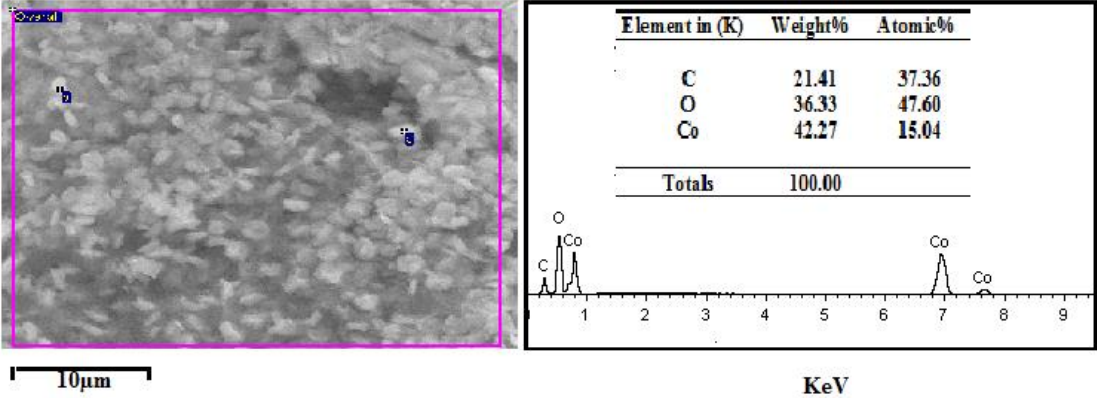


Figure 4.21: EDX of 10Co/MWCNT (M2)

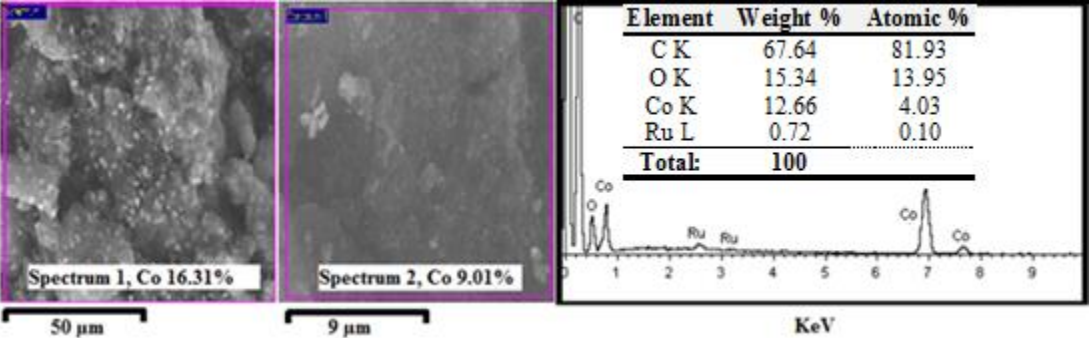


Figure 4.22: EDX of 10Co/1Ru/MWCNT (M3)

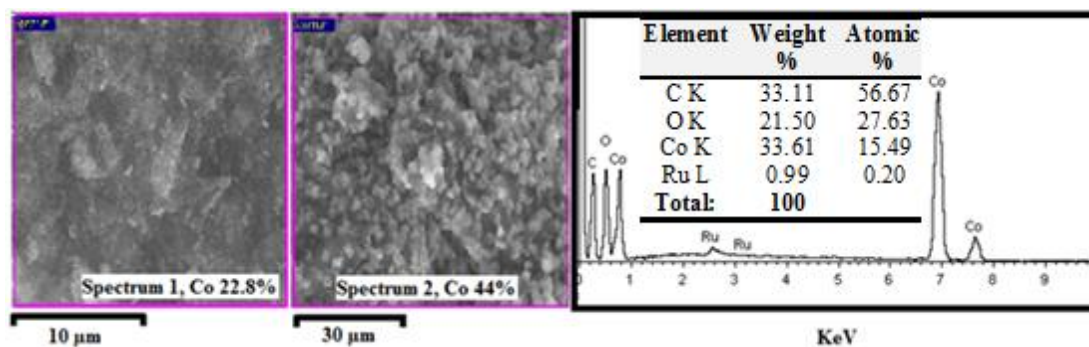


Figure 4.23: EDX of 30Co/1Ru/MWCNT (M4)

4.2.4.2 SBA-15 based catalysts

Combined EDX results of 10Co/1Ru/SBA-15 and 30Co/1Ru/SBA-15 catalysts can be viewed from Figures 4.24 and 4.25, respectively. In both catalysts certain spots were chosen for elemental composition analysis. The ratio of silica/cobalt in 10Co/1Ru/SBA-15 is 9.7/3.3 wt% while silica/cobalt ratio for 30Co/1Ru/SBA-15 is 10.7/10 wt%. Less amount of cobalt (3.3 wt%) in 10Co/1Ru/SBA-15 might be attributed to low cobalt loading which is 10 wt%. It also gives some indication that cobalt species are distributed on top of the silica surface, which can be also supported by TEM (Figure 4.19) and FESEM (Figure 4.20) images of this catalyst. The opposite phenomenon is observed in 30Co/1Ru/SBA-15. The ratio of silica versus cobalt is 10.7/10 wt% which can be explained with high loading of cobalt metal (30 wt %). The reason for silica's low weight percent may be due to the coated surface of silica with cobalt species. The same situation is observed in 30Co/1Ru/MWCNT catalyst where weight percent of carbon is quite low versus cobalt (33/34). It is shown in the spectrums of SBA-15 based catalysts and in Table 4.2 that SBA-15 based catalysts contain some amount of carbon element. Wu *et al.* [134] suggested that the signals of carbon may come from supporting membranes under the specimen.

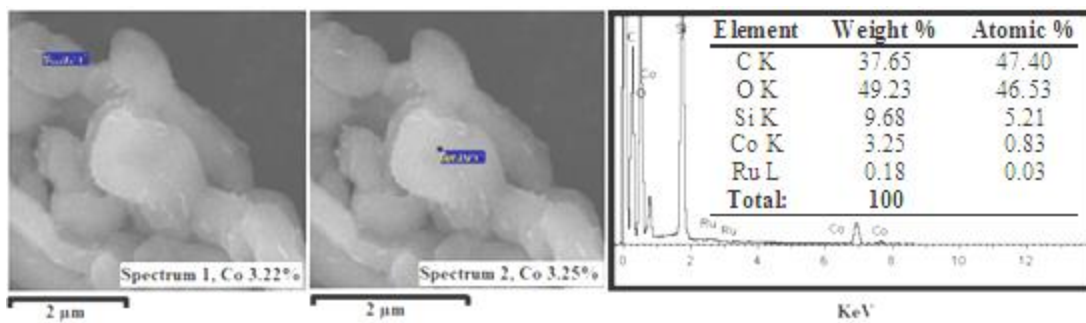


Figure 4.24: EDX of 10Co/1Ru/SBA-15 (S3)

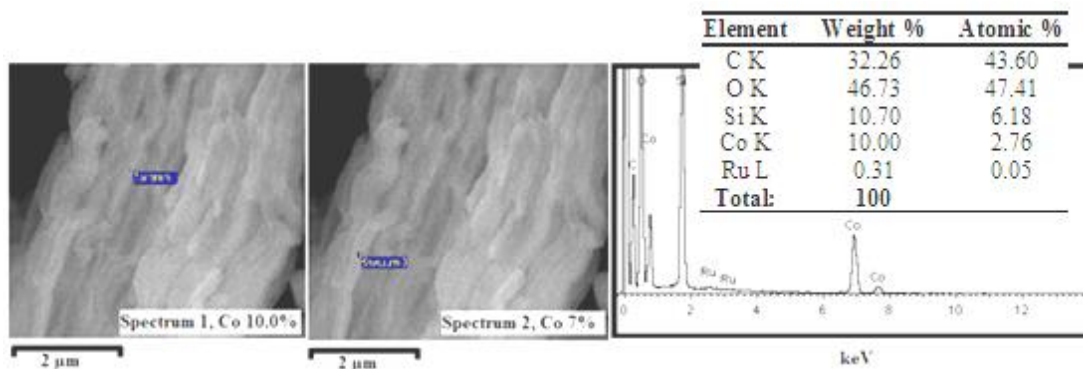


Figure 4.25: EDX of 30Co/1Ru/SBA-15 (S4)

Table 4.2: Elemental composition of MWCNT and SBA-15 based catalysts

catalyst / Element (wt %)	C	O	Co	Ru (L)	Si
10Co/MWCNT (M2)	21	36	42	-	-
10Co/1Ru/MWCNT (M3)	67.64	15	12.66	0.72	-
30Co/1Ru/MWCNT (M4)	33.11	21.5	33.61	0.99	-
10Co/SBA-15 (S2)	42	42.81	3.86	-	10.52
10Co/1Ru/SBA-15 (S3)	37.65	49.2	3.25	0.18	9.68
30Co/1Ru/SBA-15 (S4)	32.26	46.7	10	0.31	10.7

4.2.5 Surface area, pore volume and porosity of MWCNT and SBA-15 based Co/Ru catalysts

4.2.5.1 MWCNT based catalysts

Figure 4.26 represents the nitrogen adsorption/desorption isotherms of 10Co/MWCNT (M2) (A) and 30Co/1Ru/MWCNT (M4) (B) catalysts. In both cases the isotherm is convex to P/P^0 axis over the entire range and represents reversible type III. Accordingly it does not exhibit a point B [126]. The hysteresis loop of this isotherm is significant. Because of this phenomenon this isotherm can be related to type “V” [126]. At the same time the type V isotherm is highly uncommon and it is related to the type III isotherm [126]. The hysteresis loops of catalysts represent mostly type “B” or “H3”. The H3 hysteresis loops do not exhibit any limiting adsorption at high P/P^0 and is observed with aggregates of plate-like particles giving rise to slit-shaped pores [126], [127].

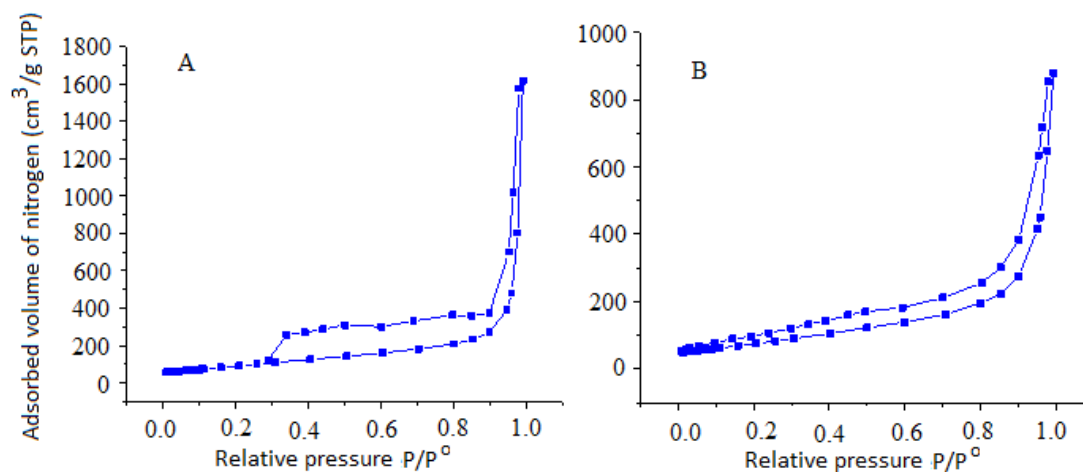


Figure 4.26: Nitrogen sorption isotherms of M2 (A) and M4 (B) catalysts

4.2.5.2 SBA-15 based catalysts

The replotted isotherms of 10Co/1Ru/SBA-15 (S3) and 30Co/1Ru/SBA-15 (S4) are shown in Figure 4.27. In both cases isotherms are convex to P/P^0 axis and belong to

isotherm type IV [126], [127]. Characteristic features of the Type IV isotherm are its hysteresis loop, which is associated with capillary condensation taking place in mesopores, and the limiting uptake over a range of high P/P^0 . Type IV isotherms are given by many mesoporous industrial adsorbents [126]. The isotherms followed by very obvious desorption hysteresis. Unlike hysteresis from pure SBA-15, the hysteresis of 10Co/1Ru/SBA-15 and 30Co/1Ru/SBA-15 can be related to “H1” or type “A” hysteresis loop, according to the IUPAC classification [126]. Type “A” hysteresis mostly happens with supports which contain cylindrical shape of pores. Based on difference in terms of hysteresis between pure SBA-15 and SBA-15 which contains active metals, it can be concluded that cobalt and ruthenium nanoparticles contributed to a changes in the pores of support materials. Initially pure SBA-15 possessed “H2” or “E” type [126], [127] hysteresis which was related to “ink bottle” type of pores. But after loading of active metals, pores changed their shapes from “ink bottle” to “cylinder” shape.

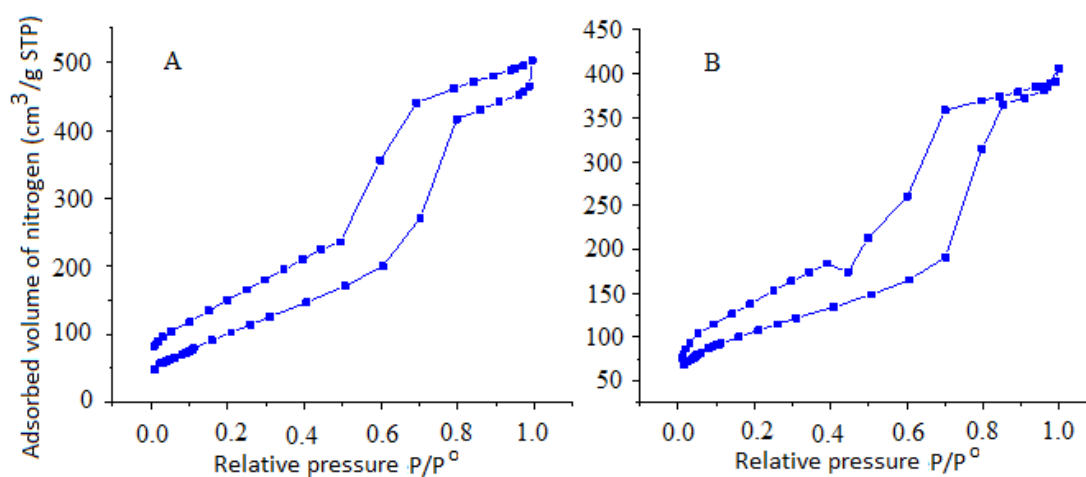


Figure 4.27: Nitrogen sorption isotherm of S3 (A) and S4 (B) catalysts

Table 4.3 summarizes results of MWCNT and SBA-15 based catalysts in respect to surface area, total pore volume, and average pore volume. These results show that BET surface area of 10Co/MWCNT 10Co/1Ru/MWCNT and 30Co/1Ru/MWCNT is 335 m²/g, 367 m²/g and 266 m²/g, respectively. At the same time total pore volume of 10Co/MWCNT, 10Co/1Ru/MWCNT and 30Co/1Ru/MWCNT is 0.774 cm³/g, 0.925 cm³/g and 0.643 cm³/g respectively. Surface area and total pore volume of

30Co/1Ru/MWCNT is lower than that of 10Co/MWCNT and 10Co/1Ru/MWCNT. Decreasing of BET parameters between these catalysts indicates pore blockage, which may occur mostly due to the higher cobalt loading on the support from 10 to 30 wt%. The same trend was observed by Trepanier *et al.* [91].

Table 4.3: Results of BET measurements of MWCNT and SBA-15 supported catalysts

Support/catalyst	Surface area (m ² /g)	Total pore volume (cm ³ /g)	Average pore size Ø(nm)
Purified MWCNT (M1)	255.3	0.7075	11.09
10Co/MWCNT (M2)	335	0.774	8.88
10Co/1Ru/MWCNT (M3)	367	0.925	10.08
30Co/1Ru/MWCNT (M4)	266	0.643	9.67
Pure SBA-15 (S1)	660	0.817	4.95
10Co/SBA-15 (S2)	913.3	1.568	6.86
10Co/1Ru/SBA-15 (S3)	409.5	0.699	6.83
30Co/1Ru/SBA-15 (S4)	383.8	0.589	6.14

The surface area of pure SBA-15 was determined as 660 m²/g, and its pore volume was 0.817 cm³/g. After loading of active metals, the surface area and total pore volume of pure SBA-15 decreased. After loading of 10 weight percent of cobalt and 1 weight percent of ruthenium, the surface area and pore volume of catalyst 10Co/1Ru/SBA-15 reduced to 409.5 m²/g and 0.699 cm³/g respectively. In addition, increasing of cobalt loading from 10 to 30 weight percent, the surface area of SBA-15 decreased from 409.5 m²/g, as it was in 10Co/1Ru/SBA-15 catalyst, to 383.8 m²/g in 30Co/1Ru/SBA-15 catalyst. Accordingly total pore volume of 30Co/1Ru/SBA-15 catalyst decreased to 0.589 cm³/g, compared with the pore volume of 10Co/1Ru/SBA-15 catalyst, which was 0.699 cm³/g.

4.2.6 Cobalt crystallite size and its chemical form in MWCNT and SBA-15 based Co/Ru catalysts

Crystallite size of cobalt compound was identified based on diffraction peak analysis using Full Width at Half Maximum (FWHM) data generated by XRD and the chemical form of cobalt crystallite was determined by comparing the obtained data for scanning angle of each peak with the existing XRD's material library. The spectrum for MWCNT and SBA-15 based catalysts from XRD is depicted in APPENDIX D. Figure 4.28 represents XRD patterns of MWCNT and SBA-15 based catalysts. The XRD patterns for both, MWCNT and SBA-15 based catalysts show that the sharpest peak for Co_3O_4 appeared in 36.9 theta value. The peak which is appeared in 26.2 theta on MWCNT based catalysts is attributed to graphite, according to XRD material library. In Figure 4.4 the XRD pattern for unpurified and purified MWCNT shows exact peaks at 26.2 theta value. The XRD pattern also shows that the sharpest and tallest peak for Co_3O_4 among all three MWCNT based catalysts is related to 10Co/MWCNT and in SBA-15 based catalysts, the sharpest and tallest peak came from 30Co/1Ru/SBA-15. The sharpness and intensity of XRD peaks are proportional to increase of Co_3O_4 crystallite size, when increasing the Co content [110]. As shown in Table 4.4, the largest Co_3O_4 crystallite size in MWCNT based catalysts was formed in 10Co/MWCNT catalyst which is 18.53 nm (with average crystallite size from all peaks 18.71 nm). However, in SBA-15 based catalysts the largest Co_3O_4 crystallite size came from 30Co/1Ru/SBA-15 which is 12.94 nm (with average crystallite size from all peaks 13.7 nm). The addition of ruthenium contributed to decrease of cobalt oxide particle size. The XRD patterns of both, MWCNT and SBA-15 based catalysts do not represent any peaks which can be related to ruthenium oxide. The reason for that may be a very small amount of ruthenium metal, which is approximately 0.04 g (1 wt %). The amount of ruthenium metal was detected by EDX analysis (Table 4.2).

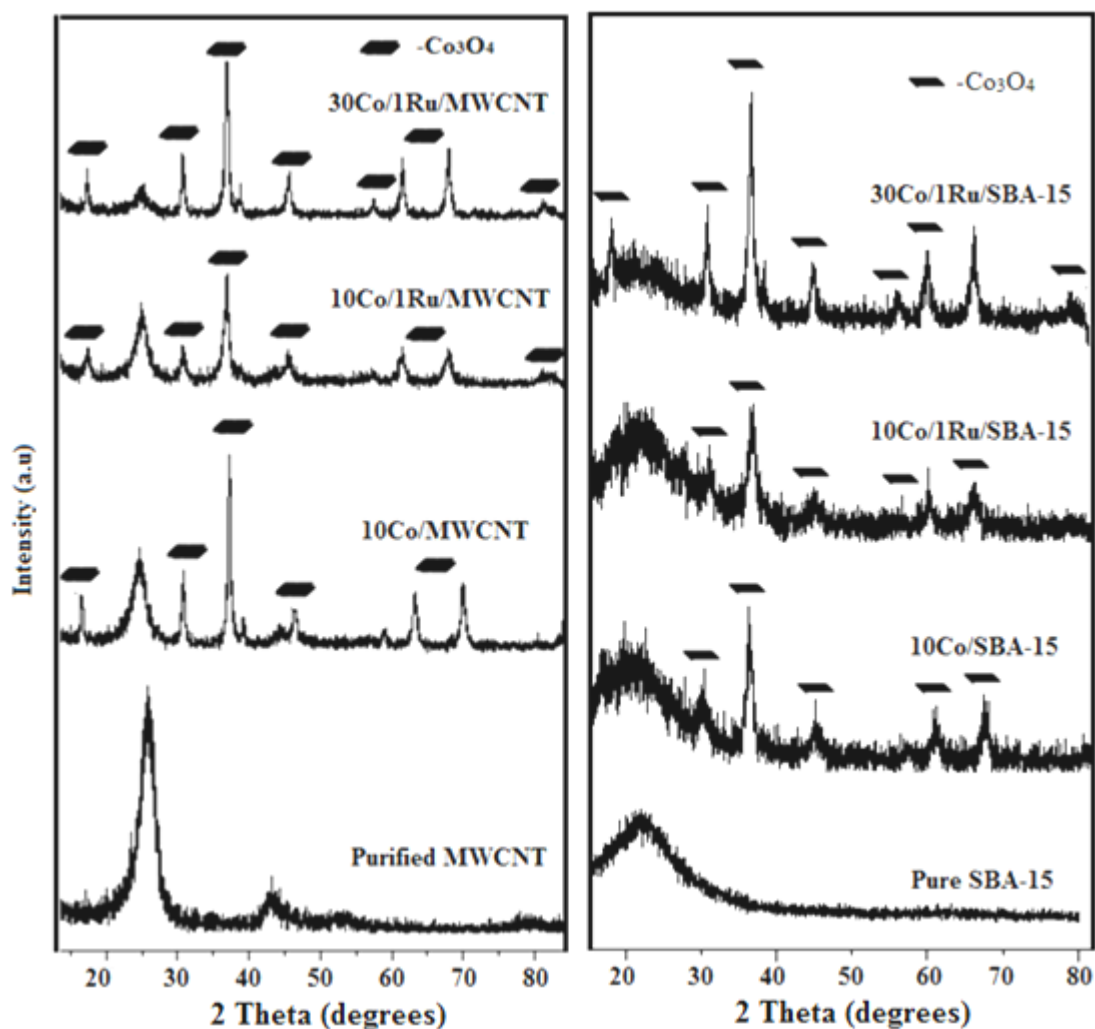


Figure 4.28: XRD patterns of MWCNT and SBA-15 based Co/Ru catalysts

In all catalysts prepared from cobalt nitrate using alcohol, XRD revealed that the cobalt chemical form as Co_3O_4 . In order to identify the cobalt particle size the sharpest peak was selected from spectrum of catalysts. However, other peaks which came from Co_3O_4 were also calculated and average crystallite size of Co_3O_4 was identified. In the XRD pattern for MWCNT and SBA-15 based catalysts, the sharpest peak for Co_3O_4 appeared in 36.9 theta value. Based on the theta value the Full Width at Half Maximum (FWHM) β was identified and “Sherrer equation” was applied for the crystallite size calculation. The calculation of crystallite size is shown in APPENDIX D. Crystallite size calculation results for MWCNT and SBA-15 based catalysts are given in Table 4.4.

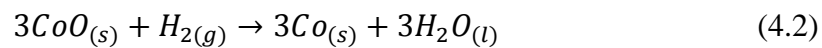
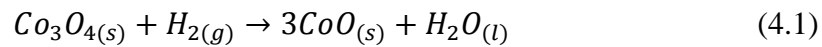
Table 4.4: Cobalt crystallite sizes of MWCNT and SBA-15 based catalysts

Catalysts	Peak (θ)	Co ₃ O ₄ crystallite size (sharpest peak (nm))	Average crystallite size from all peaks (nm)
10Co/MWCNT	36.983	18.53	18.71
10Co/1Ru/MWCNT	36.871	11.31	12.1
30Co1Ru/MWCNT	36.897	16.26	18.51
10Co/SBA-15	36.9	8.50	8.5
10Co/1Ru/SBA-15	36.86	8.52	10.9
30Co1Ru/SBA-15	36.866	12.94	13.7

Trepanier *et al.* [91] prepared a Co catalyst (15, 22 and 30 wt%) without Ru, and fixed amount of 15 wt% Co catalyst with 0.25, 0.5, and 1 wt% Ru promotion, using incipient wetness impregnation method. In their work they observed the increase in average particle size of Co₃O₄ from 9.6 to 16 nm in unpromoted catalysts, by increasing the cobalt loading. 1 wt% addition of Ru to 15 wt % Co catalyst slightly decreased the average particle size from 9.6 to 9.4 nm.

4.2.7 Catalyst reducibility

Reduction of cobalt species in catalysts is an important step as it generates active cobalt metal sites for FT synthesis. Reducibility of supported FT catalysts is a function of the fraction of Co₃O₄ crystalline phase, sizes of Co₃O₄ crystallites, and promotion with noble metals. The reduction temperature of the cobalt oxides and the effect of the ruthenium promoter in the process of catalyst reduction were investigated by TPR. TPR is a powerful tool to study the reduction behavior of the oxidized phases. The reduction features of cobalt oxides on different support materials have been studied widely. Stages of reduction consist of two steps:



At the first step Co_3O_4 is reduced until CoO and further to Co^0 when it is treated with H_2 . Figures 4.29 and 4.30 represent compiled TPR results of MWCNT and SBA-15 based catalysts.

4.2.7.1 MWCNT based catalysts

Figure 4.29 depicts the TPR results of 10Co/MWCNT, 10Co/1Ru/MWCNT and 30Co/1Ru/MWCNT catalysts, respectively. There were two reduction peaks occurred in 10Co/MWCNT: first at 392°C and 443°C. These temperatures can be assigned to the reduction of Co_3O_4 to CoO and the reduction of larger and smaller CoO particles to Co^0 , respectively [107], [94], [92]. The low temperature peak which belongs to reduction of Co_3O_4 to CoO usually occurs in the range of 300 to 400°C in the MWCNT supported catalysts [91], [107]. The second peak between 400 to 500°C is related to the reduction of CoO particles to Co^0 [107]. The 100°C interval in the reduction of $\text{Co}_3\text{O}_4 - \text{CoO} - \text{Co}^0$ in MWCNT supported catalysts may be attributed to the very low interaction of cobalt oxide with the support material (MWCNT) which is agreed by Tavasoli *et al.* [88], [92]. Also it depends on the particle size of cobalt oxides. There is also broader peak in the temperature range between 450°C to 500°C in (490°C) with low intensity which is not split from the sharp peak and tailing to it. This peak may provide the information about two phenomena: first phenomena can be the gasification of carbon support in the temperature close to 500°C [107], [94], [90]. According to H. Zhang *et al.* [94], metallic cobalt acts as a catalyst for the formation of methane through hydrogenation of the carbon nanotube support.

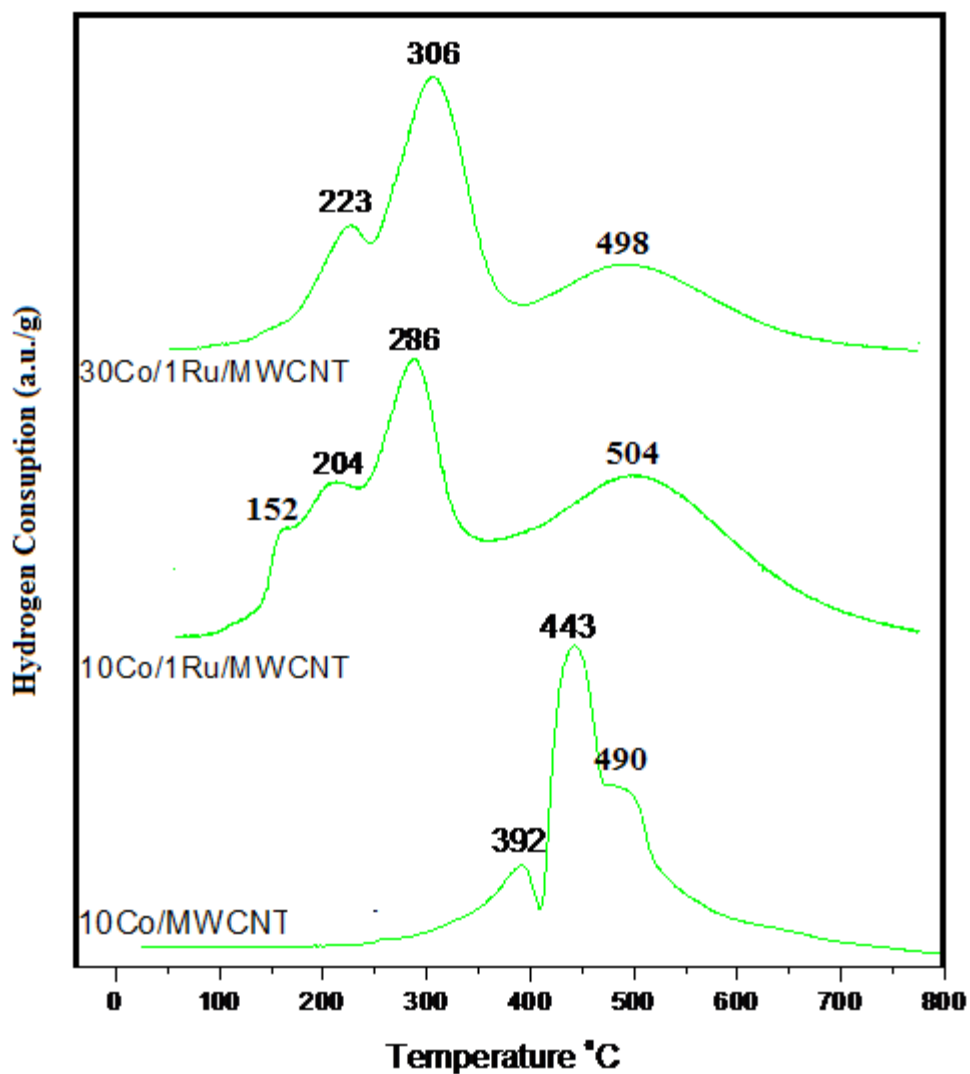


Figure 4.29: TPR results of 10Co/MWCNT (M2), 10Co/1Ru/MWCNT (M3), 30Co/1Ru/MWCNT catalysts

The stability of current MWCNT was separately investigated by calcining it in different temperatures in the oven. Result of weight loss versus temperature is provided in Figure 4.12. Lu *et al* [172] studied the thermal decomposition of MWCNT supported Co catalysts using different calcination temperatures. They found that, CNT started to decompose being consumed by oxidation in air in the temperature higher than 230°C or by methanation in H₂ at temperature higher than 450°C. The second phenomena can be attributed to the interaction of CoO with MWCNT support in some extend [91], [89]. But at the same time bulk cobalt oxide

Co₃O₄ undergoes complete reduction within the temperature of 500°C [139], 140] when there is no interaction of it with MWCNT.

The noticeable effect of a ruthenium promoter can be observed from the profiles of 10Co/1Ru/MWCNT and 30Co/1Ru/MWCNT catalysts. The TPR profile of the 10Co/1Ru/MWCNT shows that, the addition of 1 wt% ruthenium on the cobalt catalyst caused in the significant decreasing of the reduction temperature of cobalt oxide species. The first peak at 152°C of the 10Co/1Ru/MWCNT catalyst may belong to the incompletely decomposed traces of Co(NO₃) in the form of NO and CO ions [137], [15]. The TGA-MS results of this catalyst also confirm this temperature. Next peaks come at the temperature of 204°C, which can be ascribed to the reduction temperature of Co₃O₄ to CoO and the third peak in the 286°C which belongs to the reduction of CoO to Co⁰[91]. Comparing the main peaks which belong to Co₃O₄ and CoO in unpromoted 10Co/MWCNT catalyst and promoted 10Co/1Ru/MWCNT catalysts, it can be clearly seen that the addition of ruthenium made significant improvement in the reducibility of the both cobalt species by drastically lowering the percentage of reduction approximately to 42%. There is also broad peak which appears in 504°C. This broad peak can be ascribed to gasification of carbon support which was observed by a several researchers [91],[107],[94],[90]. At the same time the TGA-MS results of 10Co/1Ru/MWCNT catalyst shows that the sharp peak in the range of 500°C.

The TPR profile of 30Co/1Ru/MWCNT catalyst discloses that the increasing of cobalt loading in the ruthenium promoted catalyst caused in the slight increasing to the reduction temperature of the cobalt species, approximately to 7.5%. By increasing of cobalt loading from 10 to 30wt%, the first peak shifted from 204 to 223°C for reduction of Co₃O₄ to CoO, and the second peak increased from 286 to 306°C for reduction of CoO to Co⁰respectively. Nevertheless, the intensity of the first and the second peaks increased due to the high amount of cobalt oxides on top of the MWCNT's surface. The agglomeration of cobalt species on top of the MWCNT can be observed from the FESEM images of the catalysts shown above. Hosseini *et al.* [137] explained that the effect of Ru in terms of cobalt reduction is attributed to the interactions of cobalt and ruthenium, induced by the higher mobility

of ruthenium as well as the formation of Co-Ru oxide [108]. Das *et al.* observed that the reduction of ruthenium oxide occurs in lower temperature comparing to the reduction of cobalt oxide. They have showed that reduced ruthenium enhances the reduction of cobalt oxide by spillover of hydrogen from ruthenium to the cobalt oxide [141]. According to Dullac *et al.* [142] Co and Ru interaction forms Co_2RuO_4 oxide spinel which is isostructural to Co_3O_4 . This spinel can be reduced at lower temperature when Al_2O_3 is used as a support, as Al_2O_3 has a tendency to form a Co aluminate. Due to the fact that the interaction between active metal and MWCNT is very low comparing to alumina supports [88], [92], the reduction temperature of Ru promoted Co catalysts will be much lower, comparing to its alumina supported counterparts.

The research done by Hosseini *et al.* [137] shows that the alumina supported 20 wt% cobalt catalyst promoted by 1 wt% ruthenium completely reduced in the temperature of 408°C , which can be compared by the current work where 1wt% ruthenium promoted 10-30 wt% Co/MWCNT catalysts have completely reduced up to the temperature of 306°C .

4.2.7.2 SBA-15 based catalysts

The influence of the cobalt loading and the effect of ruthenium promoter in the SBA-15 based Fischer-Tropsch catalysts are depicted in the Figure 4.30. For unpromoted 10Co/SBA-15 catalysts four different peaks were observed in the TPR profile. First two peaks are close to each other which are 379 and 404°C . The third and fourth peaks (688 and 799°C) came later. The first peak (379°C) represents the reduction temperature of Co_3O_4 to CoO and the second peak (404°C) shows the reduction temperature of CoO to Co^0 , respectively [143], [145].

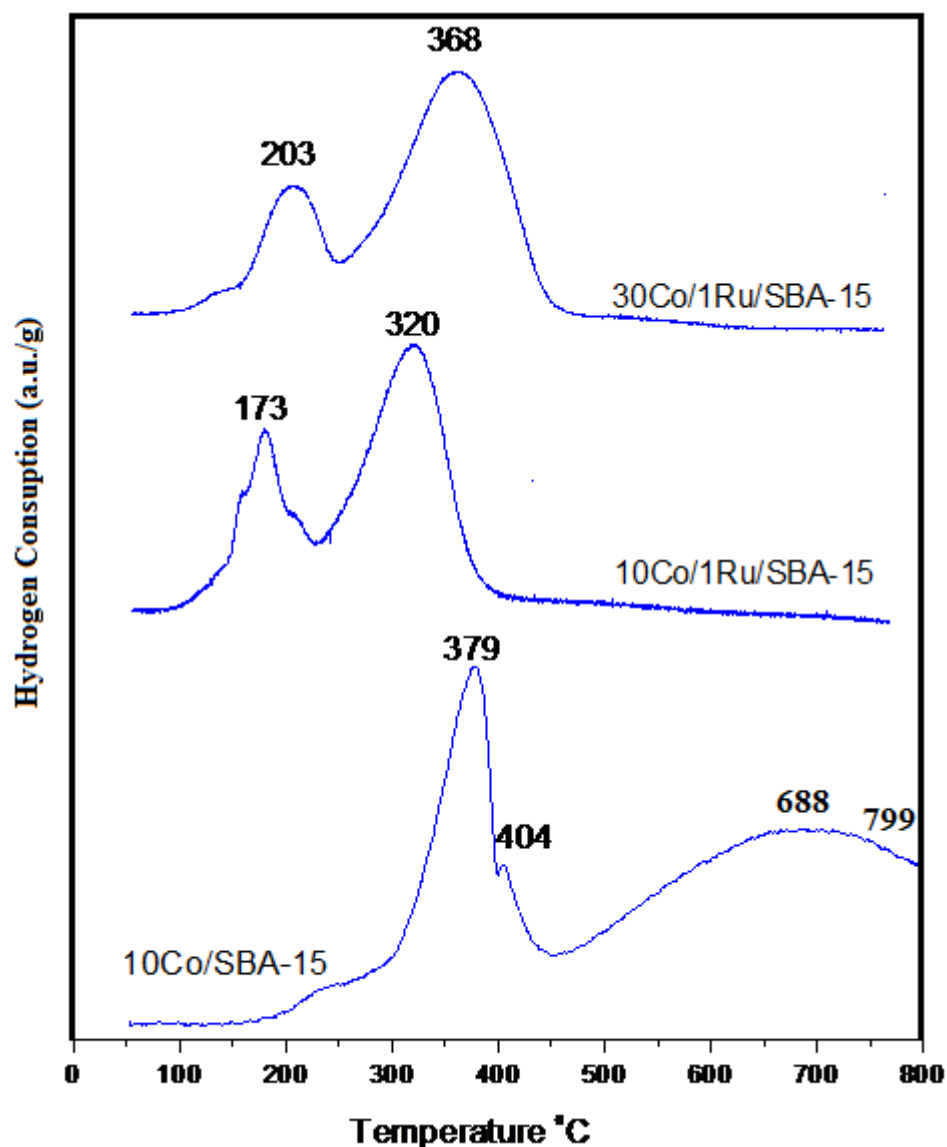


Figure 4.30: TPR results of 10Co/SBA-15 (S2), 10Co/1Ru/SBA-15 (S3) and 30Co/1Ru/SBA-15 (S4) catalysts

The temperature of the first peak is quite high comparing to TPR profiles of Co/SBA catalysts for the same peak obtained by other researchers [111], [113]. Castner *et al.* [146] suggested that a local maximum reduction rate is mostly observed in the temperature interval between 307 to 359°C. The initial reduction step is independent of particle size, pore size, and surface area and mostly occurred at the same interval. The reason for such high temperature (379°C) in present work for Co/SBA-15 catalyst may be attributed to the interaction of cobalt oxide with the

SBA-15. Martinez *et al.* suggested that the high temperature profile may occur because of the strong interaction of cobalt oxide with the support material [110]. The second peak is coming in 404°C which may be assigned to the second reduction step of the cobalt species, that is CoO to Co⁰ [28], [143], [144]. At the same time its tailing to the first peak and quite small. Based on the data obtained from TPR, 26.52% of H₂ consumption occurred in the temperature of 379°C, suggesting that 26.52% of cobalt species from Co₃O₄ to CoO had reduced. And only 10.67% of H₂ consumption occurred in the temperature of 404°C suggesting that very small amount of CoO had reduced to Co⁰. Remaining share of cobalt species reduction which is 62.81% of H₂ consumption occurred in the temperature range between 404 and 799°C, that is, 34.55% of cobalt reduction occurred in 688°C, and the rest (28.26%) reduced completely in the temperature of 799°C. Such a high temperature of reduction which occurred in the range of 688 to 799°C may explain that the cobalt species had strong interaction with silica based support material forming Co₂SiO₂ [110], even though Co₂SiO₂ was not detected in XRD measurements of this catalyst. It was found that the second step of the cobalt species' reduction at different temperatures depends on the interaction of small particles with the support material stabilizing the oxide phase [146]. The smaller CoO clusters may interact more strongly with the support than larger ones [147]. As suggested by Martinez *et al.* [110], the cobalt silicate phase may be formed during the calcination of the catalysts, and probably occurs for the low loaded cobalt catalysts prepared from cobalt nitrate.

The addition of 1 wt% ruthenium in Co/SBA-15 catalyst made significant changes in the reduction temperature of both, 10 and 30 wt% catalysts, shifting the reduction temperatures of the cobalt oxides to a much lower degrees. The TPR profile of 10Co/1Ru/SBA-15 is shown in Figure 4.30, where obvious difference in terms of cobalt species reduction can be noticed. Two temperatures were detected by TPR which are 173°C which may be assigned to the reduction of Co₃O₄ to CoO, and 320°C which belongs to the reduction of CoO to Co⁰ [111]. No other peaks were observed in the TPR profile, suggesting that there is no interaction between support and active metal, comparing to the 10Co/SBA-15 catalyst. Addition of 1 wt% ruthenium suppressed the interaction of the cobalt with the support material. The

temperature of Co_3O_4 shifted to lower degree from 379 to 173°C, and the temperature of CoO to Co^0 shifted from 404°C to 320°C, respectively. Xiong *et al.* [113] observed that, 173°C belongs to the reduction of ruthenium oxide to metal ruthenium. The reduction of RuO_2 to Ru takes place in at lower temperature than the reduction of Co_3O_4 [148]. But no separate peaks were observed in the TPR profile, most probably due to the overlapping with the first reduction peak of Co_3O_4 [111]. The 25.63% of the H_2 consumption lies to the first reduction of cobalt which is Co_3O_4 to CoO . And the remaining 74.37% of H_2 consumption belongs to the reduction of CoO to Co^0 . This is consistent with the equations (1) and (2) showing the ratio of 1:3 [144], [146], [147]. Also two peaks have different broadness, predicting that the reduction of Co_3O_4 consumed less H_2 (peak 173°C) comparing to the second peak.

Increasing in the cobalt loading slightly shifted reduction temperatures to high degrees, this can be seen from the TPR profile of 30Co/1Ru/SBA-15. The first reduction peak of the Co_3O_4 to CoO shifted from 173 to 203°C and the second peak of the CoO to Co^0 shifted from 320 to 368°C respectively. No peaks were observed after 368°C which indicates that there is no interaction of the cobalt species with the support material. Catalyst showed consistency in terms of H_2 consumption, where H_2 consumption for the first step was 24.13% and for the second step 75.87%, which is in agreement with 1:3 stoichiometric ratio of equations 1 and 2. Loosdrecht *et al.* [149] suggested that catalysts which contain larger pores usually do not contain leftovers of nitrate salts after calcination, as nitrates and water will be decomposed easily during calcination process.

4.2.8 Particle size and distribution of metal oxides

The average cobalt particle size and its distribution, cobalt crystallite size and cobalt cluster size over MWCNT and SBA-15 catalysts were identified by TEM, XRD and FESEM respectively. Average diameter of particles in inner and outer walls of the support was calculated by measuring 40 to 50 pieces of particles in each catalyst from TEM images. Cobalt cluster size was calculated by measuring several cobalt

clusters on top of MWCNT and SBA-15 supports using FESEM images of catalysts. During calculation of particle size the particles from outer and inner walls of MWCNT supported catalysts were calculated. From SBA-15 based catalysts only inner average particle size of 10Co/1Ru/SBA-15 catalyst was calculated. Because of the absence of cross section TEM view of 10Co/SBA-15 and 30Co/1Ru/SBA-15 catalysts it was not possible to measure average cobalt particle size and its distribution along the surface [112]. Also, since most of the particles in 10Co/SBA-15 and 30Co/1Ru/SBA-15 appear agglomerated (Figure 4.19), it was unattainable to measure Co_3O_4 size of these catalysts from TEM images. Particle size details of Co_3O_4 and their relation to surface area is depicted in Table 4.5. A bar graph, showing the size distribution of total cobalt particles on the walls of MWCNT and 10Co/1Ru/SBA-15 based catalysts is depicted in Figure 4.31.

Table 4.5: Particle size details of cobalt oxide deposited on MWCNT and SBA-15 catalysts

Catalysts	XRD crystallite		TEM average		FESEM	Surface
	size (nm)		particle size (nm)		average	area
	sharpest peak	average	“in”	“out”	cluster size (nm)	(m^2/g)
M1	-	-	-	-	-	255.3
M2	18.53	18.7	4.8	5.1	237	335
M3	11.31	12.1	3.4	4.1	81	367
M4	16.26	18.5	4.3	5.0	328	266
S1	-	-	-	-	-	660
S2	8.5	8.5	n.d.	n.d.	33	913.3
S3	8.52	10.9	8.3	n.d.	88	409.5
S4	12.94	13.7	n.d.	n.d.	109	383.8

4.2.8.1 MWCNT based catalysts

Table 4.5 shows that, among MWCNT based catalysts the largest average particle size in inner and outer walls of MWCNT is related to 10Co/MWCNT (M2), which

are 4.8 (in) and 5.1 (out) nm respectively. The XRD data also shows that the largest crystallite size is related to 10Co/MWCNT which is 18.53 nm. From FESEM data it can be seen that the largest average cobalt cluster size is related to 10Co/MWCNT which is 237 nm. Second largest cobalt crystallite size, particle size and average cobalt cluster size correspond to 30Co/1Ru/MWCNT (M4) which are 16.26, 4.3 (in) and 5.0 (out), and 328 nm, respectively. Among three MWCNT based catalysts the smallest particle size characteristics are related to 10Co/1Ru/MWCNT (M3), where crystallite size, particle size and average cluster size of cobalt are 11.31, 3.4 (in) and 4.1 (out) and 81 nm, respectively. In MWCNT based catalysts with addition of 1 wt% of ruthenium the size of cobalt particle significantly decreased, which can be seen by comparing unpromoted M2 and promoted M3 catalysts. Later, by increasing of cobalt loading from 10 to 30 wt%, the size of cobalt particles also increased, but still remained smaller than that of unpromoted 10Co/MWCNT catalyst. The effect of ruthenium in decreasing of cobalt particle size was significant in MWCNT based catalysts. It can be seen from Table 4.5 that the results of all three techniques are consistent and support each other. From TEM images of M3 and M4 catalysts can be seen that a lot of particles were distributed uniformly inside and outside the walls after being promoted with ruthenium metal (Figure 4.15 and 4.16). Hosseini *et al.* [150] in their studies of 15 and 25 wt% cobalt catalysts with 1 wt% ruthenium promotion reported that the average size of cobalt particles increased upon increasing the cobalt loading. Also they observed the effect of ruthenium towards cobalt loading, where they found that the addition of 1 wt% ruthenium is more favorable for the samples with lower cobalt loading than that of for catalysts with higher cobalt loading [137]. Trepanier *et al.* [91] in their work reported the proportionality of cobalt loading to the increase of cobalt particle size. Also they observed the effect of ruthenium towards cobalt particle size's decrease and reducibility. Table 4.5 also shows the surface area measurements of catalysts. Among all MWCNT based catalysts the surface area of promoted M3 catalyst is the highest, which is 367 m²/g. The second and third highest surface areas correspond to unpromoted M2 and promoted M4 catalysts with 335 and 266 m²/g, respectively. The main reason for high surface area (367 m²/g) of promoted M3 catalyst can be attributed to the smaller particle size of Co₃O₄ comparing to cobalt particle sizes of other catalysts. Smaller

particles cause less blockages of the pores unlike larger particles [91]. Because of the larger particle size on unpromoted M2 catalyst and because of the high cobalt loading on promoted M4 catalyst pores of MWCNT was blocked, and accordingly their surface areas were smaller comparing to surface area of promoted M3 catalyst [92].

As can be seen from TEM images of MWCNT catalysts (Figures 4.15, 4.16 and 4.17), the particles in all MWCNT based catalysts are spread on the outer and inner walls of the MWCNT. Based on TEM images, among all those catalysts, cobalt particles are not well dispersed in 10Co/MWCNT (M2), comparing to promoted M3 and M4 catalysts. The bar graph (Figure 4.31) shows that the particle size distribution of M2 catalyst is in the range of 4 - 9 nm, where the most abundant ones are 5 nm with 40 % frequency, and the particles with 4 nm with only 10 % frequency. By taking into consideration that the inner diameter of MWCNT is ± 4 nm (Chapter 4.1.1.1), it can be concluded that, the most of the particles with the size of ± 4 nm were deposited inside the tubes, and the larger particles (>4) were anchored on the outer surface of MWCNT. It can be also concluded that approximately 10% of cobalt particles were located inside the CNT channels.

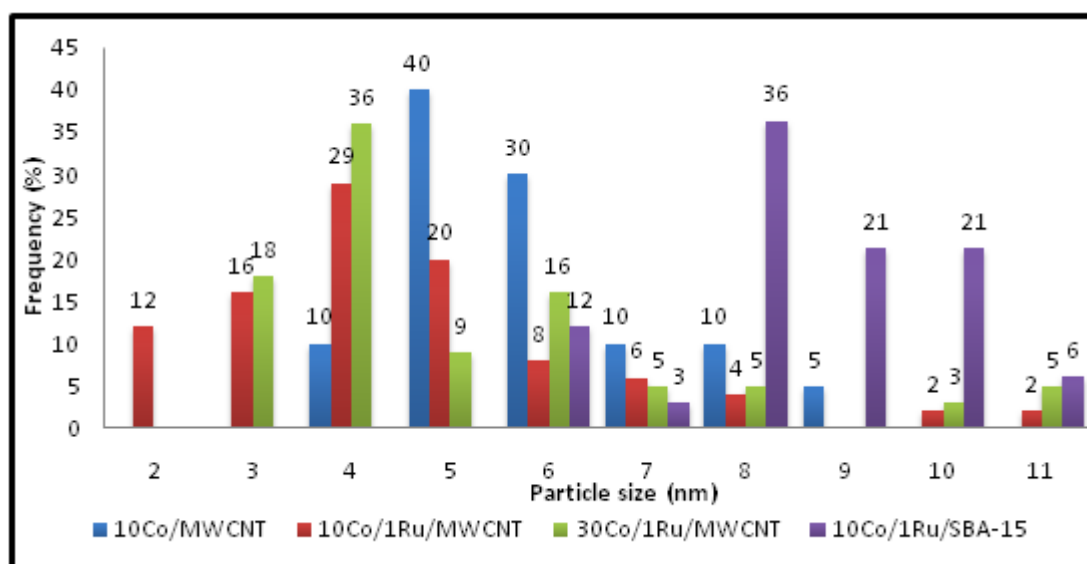


Figure 4.31: Cobalt particle size distribution in MWCNT and SBA-15 based catalysts

The smallest particle size characteristics among MWCNT based catalysts are related to 10Co/1Ru/MWCNT (M3). TEM images of promoted M3 catalyst (Figure 4.11) show that the particles are very well dispersed inside the tubes and also on the outer parameter of the walls. The distribution of the particle size can be seen from bar graph (Figure 4.31) where it shows that the particles in the range of 2-11 nm were formed in M3. The most abundant particles are in the range of 4-5 nm with 29 and 20 % frequency, respectively. Also 2 and 3 nm particles were formed with 12 and 16 % frequency, respectively. Overall percentage of the particles with size of 2 - 4 nm is around 57%. Because of such small size of the particles (2-4 nm), most of them were spread inside the MWCNT, evidenced by TEM image (Figure 4.15). Particles with size of 5-11 nm were anchored on the outer walls of the MWCNT. The effect of ruthenium was significant in dispersion and decrease of cobalt particles by breaking Co oxides apart [137].

The average particle size of cobalt in 30Co/1Ru/MWCNT (M4) increased upon increasing of cobalt loading from 10 to 30 wt%. As shown on XRD data (Table 4.5), crystallite size of Co_3O_4 increased from 11.31 to 16.26 nm, but still remaining less than unpromoted M2 catalyst, which is 18.53 nm. The main reason for increase of particle size is its agglomeration on outer walls of MWCNT [91], which can be supported by TEM images (Figure 4.16) of this catalyst. Figure 4.31 shows that the particle size distribution of M4 catalyst is in the range of 3 - 11 nm, where the most abundant ones are 3 and 4 nm with frequency of 18 and 36 %, respectively. Overall abundance of particles with 3 and 4 nm is 54 %. As inner diameter of MWCNT is ± 4 nm, it can be assumed that particles with 3 - 4 nm dispersed uniformly on the perimeter of the tube walls. Particles with size of 5-11 nm were attached on the outer surface of MWCNT (Figure 4.16). Because of the narrow inner diameter of MWCNT (± 4 nm), the growth of cobalt particles was restricted inside the tubes [91], [92]. Zhang *et al.* [94] concluded that the genesis of cobalt dispersion occurs not during the deposition of cobalt ions on CNT surface, but during decomposition of cobalt precursor, nucleation and growth of cobalt oxide crystallites. Hence, the size of cobalt crystallites in CNTs could be more affected by calcination, rather than cobalt deposition via impregnation [94].

4.2.8.2 SBA-15 based catalysts

As shown in Table 4.5, in SBA-15 based catalysts the smallest cobalt crystallite size is 8.5 nm and average cobalt cluster size is 33 nm, which is related to 10Co/SBA-15 (S2) catalyst. 10Co/1Ru/SBA-15 (S3) has mean 10.9 nm crystallite size, average particle size of 8.3 nm (in) and average cluster size of 88 nm. The largest Co_3O_4 sizes are related to 30Co/1Ru/SBA-15 (S4) where crystallite size and average cluster size of Co_3O_4 is 12.94 and 109 nm, respectively. As mentioned above, average particle size of Co_3O_4 on S2 and S4 catalyst are not measured (absence of cross section view of S2 and S4 catalysts on TEM). Table 4.5 shows that, by increasing of cobalt loading from 10 to 30 wt%, average cobalt crystallite and cluster size were increased from 10.9 to 13.7 nm, and from 88 to 109 nm, respectively [150].

After loading of 10 wt% cobalt on SBA-15 support, the surface area of SBA-15 increased from 660 to 913 m^2/g . TEM images of S2 catalyst shows that huge cobalt clusters were deposited on the outer surface of SBA-15 and were dispersed along the pores of SBA-15 by forming cobalt islands (Figure 4.19 (S2) (A, B))) [112]. Most probably these cobalt islands contributed to increase of SBA-15's surface area. It is known that metal oxides also have their own porosity which may contribute to increase of overall surface area of the catalyst. By loading of 10 and 30 wt% cobalt and 1 wt% ruthenium the surface area of SBA-15 decreased from 660 to 409.5 and 383.8 m^2/g , which belong to S3 and S4 catalysts, respectively. The drop of surface area can be due to the blocking of pores with cobalt oxide crystallites and/or partial collapse of the mesoporous structure [110], [152]. Hong *et al.* [152] suggested that decrease of surface area can be due both, to plugging silica pores with cobalt oxide crystallites and to the effect of the silica "dilution" because of the presence of cobalt species. The magnitude of surface area drop suggests, however, that pore plugging contributes more significantly to surface area decrease than silica "dilution" [152]. Khodakov *et al.* [109] observed the decrease in surface area after loading of 5 wt% cobalt via impregnation. It was attributed to clogging support pores by cobalt species, which makes them inaccessible for nitrogen adsorption. This effect was especially pronounced for narrow pore supports [61].

The XRD data (Figure 4.28) shows that the most intense and narrow peak among SBA-15 based catalysts is related to promoted S4 catalyst, next sharpest peak is related to promoted S3 catalysts. The peak with lowest intensity belongs to unpromoted S2 catalyst. This indicates the increase of the mean Co_3O_4 crystallite size when increasing the cobalt content [110]. The effect of ruthenium in SBA-15 based catalysts towards decreasing of cobalt particle size was not as significant as it was in MWCNT based catalysts. After introduction of 1 wt% ruthenium the intensity of XRD peaks of Co_3O_4 crystallites was considerably enhanced, but the size of Co_3O_4 crystallites did not change significantly. This phenomenon was observed in previous reports also [152]. The order of decrease of cobalt cluster size measured from FESEM is: S4 (109 nm) >S3 (88 nm) >S2 (33 nm), which is summarized in Table 4.5. This data is consistent with the data obtained from XRD, where the order of crystallite size decrease is: S4 (13.7 nm) >S3 (10.9 nm) >S2 (8.5 nm), respectively.

The average pore diameter of present SBA-15 was measured from TEM data (Figure 4.5), which is 5-6 nm. According to BET measurements, the average pore size of SBA-15 is 4.9 nm. This is in the range of theoretical value of type IV adsorbents (2 - 50 nm) [151]. As depicted in Table 5, the average particle size from TEM images was measured only for 10Co/1Ru/SBA-15 (S3) catalyst. The distribution of Co_3O_4 particles is shown in Figure 4.31. The bar graph shows that the particle size distribution of S3 catalyst is in the range of 6.5 -11 nm, where the most abundant one is 8.3 nm with 36 % frequency, and the particles with 6 and 7 nm with only 12 and 3% frequency. By taking into account that the average pores of SBA-15 is 5-6 nm, it can be noted that, most of the particles with the size of ± 6 nm were deposited inside the SBA-15, and the larger particles (>7) were located on the outer surface of SBA-15. As shown in TEM and FESEM images of SBA-15 based catalysts, Co_3O_4 particles were deposited in inner and outer surface of support forming different sizes of cobalt agglomerates. Khodakov *et al.* [109] concluded that the sizes of Co_3O_4 depend on the average pore diameters in mesoporous silicas; larger Co_3O_4 crystallites were found in silicas with wider pores. Later Hong *at al* [152] came to the same conclusion by identifying the larger particles in larger pores.

It can be suggested that, introduction of 1 wt% Ru actually caused the decrease of Co_3O_4 particle size. It is possible that Co_3O_4 became small enough (approximately 2-3 nm) to easily enter the SBA-15 pores and disperse deep inside the pores. Since Co_3O_4 particles could be dispersed deep inside the pores by being very small, they would not be detected by XRD. Only the particles located outside the surface could be detected by XRD. Therefore the mean size of the detected Co_3O_4 particles is high in the range of 8.5-13.7 nm. Unfortunately, because of the lack of cross section images of SBA-15 catalysts by TEM, it is not possible to see the presence of particles located inside the SBA-15 narrow channels. After impregnation with cobalt – ruthenium solution, BET surface area of SBA-15 decreased significantly, as shown in Table 4.5. The drop of surface area can be an evidence for dispersion of Co_3O_4 inside the pores. Sun *et al.* [153] did not observe any Co diffraction peak in XRD for Co/SiO₂ sample (10 wt% Co) prepared from cobalt acetate and concluded that Co should be highly dispersed on silica surface. Wang *et al.* [154] did not find any XRD diffraction peaks in calcined Co/SBA-15 catalysts prepared from cobalt acetate with cobalt loading up to 20 wt%, which was taken as evidence of the formation of nanosized Co_3O_4 clusters inside the mesopores of the SBA-15.

4.3 The Fischer-Tropsch activity of the catalysts

Catalyst activity was studied in slurry phase 200 mL autoclave reactor which is described in Chapters 3.4.3 and 3.5.1.2, respectively. The reaction conditions for FT synthesis were: P = 2 MPa, T= 220°C, stirring speed was 300 rpm and the ratio of solvent per catalyst was 50 mL per gram. The product was collected after 17 hours of reaction period and characterized in Gas Chromatograph/Mass Spectrometer (GC/MS). The chromatogram for all catalysts was until C₄₀ (APPENDIX C), based on the standard, used to obtain the qualitative and quantitative data of all products. Normal hexadecane (n-C₁₆H₃₄) was removed from data, which represents a solvent used during the reaction as an intermediate phase. Catalysts were evaluated in terms of product selectivity towards Naphtha, Kerosene and Diesel, which are in the range of C₆ to C₂₂. Remaining products were considered as wax. In commercial

applications waxes are hydrocracked to more valuable, lower chain hydrocarbons [155].

It is known that naphtha, kerosene, and diesel fractions appear in the range of C₆ to C₂₂ hydrocarbons of different structure. The naphtha consists of C₆-C₁₀. The C₉-C₁₅ represents kerosene fraction, and diesel cut contains C₁₀-C₂₂ hydrocarbons. Thereby, fraction of kerosene overlaps the fraction of naphtha, starting from C₉, fraction of diesel overlaps fraction kerosene, starting from C₁₀ and so on. Overall concentrations of all products in the range of C₈-C₄₀ and concentrations of naphtha, kerosene and diesel are shown in Table 4.6. At the same time replotted graph of products in terms of concentration versus product is shown in Figure 4.32. Gas chromatograms showed that the hydrocarbons produced from all catalysts mostly belong to light motor fuels, which are kerosene and diesel (Figures 4.32). In terms of product yield, among all catalysts, generally SBA-15 based catalysts showed better activity comparing to MWCNT based catalysts. After 17 hours of reaction period, the highest HC yield observed in 10Co/SBA-15 which is 17,765 ppm. 10 and 30 wt% Co/1Ru/SBA-15 catalysts also produced high yields of liquid hydrocarbon which are 11,668 ppm and 16,481 ppm, respectively. Among MWCNT based catalysts the best performance corresponds to 10Co/1Ru/MWCNT with HC yield of 17,125 ppm.

Table 4.6: Overall concentrations and concentrations of certain products (in ppm)

Catalyst	Overall conc. (C₈-C₄₀)	Naphtha (C₈-C₁₀)	Kerosene (C₉-C₁₅)	Diesel (C₁₀-C₂₂)	Wax (C₂₃-C₄₀)
M3	17,125	913	5614	10563	6264
M4	5,711	661	2658	3990	1391
M2	2,229	119	831	1492	698
M1	304	18	204	298	0
S3	11,668	513	3684	7047	4477
S4	16,481	1304	6014	10938	4912
S2	17,765	1477	5760	10428	6610
S1	261	18	191	254	0

The results of remaining MWCNT based catalysts are quite low which can be seen from Table 4.6 and Figure 32. In FTS, it is desired to have methane selectivity as low as possible and selectivity towards C₅₊ liquid products and waxes to be as high as possible. The kerosene yield was highest in 30Co/1Ru/SBA-15 catalyst with 6,014 ppm concentration, while second and third highest yields of kerosene are related to 10Co/SBA-15 (5,760 ppm) and 10Co/1Ru/MWCNT (5,614 ppm) catalysts, respectively. Diesel yield was the highest in 30Co/1Ru/SBA-15 with 10,938 ppm concentration. Among MWCNT based catalysts the highest diesel yield was observed in 10Co/1Ru/MWCNT with concentration of 10,563 ppm. However, among SBA-15 based catalysts the yield of wax was the highest in 10Co/SBA-15 (6,610 ppm), among MWCNT based catalysts the highest yield was observed in 10Co/1Ru/MWCNT, respectively. Figure 4.32 also shows that the yield of naphtha was quite low in all catalysts, comparing to kerosene diesel and wax. It suggests that all cobalt based catalysts were favorable towards production of high molecular weight hydrocarbons comparing to lower molecular weight ones. The performance of pure MWCNT and pure SBA-15 is obviously very low, but still there are some traces of HCs with concentrations of 304 ppm and 260 ppm, respectively. In this regard, it can be assumed that the catalyzing abilities of pure MWCNTs are greater than that of SBA-15. Eswaramoorthy *et al.* [156] demonstrated that SWNTs are good microporous materials which capable of adsorbing benzene, methanol, and other molecules and suggested that this would allow carrying out catalytic reactions in nanoscale reactors. In addition Santucci *et al.* [166] reported NO₂ and CO gas adsorption on nanotubes.

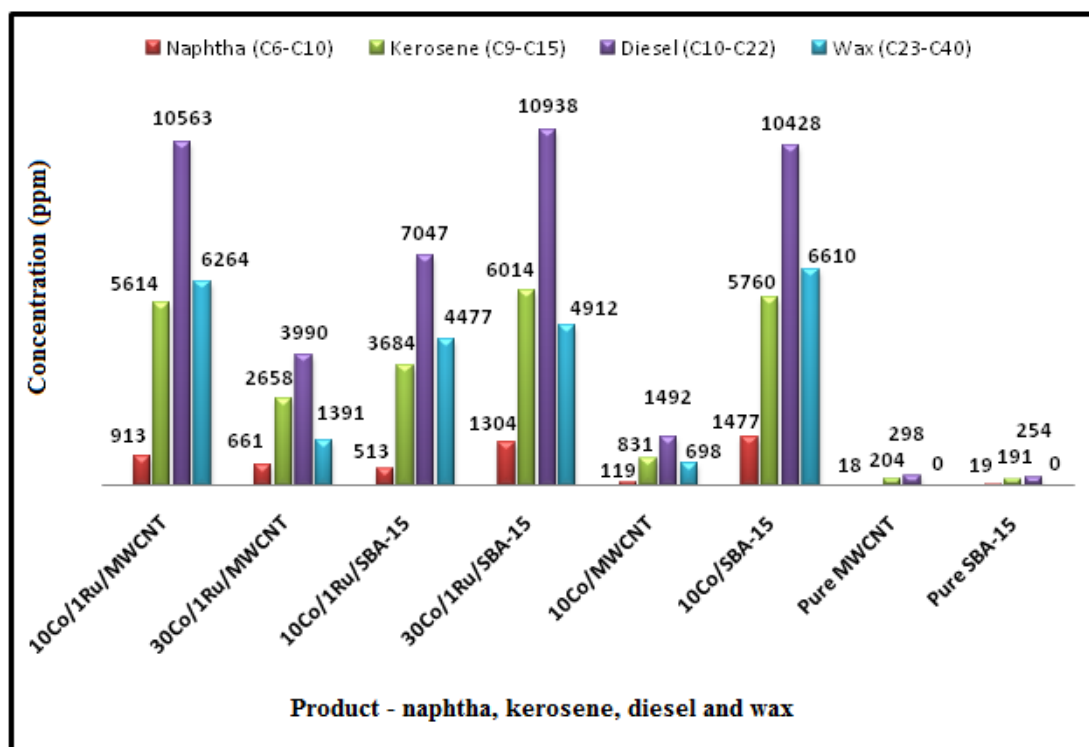


Figure 4.32: Concentration of light fuel fractions and wax

4.3.1 CH yield, and its relation to particle size and pore size

4.3.1.1 MWCNT based catalysts

The yield of hydrocarbons, their relation to particle size and pore size is depicted in Table 4.7. As shown in this table, among MWCNT based catalysts, the best performance belongs to 10Co/1Ru/MWCNT (M3). Next higher yields are 5,711 and 2,229 ppm which were produced by 30Co/1Ru/MWCNT and 10Co/MWCNT respectively. The main reason for high yield in promoted M3 (17,125 ppm) may be attributed to size of Co_3O_4 oxide, and its distribution along the support surface. The mean average crystallite size of cobalt is 12.1 nm, also particle size distribution of M3 catalyst is better comparing to M2 and M4 catalysts, which can be seen from TEM images of MWCNT based catalysts (Figures 4.15, 4.16, 4.17). However, average particle size of cobalt oxide in inner and outer walls is 3.4 and 4.1 nm,

respectively. Nevertheless, a number of researchers observed the drop in FTS activity as a size of CNT supported cobalt particles became less than 10 nm [93]. Cobalt nanoparticles are generally considered as an active phases for CO hydrogenation [94], [1]. Bezemer *et al.* [103] found that the maximum concentration of surface Co^0 sites and FTS activity are achieved with catalyst particle sizes less than 10 nm on carbon nanofiber supports. Khodakov reported that cobalt metal particles in the activated catalysts should not be smaller than an optimum size of 6-8 nm [157]. *et al.* [105] studied the activity of FT process using CNT supported cobalt catalyst at 1 bar and 220°C. It was found that the activity decreased rapidly when the catalysts with cobalt particle sizes smaller than 6 nm was used. However, the catalytic performance in the FT reaction was independent of cobalt particle size for catalysts larger than 6 nm.

In present case, in all MWCNT based catalysts, particle size, measured from TEM images are less than 5 nm, both in inner and outer surface of the tubes. Moreover, the addition of 1 wt% ruthenium facilitated in decreasing the size of Co_3O_4 particles, as can be seen from Table 4.5. Also ruthenium addition increased the activity of 10 wt % cobalt catalyst, most probably by shifting reduction temperature of cobalt to lower temperatures. However, Breejen *et al.* [158] reported the opposite results to Khodakov [157] and Bezemer [103], [105], where by the Co/CNF catalyst with cobalt particle size of 4.7 ± 0.2 nm is the most active catalyst in FT reaction at operating pressure and temperature of 1 bar and 220°C, respectively.

The particle size is not the only attribute that affect the FTS activity [159]. As can be seen from TEM images of MWCNT based catalysts, (Figures 4.15, 4.16, 4.17) the particles are mostly located inside the MWCNT. It appears that, the particles located inside the MWCNT and particle size itself influence the FTS activity [93], [103], [159]. As mentioned above, the growth of cobalt particle sizes was restricted inside the tubes. [91], [92]. Trepanier suggested that, the particle's confinement within CNT may be more important than the particle size effect for the FTS activity. In their work they observed that the methane selectivity reduced by increasing average cobalt cluster size from 3 nm to 10 nm, and C_{5+} selectivity increased by increasing average cobalt particle size from 3 to 10 nm.

The second reason for better yield may be attributed to a larger average pore size of M3 catalyst among other MWCNT based catalysts, which is 10.08 nm. Khodakov *et al.* [109] observed that cobalt species located in narrow pore silicas are much less active in Fischer-Tropsch synthesis and produce methane with selectivities higher than larger cobalt particles in the wide pore supports. In case with unpromoted M2 catalyst, the passive FT activity may be attributed to a partially reduced cobalt species (Figure 4.29) which are unable to fully convert CO to a desirable products. The cobalt particle size in M4 catalyst is also very small (Table 4.7), which is consistent with previous reports [157], [105]. Reza *et al.* [160] reported that the deposition of the metal particles inside the nanotube with narrow pore structure resulted in smaller metal particle sizes and better dispersion due to the physical restriction imposed by the CNT pores.

4.3.1.2 SBA-15 based catalysts

Unlike MWCNT catalysts, the highest yield in SBA-15 based catalysts is related to unpromoted S2 catalyst, which is 17,765 ppm. The second and third yields are related to S4 and S3, which are 16,481 and 11,668 ppm respectively. Unfortunately, because of the lack of cross section images of SBA-15 catalysts by TEM, it is not possible to see the presence of particles located inside the SBA-15 narrow channels. Only inner particle size of promoted S3 catalyst (8.3 nm) was measured from TEM histograms. As can be seen from Table 4.7, addition of 1wt % ruthenium did not make a significant effect of FT activity of the catalysts, but only facilitated in shifting the cobalt oxide reducibility to lower temperatures, which can be seen from Figure 4.30. Khodakov *et al.* [109] found that the sizes of supported Co_3O_4 crystallites are controlled by support pore diameters in mesoporous silicas. Larger pore diameters lead to larger Co_3O_4 particles, as larger pore silicas contain larger, and thus easier to reduce Co_3O_4 crystallites. In present work average pore diameter of SBA-15 is 5-6 nm, which is larger than MWCNT which possesses ± 4 nm of average pore size. With this respect in can be assumed that Co_3O_4 particles were dispersed inside the SBA-15 better, comparing to the Co_3O_4 particles on MWCNT. Location of active cobalt particles inside of the pores of the support is important, since the pores are

considered as nanoreactors where FT reaction takes place. Generally saying, because of the larger pore diameter of SBA-15 which was measured from TEM histograms (5-6 nm) comparing to MWCNT ± 4 , more Co_3O_4 particles were deposited inside the pores of SBA-15 which lead to higher product yield in all SBA-15 based catalysts unlike MWCNT based catalysts.

Table 4.7: Relation of product yield to cobalt particle size and pore size of the support

Catalysts	XRD crystallite size (nm)		TEM average particle size (nm)		Average pore size \AA (nm)	Overall conc. (ppm)
	sharpest peak	average	“in”	“out”		
M1	-	-	-	-	11.09	304
M2	18.53	18.7	4.8	5.1	8.88	2,229
M3	11.31	12.1	3.4	4.1	10.08	17,125
M4	16.26	18.5	4.3	5.0	9.67	5,711
S1	-	-	-	-	4.95	261
S2	8.5	8.5	n.d.	n.d.	6.86	17,765
S3	8.52	10.9	8.3	n.d.	6.83	11,668
S4	12.94	13.7	n.d.	n.d.	6.14	16,481

4.3.2 Analysis of CO conversion and Selectivity

The ability to convert the reactants into desired products is a critical characteristic of any catalysts in terms of catalyst activity. In present work semi batch reactor system was used which was not connected to online GC. Unfortunately, the sampling of CO in the inlet and outlet of the reactor was not carried out due to the limitation of equipment (GC). However, total moles of consumed CO under 20 bars were calculated using ideal gas equation, which is described in Chapter 3.5.2.1 and APPENDIX B. Before calculating the moles of spent CO, total volume of consumed feed gas ($\text{CO}+2\text{H}_2$) for each catalyst at pressure of 20 bars was identified by using the data generated via software “Top View”. The calculation steps of volume identification are shown in Chapter 3.5.2.1 and APPENDIX B.

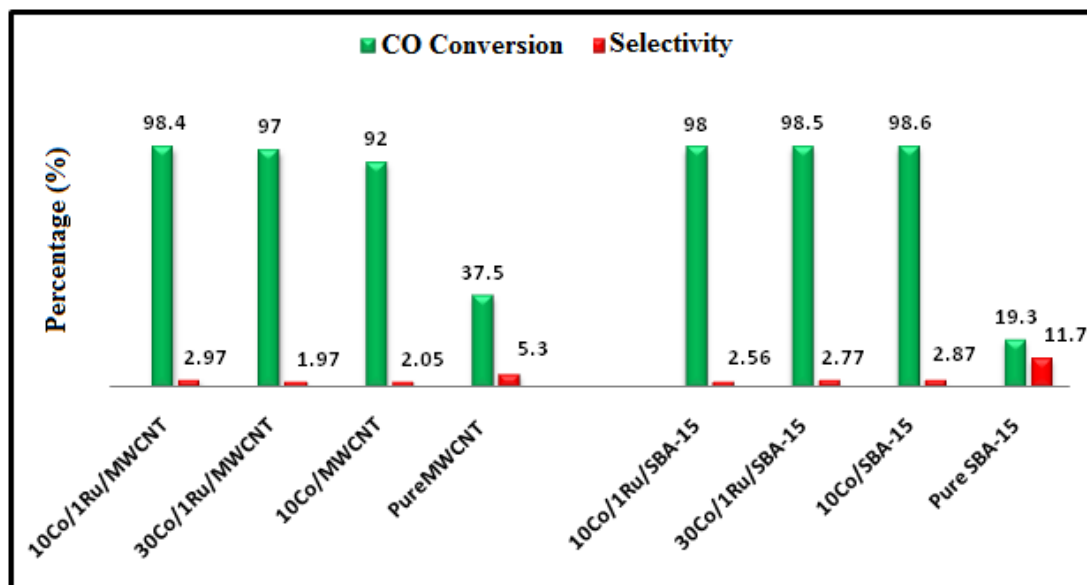


Figure 4.33: Percentage of CO conversion and C₈₊ selectivity

Figure 4.33 represents the graph of CO conversion and its comparison with C₈₊ selectivity. As shown in Figure 4.33, the catalysts containing active metals have a very high CO conversion in the range of 92% to 99%. The SBA-15 based catalysts have better CO conversion compared to MWCNT based catalysts, which is 98% and above (10Co/SBA-15 with 98.6%). In terms of selectivity towards liquid hydrocarbons, the SBA-15 based catalysts produced higher selectivities which were 2.55, 2.77, and 2.84%, compared to MWCNT based catalysts. In fact, the selectivity towards C₈-C₄₀ is almost the same for all catalysts, also the yield of C₈-C₄₀ is very low for all catalysts. Promoted and unpromoted cobalt catalysts showed similar percentage of CO conversion. The lowest CO conversion (92%) is observed in unpromoted M2 catalyst, which is probably due to partially reduced cobalt particles and smaller pore volume of the catalyst which is 8.88 nm. M3 and S2 catalysts have relatively higher pore sizes which are 10.08 and 6.86 nm, respectively (Table 4.7). In higher diameter pores most of the cobalt particles will be located inside. Reaction intermediates inside the pores can contact with cobalt particles for longer time because of the confinement effects, which promotes the growth of heavy hydrocarbons [179]. Besides, electron deficiency inside the pores can enhance the CO dissociation, further resulting in production of heavier hydrocarbons. At the same time, diffusion limitations in the smaller pores of catalysts may lead to decreased C₅₊

selectivity [179]. Smaller pore leads to feed gas diffusion limitations inside the pores [161]. Trepanier *et al.* [91] stated that reduction of ruthenium oxide occurs at temperatures lower than that of cobalt. Reduced ruthenium oxide contributes the reduction of cobalt oxides by spillover of hydrogen from ruthenium to the cobalt oxide. Also ruthenium enhances the reduction of smaller cobalt species that may not be reduced in unpromoted catalysts. Accordingly ruthenium contributes to the increase of active surface Co^0 sites available for FT reaction, and hence enhances the percentage of CO conversion and the FTS rate. Addition of ruthenium to MWCNT catalysts improved catalysts' FT activity, which is depicted in Table 4.7. Unlike the MWCNT based catalysts, addition of 1 wt% ruthenium to SBA-15 based catalysts did not have significant effect towards percentage of CO conversion, but only facilitated in shifting the cobalt oxide reducibility to lower temperatures. It is believed that the addition of ruthenium to cobalt catalysts decreases the amount of Co^{2+} and Co^{3+} species and leads to the enrichment of more cobalt active sites at the surface of supports. The dispersed cobalt active sites are available for CO adsorption. It is also believed that the bridge-type CO is more easily formed on large Co particles, as, is much more active than linear type CO, because it has a weaker C-O bond and thus can be more easily dissociated to carbon and oxygen, which is one of the crucial processes in FTS [113]. Qin *et al.* [111] applied the ruthenium metal as a promoter to Co/SBA-15 catalyst, prepared via incipient wetness impregnation method. With increasing of ruthenium loading ($0.05 < 0.1 < 0.5$ wt%) the activity of FT synthesis increased due to increased reducibility of the catalyst and the synergistic effect of ruthenium and cobalt. Meanwhile, the higher C_{5+} hydrocarbon selectivity and the lower methane selectivity were obtained with high ruthenium loading, also attributed to the higher catalyst reducibility. In addition to the contribution towards reduction, ruthenium was found to inhibit catalyst deactivation, appearance of additional sites of hydrogen activation and increase in the intrinsic reactivity of surface sites [111].

In present studies cobalt particle size in both type of catalysts are smaller than 10 nm which can be seen from Table 4.7. As described above, particles less than 10 nm are more selective to gaseous hydrocarbons and methane, rather than C_{5+}

hydrocarbons. These results are consistent with findings of other researchers as well [105], [157], [177], [178]. They found that FT results were independent from Co particle size for catalysts with sizes larger than 6 nm 8 nm. Decrease of TOF and selectivity toward C₅₊ were observed with decreasing of particle size from 16 to 2.6 nm. Regardless high CO conversion, the selectivity of the catalyst towards C₅₊ is very low. Due to the high CO conversion and low yield of liquid hydrocarbon products, it is assumed that the selectivity to methane and light gaseous hydrocarbons is high in this work comparing to liquid CH.

Hosseini *et al.* [137] reported that the selectivity to the heavier hydrocarbons decreased with decreasing of catalyst pore volume, so that the less effective mass transfer can be realized in the catalysts with small pores. Some researchers relate lower selectivity to the particle size effect [162]. It was proposed that, adsorption strength of carbon containing species would decrease with reduction of metal particle size. It is believed that in FTS the larger cobalt particles are more selective to high molecular weight hydrocarbons and smaller particles are selective to methane and light gases [163]. Zaman *et al.* [161] observed that the CH₄ selectivity was the highest and the C₅₊ selectivity was the lowest in the cobalt catalysts, supported on high surface area activated carbon (927 m²/g). They attributed this to the high specific surface area of activated carbon, leading to small cobalt crystallite sizes, which may enhance formation of methane. Bezemer *et al.* [105] also reported that the catalysts with cobalt particle sizes smaller than 5 nm have progressively high selectivity for methane. For catalysts with high methane selectivities, lower chain growth probabilities were found resulting in an even lower selectivity towards heavy weight hydrocarbons. The formation of methane indicates that dissociated hydrogen is abundantly present on the catalyst surface. The higher selectivity to methane might also indicate a lower abundance of sites active for chain growth, resulting in more carbon species at the surface that become fully hydrogenated to methane [105]. Bezemer also found that turnover frequency (TOF) was constant for the samples with cobalt particle sizes larger than 8 nm, while it decreased by decreasing the sizes of cobalt from 8 nm. Trepanier *et al.* [93] observed decrease in FTS rate and C₅₊

selectivity as cobalt particles decreased to < 10 nm. Accordingly, rapid increase in methane selectivity was observed when the cobalt particle size was less than 10 nm.

Mass transfer limitations for carbon monoxide and hydrocarbons in catalyst pores, pore filling and condensation of heavier hydrocarbons, different adsorption properties of metal particles located in narrow and wide pores are often employed to explain the effect of pore sizes on FT reaction rates and selectivities. Anderson *et al.* [164] attributed the observed increase in methane selectivity with decreasing average pore diameter to mass transport phenomenon. It was suggested that greater rate of diffusion of hydrogen inside the pores filled with liquid products compared to that of carbon monoxide caused an increase in H₂/CO in catalyst pores and thus a shift towards formation of lighter hydrocarbons. Khodakov *et al.* [109] observed high methane selectivity on smaller cobalt particles located in narrow pore silicas. Methane selectivity dropped from 30 to 15% as silica pore size increased from 2 to 10 nm. This phenomenon was attributed to the presence of either unreduced cobalt species or the small cobalt particles which produce higher relative amounts of methane than large cobalt particles. Three suppositions in research done by Khodakov *et al.* [109] have been mentioned to explain high methane selectivity in FT synthesis over small cobalt particles. At first, high methane selectivity was attributed to the sites of weak carbon monoxide adsorption. It is generally assumed that heavier hydrocarbons are favored when carbon monoxide and intermediates are strongly adsorbed by metal sites. Secondly, Reuel and Bartholomew [165] assigned high methane selectivity observed on well dispersed low loading cobalt catalysts to the presence of stable unreduced oxide phases capable of catalyzing water-gas shift reaction: $\text{CO} + \text{H}_2\text{O} \rightarrow \text{CO}_2 + \text{H}_2$, and thereby increasing H₂/CO ratio at the catalyst surface. The water-gas shift reaction causes the emission of measurable amounts of carbon dioxide which may contribute to the formation of methane. Thirdly, diffusion limitation for carbon monoxide in catalyst pores could also increase H₂/CO ratio in catalyst pore and thus methane selectivities [164]. Xiong *et al.* [112] observed the performance of small and wide pore size catalysts, where wide pore size catalysts exhibited much more CO adsorption sites, both, linear and bridge type at room

temperature. Accordingly the larger cobalt cluster sizes gave to the enhancement of bridge-type CO during FTS.

In current work, based on the characterization results of the MWCNT and SBA-15 catalysts it was found that the metal particles located in the supports have a cobalt particle size smaller than 6 nm. At the same time, the average pore size of the supports is very narrow, which are ± 4 and 5-6 nm for MWCNT and SBA-15, respectively. Narrow pores lead to the formation of smaller cobalt particles. Accordingly smaller particles lead to high yield of gaseous products rather than liquid hydrocarbons [109], [164]. These findings are also coincident with results of other researchers. In their work it was found that, the support porosity higher than 10 nm displayed high CO conversion and high C₅₊ selectivity. At the same time, CH₄ and CO₂ selectivity was higher in the pores smaller than 10 nm [112], [169], [170].

As shown in Figures 4.29 and 4.30 unpromoted M2 and S2 catalysts contain unreduced cobalt species. For M2 catalyst the peaks in 443 and 490°C correspond to partially reduced cobalt species. For S2 catalyst broad but not intense peaks in 688 and 799 correspond to unreduced cobalt species which may have a strong interaction with silica based support [110]. As described by Reuel and Bartholomew [165], the presence of unreduced cobalt species may contribute to the occurrence of water-gas shift reaction which facilitates to the formation of methane. It can be assumed that, in case of unpromoted M2 and S2 catalysts the formation of methane was higher, compared to all promoted catalysts due to the presence of unreduced cobalt species. Since water-gas shift reaction causes formation of CO₂ as well, accordingly formation of CO₂ was higher in unpromoted M2 and S2 catalysts.

CHAPTER 5

CONCLUSION AND RECOMMENDATIONS

5.1 Conclusion

The addition of 1 wt% ruthenium onto MWCNT and SBA-15 based catalysts caused significant decrease of the reduction temperature of cobalt oxide (Co_3O_4) species. The effect of ruthenium towards decreasing of cobalt particle size and distribution of cobalt particles inside and outside of the MWCNT based catalysts were also significant. By addition of ruthenium, the average size of the particles, located inside the MWCNT decreased from 4.8 to 3.4 nm.

Because of the narrow inner diameter of MWCNT (± 4 nm), the growth of cobalt particles was restricted inside the tubes. On the other hand, because of the lack of cross section images of 10Co/SBA-15 (S2) and 30Co/1Ru/SBA-15 (S4) catalysts by TEM, it was impossible to observe the presence of particles located inside the SBA-15 narrow channels. Therefore the particle size distribution of 10Co/SBA-15 (S2) and 30Co/1Ru/SBA-15 (S4) catalysts was not measured. Only inner average particle size of Ru promoted 10Co/1Ru/SBA-15 (S3) catalyst was measured from TEM histograms, which is 8.3 nm. Using TEM data, the average pore diameter of SBA-15 is 5-6 nm, thus most of the particles with size of ± 6 nm were deposited inside the SBA-15 based catalysts and the larger particles (>7) were located on the outer surface of SBA-15 based catalysts. It can be suggested that the introduction of 1 wt% ruthenium in 10Co/1Ru/SBA-15 (S3) and 30Co/1Ru/SA-15 (S4) catalysts decreased the Co_3O_4 particle size. Due to the smaller size of the Co_3O_4 particles (approximately 2-3 nm), the particles were able to penetrate and disperse deep inside the SBA-15 pores and were not detected by XRD. Only the particles located outside the surface could be detected by XRD. Therefore the mean size of the detected Co_3O_4 particles is

high in the range of 8.5-13.7 nm. After impregnation with cobalt–ruthenium solution, the surface area of 10Co/1Ru/SBA-15 (S3) and 30Co/1Ru/SA-15 (S4) decreased significantly, which are 409 and 383 m²/g, respectively, as compared to 10Co/SBA-15 (S2) which is 913 m²/g (Table 4.5). The drop of surface area can be an evidence for the dispersion of Co₃O₄ inside the pores.

In terms of liquid product yield, among all catalysts, generally SBA-15 based catalysts showed better activity comparing to MWCNT based catalysts. After 17 hours of reaction period, the liquid HC yield observed using unpromoted S2 catalyst, was 17,765 ppm compared to S3 and S4 catalyst which produced 11,668 ppm and 16,481 ppm liquid HC respectively. Experimental results show that the larger pore size of the S2 catalyst among other SBA-15 based catalysts which is 6.86 nm seems to be one of the factors that affects liquid HC yield. Addition of 1 wt% ruthenium did not make a significant effect on FT activity of the catalysts, but only facilitated in shifting the cobalt oxide reducibility to lower temperatures.

Among MWCNT based catalysts the best performance catalyst is the Ru promoted M3 catalyst which produced HC yield of 17,125 ppm. One of the reasons may be attributed to the smaller size of Co₃O₄ particle and its better distribution along the support surface. The second reason for better yield may be due to the larger average pore size of M3 catalyst among other MWCNT based catalysts which is 10.08 nm. The CO conversion using promoted and unpromoted cobalt catalysts was in the range of 92-99%. The lowest CO conversion (92%) is observed using unpromoted M2 catalyst, which is probably due to the partially reduced cobalt particles. The selectivity towards C₈-C₄₀ is almost the same for all catalysts which is 2-3%. However, the yield of C₈-C₄₀ liquid HC is very low. The main reasons for such low liquid HC yield may be due to the following:

- The narrow pores of both MWCNT and SBA-15 supports, which are ±4 and 5-6 nm respectively.
- The size of the cobalt particles which is smaller than 10 nm (MWCNT based catalysts in the range of 3.4-5 nm, and SBA-15 based catalysts in the range of approximately 5-6 nm).

Smaller pore leads to the liquid diffusion limitations inside the pores. Lower selectivity is also attributed to the particle size effect. Based on the characterization results of the MWCNT and SBA-15 catalysts it was found that the metal particles located in the supports have a cobalt particle size smaller than 6 nm. At the same time, the average pore size of the supports is very narrow, which are ± 4 and 5-6 nm for MWCNT and SBA-15, respectively. Narrow pores lead to the formation of smaller cobalt particles. Accordingly smaller particles lead to high yield of gaseous products rather than liquid HCs.

According to FT reaction results, only a few liquid HCs were produced (about 3 wt%) in 200 ml autoclave reactor, while having almost 99% of CO conversion in all cobalt containing catalysts. Unfortunately, due to unavailability of the gas chromatograph (GC), it was not possible to quantify the composition of the gaseous product in the reactor during the reaction period. Based on the CO conversion and selectivity results, it can be deduced that most of the synthesis gas (CO +H₂) was converted into either methane or lower chain gaseous hydrocarbons (<C₈).

It can be assumed that, in case of unpromoted M2 and S2 catalysts the formation of methane was higher, compared to all promoted catalysts due to the presence of unreduced cobalt species. Since water-gas shift reaction causes formation of CO₂ as well, accordingly formation of CO₂ could be higher in unpromoted M2 and S2 catalysts.

5.2 Recommendations

In this study it was found that the pore size affects the particle size of the active metal and selectivity. Therefore, it will be interesting to study the effect of pore size of the MWCNTs and SBA-15 based catalyst on the physical and chemical properties of the Co-based catalyst.

It is further recommended to study the effect of promoter by loading different concentrations of ruthenium oxide.

On the activity studies, the catalyst should be studied in a continuous flow slurry phase reactor connected to an online gas chromatograph. The reactor set-up allows researchers to perform kinetic studies. In addition it is preferable to reduce the catalyst in situ to avoid deactivation of the catalyst during transferring the reduced catalyst to the reactor. In present work, the RPM during the reaction period was 300.

It will be also interesting to test the catalysts in higher RPM than 300. Higher RPM may contribute to better mass exchange between the catalyst and feed gas.

It is recommended to apply different method such as deposition-precipitation in order to prepare SBA-15 based FT catalyst.

Different types of ruthenium salts can be tried rather than acetylacetonate, for example ruthenium (III) nitrate, since nitrate ions are easily tend to decompose in distilled water.

REFERENCES

- [1] A. P. Steynberg, M. E. Dry “Fischer-Tropsch Technology” (2004)
- [2] A. Y. Khodakov, W. Chu, P Fongarland “Advances in the Development of Novel Cobalt Fischer-Tropsch Catalysts for Synthesis of Long-Chain Hydrocarbons and Clean Fuels” *Chemical Reviews*, vol. 107, pp. 1692-1744, 2007
- [3] M. E. Dry, “The Fischer-Tropsch process: 1950-2000,” *Catalysis Today*, vol .71, pp. 227-241, 2002
- [4] H. Schulz “Short history and present trends of Fischer-Tropsch synthesis” *Applied Catalysis A: General*. 186, pp. 3-12, 1999
- [5] Sasol GTL Brochure (www.sasol.com)
- [6] W. D. Deckwer, “F-T process alternatives hold promise,” *Oil and Gas Journal*, pp. 198-213, 1980.
- [7] R. J. Farrauto, C. H. Bartholomew, “Fundamentals of Industrial Catalytic Processes”, *Blackie academic & Professional* 1998
- [8] W. Li, *et al.*, "Preparation and characterization of multiwalled carbon nanotube-supported platinum for cathode catalysts of direct methanol fuel cells," *The Journal of Physical Chemistry B*, vol. 107, pp. 6292-6299, 2003.
- [9] R. C. Reuel and C. H. Bartholomew, "Effects of support and dispersion on the CO hydrogenation activity/selectivity properties of cobalt," *Journal of Catalysis*, vol. 85, pp. 78-88, 1984.
- [10] D. Yin, *et al.*, "Mesoporous HMS molecular sieves supported cobalt catalysts for Fischer–Tropsch synthesis," *Microporous and mesoporous materials*, vol. 47, pp. 15-24, 2001.
- [11] P. Serp, *et al.*, "Carbon nanotubes and nanofibers in catalysis," *Applied Catalysis A: General*, vol. 253, pp. 337-358, 2003.

- [12] D. Zhao, *et al.*, "Triblock copolymer syntheses of mesoporous silica with periodic 50 to 300 angstrom pores," *science*, vol. 279, pp. 548-552, 1998.
- [13] J. A. Moulijn, M. Makkee, A. V. Diepen "Chemical Process Technology" 2001
- [14] M. Zaman, *et al.*, "Fischer-Tropsch synthesis over cobalt dispersed on carbon nanotubes based supports and activated carbon," *Fuel processing technology*, vol. 90, pp. 1214-1219, 2009.
- [15] A. Kogelbauer, *et al.*, "Ruthenium Promotion of Co/Al₂O₃ Fischer-Tropsch Catalysts," *Journal of Catalysis*, vol. 160, pp. 125-133, 1996.
- [16] T. Wang, *et al.*, "Slurry Reactors for Gas-to-Liquid Processes: A Review" *Ind. Eng. Chem. Res.* 2007, 46, 5824-5847
- [17] B. Jager, *et al.*, "Advances in Low Temperature Fischer-Tropsch Synthesis". *Catalysis Today*, vol. 23, 17-28. 1995.
- [18] B. Gandhi *et al.*, "Hydrodynamic Behavior of Slurry Bubble Column at High Solids Concentrations," *Powder Technology*, 103, 1999.
- [19] www.scribd.com/doc/3825160/Gas-to-Liquids-GTL-Technology
- [20] T. Fleisch, R. A. Sills, M. D. Briscoe, *Journal of Natural Gas Chemistry*. 11
- [21] A. C. Vosloo, *Fuel Process Technology*. 71, 149, 2001.
- [22] M. E. Dry *et al.* , *Encyclopedia of Catalysis*, vol. 3, Wiley, pp. 347, 2003.
- [23] www.en.wikipedia.org/wiki/Catalysis#Homogeneous_catalysts
- [24] A. Behr "Organometallic Compounds and Homogeneous Catalysis," *Encyclopedia of Industrial Chemistry*, 2002.
- [25] Masel *et al.* , "Chemical Kinetics and Catalysis," *Wiley-Inter science*, New York, 2001. ISBN 0471241970.
- [26] Brown *et al.*, "Chemistry" The central science Eighth Edition
- [27] Fischer, F.; Tropsch, H. *Brennst. Chemistry*, 4, 276. 1923.
- [28] Fischer, F.; Tropsch, H. *Brennst. Chemistry*, 7, 97. 1926.

- [29] Fischer, F.; Tropsch, H. *Ber. Dtsch. Chem. Ges.* 1926, 59, 830
- [30] Van Dyk, J. C.; Keyser, M. J.; Coertzen, M. *Int. Journal of Coal Geology.* 65 (3-4), 243. 2006,
- [31] Bartholomew, C. H. AIChE Spring Meeting, New Orleans, LA, 2003; paper 83b
- [32] R. Reuel and C. Bartholomew, *Journal of Catalysis*, vol. 85, pp. 63, 1984.
- [33] H. Shi and K. Jacobi, *Surface Science*, vol. 331, pp. 289-294, 1994
- [34] D.E. Jiang and E.A. Carter, *Surface Science*, vol. 547, pp. 85-90, 2003.
- [35] D. Klinke and L.J. Broadbelt *Surface Science*, vol. 429 pp. 160-177, 1999.
- [36] M. Watanabe and P. Wissmann, *Catalysis. Lett.*, vol. 7 pp. 15. 1990.
- [37] G. Wedler, *Chem.- Ing.- Techn.*, vol. 47 , pp. 1005, 1975.
- [38] H. Schulz, *Erdol und Kohle*, vol. 30, 123, 1977.
- [39] U. Roland *et al.*, *Journal of Molecular Catalysis. A*, vol. 127, 61, 1997.
- [40] G. Blyholder, *Journal of Physical Chemistry*, vol. 68, pp. 2772, 1964.
- [41] R. Hoffman, *Rev. Mod Phys.*, vol. 60, 601, 1988.
- [42] M. A. Van Daelen *et al.*, *Chem Phys, Lett.*, 226, 100, 1994.
- [43] B. Hammer *et al.*, *Phys. Rev.lett.*, 76, 2141, 1996.
- [44] R. Eischens and A. Pliskin, *Adv. Catal.*, 10, 1, 1958.
- [45] J. Lahtinen *et al.*, *Surface Science*, vol. 448, pp. 269-278, 2000.
- [46] G. Michalik, *Surface Science*, vol. 129, pp. 92, 1983.
- [47] S. D. Kevan *et al.*, *Phys. Rev. Lett.*, vol. 46, pp. 1629, 1981.
- [48] S. Sung *et al.*, *Journal of American Chemical Society*, vol. 107, pp. 578 (1985).
- [49] Y. Morikawa *et al.*, *Surface Science*, vol. 386, pp. 67. 1987
- [50] M. Kaminsky *et al.*, *Journal of American Chemical Society*, vol. 108 pp. 1315, 1986.

- [51] H. Yamasaki, Y. Kobori, S. Naito, T. Onishi, and K. Tamaru, *Journal of Chemical Society, Faraday Trans 1*. Vol. 77, 2913, 1981.
- [52] G. A. Somorjai *et al.*, *Journal of Physical Chemistry*, vol. 92, pp. 973, 1988.
- [53] C.J. Wang and J.G. Ekerdt, *Journal of Catalysis*, vol. 86, pp. 239, 1984.
- [54] R. Ugo, *Catal. Rev.- Sci. Eng.*, vol. 11, pp. 225, 1975.
- [55] P. M. Maitlis, H. C. Long, R. Quyoum, M.L. Tumer, and Z. -Q. Whang, *Journal of Chemical Society, Chemical Communications*. 1, 1996.
- [56] O. Malan, J. Louw, and L. Ferreira, *Brennstoff-Chem.*, 42 (1961) 209.
- [57] H.H. Storch, N. Golumbic, and R.B. Anderson, *The Fischer-Tropsch and Related Synthesis*, John Wiley & Sons, New York, 1951.
- [58] H. Pichler, and H. Shulz, *Chem.- Ing. Techn.*, 42 (1970) 1162.
- [59] M. R. Beychok, "Coal gasification and the Phenosolvan process," *American Chemical Society 168th National Meeting*, Atlantic City, September 1974
- [60] A. de Klerk, "Hydrotreating in a Fischer-Tropsch refinery," *2nd Sub-Saharan Africa Catalyst Symposium*, Swakopmund, Namibia 5-7 Nov. 2001.
- [61] J. Stell Worldwide catalyst report, *Oil Gas Journal* 99:41, pp. 56-76, 2001.
- [62] J. C. Hoogendoorn *et al.*, Sasol: world's largest oil-from-coal plant. *British Chemical Engineering*, pp. 238-244, 308-312, 368-373, 418-419, 1957
- [63] M. E. Dry, "Sasol's Fischer-Tropsch experience," *Hydrocarbon Process* August, pp. 121-124, 1982.
- [64] M. E. Dry, "Chemicals produced in a commercial Fischer-Tropsch process," *Industrial chemicals via C₁ Processes*, *ACS Symp. Ser.*, 328, 18-33. 1987
- [65] P. C. Keith "Gasoline from Natural gas," *Oil Gas Journal*, vol.1, Jun. pp. 102-112. 1946.
- [66] M. L. Kastens, L.L. Hirst and R.G. Dressier, an American Fischer-Tropsch plant. *Ind. Ehg. Chem*, 44:3, pp. 450-466. 1952.

- [67] M. D. Schlesinger *et al.*, Chemicals from Fischer-Tropsch synthesis, *Ind. Eng. Chem* 64:6, 1322-1326, 1954.
- [68] J. Meintjes, Sasol 1950-1975, Tafelberg Cape town, 1975.
- [69] M. E. Dry, in: J. R. Anderson, M. Boudart (Eds.), *Catalysis Science and Technology*, Vol. 1, Springer, Berlin, p. 159, 1981.
- [70] H. Schulz, J. H. Cronjé, Fischer–Tropsch-Synthese, in: Ullmanns Enzyklopädie der technischen Chemie, 4th ed., vol. 14, Verlag Chemie, Weinheim, p. 329, 1977.
- [71] A. N. Stranges, “Germany’s Synthetic Fuel industry 1927-45”, Presentation at AIChE 2003, New Orleans, LA. (www.fischertropsch.org)
- [72] N. R. Golumbic, Review of Fischer-Tropsch and Related Processes for Synthetic Liquid Fuel Production, Information circular, 1947 (www.fischertropsch.org).
- [73] H. Pichler, O. Roelen, F. Schnur, W. Rottig, H. Kölbel, Kohlenoxidhydrierung, in: Ullmanns Enzyklopädie der technischen Chemie, 3rd edition, vol. 9, Urban a. Schwarzenberg München-Berlin, 1957, p. 685.
- [74] F. Fischer, K. Meyer, *Brennstoff-Chem.* 12, 225, 1931.
- [75] R. J. Farrauto, C. H. Bartholomew “Fundamentals of Industrial Catalytic Processes,” *Blackie academic & Professional*, pp. 59-64. 1998.
- [76] M. J. Baird, R. R. Schehl, and W.P. Haynes, F-T processes investigated at the Pittsburgh Energy Technology Center since 1944, *Ind. Engng. Chem. Prod. Res. Dev.*, vol. 19, pp. 175-191, 1980.
- [77] M. E. Dry, *Applied Catalysis A: General*, vol. 138, p. 319. 1996.
- [78] H. Kölbel, P. Ackermann, F. Engelhart, *Erdöl u. Kohle* 9, 153, 225, 303, 1956
- [79] R. L. Espinoza, A. P. Steynberg, B. Jager, A. C. Vosloo, *Applied Catalysis. A: General.* vol. 186, p. 13. 1999.

- [80] C. M. Eidt, R. F. Bauman, B. Eisenberg, J. M. Hochman, G. C. Lahn, in: *Proceedings of the 14th World Petroleum Congress*, Wiley, New York, vol. 1, p. 249, John Wiley and Sons, UK, 1994.
- [81] B. Jager, M. E. Dry, T. Shingles, A. P. Steynberg, *Catal. Lett.*, 7, 293, 1990.
- [82] J. Tang, A. Matsushita, T. Tikegawa, M. Yudusaka, S. Bandow, S. Ijima, *Mater. Res. Soc. Symp. Proc.* 593, 2000.
- [83] J. Garcia, H.T. Gomes, P. Serp, P. Kalck, J.L. Figueiredo and J.L. Faria, *Catalysis Today* 102–103, p. 101, 2005.
- [84] H. T. Gomes, P. V. Samant, Ph. Serp, Ph. Kalck, J. L. Figueiredo and J. L. Faria, *Applied Catalysis B*, vol. 54, p. 175, 2004.
- [85] Z. Yu, *et al.*, "Carbon nanofiber supported cobalt catalysts for Fischer–Tropsch synthesis with high activity and selectivity," *Catalysis letters*, vol. 109, pp. 43-47, 2006.
- [86] J. W. Geus, A. J. van Dillen and M. S. Hoogenraad, *Mat. Res. Soc. Symp. Proc.*, 368, 87, 1995.
- [87] Y Wang *et al.*, "Synthesis of SBA-15 with different pore sizes and the utilization as supports of high loading of cobalt catalysts," *Catalysis Today*, vol. 68, pp. 3-9, 2001.
- [88] A. Tavasoli *et al.*, "Cobalt supported on carbon nanotubes – A promising novel Fischer-Tropsch synthesis catalyst," *Fuel Processing Technology*, vol. 89, pp. 491-498, 2008.
- [89] A. Tavasoli *et al.*, "Fischer –Tropsch synthesis over cobalt catalyst supported on Carbon nanotubes in a slurry reactor" *Applied Catalysis A: General*, vol. 345, pp. 134-142, 2008.
- [90] M. Trépanier, *et al.*, "Fischer–Tropsch synthesis over carbon nanotubes supported cobalt catalysts in a fixed bed reactor: Influence of acid treatment," *Fuel Processing Technology*, vol. 90, pp. 367-374, 2009.

- [91] M. Trépanier, *et al.*, "Co, Ru and K loadings effects on the activity and selectivity of carbon nanotubes supported cobalt catalyst in Fischer–Tropsch synthesis," *Applied Catalysis A: General*, vol. 353, pp. 193-202, 2009.
- [92] A. Tavasoli, *et al.*, "Fischer–Tropsch synthesis on mono-and bimetallic Co and Fe catalysts supported on carbon nanotubes," *Fuel Processing Technology*, vol. 90, pp. 1486-1494, 2009.
- [93] M. Trépanier, *et al.*, "Synthesis of CNT-supported cobalt nanoparticle catalysts using a microemulsion technique: Role of nanoparticle size on reducibility, activity and selectivity in Fischer–Tropsch reactions," *Applied Catalysis A: General*, vol. 374, pp. 79-86, 2010.
- [94] H. Zhang, *et al.*, "The nature of cobalt species in carbon nanotubes and their catalytic performance in Fischer–Tropsch reaction," *Journal of Materials Chemistry*, vol. 19, pp. 9241-9249, 2009
- [95] M. Rangel *et al.*, "Characterization of cobalt nanoparticles on different supports for Fischer-Tropsch synthesis," *Studies in Surface Science and Catalysis*, vol. 175, pp. 763-766, 2010.
- [96] H. Zhang *et al.*, "Carbon nanotube promoted Co-Cu catalyst for highly efficient synthesis of higher alcohols from syngas" *Chemical Communications*, pp. 5094-5096, 2005.
- [97] X. MA, *et al.*, "Co-Mo-K sulfide-based catalyst promoted by multiwalled carbon nanotubes for higher alcohol synthesis from syngas," *Chinese Journal of Catalysis*, vol. 27, pp. 1019-1027, 2006.
- [98] X.M. Wu *et al.*, "Co decorated carbon nanotubes as a promoter of Co-Mo-K oxide catalyst for synthesis of higher alcohols from syngas," *Applied Catalysis A*: vol. 340, 87-97, 2008.
- [99] X. Dong *et al.*, "Preparation and characterization of carbon nanotube promoted Co-Cu catalyst for higher alcohol synthesis from syngas," *Catalysis Today*, vol. 147, pp. 158-165, 2009.

- [100] V. Surisetty *et al.*, "Synthesis of higher alcohols from synthesis gas over Co promoted alkali modified MoS₂ catalysts supported on MWCNTs," *Applied Catalysis A. General*, 2010.
- [101] S. Sigurdsona, V. Sundaramurthya, A.K Dalaia, J. Adjaye, *J. Mol. Catal A: Chemistry*, vol. 306, 23-32, 2009.
- [102] G. L. Bezemer, *et al.*, "Investigation of promoter effects of manganese oxide on carbon nanofiber-supported cobalt catalysts for Fischer-Tropsch synthesis," *Journal of Catalysis*, vol. 237, pp. 152-161, 2006.
- [103] G. L. Bezemer, *et al.*, "Preparation of Fischer-Tropsch cobalt catalysts supported on carbon nanofibers and silica using homogeneous deposition-precipitation," *Journal of Catalysis*, vol. 237, pp. 291-302, 2006.
- [104] Z. Yu *et al.*, "Role of surface oxygen in the preparation and deactivation of carbon nanofiber supported cobalt Fischer-Tropsch catalysts," *Topics in catalysis*, vol. 45, pp. 1-4, 2007.
- [105] G. L. Bezemer, *et al.*, "Cobalt particle size effects in the Fischer-Tropsch reaction studied with carbon nanofiber supported catalysts," *Journal of the American Chemical Society*, vol. 128, pp. 3956-3964, 2006.
- [106] J. P. Breejen, *et al.*, "Design of supported cobalt catalysts with maximum activity for the Fischer-Tropsch synthesis," *Journal of Catalysis*, vol. 270 pp. 146-152, 2010.
- [107] A. Tavasoli, *et al.*, "Effects of Confinement in Carbon Nanotubes on the Activity, Selectivity, and Lifetime of Fischer-Tropsch Co/Carbon Nanotube Catalysts," *Journal of Chemical & Engineering Data*, vol. 55, pp. 2757-2763, 2010.
- [108] E. Iglesia, *et al.*, "Bimetallic Synergy in Cobalt Ruthenium Fischer-Tropsch Synthesis Catalysts," *Journal of Catalysis*, vol. 143, pp. 345-368, 1993.
- [109] A. Y. Khodakov, *et al.*, "Pore size effects in Fischer Tropsch synthesis over cobalt-supported mesoporous silicas," *Journal of Catalysis*, vol. 206, pp. 230-241, 2002.

- [110] A. Martinez, *et al.*, "Fischer-Tropsch synthesis of hydrocarbons over mesoporous Co/SBA-15 catalysts: the influence of metal loading, cobalt precursor and promoters," *Journal of Catalysis*, vol. 220, pp. 486-499, 2003.
- [111] Q. Cai and J. Li, "Catalytic properties of the Ru promoted Co/SBA-15 catalysts for Fischer-Tropsch synthesis," *Catalysis Communications*, vol. 9, pp. 2003-2006, 2008.
- [112] H. Xiong, *et al.*, "Fischer-Tropsch synthesis: The role of pore size for Co/SBA-15 catalysts," *Journal of Molecular Catalysis A: Chemical*, vol. 295, pp. 68-76, 2008.
- [113] H. Xiong, *et al.*, "Ruthenium promotion of Co/SBA-15 catalysts with high cobalt loading for Fischer-Tropsch synthesis," *Fuel Processing Technology*, vol. 90, pp. 237-246, 2009
- [114] G. Prieto, *et al.*, "Cobalt supported on morphologically tailored SBA-15 mesostructures: The impact of pore length on metal dispersion and catalytic activity in the Fischer-Tropsch synthesis," *Applied Catalysis A: General*, vol. 367, pp. 146-156, 2009.
- [115] www.baytube.com, www.bayercoating.com
- [116] C. Perego and P. Villa, "Catalyst preparation methods," *Catalysts Today*, vol. 34, pp. 281-305, 1997.
- [117] Cupertino, CA 95014 U.S.A. "Chapter 7: Basics of X-ray Diffraction"
- [118] J. P. Tessonier *et al.*, "Analysis of the structure and chemical properties of some commercial carbon nanostructures," *Carbon*, vol. 47 pp. 1779-1789, 2009.
- [119] R. Marega, *et al.*, "Cap removal and shortening of double-walled and very-thin multi-walled carbon nanotubes under mild oxidative conditions," *Carbon*, vol. 47, pp. 675-682, 2009.
- [120] Y. Li, *et al.*, "Purification of CVD synthesized single-wall carbon nanotubes by different acid oxidation treatments," *Nanotechnology*, vol. 15, p. 1645, 2004.

- [121] T.G. Ros, A.J. van Dillen, J.W. Gues, D.C. Koningsberger *Chem. Eur. Journal*, vol. 8 p. 1151, 2002.
- [122] A. Solhy, B.F. Machado, J. Beausoleil, Y. Kihn, F. Goncalves, M.F.R. Pereira, J.J.M. Orfao, J.L. Fuguriredo, J.L. Fariab, P. Sepra, *Carbon*, vol. 46, p. 1194, 2008.
- [123] C. M. Yang *et al.*, "Highly Dispersed Metal Nanoparticles in Functionalized SBA-15," *Chemistry of Materials*, vol.15, pp. 275-280, 2003.
- [124] L. F. Chen, *et al.*, "Preparation of Cu/SBA-15 catalysts by different methods for the hydrogenolysis of dimethyl maleate to 1,4-butanediol," *Applied Catalysis A: General*, vol. 356 pp. 129–136, 2009.
- [125] M. Kruk, M. Jaroniec, "Characterization of the Porous Structure of SBA-15" *Chemistry of Materials*, vol. 12, pp. 1961-1968, 2000.
- [126] K. S. W. Sing *et al.*, *Pure & Applied Chemistry*, vol. 57, No. 4, pp. 603—619, 1985, IUPAC
- [127] S. Lowell & J. E. Shields, "Powder Surface Area and Porosity", 3rd Ed. Chapman & Hall, New York, 1991
- [128] S. W. Song *et al.*, "Functionalized SBA-15 Materials as Carriers for Controlled Drug Delivery: Influence of Surface Properties on Matrix-Drug Interactions," *Langmuir*, vol. 21, pp. 9568-9575, 2005.
- [129] P. Woontranont, W. Pecharapa, "Effects of Surface Modification of Carbon Nanotubes on the Deposition of NiO/CNTs Nanocomposites" *Journal of the Microscopy Society of Thailand*, vol. 4 (2), pp. 116-119, 2011.
- [130] N. A. Buang, *et al.*, "Characteristic Of Mild Acid Functionalized Multiwalled Carbon Nanotubes Towards High Dispersion With Low Structural Defects," *Digest Journal of Nanomaterials and Biostructures* vol. 7, No. 1, , pp. 33 – 39, 2012.
- [131] M. Chareonpanich, *et al.*, "Short-period synthesis of ordered mesoporous silica SBA-15 using ultrasonic technique," *Materials Letters*, vol. 61, pp. 5153–5156, 2007.

- [132] F. Azimov, et al., "Synthesis and characterization of SBA-15 and Ti/SBA-15 nanoporous materials for DME catalysts," *Journal of the University of Chemical Technology and Metallurgy*, vol. 47, No 3, pp. 333-340, 2012.
- [133] C. Jo, et al., "Syntheses of high quality KIT-6 and SBA-15 mesoporous silicas using low-cost water glass through rapid quenching of silicate structure in acidic solution water glass, through rapid quenching of silicate structure in acidic solution," *Microporous and Mesoporous Materials*, vol. 124, pp. 45–51, 2009.
- [134] S. Wu, et al., "Synthesis of Heteroatom Substituted SBA-15 by the "pH-Adjusting," *Method Chem. Mater.*, vol. 16, pp. 486-492, 2004.
- [135] P. Shah, et al., "Direct hydrothermal synthesis of mesoporous Sn-SBA-15 materials under weak acidic conditions," *Microporous and Mesoporous Materials*, vol. 100, pp. 210–226, 2007.
- [136] C. Chen et al., "Fischer-Tropsch Synthesis over one Eggshell-Type Co/SiO₂ catalyst In a slurry phase reactor" *Applied Catalysis A, General*, 2010.
- [137] S.A. Hosseini, et al., "Fischer-Tropsch synthesis over Ru promoted Co/ γ -Al₂O₃ catalysts in a CSTR," *Catalysis communications*, vol. 5 pp. 137-143, 2004.
- [138] S. Storsater, B. Totdal, J. C. Walmsley, B.C. Tanem, A. Holmen, *Journal of Catalysis*, vol. 236, pp. 139-152, 2005.
- [139] A. Tavasoli, Y.Mortazavi, A.Khodadadi, K.Sadagiani: *Iran Journal of Chemical Engineering*, vol. 35, pp. 9-15, 2005.
- [140] A. Tavasoli, K.Sadagiani, A. Nakhaeipour, M.G. Ahangari: *Iran Journal of Chemical Engineering*, vol. 26 , pp. 1-9, 2007.
- [141] T. K. Das, et al., "Fischer–Tropsch synthesis: characterization and catalytic properties of rhenium promoted cobalt alumina catalysts," *Fuel*, vol. 82, pp. 805-815, 2003.
- [142] J. Dullac, Bull. Soc. Fr. *Mineral. Crystallography*, vol. 92, p. 487, 1969.
- [143] P. Arnoldy, J. A. Moulijn, *Journal of Catalysis*, vol. 93, p. 38, 1985.

- [144] B. Viswanathan and R. Gopalakrishnan, "Effect of support and promoter in Fischer-Tropsch cobalt catalysts," *Journal of Catalysis*, vol. 99, pp. 342-348, 1986
- [145] Y. Wang, *et al.*, "Effect of preparation methods on the catalytic properties of Co/SBA-15 catalysts for Fischer-Tropsch synthesis," *Natural Gas Conversion VIII* F.B. Noronha, M. Schmal, E.F. Sousa-Aguiar (Editors) 2007 Published by Elsevier B.V.
- [146] D. G. Castner, *et al.*, "X-ray absorption spectroscopy, X-ray photoelectron spectroscopy, and analytical electron microscopy studies of cobalt catalysts. 2. Hydrogen reduction properties," *Journal of Physical Chemistry*, vol. 94, pp. 819-828, 1990
- [147] G. Jacobs, *et al.*, "Fischer-Tropsch synthesis: study of the promotion of Re on the reduction property of Co/Al₂O₃ catalysts by in situ EXAFS/XANES of Co K and Re L_{III} edges and XPS," *Applied Catalysis A: General*, vol. 264, pp. 203-212, 2004.
- [148] J. Panpranot, *et al.*, "Synthesis and characteristics of MCM-41 supported CoRu catalysts," *Catalysis Today*, vol. 77, pp. 269-284, 2002.
- [149] J. van de Loosdrecht, *et al.*, "Calcination of Co-Based Fischer-Tropsch Synthesis Catalysts," *Topics in Catalysis*, vol. 26, pp. 121-127, 2003/12/01 2003.
- [150] S. A. Hosseini, *et al.*, "Evaluation of Ru-promoted Co/ γ -Al₂O₃ catalysts in Fischer-Tropsch synthesis in a CSTR," *Catalysis communications*, vol. 6, pp. 233-240, 2005.
- [151] Brunauer, S. Deming, L.S. Deming, W.S. and Teller, E. *Journal of American Chemical Society*, vol. 62, p. 1723, 1940.
- [152] J. Hong, *et al.*, "Effect of promotion with Ru on the structure and catalytic performance of mesoporous silica (smaller and larger pore) supported cobalt Fischer-Tropsch catalysts," *Catalysis Today*, vol. 140, pp. 135-141, 2009.

- [153] S. Sun, N. Tsukabi, K. Fujimoto, *Applied Catalysis. A: General*, vol. 202, p. 121, 2000.
- [154] Y. Wang, M. Noguchi, Y. Takahashi, Y. Ohtsuka, *Catalysis Today*, vol. 68 p. 3, 2001.
- [155] A. de. Klerk and E. Furimsky, "Catalysts in the Refining of Fischer-Tropsch syncrude" *RSC Publishing Catalysis Series*, 2010.
- [156] M. Eswaramoorthy, R. Sen, and C.N.R. Rao, *Chem. Phys. Lett.*, vol. 304, p. 207, 1999.
- [157] A. Y. Khodakov "Fischer-Tropsch synthesis: Relations between structure of cobalt catalysts and their catalytic performance," *Catalysis Today*, vol. 144, pp. 251–257, 2009.
- [158] J. P. den. Breejen, *et al.*, "Design of supported cobalt catalysts with maximum activity for the Fischer-Tropsch synthesis," *Journal of Catalysis*, vol. 270, pp. 146-152, 2010.
- [159] W. Chen, Z. Fan, X. Pan, X. Bao, *Journal of American Chemical Society* 130, pp. 9414, 2008.
- [160] R. M. M. Abbaslou, *et al.*, "Effects of Nanotubes Pore Size on the Catalytic Performances of Iron Catalysts Supported on Carbon Nanotubes for Fischer-Tropsch Synthesis," *Applied Catalysis A: General*, vol. 379, issues 1-2, pp. 129–134, 2010.
- [161] M. Zaman, *et al.*, "Fischer–Tropsch synthesis over cobalt dispersed on carbon nanotubes-based supports and activated carbon," *Fuel Processing Technology*, vol. 90, pp. 1214-1219, 2009.
- [162] A. Feller, *et al.*, "Cobalt Cluster Effects in Zirconium Promoted Co/SiO₂ Fischer–Tropsch Catalysts," *Journal of Catalysis*, vol. 185, pp. 120-130, 1999.
- [163] A. Tavassoli, "Catalyst composition and its distribution effects on the enhancement of activity, selectivity and suppression of deactivation rate of FTS cobalt catalysts," Ph.D. Thesis, University of Tehran, 2005.

- [164] R. B. Anderson, *et al.*, "Studies of the Fischer-Tropsch synthesis. V. Activities and surface areas of reduced and carburized cobalt catalysts," *Journal of the American Chemical Society*, vol. 71, pp. 183-188, 1949.
- [165] R. C. Reuel and C. H. Bartholomew, "Effects of support and dispersion on the CO hydrogenation activity/selectivity properties of cobalt," *Journal of Catalysis*, vol. 85, pp. 78-88, 1984.
- [166] S. Santucci *et al.*, *Journal of Chem. Phys.*, vol. 119, 10904, 2003.
- [167] Z. Yu, *et al.*, "Carbon nanofiber supported cobalt catalysts for Fischer-Tropsch synthesis with high activity and selectivity," *Catalysis letters*, vol. 109, pp. 43-47, 2006.
- [168] D. Song and J. Li, "Effect of catalyst pore size on the catalytic performance of silica supported cobalt Fischer-Tropsch catalysts," *Journal of Molecular Catalysis A: Chemical*, vol. 247, pp. 206-212, 2006.
- [169] T. Witoon, *et al.*, "Effect of hierarchical meso-macroporous silica supports on Fischer-Tropsch synthesis using cobalt catalyst," *Fuel Processing Technology*, vol. 92, pp. 1498-1505, 2011.
- [170] J. S. Jung, *et al.*, "Fischer-Tropsch Synthesis over cobalt based catalyst supported on different mesoporous silica," *Catalysis Today*, vol. 185, pp. 168-174, 2012.
- [171] J. J. Rodrigues, *et al.*, "Ruthenium promotion of Co/SBA-15 catalysts for Fischer-Tropsch synthesis in slurry-phase reactors," *Journal of Natural Gas Chemistry*, vol. 21, pp. 722-728, 2012.
- [172] J. Lü, *et al.*, "Thermal decomposition and cobalt species transformation of carbon nanotubes supported cobalt catalyst for Fischer-Tropsch synthesis," *Journal of Natural Gas Chemistry*, vol. 21, pp. 37-42, 2012.
- [173] A. Saib, *et al.*, "Silica supported cobalt Fischer-Tropsch catalysts: effect of pore diameter of support," *Catalysis Today*, vol. 71, pp. 395-402, 2002.

- [174] Ø. Borg, *et al.*, "Fischer–Tropsch synthesis: Cobalt particle size and support effects on intrinsic activity and product distribution," *Journal of Catalysis*, vol. 259, pp. 161-164, 2008.
- [175] G. Prieto, *et al.*, "Cobalt particle size effects in Fischer–Tropsch synthesis: structural and in situ spectroscopic characterization on reverse micelle-synthesized Co/ITQ-2 model catalysts," *Journal of Catalysis*, vol. 266, pp. 129-144, 2009.
- [176] I. Ghampson, *et al.*, "Effects of pore diameter on particle size, phase, and turnover frequency in mesoporous silica supported cobalt Fischer–Tropsch catalysts," *Applied Catalysis A: General*, vol. 388, pp. 57-67, 2010.
- [177] Z. Wang, *et al.*, "Particle size effects in Fischer–Tropsch synthesis by cobalt," *Catalysis Today*, vol. 181, pp. 75-81, 2012.
- [178] S. Rane, *et al.*, "Relation between hydrocarbon selectivity and cobalt particle size for alumina supported cobalt Fischer–Tropsch catalysts," *Applied Catalysis A: General*, vol. 437–438, pp. 10-17, 2012.
- [179] T. Fu, *et al.*, "Effect of carbon support on Fischer–Tropsch synthesis activity and product distribution over Co-based catalysts," *Fuel Processing Technology*, 2013.
- [180] N. Fischer, *et al.*, "Structure sensitivity of the Fischer–Tropsch activity and selectivity on alumina supported cobalt catalysts," *Journal of Catalysis*, vol. 299, pp. 67-80, 2013.
- [181] Y. Liu, *et al.*, "Fischer–Tropsch synthesis in slurry-phase reactors over Mn- and Zr-modified Co/SiO₂ catalysts," *Fuel Processing Technology*, vol. 90, pp. 901-908, 2009.
- [182] K. J. Woo, *et al.*, "Performance of a slurry bubble column reactor for Fischer–Tropsch synthesis: Determination of optimum condition," *Fuel Processing Technology*, vol. 91, pp. 434-439, 2010.

- [183] S. Chambrey, *et al.*, "Fischer–Tropsch synthesis in milli-fixed bed reactor: Comparison with centimetric fixed bed and slurry stirred tank reactors," *Catalysis Today*, vol. 171, pp. 201-206, 2011
- [184] S. H. Kwack, *et al.*, "Modeling a slurry CSTR with Co/P–Al₂O₃ catalyst for Fischer–Tropsch synthesis," *Fuel Processing Technology*, vol. 92, pp. 2264-2271, 2011.
- [185] X. Liu, *et al.*, "Anti-ASF distribution in Fischer-Tropsch synthesis over unsupported cobalt catalysts in a batch slurry phase reactor," *Catalysis Today*, vol. 175, pp. 494-503, 2011.

APPENDIX A

CALCULATION OF REQUIRED AMOUNTS OF COBALT AND RUTHENIUM FROM PRECURSORS

The calculation of 10 wt % Co is given in the table A-1. Accordingly, using the following equation necessary “weight percent” was calculated from cobalt and ruthenium precursors.

Table A-1: Calculation of 10 wt% cobalt from cobalt nitrate precursor

Support mass – 1 gm	$\frac{Y}{1+Y} \times 100 \% = 10\text{wt}\%$
MM of $\text{Co}(\text{NO}_3)_2 \cdot 6\text{H}_2\text{O}$ – 291.04 g/mol	
Co mass – Y	
10 wt% Cobalt is required	
$\frac{Y}{1+Y} \times 100 \% = 10\text{wt}\%$	• Number of moles of Cobalt
$\frac{Y}{1+Y} = 10\text{wt}\% / 100\%$	1 mole ----- 58.93 g
$\frac{Y}{1+Y} = 0.1$	X mole ----- 0.1111 g
$Y = 0.1 (1+y)$	$0.1111 \text{ g} = \frac{1 \text{ mole}}{58.93 \text{ g}} = 0.002 \text{ mole}$
$Y = 0.1 + 0.1y$	291.04g ----- 1mole
$Y - 0.1y = 0.1$	X g ----- 0.002 mole
$0.9y = 0.1$	$X = \frac{291.04 \text{ g} \cdot 0.002 \text{ mole}}{1 \text{ mole}} = \mathbf{0.5821g}$
$Y = \frac{0.1}{0.9} = 0.1111\text{g}$	Amount of $\text{Co}(\text{NO}_3)_2 \cdot 6\text{H}_2\text{O}$ required to obtain 10wt% Co is: 0.5821g

APPENDIX B

CALCULATION OF MOLES OF EACH CATALYST USING EQUATION 3.3

Calculation of consumed moles of each product was determined by equation 3.3

$n = \frac{PV}{zRT} \tag{3.3}$

$$P = 20 \text{ bar} = 19.738 \text{ atm,}$$

$$T = 220^\circ\text{C} = 493 \text{ K}$$

$$R = 0.08206 \text{ atm L/K mol}$$

$$Z = 0.9996$$

V = value of V for each catalyst is obtained from Table 3.8.

$$n (M3) = \frac{19.738\text{-atm} * 3.204 \text{ L}}{0.9996 * 0.08206 \left(\frac{\text{atmL}}{\text{K}} \text{ mol}\right) * 493 \text{ K}} = 1.585 \text{ mol}$$

$$n (M4) = \frac{19.738\text{-atm} * 1.639 \text{ L}}{0.9996 * 0.08206 \left(\frac{\text{atmL}}{\text{K}} \text{ mol}\right) * 493 \text{ K}} = 0.811 \text{ mol}$$

$$n (S3) = \frac{19.738\text{-atm} * 2.531 \text{ L}}{0.9996 * 0.08206 \left(\frac{\text{atmL}}{\text{K}} \text{ mol}\right) * 493 \text{ K}} = 1.252 \text{ mol}$$

$$n (S4) = \frac{19.738\text{-atm} * 3.288 \text{ L}}{0.9996 * 0.08206 \left(\frac{\text{atmL}}{\text{K}} \text{ mol}\right) * 493 \text{ K}} = 1.626 \text{ mol}$$

$$n (M2) = \frac{19.738\text{-atm} * 0.59 \text{ L}}{0.9996 * 0.08206 \left(\frac{\text{atmL}}{\text{K}} \text{ mol}\right) * 493 \text{ K}} = 0.292 \text{ mol}$$

$$n(S2) = \frac{19.738 \text{ atm} * 3.455 \text{ L}}{0.9996 * 0.08206 \left(\frac{\text{atmL}}{\text{K}} \text{ mol} \right) * 493 \text{ K}} = 1.709 \text{ mol}$$

$$n(M1) = \frac{19.738 \text{ atm} * 0.03 \text{ L}}{0.9996 * 0.08206 \left(\frac{\text{atmL}}{\text{K}} \text{ mol} \right) * 493 \text{ K}} = 0.015 \text{ mol}$$

$$n(S1) = \frac{19.738 \text{ atm} * 0.013 \text{ L}}{0.9996 * 0.08206 \left(\frac{\text{atmL}}{\text{K}} \text{ mol} \right) * 493 \text{ K}} = 0.006 \text{ mol}$$

**CALCULATION OF CO CONVERSION FOR EACH CATALYST USING
EQUATION 3.1**

$CO \text{ conversion } \% = \frac{\Sigma \text{ moles of CO consumed}}{\Sigma \text{ moles of CO (initial+consumed)}} \times 100\% \quad (3.1)$
--

$$CO \text{ conv}(M3) = \frac{1.585 \text{ mol}}{0.025 \text{ mol} + 1.585 \text{ mol}} \times 100\% = 98.44\%$$

$$CO \text{ conv}(M4) = \frac{0.811 \text{ mol}}{0.025 \text{ mol} + 0.811 \text{ mol}} \times 100\% = 97\%$$

$$CO \text{ conv}(S3) = \frac{1.252 \text{ mol}}{0.025 \text{ mol} + 1.252 \text{ mol}} \times 100\% = 98\%$$

$$CO \text{ conv}(S4) = \frac{1.626 \text{ mol}}{0.025 \text{ mol} + 1.626 \text{ mol}} \times 100\% = 98.5\%$$

$$CO \text{ conv}(M2) = \frac{0.292 \text{ mol}}{0.025 \text{ mol} + 0.292 \text{ mol}} \times 100\% = 92\%$$

$$CO \text{ conv}(S2) = \frac{1.709 \text{ mol}}{0.025 \text{ mol} + 1.709 \text{ mol}} \times 100\% = 98.6\%$$

$$CO \text{ conv}(M1) = \frac{0.015 \text{ mol}}{0.025 \text{ mol} + 0.015 \text{ mol}} \times 100\% = 37.5\%$$

$$CO \text{ conv}(S1) = \frac{0.006 \text{ mol}}{0.025 \text{ mol} + 0.006 \text{ mol}} \times 100\% = 19.3\%$$

CONVERSION OF PPM INTO MOLES

$$PPM = \frac{\text{mass solute} \times 10^6}{\text{mass solvent}} \quad \text{B 1}$$

$$PPM = \text{mass solute} \times \frac{10^6}{\text{mass solvent}} \quad \text{B 2}$$

Mass solute can be solved by dividing both sides of equation (B 2) by $10^6 / \text{mass solvent}$:

$$\text{mass solute} = \frac{PPM \times \text{mass solvent}}{10^6} \quad \text{B 3}$$

At the same time mass solvent is identified by following equation:

$$\rho = \frac{M}{V}$$

Where: $M = \rho V$

ρ - density 0.773g/mL, V - volume of a solvent ($C_{16}H_{34}$) 50 mL, M - mass of a solvent

$$M = 0.773 \text{g/mL} \times 50 \text{ml} = \mathbf{38.65 \text{ g (constant for all cases)}}$$

Example:

The $C_{12}H_{26}$ is among the produced HCs with quantity of 1014.47 ppm.

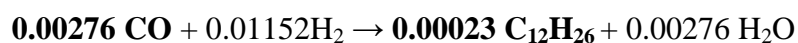
Using equation B 3:

$$\text{Mass solute } (C_{12}H_{26}) = \frac{1014.47 \text{ ppm} \times 38.65 \text{g}}{10^6 \text{ ppm}} = 0.03921 \text{g}$$

Based on the actual gram/mole of the $C_{12}H_{26}$, mole of CO spent was calculated:

$$0.03921 \text{g} \times \left(1 \text{mole} \frac{C_{12}H_{26}}{170.328 \text{g}} \right) = 0.00023 \text{ mol}$$

Based on moles of produced $C_{12}H_{26}$, the CO moles spent were calculated:



SELECTIVITY

The selectivity of catalysts towards C₈-C₄₀ was calculated using the equation 3.5:

$$\text{Selectivity (C}_{8+}) = \frac{\text{Moles of liquid C}_{8+}}{\text{Moles of CO consumed}} \times 100\% \quad (3.5)$$

$$\text{Selectivity (M3)} = \frac{0.047 \text{ mol}}{1.585 \text{ mol}} \times 100 = 2.97 \%$$

$$\text{Selectivity (M4)} = \frac{0.016 \text{ mol}}{0811 \text{ mol}} \times 100 = 1.97 \%$$

$$\text{Selectivity (M2)} = \frac{0.006 \text{ mol}}{0.292 \text{ mol}} \times 100 = 2.05 \%$$

$$\text{Selectivity (M1)} = \frac{0.0008 \text{ mol}}{0.015 \text{ mol}} \times 100 = 5.3 \%$$

$$\text{Selectivity (S3)} = \frac{0.032 \text{ mol}}{1.252 \text{ mol}} \times 100 = 2.56 \%$$

$$\text{Selectivity (S4)} = \frac{0.045 \text{ mol}}{1.626 \text{ mol}} \times 100\% = 2.77 \%$$

$$\text{Selectivity (S2)} = \frac{0.049 \text{ mol}}{1.709 \text{ mol}} \times 100\% = 2.87 \%$$

$$\text{Selectivity (S1)} = \frac{0.0007 \text{ mol}}{0.006 \text{ mol}} \times 100\% = 11.7 \%$$

APPENDIX C

CHROMATOGRAMS OF PRODUCTS AND STANDARD MIXTURE OBTAINED FROM GC-MS

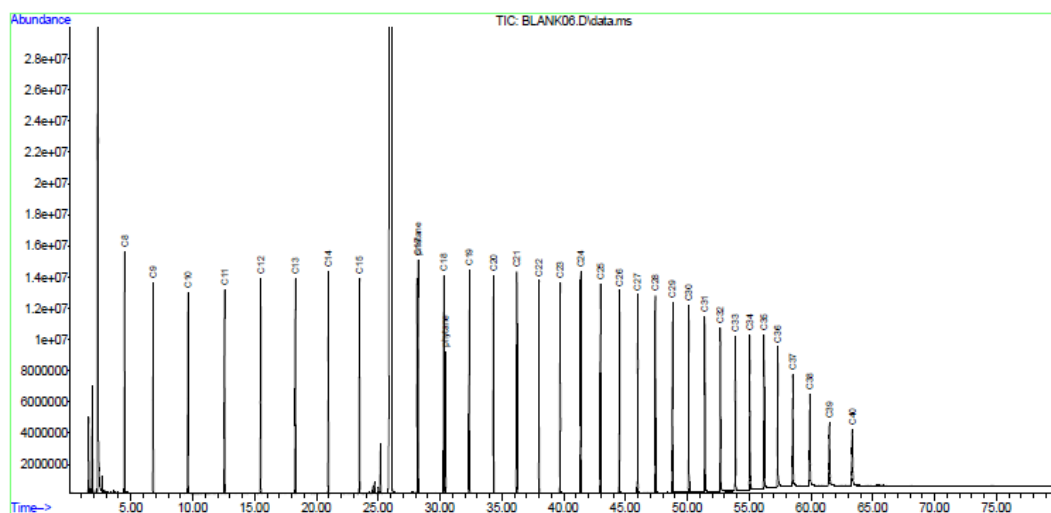


Figure C-1. Diesel standard

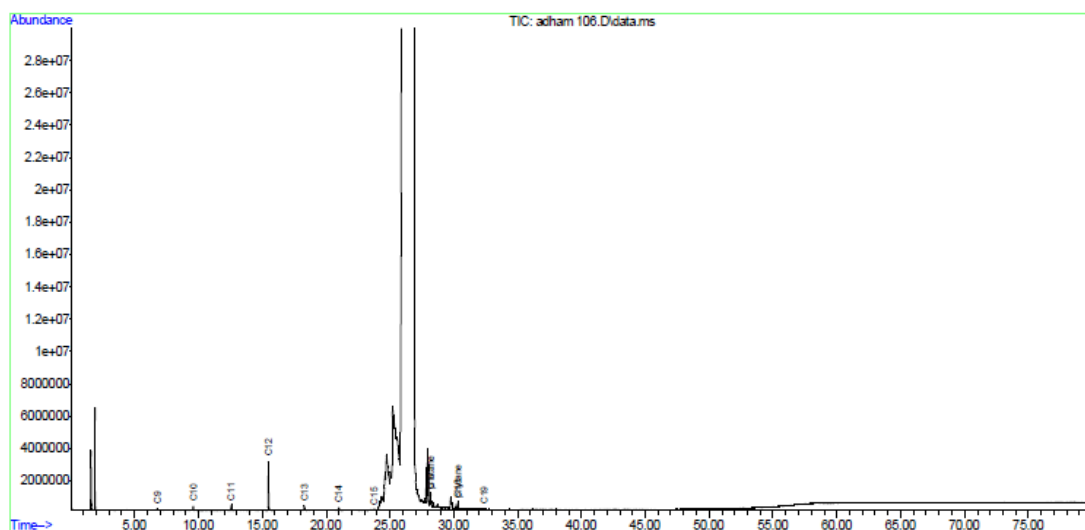


Figure C-2. Pure MWCNT (M1)

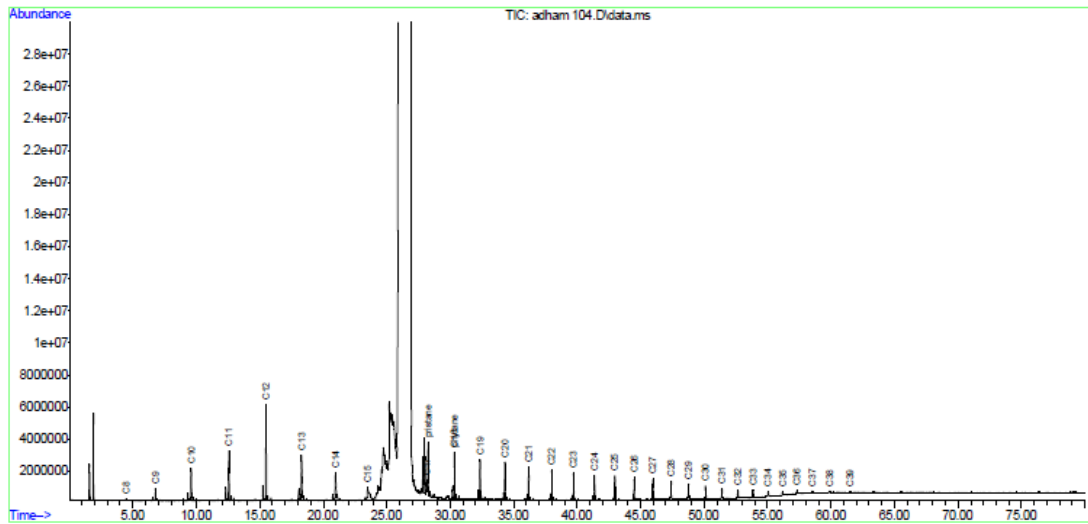


Figure C-3. 10Co/MWCNT (M2)

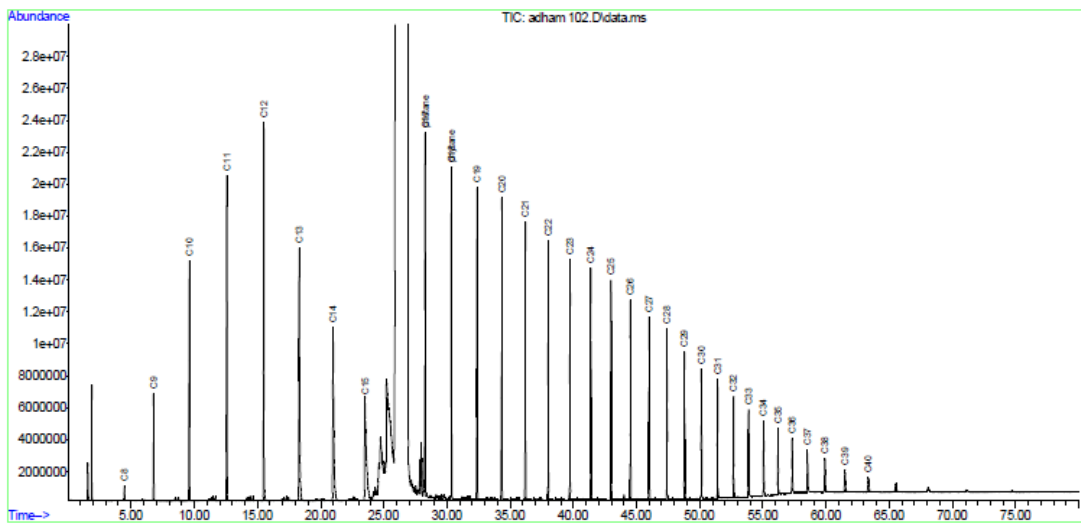


Figure C-4. 10Co/1Ru/MWCNT (M3)

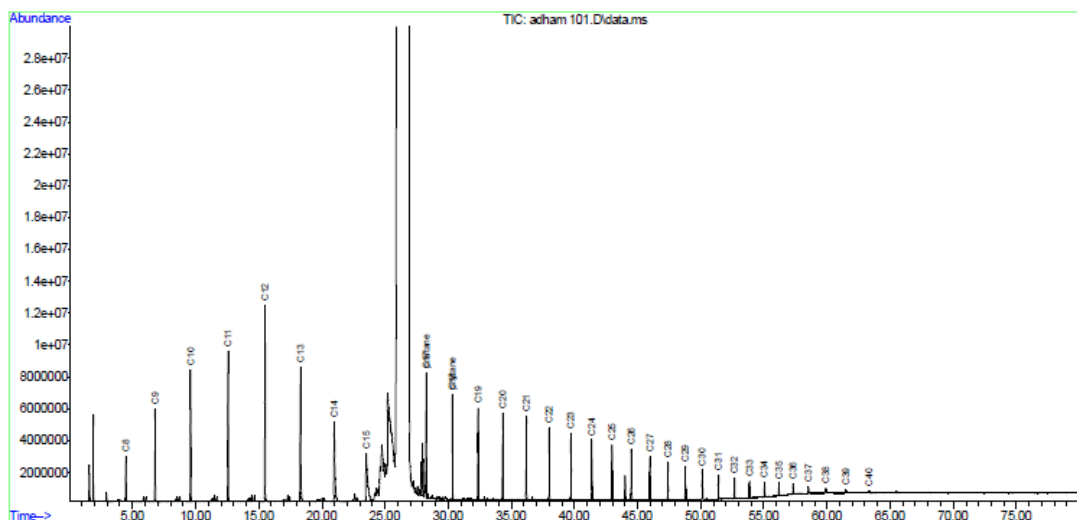


Figure C-5. 30Co/1Ru/MWCNT (M4)

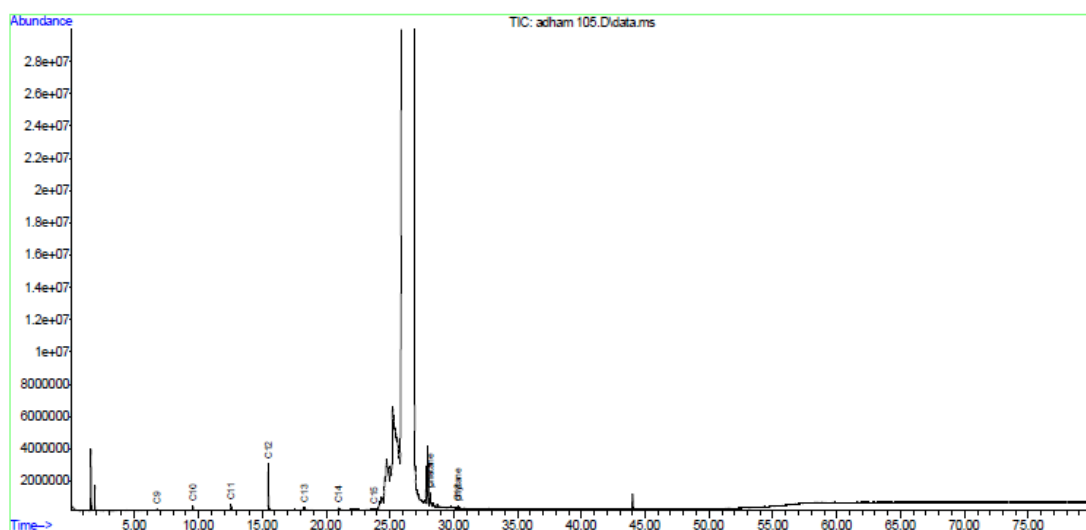


Figure C-6. Pure SBA-15 (S1)

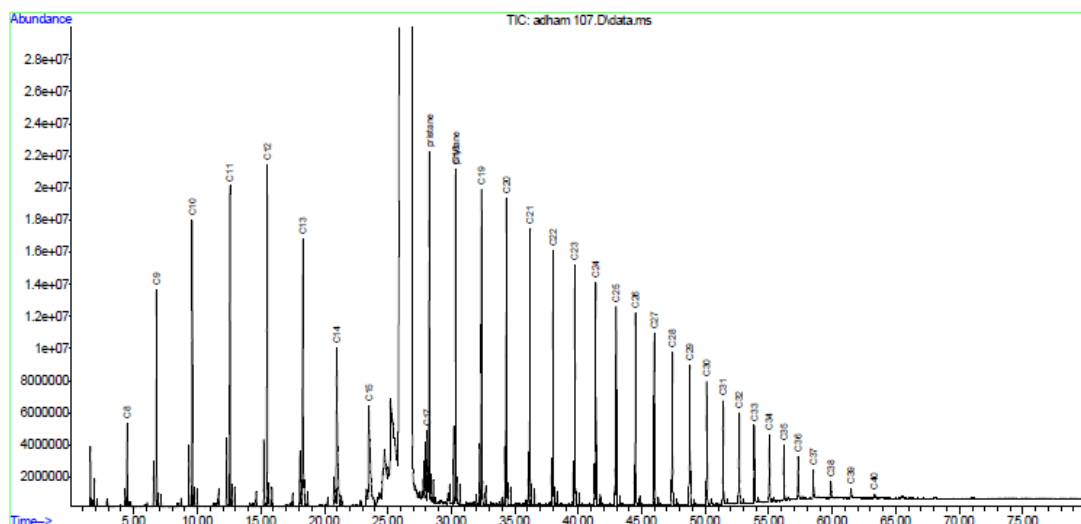


Figure C-7. 10Co/SBA-15 (S2)

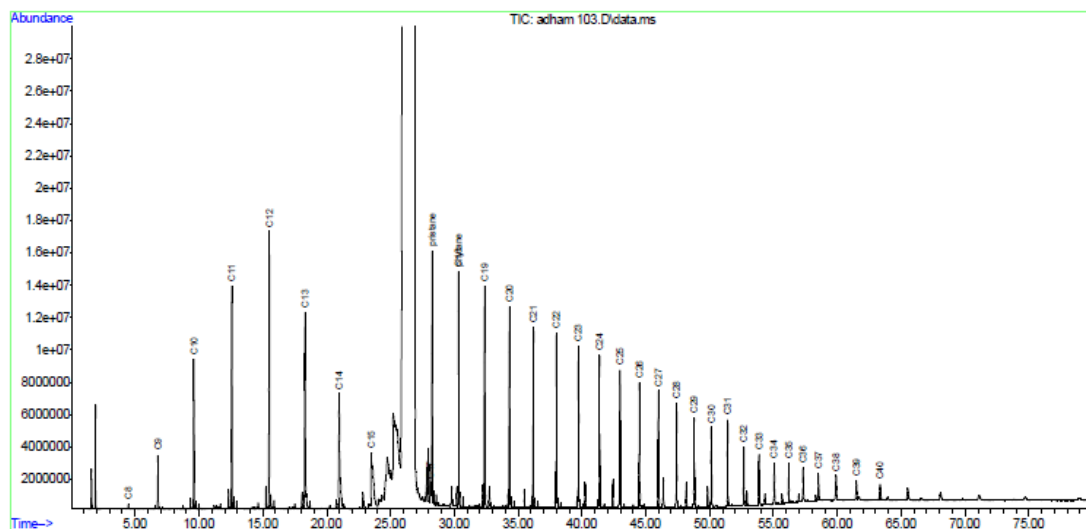


Figure C-8. 10Co/1Ru/SBA-15 (S3)

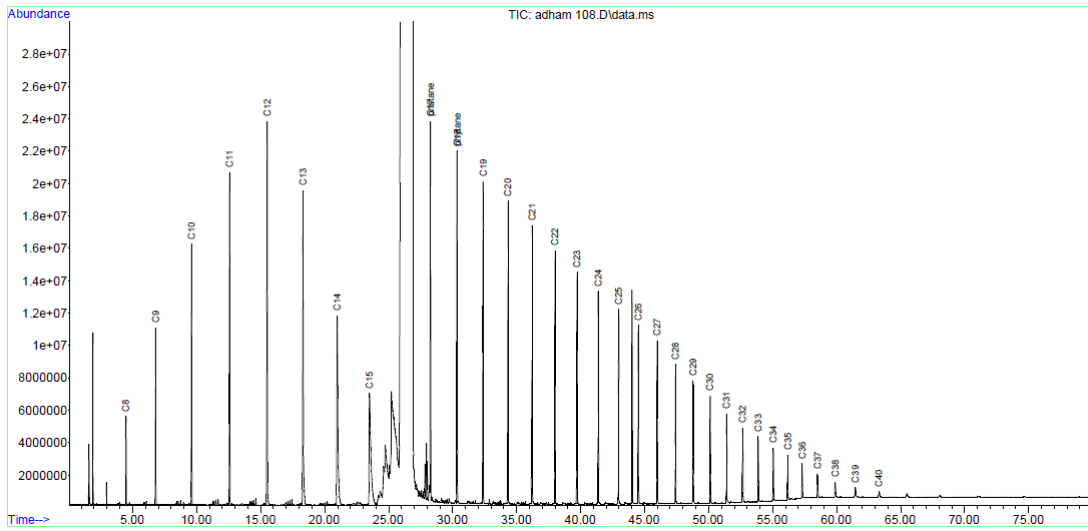


Figure C- 9. 30Co/1Ru/SBA-15 (S4)

QUANTITATION REPORT OBTAINED FROM GC/MS

Table C-1. Standard mixture

#	compound	Retention time (min)	Response factor	Concentration (ppm)
1)	C8	4.486	218041688	514.04
2)	C9	6.793	239016610	519.51
3)	C10	9.601	258533872	518.2
4)	C11	12.569	281105715	511.6
5)	C12	15.495	302049202	515.16
6)	C13	18.301	312175293	517.01
7)	C14	20.965	320193902	515.39
8)	C15	23.488	323459091	513.59
9)	C17	28.228	683818625	510.86
10)	pristane	28.228	678923646	509.1
11)	C18	30.308	340319228	514.87
12)	phytane	30.43	345784865	509.45
13)	C19	32.362	337324780	509.38
14)	C20	34.324	333325065	510.82
15)	C21	36.2	333141521	509.49
16)	C22	37.997	332919228	508.36
17)	C23	39.721	328754262	504.8
18)	C24	41.376	325709136	511.35
19)	C25	42.968	323599026	512.93
20)	C26	44.5	324999799	511.9
21)	C27	45.978	319742591	516
22)	C28	47.404	316367060	516.74
23)	C29	48.782	310449486	516.03
24)	C30	50.115	306272312	514.18
25)	C31	51.404	303971209	521.66
26)	C32	52.655	292608505	515.42
27)	C33	53.868	275534193	532.31
28)	C34	55.044	277931285	534.95
29)	C35	56.188	274535706	536.75
30)	C36	57.304	274689385	547.33
31)	C37	58.515	257899549	558.12
32)	C38	59.89	243092782	555.26
33)	C39	61.476	188614845	564.1
34)	C40	63.326	193423420	570.54

Table C-2. Pure MWCNT (M1)

#	compound	Retention time	response factor	concentration (ppm)
1)	C8	0	N.D.	
2)	C9	6.792	2681663	5.83
3)	C10	9.6	6207933	12.44
4)	C11	12.566	7403461	13.47
5)	C12	15.494	75223303	128.3
6)	C13	18.303	12130352	20.09
7)	C14	20.989	11945792	19.23
8)	C15	23.782	3001623	4.77
9)	C17	28.169	43039411	32.15
10)	pristane	28.169	43280293	32.45
11)	C18	30.329	11520704	17.43
12)	phytane	30.329	12026170	17.72
13)	C19	32.37	1832316	2.77
14)	C20	0	N.D.	
15)	C21	0	N.D.	
16)	C22	0	N.D.	
17)	C23	0	N.D.	
18)	C24	0	N.D.	
19)	C25	0	N.D.	
20)	C26	0	N.D.	
21)	C27	0	N.D.	
22)	C28	0	N.D.	
23)	C29	0	N.D.	
24)	C30	0	N.D.	
25)	C31	0	N.D.	
26)	C32	0	N.D.	
27)	C33	0	N.D.	
28)	C34	0	N.D.	
29)	C35	0	N.D.	
30)	C36	0	N.D.	
31)	C37	0	N.D.	
32)	C38	0	N.D.	
33)	C39	0	N.D.	
34)	C40	0	N.D.	

Table C-3. 10Co/MWCNT (M2)

#	compound	Retention time	response factor	concentration (ppm)
1)	C8	4.486	3101181	7.31
2)	C9	6.793	14675813	31.9
3)	C10	9.602	39955572	80.09
4)	C11	12.569	70196933	127.76
5)	C12	15.498	138660152	236.49
6)	C13	18.304	93091587	154.17
7)	C14	20.977	91021916	146.51
8)	C15	23.509	34061199	54.08
9)	C17	28.145	48349108	36.12
10)	pristane	28.265	82807138	62.09
11)	C18	30.336	76902990	116.35
12)	phytane	30.336	76470829	112.66
13)	C19	32.366	64874284	97.96
14)	C20	34.317	60262165	92.35
15)	C21	36.196	54629004	83.55
16)	C22	37.993	60098933	91.77
17)	C23	39.718	53525184	82.19
18)	C24	41.374	49388373	77.54
19)	C25	42.966	44334037	70.27
20)	C26	44.499	41757260	65.77
21)	C27	45.979	37574475	60.64
22)	C28	47.404	33186097	54.2
23)	C29	48.781	29370804	48.82
24)	C30	50.114	24817116	41.66
25)	C31	51.404	21511088	36.92
26)	C32	52.653	16565627	29.18
27)	C33	53.865	13725981	26.52
28)	C34	55.042	13767885	26.5
29)	C35	56.186	9211473	18.01
30)	C36	57.303	8921917	17.78
31)	C37	58.511	7659800	16.58
32)	C38	59.885	4782215	10.92
33)	C39	61.476	4853019	14.51
34)	C40	0	N.D.	

Table C-4. 10Co/1Ru/MWCNT (M3)

#	Compound	Retention time	Response factor	Concentration (ppm)
1)	C8	4.487	14523891	34.24
2)	C9	6.796	121371844	263.81
3)	C10	9.61	306708189	614.76
4)	C11	12.582	463567971	843.68
5)	C12	15.513	594806274	1014.47
6)	C13	18.32	591610445	979.8
7)	C14	20.996	604734350	973.39
8)	C15	23.523	581995020	924.1
9)	C17	28.28	590254075	440.96
10)	pristane	28.28	577867911	433.32
11)	C18	30.357	525211286	794.59
12)	phytane	30.357	525862423	774.75
13)	C19	32.39	494099708	746.11
14)	C20	34.341	468566874	718.08
15)	C21	36.215	441255696	674.83
16)	C22	38.009	412822300	630.37
17)	C23	39.732	387399921	594.85
18)	C24	41.387	360803853	566.45
19)	C25	42.979	336072626	532.71
20)	C26	44.511	314094911	494.72
21)	C27	45.989	287316843	463.67
22)	C28	47.415	264696346	432.34
23)	C29	48.792	240324767	399.47
24)	C30	50.124	216798432	363.97
25)	C31	51.413	196376661	337.01
26)	C32	52.663	173979820	306.46
27)	C33	53.875	152646192	294.9
28)	C34	55.052	135415791	260.64
29)	C35	56.193	119798503	234.22
30)	C36	57.311	105931906	211.07
31)	C37	58.521	96023452	207.8
32)	C38	59.899	84223780	192.38
33)	C39	61.488	70637276	211.26
34)	C40	63.34	54239993	159.99

Table C-5. 30Co/1Ru/MWCNT (M4)

#	Compound	Retention time	Response factor	Concentration (ppm)
1)	C8	4.487	42632938	100.51
2)	C9	6.797	105757933	229.87
3)	C10	9.607	164798769	330.32
4)	C11	12.575	202888070	369.25
5)	C12	15.505	283977171	484.34
6)	C13	18.31	239417135	396.51
7)	C14	20.986	257782753	414.93
8)	C15	23.522	272802203	433.16
9)	C17	28.272	205028356	153.17
10)	pristane	28.272	205311289	153.95
11)	C18	30.348	155905340	235.87
12)	phytane	30.348	156674132	230.83
13)	C19	32.38	141679967	213.94
14)	C20	34.332	130046201	199.3
15)	C21	36.205	134980446	206.43
16)	C22	38.003	110003075	167.97
17)	C23	39.725	101669352	156.11
18)	C24	41.381	92193034	144.74
19)	C25	42.974	83497166	132.35
20)	C26	44.506	77402732	121.91
21)	C27	45.983	68096904	109.9
22)	C28	47.41	60733664	99.2
23)	C29	48.788	53811413	89.45
24)	C30	50.121	46883923	78.71
25)	C31	51.41	40580589	69.64
26)	C32	52.659	34145695	60.15
27)	C33	53.873	28987529	56
28)	C34	55.05	26027895	50.1
29)	C35	56.193	21691696	42.41
30)	C36	57.31	20511182	40.87
31)	C37	58.521	17252011	37.34
32)	C38	59.896	14796329	33.8
33)	C39	61.486	12241091	36.61
34)	C40	63.336	10707783	31.58

Table C-6. Pure SBA-15 (S1)

#	Compound	Retention time	Response factor	Concentration (ppm)
1)	C8	0	N.D.	
2)	C9	6.784	2965852	6.45
3)	C10	9.592	6015102	12.06
4)	C11	12.56	7997260	14.55
5)	C12	15.491	73647806	125.61
6)	C13	18.306	8254878	13.67
7)	C14	20.989	8569508	13.79
8)	C15	23.785	2934123	4.66
9)	C17	28.168	39130069	29.23
10)	pristane	28.167	39245881	29.43
11)	C18	30.339	3916005	5.92
12)	phytane	30.339	3546411	5.22
13)	C19	0	N.D.	
14)	C20	0	N.D.	
15)	C21	0	N.D.	
16)	C22	0	N.D.	
17)	C23	0	N.D.	
18)	C24	0	N.D.	
19)	C25	0	N.D.	
20)	C26	0	N.D.	
21)	C27	0	N.D.	
22)	C28	0	N.D.	
23)	C29	0	N.D.	
24)	C30	0	N.D.	
25)	C31	0	N.D.	
26)	C32	0	N.D.	
27)	C33	0	N.D.	
28)	C34	0	N.D.	
29)	C35	0	N.D.	
30)	C36	0	N.D.	
31)	C37	0	N.D.	
32)	C38	0	N.D.	
33)	C39	0	N.D.	
34)	C40	0	N.D.	

Table C-7. 10Co/SBA-15 (S2)

#	Compound	Retention time	Response factor	Concentration (ppm)
1)	C8	4.485	79086832	186.45
2)	C9	6.795	248698131	540.56
3)	C10	9.608	374261604	750.16
4)	C11	12.577	443250665	806.7
5)	C12	15.505	531141071	905.89
6)	C13	18.311	557913659	924
7)	C14	20.99	578145175	930.6
8)	C15	23.517	568153260	902.12
9)	C17	28.12	132546915	99.02
10)	pristane	28.273	593630201	445.14
11)	C18	30.351	572014606	865.4
12)	phytane	30.351	574038246	845.73
13)	C19	32.384	527330395	796.29
14)	C20	34.334	496210053	760.45
15)	C21	36.208	472135990	722.06
16)	C22	38.004	441734657	674.52
17)	C23	39.726	476747257	732.04
18)	C24	41.381	445856836	699.98
19)	C25	42.972	407522841	645.96
20)	C26	44.504	373429483	588.18
21)	C27	45.982	333322985	537.92
22)	C28	47.406	300580566	490.95
23)	C29	48.784	270638470	449.86
24)	C30	50.116	239135471	401.47
25)	C31	51.405	209666783	359.82
26)	C32	52.655	185376768	326.54
27)	C33	53.866	160659952	310.38
28)	C34	55.042	137345346	264.35
29)	C35	56.184	114431473	223.73
30)	C36	57.3	93421977	186.15
31)	C37	58.508	67481157	146.04
32)	C38	59.883	46905483	107.14
33)	C39	61.469	29336696	87.74
34)	C40	63.319	17657846	52.08

Table C-8. 10Co/1Ru/SBA-15 (S3)

#	Compound	Retention time	Response factor	Concentration (ppm)
1)	C8	4.486	5117252	12.06
2)	C9	6.795	60546206	131.6
3)	C10	9.607	184097679	369
4)	C11	12.577	301491983	548.71
5)	C12	15.507	406053068	692.54
6)	C13	18.313	396681067	656.97
7)	C14	20.987	406091950	653.65
8)	C15	23.512	397974348	631.91
9)	C17	28.131	62200473	46.47
10)	pristane	28.271	389772920	292.28
11)	C18	30.345	368952258	558.18
12)	phytane	30.345	369382264	544.21
13)	C19	32.375	348061509	525.59
14)	C20	34.326	328557511	503.52
15)	C21	36.203	329191122	503.45
16)	C22	38	340879138	520.51
17)	C23	39.726	285535200	438.44
18)	C24	41.382	264185942	414.76
19)	C25	42.974	240890329	381.83
20)	C26	44.504	272070999	428.53
21)	C27	45.984	197526720	318.77
22)	C28	47.41	179565860	293.29
23)	C29	48.788	159382291	264.93
24)	C30	50.12	144278827	242.22
25)	C31	51.411	161367036	276.93
26)	C32	52.66	110184516	194.09
27)	C33	53.872	94529322	182.62
28)	C34	55.048	83228638	160.19
29)	C35	56.191	72858917	142.45
30)	C36	57.309	42895238	85.47
31)	C37	58.519	61226994	132.5
32)	C38	59.891	73915706	168.83
33)	C39	61.487	58545753	175.1
34)	C40	63.338	59829798	176.48

Table C-9. 30Co/1Ru/SBA-15 (S4)

#	Compound	Retention time	Response factor	Concentration (ppm)
1)	C8	4.484	84534020	199.29
2)	C9	6.793	198600150	431.67
3)	C10	9.606	335907898	673.29
4)	C11	12.576	458440736	834.35
5)	C12	15.506	601925413	1026.61
6)	C13	18.312	615531203	1019.42
7)	C14	20.988	643890312	1036.42
8)	C15	23.518	624901929	992.23
9)	C17	28.272	605555503	452.39
10)	pristane	28.272	606109204	454.5
11)	C18	30.349	544279110	823.44
12)	phytane	30.349	550394303	810.9
13)	C19	32.382	511629206	772.58
14)	C20	34.331	473000991	724.88
15)	C21	36.205	460738399	704.63
16)	C22	38.001	401083079	612.44
17)	C23	39.723	367651358	564.53
18)	C24	41.377	335485911	526.7
19)	C25	42.969	304508447	482.67
20)	C26	44.5	278924049	439.32
21)	C27	45.977	248413052	400.89
22)	C28	47.404	222001375	362.61
23)	C29	48.78	194085131	322.61
24)	C30	50.113	170448279	286.15
25)	C31	51.403	148858817	255.46
26)	C32	52.651	127620959	224.8
27)	C33	53.863	107590980	207.86
28)	C34	55.039	93169688	179.33
29)	C35	56.183	76646074	149.85
30)	C36	57.299	66623233	132.75
31)	C37	58.507	51555055	111.57
32)	C38	59.881	40714249	93
33)	C39	61.465	29563157	88.42
34)	C40	63.315	21375818	63.05

**CALCULATION OF CONCENTRATION OF EACH FRACTION BY
COMPARING RESPONSE FACTORS**

Concentration of each fraction was determined using following equation:

$\mathbf{Concentration (C_n) = Response factor}_{(fr)} \frac{\mathbf{Concentration}_{(st)}}{\mathbf{Response factor}_{(st)}} \quad \mathbf{(3.6)}$
--

Concentration (C₈) in 10Co/1Ru/MWCNT is used as example for equation 3.6

$$Concentration (C_8) = Response factor_{(fr)} \times \frac{Concentration_{(st)}}{Response factor_{(st)}}$$

$$Response factor_{(fr)} = 14523891$$

$$Concentration_{(st)} = 514.04$$

$$Response factor_{(st)} = 218041688$$

$$Concentration (C_8) = 14523891 \times \frac{514.04 \text{ ppm}}{218041688} = 34.24 \text{ ppm}$$

APPENDIX D

XRD SPECTRUMS AND CALCULATION OF COBALT CRYSTALLITE
SIZE USING SCHERRER EQUATION

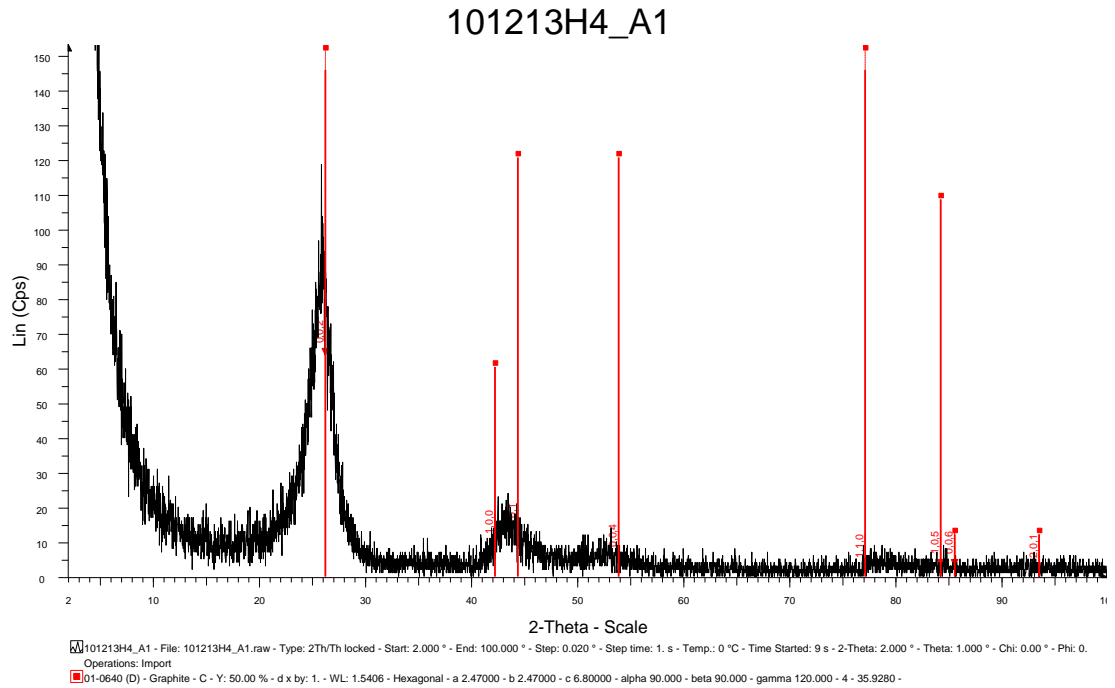


Figure D-1: XRD Spectrum of unpurified MWCNT

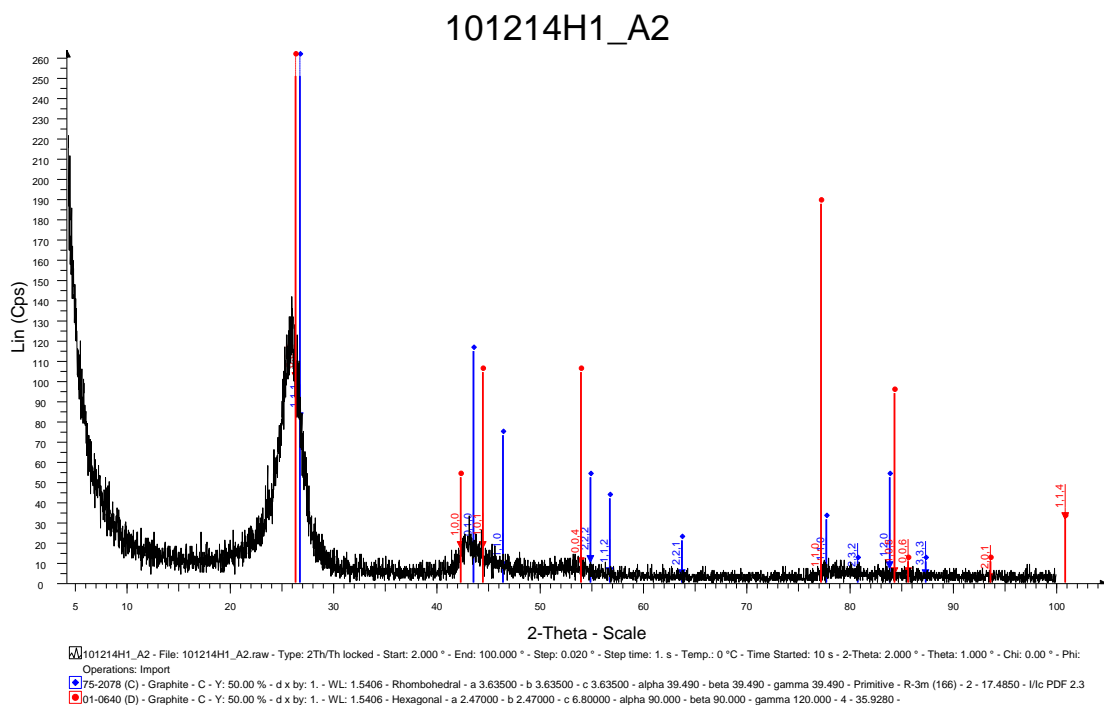


Figure D-2: XRD Spectrum of purified MWCNT

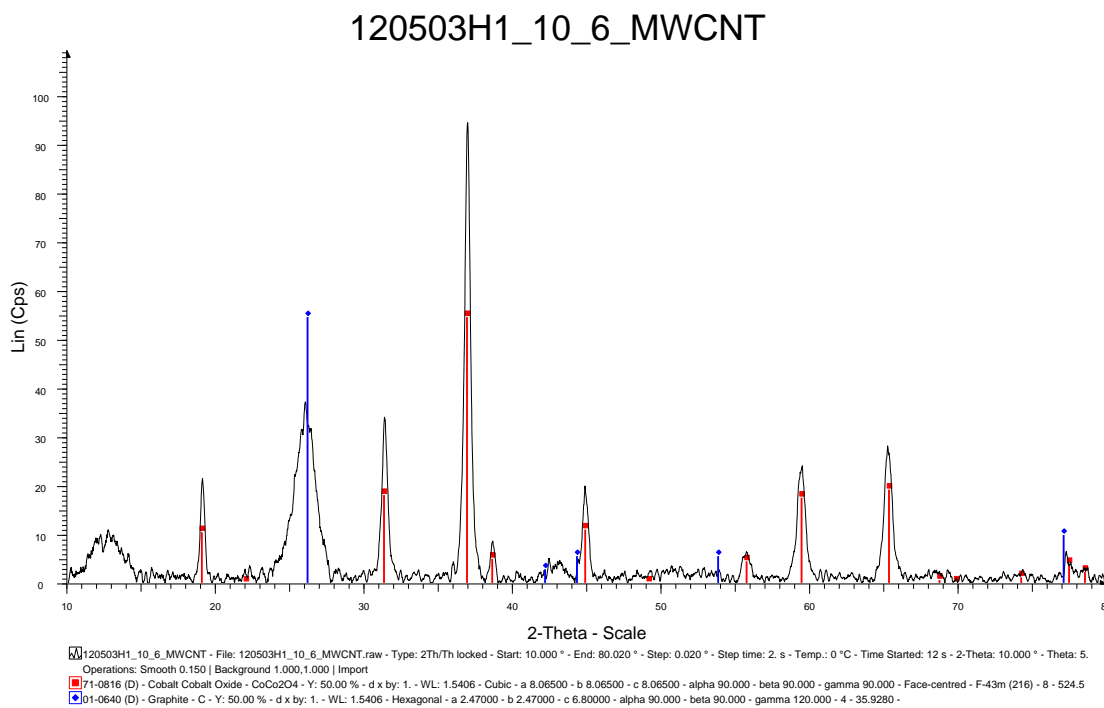


Figure D-3: XRD Spectrum of 10Co/MWCNT (M2) catalyst

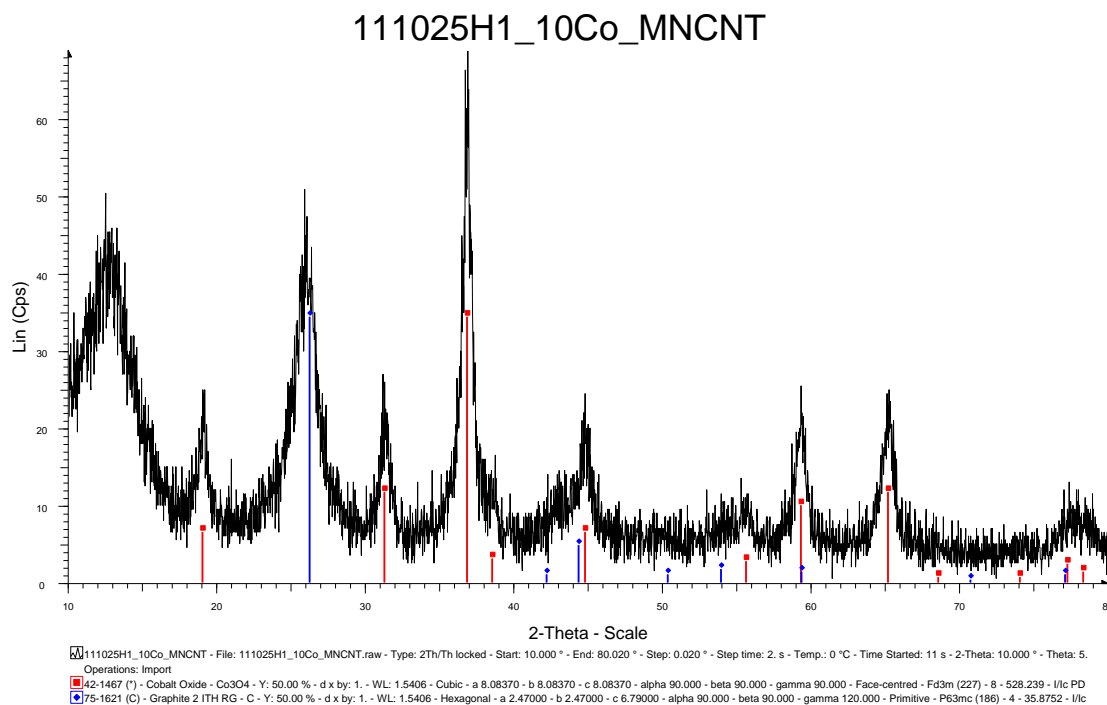


Figure D-4: XRD Spectrum of 10Co/1Ru/MWCNT (M3) catalyst

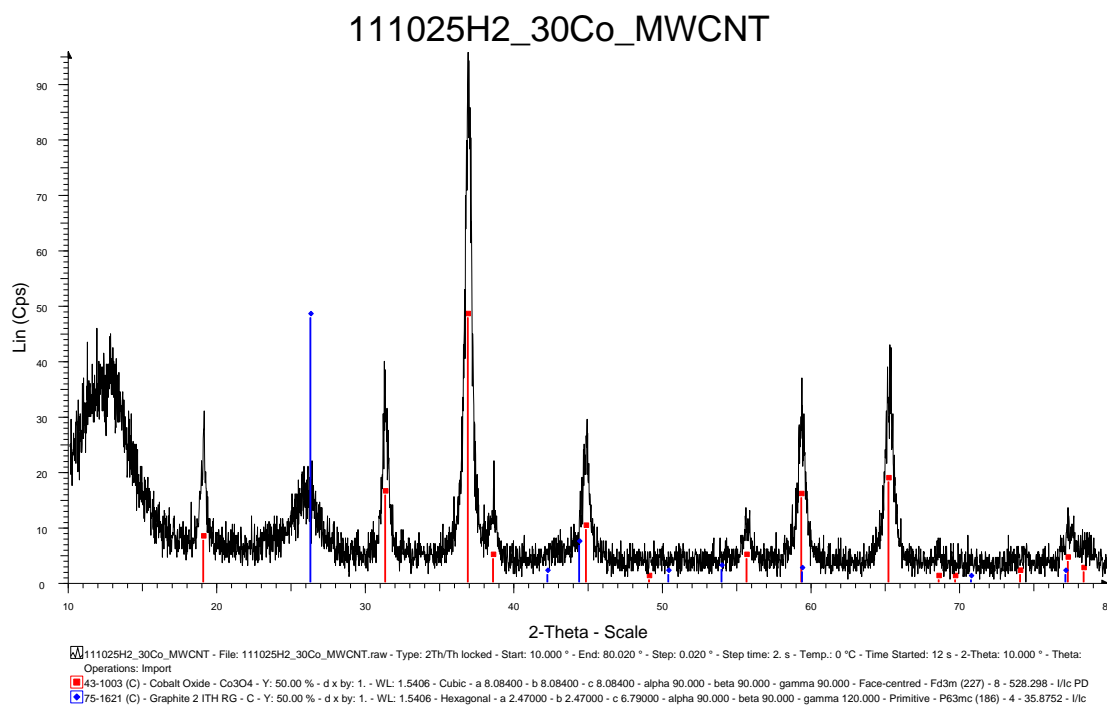


Figure D-5: XRD Spectrum of 30Co/1Ru/MWCNT (M4) catalyst

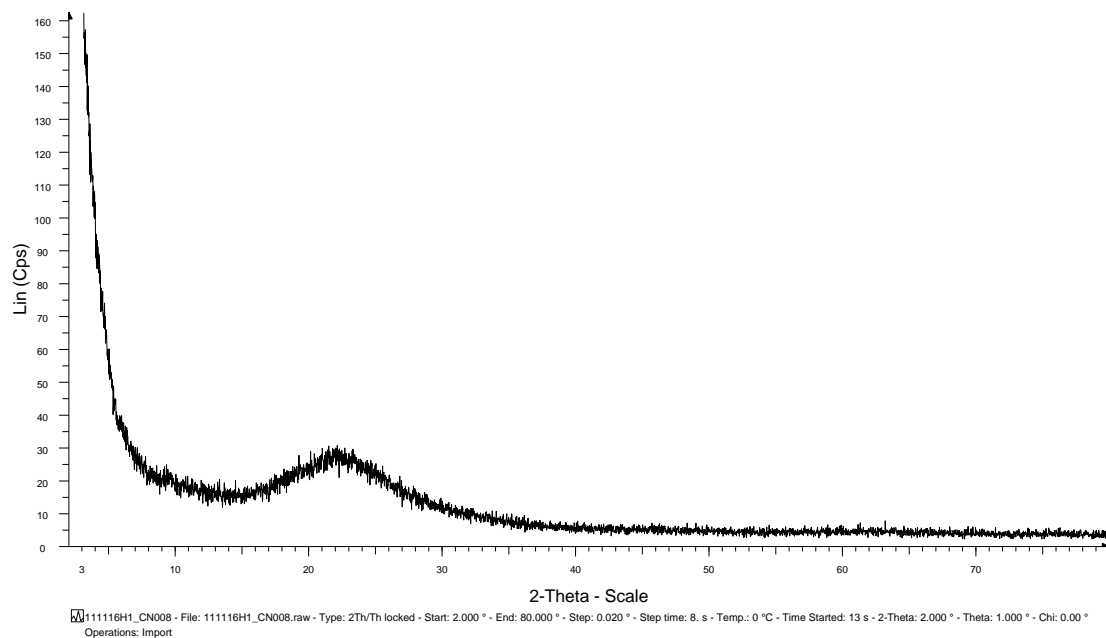


Figure D-6: XRD Spectrum of Pure SBA-15 (S1)

111024H1_10Co_SBA15

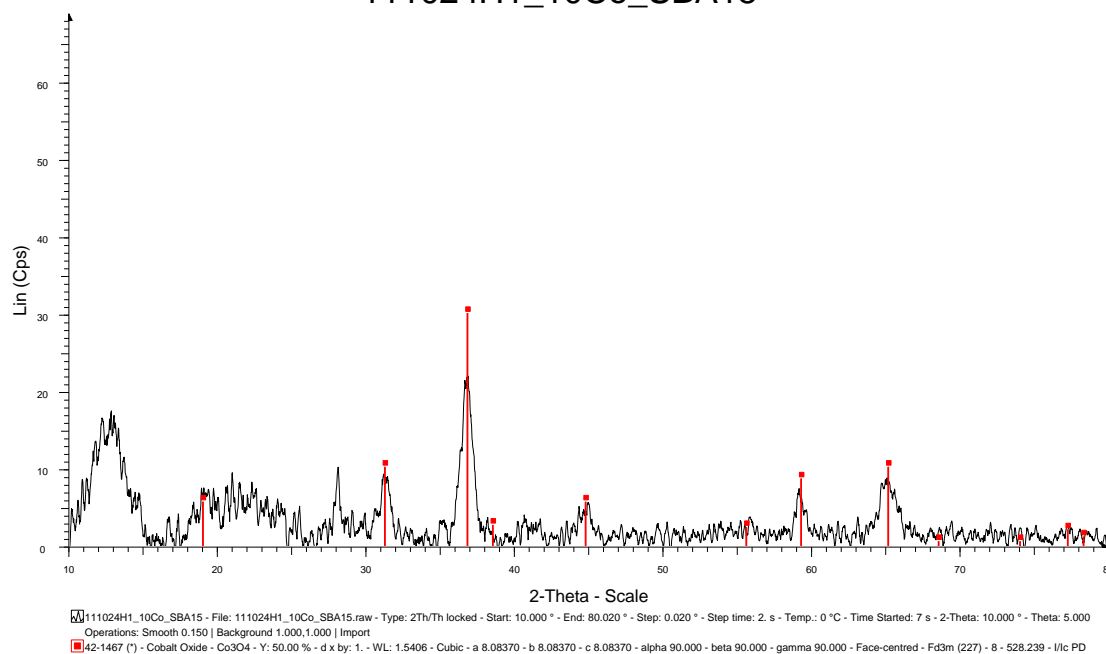


Figure D-7: XRD Spectrum of 10/SBA-15 (S2) catalyst

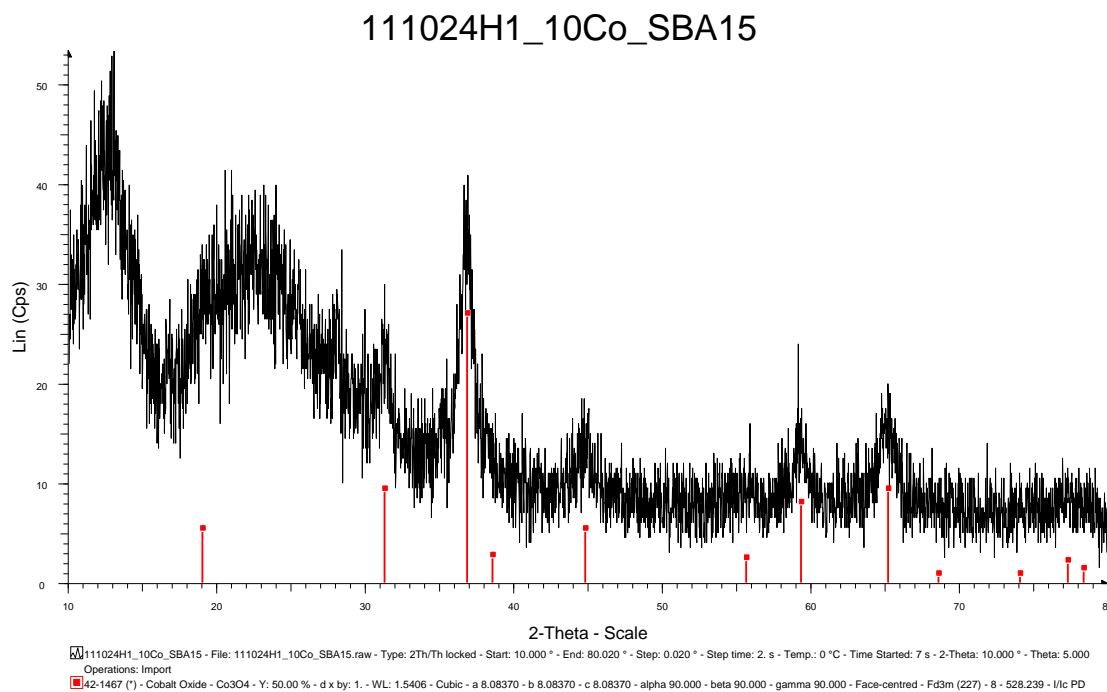


Figure D-8: XRD Spectrum of 10/1Ru/SBA-15 (S3) catalyst

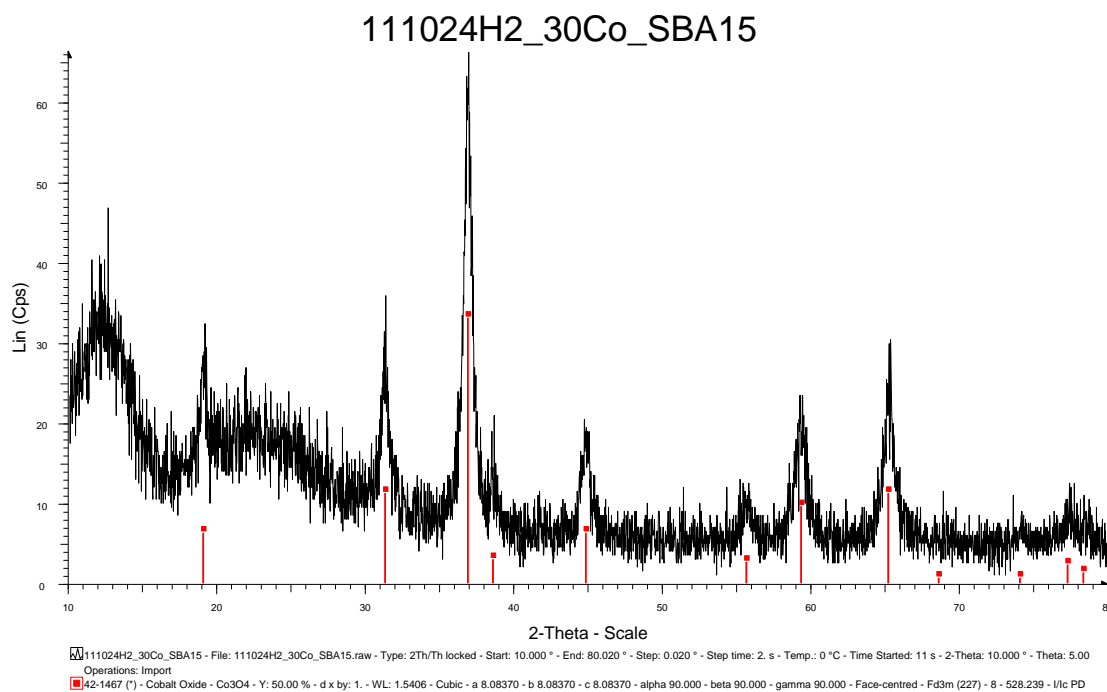


Figure D-9: XRD Spectrum of 30/1Ru/SBA-15 (S4) catalyst

CALCULATION OF COBALT CRYSTALLITE SIZE USING SCHERRER EQUATION

$$\tau = \frac{K\lambda}{\beta \cos \theta}$$

Where:

K – Shape factor, 0.89 [15] [59],

λ – X Ray Wavelength, 1.5405 Å

β – Line broadening at half the maximum intensity (FWHM) in radians

θ – The Bragg angle

Example of calculation for peak profile analysis (Sample 10Co/MWCNT (M2)):

Data obtained from XRD:

FWHM (°) β – 0.447,

Angle (2 θ) – 36.983

- Because of the unit for $\lambda=1.5405$ is given in Å, it is converted to nm by dividing to 10:

$$\frac{1.5405}{10} = 0.15405 \text{ nm}$$

- Angle (2 θ) was divided by 2 in order to get θ :

$$\frac{36.983}{2} = 18.4915$$

- The unit of FWHM is given in (°). It is converted from (°) to radian by being multiplied with $(\frac{\pi}{180})$

$$0.447 \times \frac{3.142}{180} = 0.00780$$

Hence:

$$D \text{ size} = \frac{0.89 \times 0.15405}{0.007802 \times \cos 18.4915} = 18.53 \text{ nm}$$

Accordingly other peaks for Co_3O_4 were calculated and average crystallite size was obtained:

$$\text{Average D} = \frac{23.22446 + 18.7584 + 18.53057 + 22.20075 + 14.23076 + 15.34933}{6} = 18.71 \text{ nm}$$